REVISTA MEXICANA
DE ASTRONOMÍA
Y ASTROFÍSICA

ISSN:3061-8649

Volume 61, Number 2
September, 2025

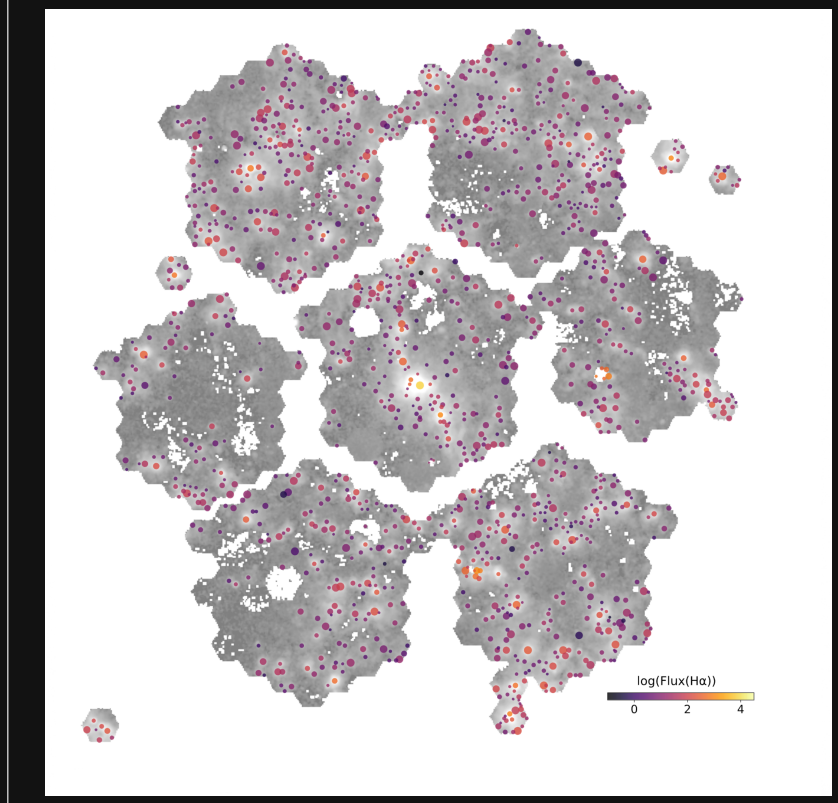

HII regions in grand design galaxy IC 342

Barrera-Ballesteros, J. K. et al., page 98 – 119

https://doi.org/10.22201/ia.01851101p.2025.61.02

The RMxAA paper template is based on the rho LaTeX class,
created by Luis Guillermo Jiménez López and Eduardo Gracidas Reyes.

Revista Mexicana de Astronomía y Astrofísica
Vol. 61, Number 2

Revista Mexicana de Astronomía y Astrofísica, 61, 1-10, (2025)

OPEN ACCESS https://doi.org/10.22201/ia.01851101p.2025.61.02.01

An Oscillating Rastall Universe Crossing the Phantom Divide Line

Nasr Ahmed[1,2], **Anirudh Pradhan**[3] **and Archana Dixit**[4]

[1]*Mathematics Department, Faculty of Science, Taibah University, Saudi Arabia.*
[2]*Astronomy Department, National Research Institute of Astronomy and Geophysics, Helwan, Cairo, Egypt.*
[3]*Centre for Cosmology, Astrophysics and Space Science (CCASS), GLA University, Mathura-281 406, Uttar Pradesh, India.*
[4]*Department of Mathematics, Gurugram University, Gurugram-122003, Haryana, India.*

Keywords: *Causality, Cyclic universe, Modified gravity, PACS number: 04.50+h, 04.20.Jb, 95.35+d, 98.80.Es, Phantom crossing*

Abstract

A cyclic flat universe with Quintom behavior and a future Big Rip as presented in the framework of Rastall gravity, which is an extension of the standard ΛCDM model. The Hubble parameter oscillates periodically between positive and negative values in each cycle. Cosmic transit has been simulated through an oscillating time-dependent deceleration parameter and is expected to occur at approximately 8.7 Gyr. Causality is satisfied at all times, except near the initial singularity and the future Big Rip singularity. The apparent horizon, entropy, and other thermodynamic quantities associated with the current model were analyzed. The energy conditions were investigated.

Resumen

Se presenta un modelo de universo plano y cíclico con comportamiento *Quintom* y *Big Rip* o gran desgarramiento futuro, en el contexto de gravedad tipo Rastall. El modelo es una extensión del modelo estándar ΛCDM. El parámetro de Hubble oscila periódicamente de un ciclo a otro entre valores positivos y negativos. El tránsito cósmico se ha simulado con un parámetro de desaceleración oscilante en el tiempo y se espera que ocurra en aproximadamente 8.7 Gyr. Se satisface la causalidad todo el tiempo, excepto en las singularidades inicial y la futura del *Big Rip*. Se analizan cantidades termodinámicas asociadas al modelo como horizonte aparente y entropía, entre otros. Se han investigado las condiciones energéticas.

Corresponding author: Nasr Ahmed *E-mail address:* abualansar@gmail.com
Received: February 11, 2025 **Accepted:** March 17, 2025

1. Introduction and Motivation

One of the most significant and fascinating phenomena in contemporary cosmology is the accelerating expansion of the universe. Our understanding of the composition and development of the cosmos underwent a paradigm shift when it was discovered in the late 1990s through the observation of Type Ia Supernovae (Perlmutter et al., 1999; Riess et al., 1998). Numerous independent observations, including large-scale structural surveys and measurements of cosmic microwave background radiation, support this groundbreaking discovery (Spergel et al., 2003a; Komatsu et al., 2009; Astier et al., 2006). At both large scales and strong curvature, the Einstein theory of General Relativity (GR) is inconsistent with observations. Cosmic acceleration has been a basic motivation behind modified gravity theories since it cannot be explained by GR without assuming dark energy (Riess et al., 1998; Copeland et al., 2006). Examples of such modified gravity theories are $f(R)$ gravity (Nojiri & Odintsov, 2006), Gauss-Bonnet gravity (Nojiri et al., 2008; Ahmed et al., 2023) where the Gauss-Bonnet term $\mathcal{G} = R^2 - 4R^{\mu\nu}R_{\mu\nu} + R^{\mu\nu\rho\delta}R_{\mu\nu\rho\delta}$ has been used in the action instead of the Ricci scalar R, and f(T) gravity (Ferraro & Fiorini, 2007) where the torsion scalar (T) has been used; the generalized $f(R,T)$ gravity, where T is the trace of the energy-momentum tensor. Additional examples include $\kappa(R,T)$ gravity (Ahmed & Pradhan, 2022) and extra-dimensional gravity theories (Overduin & Wesson, 1997; Sotiriou, 2011; Ahmed et al., 2020; Ahmed & Rafat, 2018).

Bouncing scenarios (also known as cyclic cosmology) were initially proposed as an alternative method to solve some of the problems of the standard model of cosmology, such as flatness and initial singularity. The universe in the singularity-free Big Bounce emerges from a previous contracting stage (Novello & Bergliaffa, 2008; Ijjas & Steinhardt, 2018; Sahoo et al., 2020; Nojiri et al., 2019), where the contraction-expansion cycle is assumed to continue forever. Cyclic cosmological models have been extensively studied through numerous modified gravity theories (Sahoo et al., 2020; Nojiri et al., 2019; Bamba et al.,

2014a,b, 2015; Tripathy et al., 2019; de la Cruz-Dombriz et al., 2018; Ahmed et al., 2022; Singh & Shukla, 2020). A general cyclic model in $f(R)$ gravity was constructed by Pavlovic & Sossich (2017). A unitary version of Conformal Cyclic Cosmology (CCC) was suggested by Frampton (2018). An M-theory-inspired cyclic model with two branes was presented by Steinhardt & Turok (2002), where the EoS parameter satisfies $\omega \gg 1$ during the contraction phase. A new cyclic theory of the universe was presented in Ijjas & Steinhardt (2019), where the scale factor increased exponentially from one cycle to the next. This recent cyclic model resolves many problems and generates a nearly scale-invariant spectrum of density perturbations. An interesting singularity-free oscillatory model was discussed by Sharma et al. (2023), where the late-time evolution was probed in the context of quasi-steady-state cosmology (QSSC) (Hoyle et al., 1993, 1994) to alleviate the Hubble tension. The cosmic scale factor parametrization has been chosen according to the description in (Hoyle et al., 1993, 1994, 1995; Sachs et al., 1996) as

$$a(t) = e^{t/P}\left[1 + \eta\cos(2\pi t/Q)\right]. \tag{1}$$

Here, η is a dimensionless constant, and P and Q have dimensions of time. In the limit when the dimensionless constant η approaches zero, a de Sitter-like evolution occurs. As time goes to zero, the scale factor tends to the value $1+\eta$, where no singularity exists.

Rastall gravity is one such modification, proposed by Peter Rastall in 1972 (Rastall, 1972). Rastall gravity (RG) is a modified theory of gravity that features a non-conserved stress-energy tensor and a peculiar non-minimal coupling between geometry and matter. This has become an interesting and important theory of gravity in modern times. The conservation law that demonstrates a divergence-free energy momentum tensor in general relativity (GR) has been accepted; that is, $\nabla_\nu T^{\mu\nu} = 0$, where ∇_ν is the covariant derivative. Rastall adopted a new and distinct conservation law that conjectured GR concepts. In this theory, the energy momentum tensor does not a conserved quantity. Rastall formulation is defined as $\nabla_\mu T^\mu_\nu = \left(\frac{\kappa}{16\pi}\right)\nabla_\nu R$, where κ is the coupling constant and R is the Ricci scalar. The second Bianchi identity in this theory remains the same i.e., $\nabla^\mu G_{\nu\mu} = 0$, where $G_{\mu\nu} = R_{\mu\nu} - \frac{1}{2}Rg_{\mu\nu}$ be the Einstein tensor. A notable feature of RG is that, whereas the mathematical component of this theory remains invariant, modifications have been applied exclusively to the matter component (De Moraes & Santos, 2019; Majernik & Richterek, 2006; Rastall, 1976). For the Rastall gravity framework, Visser (Visser, 2018) claimed that Rastall gravity may be completely equivalent to general relativity. In contrast, Darabi et al. (2018) have argued that Rastall gravity can be interpreted as a modified theory of gravity distinct from GR. Das et al. (2018) demonstrated that RG is equal to Einstein gravity and offered some cosmological implications in the structure of modified RG. Recently, Golovnev (2024) claimed that Rastall gravity may be equivalent to General Relativity by analyzing the claims of Visser (2018) and Darabi et al. (2018). The derivation of the action for Rastall gravity is subjected to the condition $\sqrt{-g} = 1$ (Golovnev, 2024). Holographic dark energy in RG was introduced by Ghaffari et al. (2020), considering vacuum energy, which serves as DE. They accepted the idea that the current accelerating cosmos is caused by the sum of this energy and the Rastall term. Assuming that the universe comprises interacting/non-interacting dark energy (DE) and dark matter (DM), Saleem & Shahnila (2021) investigated the phenomenon of cosmic evolution using curved FLRW spacetime bounded by an apparent horizon with a particular holographic cut-off in the framework of Rastall gravity. Saleem et al. (2024) recently introduced constant-roll warm inflation, a novel method for determining the precise inflationary solutions to the Friedman equations within the framework of Rastall theory of gravity (RTG). Using a linear parameterization of the Equation of State (EoS) in the FLRW background, Singh et al. (2024) examined the evolution of the universe within the framework of RTG. In the framework of RTG, Saleem & Hassan (2020) studied the dynamics of warm inflation induced by vector fields and concluded that the modified theory was compatible with the 2018 Planck observational data. In various contexts, several researchers have examined cosmological scenarios within the framework of Rastall gravity (Banerjee et al., 2023; Tangphati et al., 2023, 2024; Banerjee et al., 2024; Shaily et al., 2024; Singh et al., 2021, 2022; Singh & Pradhan, 2023; Singh & Mishra, 2020; Akarsu et al., 2020). This theory has received widespread attention in discussions and explanations of different phenomena related to the evolution of the universe. We aim to study the evolution of the universe exhibiting oscillatory expansion by analyzing its thermodynamic behavior. It is worth mentioning that Rastall gravity possesses oscillatory solutions subjected to a fixed point, which are marginally stable (Singh et al., 2021, 2022).

Models of dark energy that permit the equation of state parameter, w, to cross the “phantom divide line" (w=-1) investigate possibilities in which the expansion of the universe can go from accelerating to accelerating at an ever-increasing rate, which could result in a “Big Rip" (Astashenok & Tepliakov, 2022). The long-term destiny of the universe depends on our ability to comprehend dark energy and its behavior, particularly the potential for crossing the phantom divided line (PDL). Mohseni Sadjadi (2009) discusses the conditions required to cross the phantom divide line in a closed Friedmann-Robertson-Walker universe using an interacting holographic dark energy model. Huang et al. (2010) reconstitute the dark energy parameters from the most recent 397 Sne Ia, CMB, and BAO using three distinct parameterized dark energy models with the specified current matter density, Ω_{m0}. They discovered

that an evolving dark energy with a crossing of the phantom dividing line is preferred when Ω_{m0} is not modest, such as when $\Omega_{m0} = 0.28$ or 0.32. For a more in-depth understanding of this discovery, we recommend the following papers Fang et al. (2008); Wei & Cai (2006); Ahmed & Pradhan (2020); Varshney et al. (2021); Dixit et al. (2022); Debnath et al. (2022).

The acceleration of the expansion of the universe, which defies the predictions of General Relativity (GR) without including dark energy, is the driving force behind this investigation. Consequently, modified gravity theories have been examined, such as Rastall gravity, which adds a non-minimal link between geometry and matter and a non-conserved stress-energy tensor. The goal of the authors' cyclic universe model is to address problems such as the initial singularity and future Big Rip scenarios, in addition to Quintom behavior, which is the transition between quintessence and phantom phases with a crossing of the phantom dividing line.

The oscillating Hubble parameter that alternates between positive and negative values across cycles is the result of the authors' proposed periodic parametrization of the deceleration parameter in the current model. With an anticipated occurrence at approximately 8.7 Gyr, this periodic behavior effectively simulates cosmic transit by suggesting that the cosmos experiences periods of acceleration and deceleration. In addition to the area around the initial singularity and future Big Rip, the model satisfies causality. To ensure that the model is physically feasible, thermodynamic characteristics such as entropy and energy conditions were examined.

Owing to the ad hoc periodic parameterization of the deceleration parameter q with the correct sign flipping as $q = m\cos kt - 1$ (Shen & Zhao, 2014), the universe accelerates after an epoch of deceleration (for every single cycle), which agrees with recent observations. Such periodic form of q leads to the following forms for the Hubble parameter and scale factor

$$H = \frac{k}{m\sin kt + c}\ ,\ a = a_0\left[\tan(\frac{1}{2}kt)\right]^{\frac{1}{m}}, \tag{2}$$

where $m > 0$, $k > 0$ and k acts as a cosmic frequency parameter. This specific form of the deceleration parameter was first introduced by Shen & Zhao (2014), who constructed a new oscillating Quintom Model. Using the well known redshift relation $z = \frac{1}{a} - 1$ we get

$$t = \frac{2}{k}\tan^{-1}\frac{1}{a_0^m(z+1)^m}. \tag{3}$$

Observations suggest that the signature change of q occurs at $z = 0.64$ for $m = 1.55$ (Capozziello et al., 2014; Capozziello et al., 2015; Farooq et al., 2017; Moraes et al., 2016). Since cosmic transit happens when $q = 0\,(i.e.\,\ddot{a} = 0)$, we have

$$t_{q=0} = \frac{1}{k}\cos^{-1}\frac{1}{m} \approx 8.7\ \text{Gyr for } m = 1.55,\ k = 0.1. \tag{4}$$

The scale factor (2) suffers from a future Big Rip singularity, where the slope of $a(t)$ increases significantly and goes to infinity $\frac{da}{dt} \to \infty \Rightarrow$ which eventually tears apart the spacetime fabric.

2. Framework of the Model

Our goal is to obtain solutions by carefully considering the matter source and gravitational background. The basic idea behind Rastall gravity (Rastall, 1972) is that the energy-momentum conservation in GR can't be always valid in curved space-time and, instead of $T^{\mu\nu}_{;\mu} = 0$, we should have

$$T^{\mu\nu}_{;\mu} = \lambda R^{,\nu}, \tag{5}$$

which leads to the generalized field equations

$$G_{\mu\nu} + K\lambda g_{\mu\nu}R = KT_{\mu\nu}. \tag{6}$$

The GR is recovered for $\lambda = 0$. $G_{\mu\nu}$ is the Einstein tensor and K is the coupling constant. The FRW metric given by

$$ds^2 = -dt^2 + a^2(t)\left[\frac{dr^2}{1-\kappa r^2} + r^2d\theta^2 + r^2\sin^2\theta d\phi^2\right], \tag{7}$$

where $a(t)$ is the scale factor and κ is equal to 0 for a flat universe. Applying equation (6) to the metric (7) we obtain the cosmological equations as

$$3(1-4K\lambda)H^2 - 6K\lambda\dot{H} + 3(1-2K\lambda)\frac{\kappa}{a^2} = K\rho, \tag{8}$$

$$3(1-4K\lambda)H^2 + 2(1-3K\lambda)\dot{H} + (1-6K\lambda)\frac{\kappa}{a^2} = -Kp. \tag{9}$$

In the current work, we are interested only in the observationally supported flat case where $\kappa = 0$ (Tegmark et al., 2004; Bennett et al., 2003; Spergel et al., 2003b; Ahmed & Alamri, 2019a). The energy density ρ, cosmic pressure p and EoS parameter ω are written as

$$\rho = -\frac{1}{K}\left(12\lambda KH^2 + 6\lambda K\dot{H} - 3H^2\right), \tag{10}$$

$$p = \frac{1}{K}\left(12\lambda KH^2 + 6\lambda K\dot{H} - 3H^2 - 2\dot{H}\right), \tag{11}$$

where the dot denotes differentiation w.r.t time and the EoS parameter $\omega = p/\rho$. Equations (10) and (11) show that

$$p = -\rho - \frac{2}{K}\dot{H}, \tag{12}$$

where $\dot{H}$ expresses the rate of change of the Hubble parameter as

$$\dot{H} = -\frac{K}{2}(\rho + p) = -\frac{K}{2}(\gamma\rho). \tag{13}$$

We have considered the EoS $p = (\gamma - 1)\rho$ with $\frac{2}{3} \le \gamma \le 2$. As pointed out by Bamba et al. (2018), inserting this

equation for $\dot{H}$ in Eq. (8) for the flat case results in.

$$H^2 = \frac{K\rho(3K\lambda\gamma - 1)}{3(4k\lambda - 1)}. \tag{14}$$

The physical behavior of the energy density is shown in Figure 1. The pressure changes from positive in a decelerating era to negative in an accelerating era dominated by dark energy with negative pressure. As a function of redshift, The EoS parameter $\omega(z)$ meets -1 at $z = 0$. The time evolution of the EoS parameter reveals quintum behavior as it passes the phantom divide line in the far future. The Hubble parameter H decreases during expansion as $\dot{H} < 0$, whereas it increases during contraction as $\dot{H} > 0$. The general dynamical behavior can be deduced from the negative values of q. In each cycle, the EoS parameter $\omega(t)$ lies between -2.25 and $\frac{1}{3}$, which agrees with the observations (Komatsu et al., 2011; Eisenstein et al., 2005). It starts from a positive value (radiation-like era), continues to decrease to zero (dust era $\omega = 0$), and finally passes to negative values. After reaching the DE-dominated era, it crosses the cosmological constant boundary to the phantom era, where $\omega < -1$ possesses a Quintom feature. The Quintom dynamics associated with the crossing of the phantom divide line leads to $\omega < -1$ today, which is also observationally supported (Zhao et al., 2007). A cosmological bouncing Quintom model was studied by Cai et al. (2007). ω is an increasing function in the second half of the cosmic cycle, starting from -2.25. Some observations favor DE with ω less than -1 (Vikman, 2005; Allen et al., 2004; Riess et al., 2004). Whether DE can evolve into the phantom era has been extensively investigated. In Vikman (2005), it was shown that in a DE dominated universe, the transition of DE from $\omega \geq -1$ to $\omega < -1$ cannot be explained by models of classical scalar field dynamics unless more complicated physics is included (Armendáriz-Picón, 2004; Feng et al., 2005; Sahni & Shtanov, 2003).

3. Work Density and Entropy

In this section, we calculate and analyze some thermodynamic quantities. The $(n+1)$-dimensional FRW metric is written as

$$ds^2 = -dt^2 + a^2(t)\left(\frac{dr^2}{1-\kappa r^2} + r^2 d\Omega^2_{n-1}\right), \tag{15}$$

where the line element of an $(n-1)$-dimensional unit sphere is denoted by Ω^2_{n-1}. This metric can also be written as (Bak & Rey, 2000)

$$ds^2 = h_{ab}dx^a dx^b + \widetilde{r}^2\Omega^2_{n-1}, \tag{16}$$

where $\widetilde{r} = a(t)r$, $x^0 = t$, $x^1 = r$ and the 2-dimensional metric $h_{ab} = diag(-1, \frac{a^2}{1-\kappa r^2})$. The apparent horizon is defined geometrically as an imaginary surface beyond which the null geodesic congruences recede from the observer (Saha, 2018). It is a dynamical structure that evolves with time and is determined by the relation $h_{ab}\partial_a\widetilde{r}\partial_b\widetilde{r} = 0$. This leads to the expression of the apparent horizon's radius in terms of the Hubble parameter as

$$\widetilde{r}_A = \frac{1}{\sqrt{H^2 + \frac{\kappa}{a^2}}}. \tag{17}$$

For a flat universe (the case considered here), the apparent horizon radius is the inverse of the Hubble parameter $1/H$, which is the same definition as the Hubble horizon $\widetilde{r}_H$. That means

$$\widetilde{r}_A = \widetilde{r}_H = \frac{1}{H}, \quad \text{for} \quad \kappa = 0. \tag{18}$$

Consequently, the rate of change of the horizon radius $\dot{\widetilde{r}}_A = -\frac{\dot{H}}{H^2} = -\widetilde{r}_A^2\dot{H}$ or can be written in general as

$$\dot{\widetilde{r}}_A = -\widetilde{r}_A^3 H\left(\dot{H} - \frac{\kappa}{a^2}\right). \tag{19}$$

The work density W is defined as the work performed by the cosmic volume change owing to the change in the radius of the apparent horizon. For the current model we get

$$W = -\frac{1}{2}T^{ab}h_{ab} = \frac{1}{2}(\rho - p) \tag{20}$$

$$= -\frac{1}{K}\left(12\lambda KH^2 + 6\lambda K\dot{H} - 3H^2 - \dot{H}\right). \tag{21}$$

In the case of FRW spacetime with a perfect fluid, the surface gravity κ_{sg} is also defined as

$$\kappa_{sg} = \frac{1}{2\sqrt{-h}}\partial_a(\sqrt{-h}h^{ab}\partial_b\widetilde{r}_A) = -\frac{1}{\widetilde{r}_A}\left(1 - \frac{1}{2}\frac{\dot{\widetilde{r}}_A}{H\widetilde{r}_A}\right), \tag{22}$$

where h is the determinant of h_{ab}. In terms of κ_{sg}, the temperature on the horizon is given as $\frac{|\kappa_{sg}|}{2\pi}$

$$T_A = \frac{1}{2\pi\widetilde{r}_A}\left|1 - \frac{1}{2}\frac{\dot{\widetilde{r}}_A}{H\widetilde{r}_A}\right|. \tag{23}$$

Therefore, the temperature depends on the Hubble parameter H, the radius of the apparent horizon $\widetilde{r}_A$ and its rate of change during evolution $\dot{\widetilde{r}}_A$ which is a result of the dynamical nature of the apparent horizon. If the change in the apparent horizon is very slow, then $\frac{\dot{\widetilde{r}}_A}{H\widetilde{r}_A} \ll 1$ and we obtain the expression for Hawking temperature $T_H = \frac{1}{2\pi\widetilde{r}_A}$ which resembles the temperature of a spherically symmetric black hole with horizon radius $\widetilde{r}_A$ (Sánchez & Quevedo, 2023).

The modified Bekenstein-Hawking entropy in Rastall gravity on the apparent horizon is given as (Bamba et al., 2018; Moradpour & Salako, 2016)

$$\widetilde{S} = \left(1 + \frac{2\gamma}{4\gamma - 1}\right)S_0, \tag{24}$$

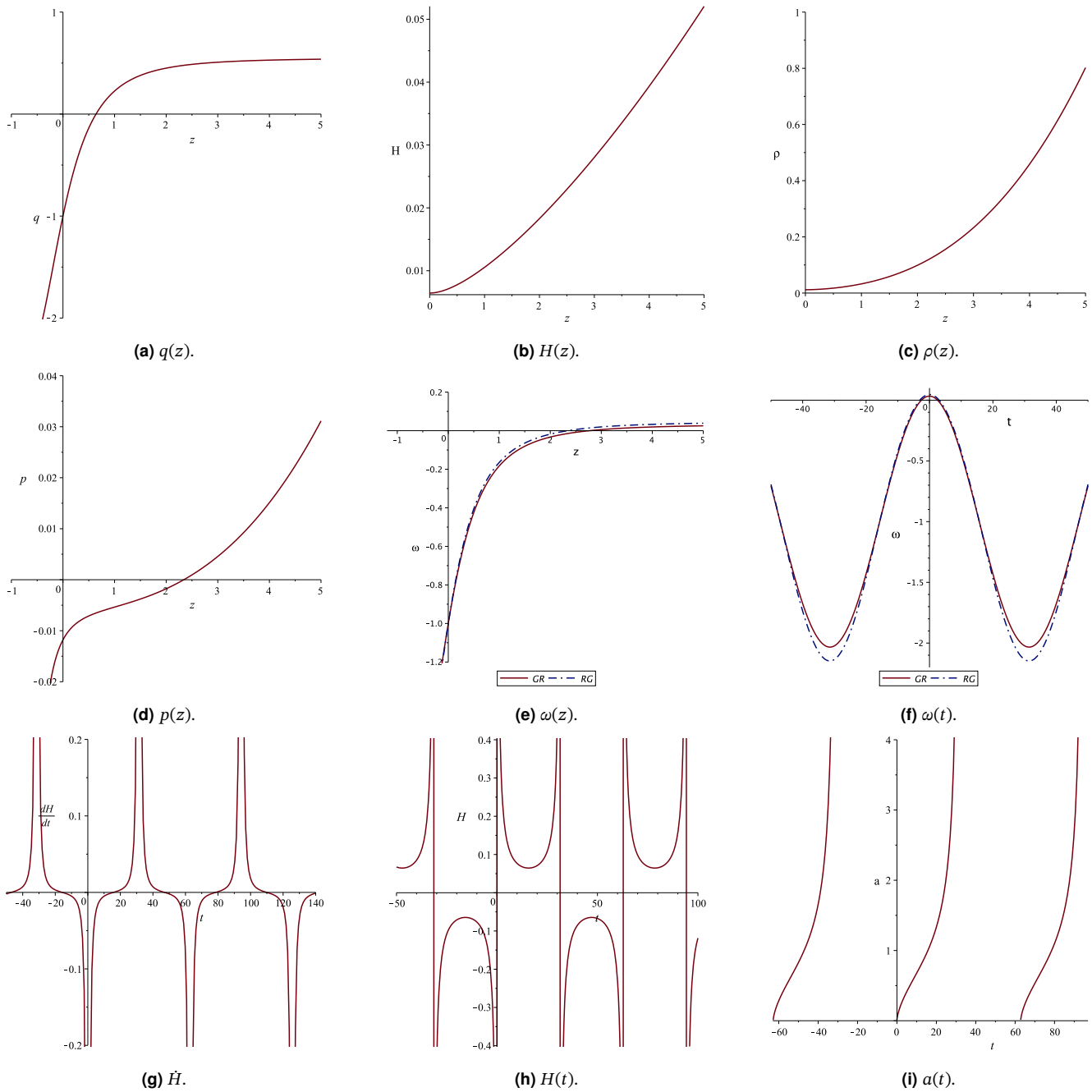

(a) $q(z)$. **(b)** $H(z)$. **(c)** $\rho(z)$.

(d) $p(z)$. **(e)** $\omega(z)$. **(f)** $\omega(t)$.

(g) $\dot{H}$. **(h)** $H(t)$. **(i)** $a(t)$.

Figure 1. Evolution of the model parameters against the redshift z (a) The DP $q(z)$ changes sign for $m > 1$ and equals -1 at $z = 0$. (b) The Hubble parameter $H(z)$. (c) Physical behavior of energy density $\rho(z)$. (d) A sign flipping in the evolution of cosmic pressure $p(z)$ (e) The EoS parameter $\omega(z)$ equals to -1 at $z = 0$. (f) $\omega(t)$ evolution shows a Quintum behavior, where it crosses the phantom divide line at very late times. GR stands for General Relativity and RG for Rastall Gravity. (g) The rate of change of the Hubble parameter $\dot{H} < 0$ during the expansion, which means a decreasing H, whereas this rate is > 0 during the contraction. (h) The Hubble parameter $H > 0$ during expansion and $H < 0$ during contraction. (i) The evolution of the scale factor shows an enormous increase over a short period of time (a future big rip). The unit of time t is taken as Gyr. Here $m = 1.55$, $\lambda = 1.4$, $K = 0.01$, $k = 0.1$ and $a_0 = 1$.

with $S_0 = \frac{A}{4}$ is the Bekenstein-Hawking entropy on the apparent horizon and $A = 4\pi\tilde{r}_A^2$ is the area. The normal Bekenstein-Hawking entropy in GR is recovered for $\gamma \to 0$. So, the area $A = 4\pi\tilde{r}_A^2$ is related to the modified area $\tilde{A}$ by $\tilde{A} = (1 + \frac{2\gamma}{4\gamma-1})A$ where the units $c = G = \hbar = 1$ has been considered. As a function of cosmic time t, the entropy should always be an increasing function, where the Universe evolves to the equilibrium state of maximum entropy. That means the two conditions

$$\dot{S} \geq 0 \quad \text{and} \quad \ddot{S} \leq 0, \tag{25}$$

should be satisfied. We recall that for a system at equilibrium, entropy has the maximum value, which means that it cannot increase anymore. On the other hand, any decrease is not possible as it violates the second law of thermodynamics which states that

$$d(S_m + S_h) > 0, \tag{26}$$

where S_h is the horizon entropy and S_m is the entropy of the entire matter field. At the apparent horizon, the FRW equations can be written as $dE = TdS + WdV$ where E is the total energy and $W = \frac{1}{2}(\rho - p)$ is the work density (Cai & Kim, 2005; Akbar & Cai, 2007). The cosmological work density is related to the cosmological constant in Ahmed & Alamri (2019b). The thermodynamic quantities w, $\tilde{r}_A$, $T_A =$ and S can be expressed as a function of the redshift z to probe their behavior. Figure 2 shows that the work density W has the same physical behavior as the energy density ρ versus z. In terms of cosmic time, it is a decreasing function during expansion, which means that the work done by the cosmic volume change decreases, resulting from variations in the apparent horizon radius. The first derivative of the event horizon radius is positive during expansion $\dot{\tilde{r}}_A > 0$ and negative during contraction $\dot{\tilde{r}}_A < 0$. A comparison between the evolution of the Hawking temperature T_H and the temperature on the horizon T_A as a function of z is shown in Figure 2c. Entropy $\tilde{S}$ is always positive. While the condition $\dot{\tilde{S}} > 0$ is satisfied, the non-positivity of the equilibrium condition $\ddot{\tilde{S}}$ exists only for the second half of the cosmic cycle.

4. Causality and Energy Conditions

One way to investigate physical acceptability is to test the classical linear energy conditions (ECs) (Hawking & Ellis, 1973; Wald, 1984), as the quantum corrections are ignored in the present model. The null, weak, strong, and dominant ECs are $\rho + p \geq 0$, $\rho \geq 0$, $\rho + p \geq 0$, $\rho + 3p \geq 0$ and $\rho \geq |p|$. These linear conditions cannot be satisfied in the presence of quantum effects (Martín-Moruno & Visser, 2013). The strong energy condition (SEC), for example, implies that gravity should always be attractive, which is not realistic when describing cosmic acceleration or inflation (Visser, 1997), (Visser, 1997). For the present model,

$$\begin{aligned} \rho + p &= -\frac{2}{K}\dot{H}, \\ \rho - p &= -\frac{2}{K}(12\lambda KH^2 + 6\lambda K\dot{H} - 3H^2 - \dot{H}), \\ \rho + 3p &= \frac{6}{K}(4\lambda KH^2 + 2\lambda K\dot{H} - H^2 - \dot{H}). \end{aligned}$$

The SEC is not expected to be valid during the negative pressure-dominated accelerating era, as negative pressure represents a repulsive gravity effect. The DEC is valid at all times for this model, which is expected, as it implies the non-negativity of the energy density. The SEC is valid only with the domination of attractive gravity in the decelerating era (at the first half of each cycle), and then becomes invalid with the domination of repulsive gravity during the accelerating era.

The causality condition for the adiabatic square sound speed $0 \leq \frac{dp}{d\rho} \leq 1$ should be satisfied through cosmic evolution. For the current model, using (10) and (11), we get

$$c_s^2 = -\frac{1}{3}\frac{12\lambda KH\dot{H} + 3\lambda K\ddot{H} - 3H\dot{H} - \dddot{H}}{4\lambda KH\dot{H} + \lambda K\ddot{H} - H\dot{H}}. \tag{27}$$

Figure 2h shows that the causality is satisfied except near the initial and the future Big Rip singularities

5. Conclusions

We presented a cyclic cosmological model of a flat universe with a future Big Rip singularity in the framework of Rastall gravity. The model possesses a Quintom behavior where the EoS parameter crosses the phantom divide line (cosmological constant boundary) at $\omega = -1$. In such oscillatory cosmic evolution, the deceleration-to-acceleration cosmic transit occurs at approximately 8.7Gyr. A recent analysis that included data from cosmic chronometers and the Pantheon compilation of supernovae calculated the transition redshift to be $z_t = 0.61^{+0.24}_{-0.16}$ (Yang & Gong, 2020). Given that the universe is currently 13.8 Gyr old, this correlates to a transition period of roughly 7.5 to 9.8 Gyr ago. A transition redshift of $z_t = 0.60^{+0.21}_{-0.12}$ was discovered by another study that looked at a parametrization of the deceleration parameter (Arora & Sahoo, 2024). This estimate, which places the transition era between 7.7 and 9.6 Gyr ago, is in good agreement with the previous one. A cosmic deceleration-to-acceleration transition that occurred approximately 8.7 Gyr ago is within the observed range based on these observational estimations. Thus, our conclusion seems to be in accordance with recent evidence from observations.

The EoS parameter ω meets -1 at redshift $z = 0$. The model exhibits the correct physical evolution of energy density and a sign flipping of cosmic pressure compatible with cosmic transit. Observational evidence supports that the EoS parameter ω is close to -1 at the present epoch (redshift $z = 0$) (Tripathi et al., 2017; Dinda & Banerjee, 2024).

The first derivative of the Hubble parameter $\dot{H}$ is negative during expansion, which means a decreasing H, and positive during contraction, which means an increasing H. The EoS parameter ω lies in the range $-2.25 \leq \omega(t) \lesssim \frac{1}{3}$. It begins in the radiation-like era, then passes through the dust era, the current dark energy-dominated era, before crossing the cosmological constant boundary to the phantom era. Simultaneously, plotting the ω evolution in Rastall Gravity (RG) and General relativity (GR) together shows a tiny difference between the two curves.

The evolution of the temperature on the dynamical horizon and Hawking temperature has been plotted against

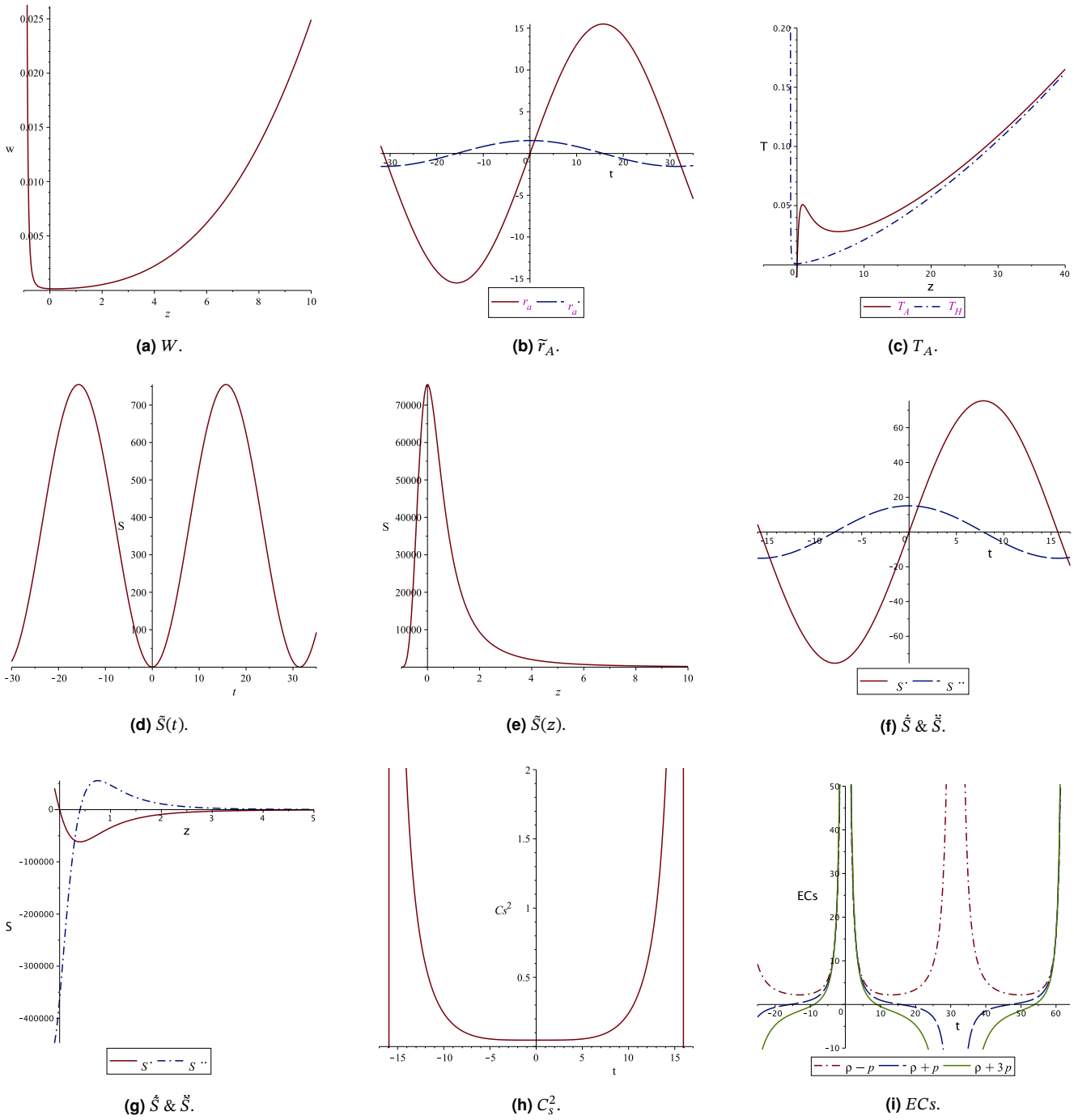

(a) W. **(b)** $\widetilde{r}_A$. **(c)** T_A.

(d) $\tilde{S}(t)$. **(e)** $\tilde{S}(z)$. **(f)** $\dot{\tilde{S}}$ & $\ddot{\tilde{S}}$.

(g) $\dot{\tilde{S}}$ & $\ddot{\tilde{S}}$. **(h)** C_s^2. **(i)** ECs.

Figure 2. (a) Work density versus redshift. (b) Radius of the apparent horizon versus redshift. (c) Temperature on dynamical horizon versus Hawking temperature of a spherically symmetric black hole. (d) & (e) evolution of entropy versus t and z shows that $\tilde{S} \geq 0$. (f) $S(\dot{\tilde{t}})$ and $S(\ddot{\tilde{t}})$, while the condition $\dot{\tilde{S}} > 0$ is satisfied, the non-positivity of the equilibrium condition $\ddot{\tilde{S}} < 0$ exists only for the second half of cosmic cycle. (g) $S(\dot{\tilde{z}})$ and $S(\ddot{\tilde{z}})$. A violation of $S(\ddot{\tilde{t}}) < 0$ starts at $z \gtrapprox 0.4$ (h) The causality condition $0 \leq \frac{dp}{d\rho} \leq 1$ is satisfied except near the initial and the future Big Rip singularities (i) Linear energy conditions. Here $m = 1.55$, $\lambda = 1.4$, $K = 0.01$, $k = 0.1$ and $a_0 = 1$.

redshift. The entropy in the model was always positive. It starts as an increasing function of time in the first expanding half-cycle until it reaches the maximum value corresponding to the equilibrium state. The rate of change of entropy along with the equilibrium condition was calculated and plotted. The causality is satisfied all the time except near the initial singularity and the future Big Rip singularity.

In order to solve problems such as the initial singularity and future big rip situations, the oscillating Rastall universe model sets itself apart by including Rastall gravity to produce a cyclic cosmological model with

Quintom behavior. However, other studies have used alternative processes to help transcend the phantom divide, including parameterized post-Friedmann approaches, two-field models, holographic dark energy models, and gravity modifications such as $f(Q)$ gravity. To address the difficulties in simulating the accelerated expansion of the universe and the dynamic characteristics of the equation of state for dark energy, each framework provides distinct perspectives and approaches. The Introduction contains a comprehensive discussion with up-to-date references.

It is pertinent to investigate an oscillating Rastall universe that crosses the phantom division line because it provides a theoretical foundation for investigating dynamic dark energy models and possible gravitational alterations. Therefore, our research is useful and pertinent to the oscillating Rastall cosmos.

The authors (A. Pradhan & A. Dixit) are grateful for the resources and support provided during their visit to the Inter-University Centre for Astronomy & Astrophysics (IUCAA), Pune, India, as part of their Associateship program. To improve the manuscript in its current form, the authors would like to thank the anonymous reviewer for their insightful remarks.

References

Ahmed, N., & Alamri, S. Z. 2019a, IJGMMP, 16, 1950159, doi: 10.1142/S0219887819501597

—. 2019b, CJPh, 97, 1075, doi: 10.1139/cjp-2018-0635

Ahmed, N., Alfreedi, A. A., & Alzulaibani, A. A. 2023, IJGMMP, 20, 2350053, doi: 10.1142/S0219887823500536

Ahmed, N., Bamba, K., & Salama, F. 2020, IJGMMP, 17, 2050075, doi: 10.1142/S0219887820500759

Ahmed, N., Kamel, T. M., & Nouh, M. I. 2022, RMxAA, 58, 245, doi: 10.22201/ia.01851101p.2022.58.02.07

Ahmed, N., & Pradhan, A. 2020, NewA, 80, 101406, doi: 10.1016/j.newast.2020.101406

—. 2022, InJPh, 96, 301, doi: 10.1007/s12648-020-01948-4

Ahmed, N., & Rafat, H. 2018, IJGMMP, 15, 1850131, doi: 10.1142/S0219887818501311

Akarsu, Ö., Katırcı, N., Kumar, S., et al. 2020, EPJC, 80, 1050, doi: 10.1140/epjc/s10052-020-08586-4

Akbar, M., & Cai, R.-G. 2007, PhRvD, 75, 084003, doi: 10.1103/PhysRevD.75.084003

Allen, S. W., Schmidt, R. W., Ebeling, H., Fabian, A. C., & Van Speybroeck, L. 2004, MNRAS, 353, 457, doi: 10.1111/j.1365-2966.2004.08080.x

Armendáriz-Picón, C. 2004, JCAP, 2004, 007, doi: 10.1088/1475-7516/2004/07/007

Arora, S., & Sahoo, P. 2024, PDU, 45, 101510, doi: https://doi.org/10.1016/j.dark.2024.101510

Astashenok, A. V., & Tepliakov, A. 2022, Univ, 8, 265, doi: 10.3390/universe8050265

Astier, P., Guy, J., Regnault, N., et al. 2006, A&A, 447, 31, doi: 10.1051/0004-6361:20054185

Bak, D., & Rey, S.-J. 2000, CQGra, 17, L83, doi: 10.1088/0264-9381/17/15/101

Bamba, K., Jawad, A., Rafique, S., & Moradpour, H. 2018, EPJC, 78, 986, doi: 10.1140/epjc/s10052-018-6446-0

Bamba, K., Makarenko, A. N., Myagky, A. N., Nojiri, S., & Odintsov, S. D. 2014a, JCAP, 2014, 008, doi: 10.1088/1475-7516/2014/01/008

—. 2014b, JCAP, 2014, 008, doi: 10.1088/1475-7516/2014/01/008

Bamba, K., Makarenko, A. N., Myagky, A. N., & Odintsov, S. D. 2015, JCAP, 2015, 001, doi: 10.1088/1475-7516/2015/04/001

Banerjee, A., Islam, S., Dixit, A., & Pradhan, A. 2024, GrCo, 30, 496, doi: 10.1134/S0202289324700397

Banerjee, A., Tangphati, T., Hansraj, S., & Pradhan, A. 2023, AnPhy, 451, 169267, doi: https://doi.org/10.1016/j.aop.2023.169267

Bennett, C. L., Halpern, M., Hinshaw, G., et al. 2003, ApJS, 148, 1, doi: 10.1086/377253

Cai, R.-G., & Kim, S. P. 2005, JHEP, 2005, 050, doi: 10.1088/1126-6708/2005/02/050

Cai, Y.-F., Qiu, T., Zhang, X., Piao, Y.-S., & Li, M. 2007, JHEP, 2007, 071, doi: 10.1088/1126-6708/2007/10/071

Capozziello, S., Farooq, O., Luongo, O., & Ratra, B. 2014, PhRvD, 90, 044016, doi: 10.1103/PhysRevD.90.044016

Capozziello, S., Luongo, O., & Saridakis, E. N. 2015, PhRvD, 91, 124037, doi: 10.1103/PhysRevD.91.124037

Copeland, E. J., Sami, M., & Tsujikawa, S. 2006, IJMPD, 15, 1753, doi: 10.1142/S021827180600942X

Darabi, F., Moradpour, H., Licata, I., Heydarzade, Y., & Corda, C. 2018, EPJC, 78, 25, doi: 10.1140/epjc/s10052-017-5502-5

Das, D., Dutta, S., & Chakraborty, S. 2018, EPJC, 78, 810, doi: 10.1140/epjc/s10052-018-6293-z

de la Cruz-Dombriz, A., Farrugia, G., Said, J. L., & Gómez, D. S.-C. 2018, PhRvD, 97, 104040, doi: 10.1103/PhysRevD.97.104040

De Moraes, W. A. G., & Santos, A. F. 2019, GeReG, 51, 167, doi: 10.1007/s10714-019-2652-9

Debnath, U., Chakraborty, S., Maity, S., & Pradhan, A. 2022, IJMPA, 37, 2250198, doi: 10.1142/S0217751X22501986

Dinda, B. R., & Banerjee, N. 2024, EPJC, 84, 688, doi: 10.1140/epjc/s10052-024-13064-2

Dixit, A., Maurya, D. C., & Pradhan, A. 2022, IJGMMP, 19, 2250198, doi: 10.1142/S0219887822501985

Eisenstein, D. J., Zehavi, I., Hogg, D. W., et al. 2005, AJ, 633, 560, doi: 10.1086/466512

Fang, W., Hu, W., & Lewis, A. 2008, PhRvD, 78, 087303, doi: 10.1103/PhysRevD.78.087303

Farooq, O., Madiyar, F. R., Crandall, S., & Ratra, B. 2017, AJ, 835, 26, doi: 10.3847/1538-4357/835/1/26

Feng, B., Wang, X., & Zhang, X. 2005, PhLB, 607, 35, doi: https://doi.org/10.1016/j.physletb.2004.12.071

Ferraro, R., & Fiorini, F. 2007, PhRvD, 75, 084031, doi: 10.1103/PhysRevD.75.084031

Frampton, P. H. 2018, IJMPA, 33, 1844028, doi: 10.1142/S0217751X18440281
Ghaffari, S., Mamon, A. A., Moradpour, H., & Ziaie, A. H. 2020, MPLA, 35, 2050276, doi: 10.1142/S0217732320502764
Golovnev, A. 2024, AnPhy, 461, 169580, doi: https://doi.org/10.1016/j.aop.2023.169580
Hawking, S. W., & Ellis, G. F. R. 1973, The large-scale structure of space-time.
Hoyle, F., Burbidge, G., & Narlikar, J. V. 1993, ApJ, 410, 437, doi: 10.1086/172761
—. 1994, MNRAS, 267, 1007, doi: 10.1093/mnras/267.4.1007
—. 1995, RSPA, 448, 191, doi: 10.1098/rspa.1995.0012
Huang, T., Wu, P., & Yu, H. 2010, CPMA, 53, 419, doi: 10.1007/s11433-010-0125-y
Ijjas, A., & Steinhardt, P. J. 2018, CQGra, 35, 135004, doi: 10.1088/1361-6382/aac482
—. 2019, PhLB, 795, 666, doi: https://doi.org/10.1016/j.physletb.2019.06.056
Komatsu, E., Dunkley, J., Nolta, M. R., et al. 2009, ApJS, 180, 330, doi: 10.1088/0067-0049/180/2/330
Komatsu, E., Smith, K. M., Dunkley, J., et al. 2011, ApJS, 192, 18, doi: 10.1088/0067-0049/192/2/18
Majernik, V., & Richterek, L. 2006, arXiv e-prints, gr, doi: 10.48550/arXiv.gr-qc/0610070
Martín-Moruno, P., & Visser, M. 2013, JHEP, 2013, 50, doi: 10.1007/JHEP09(2013)050
Mohseni Sadjadi, H. 2009, EPJC, 62, 419, doi: 10.1140/epjc/s10052-009-1045-8
Moradpour, H., & Salako, I. G. 2016, AHEP, 2016, 3492796, doi: https://doi.org/10.1155/2016/3492796
Moraes, P. H. R. S., Ribeiro, G., & Correa, R. A. C. 2016, Ap&SS, 361, 227, doi: 10.1007/s10509-016-2788-y
Nojiri, S., & Odintsov, S. D. 2006, PhRvD, 74, 086005, doi: 10.1103/PhysRevD.74.086005
Nojiri, S., Odintsov, S. D., Oikonomou, V. K., & Paul, T. 2019, PhRvD, 100, 084056, doi: 10.1103/PhysRevD.100.084056
Nojiri, S., Odintsov, S. D., & Tretyakov, P. V. 2008, PThPS, 172, 81, doi: 10.1143/PTPS.172.81
Novello, M., & Bergliaffa, S. P. 2008, PhR, 463, 127, doi: 10.1016/j.physrep.2008.04.006
Overduin, J. M., & Wesson, P. S. 1997, PhR, 283, 303, doi: 10.1016/S0370-1573(96)00046-4
Pavlovic, P., & Sossich, M. 2017, PhRvD, 95, 103519, doi: 10.1103/PhysRevD.95.103519
Perlmutter, S., Aldering, G., Goldhaber, G., et al. 1999, AJ, 517, 565, doi: 10.1086/307221
Rastall, P. 1972, PhRvD, 6, 3357, doi: 10.1103/PhysRevD.6.3357
—. 1976, CJPh, 54, 66, doi: 10.1139/p76-008
Riess, A. G., Filippenko, A. V., Challis, P., et al. 1998, AJ, 116, 1009, doi: 10.1086/300499
Riess, A. G., Strolger, L.-G., Tonry, J., et al. 2004, AJ, 607, 665, doi: 10.1086/383612
Sachs, R., Narlikar, J. V., & Hoyle, F. 1996, A&A, 313, 703
Saha, S. 2018, Elements of Cosmological Thermodynamics, doi: 10.1007/978-3-319-74706-4
Sahni, V., & Shtanov, Y. 2003, JCAP, 2003, 014, doi: 10.1088/1475-7516/2003/11/014
Sahoo, P., Bhattacharjee, S., Tripathy, S. K., & Sahoo, P. K. 2020, MPLA, 35, 2050095, doi: 10.1142/S0217732320500959
Saleem, R., & Hassan, J. 2020, PDU, 28, 100515, doi: https://doi.org/10.1016/j.dark.2020.100515
Saleem, R., Shahid, I., Israr Aslam, M., & Wahab, A. 2024, NuPhB, 1009, 116728, doi: 10.1016/j.nuclphysb.2024.116728
Saleem, R., & Shahnila. 2021, PDU, 32, 100808, doi: https://doi.org/10.1016/j.dark.2021.100808
Shaily, Singh, A., Singh, J. K., Hussain, S., & Myrzakulov, R. 2024, Stability analysis of a dark energy model in Rastall gravity. https://arxiv.org/abs/2402.08709
Sharma, M. K., Pacif, S. K. J., Yergaliyeva, G., & Yesmakhanova, K. 2023, AnPhy, 454, 169345, doi: https://doi.org/10.1016/j.aop.2023.169345
Shen, M., & Zhao, L. 2014, ChPhL, 31, 010401, doi: 10.1088/0256-307X/31/1/010401
Singh, A., & Mishra, K. C. 2020, EPJP, 135, 752, doi: 10.1140/epjp/s13360-020-00783-0
Singh, A., & Pradhan, A. 2023, InJPh, 97, 631, doi: 10.1007/s12648-022-02406-z
Singh, A., Raushan, R., & Chaubey, R. 2021, CJPh, 99, 1073, doi: 10.1139/cjp-2020-0061
Singh, A., & Shukla, A. K. 2020, IJMPA, 35, 2050054, doi: 10.1142/S0217751X20500542
Singh, A., Singh, G. P., & Pradhan, A. 2022, IJMPA, 37, 2250104, doi: 10.1142/S0217751X22501044
Singh, J. K., Singh, A., , S., Ghosh, S. G., & Maharaj, S. D. 2024, PhyS, 99, 125001, doi: 10.1088/1402-4896/ad8841
Sotiriou, T. P. 2011, JPhCS, 283, 012034, doi: 10.1088/1742-6596/283/1/012034
Spergel, D. N., Verde, L., Peiris, H. V., et al. 2003a, ApJS, 148, 175, doi: 10.1086/377226
—. 2003b, ApJS, 148, 175, doi: 10.1086/377226
Steinhardt, P. J., & Turok, N. 2002, PhRvD, 65, 126003, doi: 10.1103/PhysRevD.65.126003
Sánchez, L. M., & Quevedo, H. 2023, PhLB, 839, 137778, doi: https://doi.org/10.1016/j.physletb.2023.137778
Tangphati, T., Banerjee, A., Hansraj, S., & Pradhan, A. 2023, AnPhy, 452, 169285, doi: https://doi.org/10.1016/j.aop.2023.169285
Tangphati, T., Banerjee, A., İzzet Sakallı, & Pradhan, A. 2024, ChJPh, 90, 422, doi: https://doi.org/10.1016/j.cjph.2024.03.045
Tegmark, M., Strauss, M. A., Blanton, M. R., et al. 2004, PhRvD, 69, 103501, doi: 10.1103/PhysRevD.69.103501
Tripathi, A., Sangwan, A., & Jassal, H. K. 2017, JCAP, 06, 012, doi: 10.1088/1475-7516/2017/06/012
Tripathy, S. K., Khuntia, R. K., & Parida, P. 2019, Bouncing cosmology in an Extended Theory of Gravity. https://arxiv.org/abs/1905.09477

Varshney, G., Sharma, U. K., Pradhan, A., & Kumar, N. 2021, ChJPh, 73, 56, doi: https://doi.org/10.1016/j.cjph.2021.04.014
Vikman, A. 2005, PhRvD, 71, 023515, doi: 10.1103/PhysRevD.71.023515
Visser, M. 1997, Sci, 276, 88, doi: 10.1126/science.276.5309.88
Visser, M. 1997, PhRvD, 56, 7578, doi: 10.1103/PhysRevD.56.7578
—. 2018, PhLB, 782, 83, doi: https://doi.org/10.1016/j.physletb.2018.05.028
Wald, R. M. 1984, General Relativity
Wei, H., & Cai, R.-G. 2006, PhLB, 634, 9, doi: https://doi.org/10.1016/j.physletb.2006.01.043
Yang, Y., & Gong, Y. 2020, JCAP, 2020, 059, doi: 10.1088/1475-7516/2020/06/059
Zhao, G.-B., Xia, J.-Q., Li, H., et al. 2007, PhLB, 648, 8, doi: https://doi.org/10.1016/j.physletb.2007.02.070

Revista Mexicana de Astronomía y Astrofísica, 61, 11-24, (2025)

OPEN ACCESS https://doi.org/10.22201/ia.01851101p.2025.61.02.02

Asymmetry and Concentration Parameters for Dwarf Late-Type Spiral Galaxies

I. Vega-Acevedo[1], **A. M. Hidalgo-Gámez**[1] **and B. E. Miranda-Pérez**[1,2]

[1]*Departamento de Física, ESFM, Instituto Politécnico Nacional, México.*
[2]*Departamento de Matemáticas, ESIME, Instituto Politécnico Nacional, México.*

Keywords: *galaxies: dwarf, galaxies: irregular, galaxies: photometry, galaxies: star formation, galaxies: structure*

Abstract

We analyzed the asymmetry and concentration parameters in a sample of late-type spiral galaxies using V and R broadband images. Asymmetry values were computed for different rotation angles and radii, revealing low asymmetry overall, with smaller values in the inner regions. No preferred angle significantly affected the asymmetry measurements. The concentration indices lie between those of large spirals and irregular galaxies. We compared our sample distribution in the $C-A$ plane with other late-type systems (dwarfs and normal spirals). Additionally, we explored the correlations between asymmetry and star formation rate and between concentration and stellar mass, contrasting our results with those of prior studies.

Resumen

En este trabajo se estudian los parámetros de asimetría y concentración en una muestra de galaxias espirales tardías, utilizando imágenes en bandas V y R. La asimetría se calculó para distintos ángulos y radios, mostrando valores bajos (especialmente en regiones internas), sin dependencia sistemática con el ángulo. La concentración presenta valores intermedios entre galaxias espirales grandes e irregulares. Analizamos la distribución de estas galaxias en el plano $C-A$ en comparación con espirales normales y enanas. Además, exploramos las correlaciones entre asimetría y tasa de formación estelar y entre concentración y masa estelar, contrastando nuestros resultados con estudios previos.

Corresponding author: I. Vega-Acevedo *E-mail address:* ivegaa@ipn.mx
Received: July 21, 2024 **Accepted:** March 27, 2025

1. General

Galaxies exhibit a wide variety of forms, and their classification is a challenging task. The classical classification method was introduced by Hubble (1936) and later refined by de Vaucouleurs (1959) is based on morphology. While this method is powerful, it has notable limitations, particularly its subjectivity, as the classification relies on the observer's judgement (Conselice et al., 2000b). Traditionally, this classification was based on photographic plate images, which are more sensitive to blue light. Consequently, blue filters are commonly used, as they emphasize star formation events, which are particularly important in late-type galaxies.

A new classification scheme was proposed by Conselice et al. (2000a), which relies on three parameters: concentration, asymmetry, and clumpiness, collectively known as the CAS system. Although related to morphology, these parameters are defined quantitatively, enabling a more objective classification of galaxies. This classification system was defined by Abraham et al. (1996b). Symmetry has long been a fundamental aspect of galaxy morphology but has often been overlooked in more detailed studies. Early papers on galaxy morphology, such as those by Curtis (1918) and Hubble (1926), described galaxies in terms of their symmetry, typically 180^o symmetry. In general, galaxies are dynamically relaxed systems, leading to a high degree of symmetry (Binney & Tremaine, 2008). Indeed, galaxy models often assume a symmetric mass distribution (Carroll & Ostlie, 2006). Understanding deviations from symmetry in the light distribution of galaxies can reveal underlying dynamical processes. For instance, galaxies affected by interactions or mergers tend to exhibit significant asymmetries (Conselice et al., 2000b).

Schade et al. (1995) first introduced the quantitative use of asymmetry as a morphological parameter to characterize distant galaxies observed with the Hubble Space Telescope (HST). Subsequent studies by Abraham et al. (1996a), Abraham et al. (1996b) and van den Bergh et al. (1996) utilized asymmetry to broadly classify distant galaxies within the Hubble Sequence framework.

Concentration, on the other hand, was initially employed by Morgan (1958, 1959) to develop a more refined classification model. More recently, it has been used to explore the central regions of galaxies, uncovering correlations between concentration and properties, such as X-ray flux (Pović et al., 2009) and central black hole mass (Graham et al., 2001a).

As mentioned, Conselice et al. (2000a) used these three parameters (considering the clumpiness, which is not included in the present investigation) for an alternative classification of galaxies using a sample of galaxies of all morphological types. These parameters can be easily determined from direct images in broadband images. In addition, they seem to be related to the intrinsic properties of galaxies, such as the color index, $(B-V)$, or the absolute magnitude, M_B (Conselice, 2003). He concluded that such classification can be as useful as the Hubble classification, since galaxies with similar CAS values might have similar properties. In his investigation, only two of the galaxies in his sample were classified as Sm (NGC 4861 and NGC 5204), and another two were classified as Sdm. This is not unusual because Sm and dS galaxies are underrepresented in the samples used for asymmetry determination, and they are considered as late-type galaxies in general. They are expected to have concentration and asymmetry parameters midway between those of Sd and irregular galaxies because they have looser spiral arms than other spirals (Sa-Sd), but they are not as disordered as irregular galaxies, and their bulges are quite dim when present.

In this study, we focus on the asymmetry and concentration parameters of a sample of Sm and dS galaxies to determine their proper placement in the $C-A$ diagram. These galaxies have traditionally been located within the late-type galaxy locus (e.g. Conselice 2003), despite the fact that star formation is not confined to the spiral arms but rather extends throughout the entire disk, albeit in a non-homogeneous manner. In fact, H II regions are not uniformly distributed across the galaxy, as observed in other spirals (Magaña-Serrano et al., 2020). Such characteristics may significantly influence the asymmetry and concentration parameters, potentially altering their position in the $C-A$ plane.

We also examined the variations in both asymmetry and concentration parameters depending on the filter used, as well as the effects of rotation angle and radius. In previous studies, only a 180^o rotation have been considered, with the exception of Conselice et al. (2000b) and Abraham et al. (1996a). Notably, most investigations have reported that asymmetry values strongly depend on the rotation angle, with most galaxies appearing nearly symmetrical under a 180^o rotation but not at other angles. This effect may be particularly relevant when emissions from star-forming regions dominate the total flux in certain bands, such as the B band or bluer wavelengths, which is typically the case for Sm and dS galaxies.

Additionally, the flux in the red bands is primarily determined by the underlying stellar population, which is more smoothly distributed throughout the disk (Conselice et al., 2000b). While this phenomenon occurs in all star-forming galaxies, it may be more pronounced in Sm and dS galaxies because of their smaller size relative to other spiral types but comparatively high star formation rates. Consequently, the observed differences in the asymmetry and concentration parameters could be more significant in these galaxies.

Finally, we obtained the dependence of the A and C values on the star formation rate and stellar mass, respectively, and compared them to those obtained for larger galaxies by Conselice (2003) and for tidal dwarf galaxies by Vega-Acevedo & Hidalgo-Gámez (2022).

The manuscript is structured as follows: § 2 describes the sample of galaxies studied as well as the data used for the determination of the parameters. In § 3, a brief description of the determination of the A and C values is presented, while the results, general as well as with different filters, angles, and radii, are presented in § 4. Finally, a discussion on the location of these galaxies in the $C-A$ plane is presented in § 5 as well as the relationship between the A and C parameters with some other characteristics of the galaxies. Finally, our conclusions are presented in § 6.

2. Observations and Data Reduction

The observations of the galaxies analyzed in this study were obtained by one of the authors using the 1.5m telescope at the OAN-SPM during two separate observation campaigns: March 7-9 and November 1-4, 2002. During both campaigns, most nights were not entirely photometric due to the presence of high clouds. However, the extinction was sufficiently low to obtain accurate flux measurements.

Table 1 summarizes the observations of the sample of dwarf spiral galaxies studied in this investigation. Column (1) lists the galaxy name, Columns (2) and (3) provide the exposure time for the R and V filters, respectively, Column (4) presents the signal-to-noise (S/N) ratio, Column (5) contains the seeing conditions, and Column (6) shows the air mass.

Data reduction and calibration were performed using the ESO-MIDAS software following standard procedures (Banse et al., 1983; Warmels, 1992). Atmospheric corrections were applied using the tables for the San Pedro Mártir Observatory (Schuster & Parrao, 2001). Several standard stars were used for flux calibration.

Figures (1) and (2) display the calibrated V-band images of the galaxies UGC 9570 and UGCA 74, respectively in the V filter.

The intensities in these images were normalized relative to I_0, which corresponds to the pixel located at the defined central position. The process for determining this central point is detailed in § 3. To avoid interference with the center determination, which could affect the asymmetry parameter measurements, bright foreground stars were

Table 1. Sample of dwarf spiral galaxies.

Galaxy[1]	Integration time[2]		SNR[3]	seeing[4]	Air mass[5]
	R	V		[$arcsec$]	[mag]
UGCA 5	1200	···	9.5	1.6	1.730
UGCA 74	1000	1200	9.7	1.8	1.840
UGC 891	1000	1200	8.7	1.5	1.260
UGC 2301	1100	1200	8.8	1.6	1.090
UGC 3775	1200	1200	9.1	1.9	1.120
UGC 5242	1200	1000	10.0	1.9	1.570
UGC 5296	1400	1200	4.1	2.0	1.178
UGC 6205	1600	1200	6.1	1.6	1.049
UGC 6304	1200	1200	4.0	1.7	1.280
UGC 9570	1200	1200	4.5	1.6	1.135
UGC 11820	1200	900	8.0	1.9	1.270
UGC 12212	1000	1200	9.2	1.8	1.010

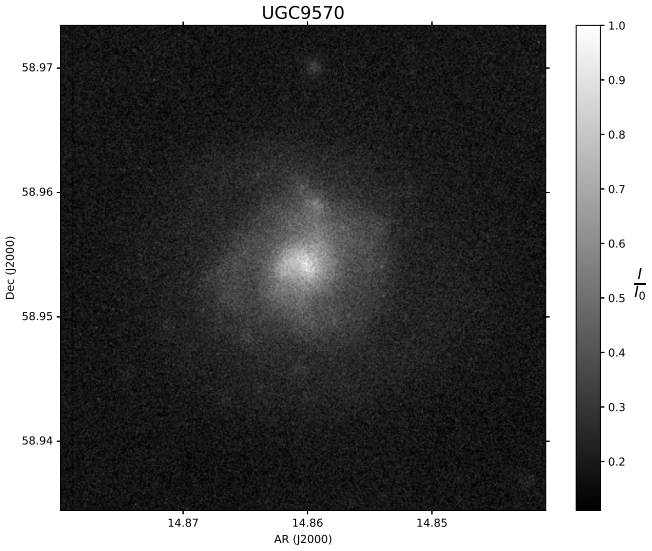

Figure 1. Reduced image of the galaxy UGC 9570 in the V filter observed at OAN-San Pedro Martir. The intensity in the image is normalized with respect to I_0 (see § 3).

removed and replaced by interpolating the background emission.

2.1. Sample description

All galaxies analyzed in this study were selected from the list of dwarf spiral galaxies compiled by Hidalgo-Gámez (2004), except for UGC 2301, which is a dS candidate. Thus, all of them are classified as dS, although UGCA 74 is categorized as a peculiar galaxy. Four of these galaxies (UGCA 5, UGCA 74, UGC 891, and UGC 5242) are considered barred galaxies (de Vaucouleurs et al., 1991).

Table 2 presents some of the main properties of the galaxies in our sample. Column (1) lists the galaxy name, while Columns (2) and (3) provide the right ascension (α) and declination (δ) coordinates, respectively. Column (4) lists the inclinations. Most of the galaxies are either

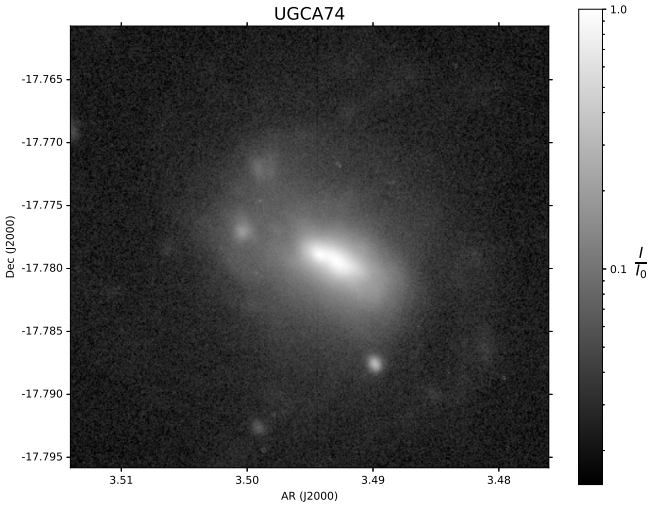

Figure 2. Reduced image of the galaxy UGCA 74 in the V filter observed at OAN-San Pedro Martir. The intensity in the image is normalized with respect to I_0 (see § 3).

face-on or have an intermediate inclination, with values ranging from 14^o to 56^o. Only two galaxies, UGC 891 and UGC 2301, exhibited high inclinations. This is a relevant factor, as lower inclinations facilitate the determination of both the asymmetry and concentration parameters. The two highly inclined galaxies were retained in our sample to assess the impact of inclination on the measurement of these parameters. Columns (5), (6), and (7) provide the optical radius, distance, and absolute magnitude (M_B), respectively. The radii and absolute magnitudes were determined following Hidalgo-Gámez (2004), incorporating the latest distance measurements from NED-NASA. Galactic extinction corrections were applied to these calculations. Finally, the last column presents the morphological classification according to NED-NASA.

With this homogeneous although small sample, it is very interesting to study the asymmetry and concentration parameters and check if dS are located near the spiral galaxies or closer to the locus on irregular ones in the $C-A$ plane.

3. Determination of the A and C parameters

3.1. Where is the center?

To determine both the asymmetry and concentration parameters, it is necessary to determine the center of the galaxy.

In this investigation, the weighted center (C_w), defined as the point obtained by weighting the pixel intensities in a specific region, was chosen instead of the photometric center because it can be determined more easily without additional processing. The distance between the weighted center and the photometric center in these galaxies is less than the seeing (Vega-Acevedo, 2013). The weighted center,

Table 2. Galaxy sample

Galaxy[(1)]	$\alpha^{(2)}_{J2000}$	$\beta^{(3)}_{J2000}$	$r^{(4)}_{25}$ [kpc]	D[(5)] [Mpc]	$M^{(6)}_B$	Morphology[(7)]
UGCA5	00h18m48.3s	-19d00m28s	9.14	42.5±	-18.46	SAB(s)m
UGCA74	03h29m31.7s	-17d46m42s	4.5	20.5±	-18.05	SB(s)c pec
UGC891	01h21m18.9s	+12d24m43s	1.62	4.86±	-14.28	SABm
UGC2301	02h49m38.2s	+38d15m41s	⋯	⋯	-18	dwarf*
UGC3775	07h15m52.6s	+12d06m54s	7.69	34.1	-16.56	Sm
UGC5242	09h47m05.5s	+00d57m51s	6.36	32.4	-17.75	SB(s)m
UGC5296	09h53m11.6s	+58d28m42s	3.65	24.5	-15.54	Sm
UGC6205	11h09m58.3s	+46d05m42s	6.37	24.0	-17.13	Sm
UGC6304	11h17m49.1s	+58d21m08s	5.67	28.3	-15.84	Sm
UGC9570	14h51m35.9s	+58d57m14s	⋯	33.5	-16.22	dS*
UGC11820	21h49m28.4s	+14d13m52s	3.22	11.3	-14.20	Sm
UGC12212	22h50m30.3s	+29d08m18s	1.82	8.1	-14.04	Sm

[a]Column (1) is the name of the galaxy, Columns (2) y (3) are the right ascension and declination respectively in $J2000$, Column (4) is the mayor axis, the distance of galaxy is in Column (5) and Column (6) is the absolute magnitude in B, using the most recent distance determination, and Column (7) is the morphological classification (de Vaucouleurs et al., 1991; Nilson, 1973).

$C_w = (C_{w,x}, C_{w,y})$, was obtained as:

$$C_w = (C_{w,x}, C_{w,y}) = \frac{\left(\sum_{i,j}(x_i I_{i,j}), \sum_{i,j}(y_j I_{i,j})\right)}{I}, \quad (1)$$

where the $I_{i,j}$ is the intensity of each pixel located in (i,j), and x_i, y_j are the coordinates of the pixel (i,j), the $\sum(x_i I_{i,j})$ is the sum of the product between the position in the x coordinate and the intensity in the position (i,j) and $I = \sum_{i,j} I_{i,j}$

The challenge in determining the weighted center, as previously mentioned, is the variation in the average intensity (and consequently, in the coordinates of the weighted center) caused by the presence of field stars near the galaxy. To mitigate this effect, these stars must be masked to eliminate their contributions.

In addition to determining the weighted center, it is also necessary to define the galaxy′s size for the calculation of the asymmetry (A) parameter. Following Conselice (2003), we adopted the Petrosian radius. To determine this radius, the surface brightness profile must be obtained (Graham et al., 2005), which in this study was modeled using Sérsic's law (Sérsic et al., 1968).

3.2. Asymmetry

The asymmetry parameter (A) quantifies the irregularity or unevenness of the brightness and structure of a galaxy across different regions. It measures the extent to which the shape of a galaxy changes during a specific rotation. Asymmetry can provide valuable insights into past dynamical events, such as galactic mergers or interactions with other galaxies, as interacting galaxies typically exhibit higher asymmetries. To determine this parameter, the luminosity distribution in the opposite regions of the galaxy was compared to identify imbalances in the light distribution. In this study, we proceeded as follows: First, the original image, Ima, was rotated by an angle, θ, counterclockwise, considering the weighted center as the rotation point. This rotated image is denoted as Rot. Then, the following operation was performed on the images:

$$A = \left|\frac{Rot - Ima}{Ima}\right| \quad (2)$$

Finally, the intensity of a region, centered at the weighted center and with a radii of the r_{25}, is measured at the image obtained from equation 2, which will be defined as parameter A (Abraham et al., 1996b). With that definition, the parameter takes values from 0 to 1, where 0 means a symmetric system under that rotation and 1 is a completely asymmetric one. In general, spiral galaxies are quite symmetric for a 180^o rotation, but they are asymmetric for 90^o or 45^o rotations. Elliptical galaxies are very symmetrical for most angles, with asymmetry values between 0.1 and 0.3. In contrast, irregular galaxies have average values of $0.4 - 0.5$ under all the angles (Conselice et al., 2000b; Abraham et al., 1996b).

In general, the asymmetry parameter is determined using a single angle, mostly 180^o, and a fixed size for every galaxy (Conselice, 2003), although some authors used several radii, filters, and angles to determine how this parameter changes. Hernández-Toledo et al. (2005) measured CAS parameters in BVRI bands for a sample of 66 galaxies and found that the differences in CAS parameters for paired galaxies from the B to I bands are, on average, small. In addition, only a single size of the galaxy was considered, although Conselice

et al. (2000b) concluded that the internal part of the galaxies might be more symmetrical.

3.3. Concentration

The concentration, C, of a galaxy refers to the relationship between the luminosity in its central core and the total luminosity along its extension. This parameter is useful for distinguishing between different types of galaxies, especially between elliptical and spiral galaxies. Higher values of C indicate that a larger amount of light in a galaxy is contained within its central region (for example, Bershady et al. 2000; Graham et al. 2001a, 2005). Elliptical galaxies tend to have a higher concentration because most of their light is centered in the nucleus, whereas spirals with extended arms have a lower value. The concentration is calculated as the ratio of two radii containing a specific percentage of the total luminosity of the galaxy. In this study, we use the definition by Conselice (2003) which quantifies how much light is at the center of a galaxy as opposed to its outer parts, that is

$$C = 5log\left(\frac{r_{80}}{r_{20}}\right), \quad (3)$$

In this equation, r_{80} and r_{20} are the radii enclosing the 80% and 20% of the total flux, respectively, respectively. To obtain these radii, we fit a Petrosian-type brightness profile to each galaxy under study and determined the integral of the profiles to obtain the radii that contain 20% and 80% of the total flux.

4. Results

4.1. Asymmetry for dwarf spiral galaxies

In this investigation, we used three different angles (45^o, 90^o, and 180^o), two filters (V and R) and two radii (r_p and $2r_p$) in the determination of the asymmetry. These configurations were employed to evaluate whether the conclusions drawn for large galaxies -such as lower asymmetry values in the inner regions, higher symmetry under a 180^o rotation, and minimal differences between filters- are consistent for smaller galaxies. The motivation for this comparison lies in the distinct structural differences: large galaxies typically exhibit a canonical spiral structure, whereas the smaller galaxies in our sample exhibit a looser spiral pattern with a more disordered light distribution.

The values of the asymmetry parameter for the sample in filters V and R at radii $r = r_p$ and $r = 2r_p$ are listed in Table 3. Column (1) has the galaxy name, Columns (2), (3), and (4) are the values for rotation angles 45^o, 90^o and 180^o in filter V, and Columns (5), (6), and (7) are the ones for rotation angles 45^o, 90^o and 180^o in filter R. The top part of this table shows the A values determined for a radius r_p, which considers the innermost part of the galaxy, while the values at the bottom correspond to $r = 2r_p$, which includes most of the total galaxy.

4.1.1. Asymmetry at different filters

As previously mentioned, the R filter is typically used for asymmetry determination because the luminosity from K-type stars, which dominate this filter, is assumed to be virialized, following a more symmetric and homogeneous distribution (Conselice, 2003). However, this assumption may not be entirely appropriate for star-forming galaxies. If the star formation rate (SFR) is sufficiently high, the R-filter emission may be contaminated by Hα line emission at 6562Å, originating from H II regions. Additionally, the scattered distribution and high luminosity of H II regions in Sm and dS galaxies could affect the weighted center determination, subsequently influencing the asymmetry. Since most of the galaxies in our sample are star-forming (Magaña-Serrano et al., 2020), a comparison with a bluer filter (V) allows us to assess the significance of these effects on the results.

As shown in Table 3, no significant differences in asymmetry values were observed between the two filters. A similar conclusion can be drawn from Figure 3, which plots the asymmetry values obtained with the R filter (y-axis) against those obtained with the V filter (x-axis) for all galaxies in the sample. The plot also includes the 1:1 reference line and the 1σ confidence interval (dotted lines) for the internal regions of the galaxies (r_p) across the three rotation angles used in this work. We focus on r_p because asymmetry values are generally lower in this region, making any differences more likely attributable to filter effects (See § 4.3). For completeness, a square-root function fit is shown as a dashed line.

At 90^o and 180^o there are four galaxies that do not fit into the 1σ. As one of the sources of asymmetry might be the distribution of the H II regions, those galaxies with the largest SFR might be those with the largest asymmetry. The galaxy with the largest differences in the A values between the filters in our sample, UGCA 74, is also the galaxy with the highest SFR ($0.186 M_\odot yr^{-1}$, Hodge & Kennicutt 1983).

These results are predictable because both filters have very close central wavelengths; therefore, the light in both is dominated by a similar stellar population, especially if the star formation rates are low. They are very similar to those obtained by Hernández-Toledo et al. (2005) and Conselice et al. (2000b), where the differences in the asymmetry between the values in the blue (B, g) and red (R, r) filters are smaller than 0.1.

4.1.2. Asymmetry at different radii

In contrast to intermediate (Sbc, Sc, Sd) types of galaxies, where the H II regions are preferably located along the spiral arms, the regions of star formation in late types are disorderly distributed throughout the galaxy (see, for example, Magaña-Serrano et al. (2020); Roye & Hunter (2000)). Moreover, Conselice et al. (2000b) concluded that the internal part of galaxies might be more symmetrical because the spiral pattern is clearer. Another reason is that, in general, in normal spiral galaxies, the number of H II regions is smaller in the internal part (Hodge &

Table 3. Summary of Asymmetry

Galaxy	*V* filter			*R* filter		
	45^o	90^o	180^o	45^o	90^o	180^o
	$r = r_p$					
UGCA 5	0.18 ± 0.01	0.23 ± 0.04	0.25 ± 0.04	...	...	...
UGCA 74	0.19 ± 0.02	0.28 ± 0.01	0.17 ± 0.02	0.21 ± 0.03	0.33 ± 0.02	0.49 ± 0.01
UGC 891	0.14 ± 0.02	0.18 ± 0.02	0.18 ± 0.02	0.13 ± 0.01	0.15 ± 0.01	0.17 ± 0.01
UGC 2301	0.2 ± 0.02	0.3 ± 0.01	0.13 ± 0.01	0.18 ± 0.01	0.29 ± 0.01	0.12 ± 0.01
UGC 3775	0.2 ± 0.01	0.28 ± 0.01	0.32 ± 0.01	0.23 ± 0.01	0.29 ± 0.01	0.32 ± 0.01
UGC 5242	0.09 ± 0.01	0.13 ± 0.01	0.16 ± 0.01	0.11 ± 0.04	0.14 ± 0.03	0.17 ± 0.03
UGC 5296	0.12 ± 0.01	0.11 ± 0.01	0.09 ± 0.02	0.16 ± 0.04	0.14 ± 0.05	0.09 ± 0.07
UGC 6205	0.07 ± 0.02	0.09 ± 0.01	0.07 ± 0.02	0.07 ± 0.01	0.08 ± 0.01	0.07 ± 0.01
UGC 6304	0.09 ± 0.01	0.11 ± 0.01	0.12 ± 0.01	0.09 ± 0.01	0.12 ± 0.01	0.12 ± 0.01
UGC 9570	0.07 ± 0.01	0.1 ± 0.01	0.09 ± 0.01	0.07 ± 0.04	0.08 ± 0.04	0.08 ± 0.04
UGC 11820	0.13 ± 0.02	0.15 ± 0.01	0.15 ± 0.01	0.10 ± 0.04	0.11 ± 0.03	0.10 ± 0.03
UGC 12212	0.12 ± 0.02	0.18 ± 0.01	0.22 ± 0.01	0.09 ± 0.04	0.14 ± 0.03	0.17 ± 0.02
	$r=2r_p$					
UGCA 5	0.25 ± 0.01	0.32 ± 0.01	0.37 ± 0.01	...	...	...
UGCA 74	0.36 ± 0.02	0.5 ± 0.02	0.34 ± 0.02	0.35 ± 0.01	0.51 ± 0.04	0.39 ± 0.04
UGC 891	0.18 ± 0.05	0.22 ± 0.04	0.18 ± 0.05	0.14 ± 0.04	0.17 ± 0.03	0.15 ± 0.03
UGC 2301	0.15 ± 0.02	0.32 ± 0.02	0.13 ± 0.02	0.13 ± 0.01	0.29 ± 0.01	0.12 ± 0.01
UGC 3775	0.28 ± 0.01	0.4 ± 0.01	0.49 ± 0.01	0.29 ± 0.01	0.41 ± 0.01	0.48 ± 0.01
UGC 5242	0.13 ± 0.04	0.17 ± 0.03	0.16 ± 0.03	0.15 ± 0.02	0.21 ± 0.01	0.19 ± 0.01
UGC 5296	0.11 ± 0.04	0.14 ± 0.03	0.13 ± 0.04	0.12 ± 0.02	0.15 ± 0.01	0.14 ± 0.01
UGC 6205	0.11 ± 0.03	0.14 ± 0.02	0.08 ± 0.04	0.1 ± 0.01	0.13 ± 0.01	0.08 ± 0.02
UGC 6304	0.11 ± 0.02	0.13 ± 0.02	0.12 ± 0.02	0.11 ± 0.03	0.15 ± 0.02	0.14 ± 0.02
UGC 9570	0.08 ± 0.03	0.11 ± 0.03	0.11 ± 0.02	0.08 ± 0.01	0.1 ± 0.01	0.1 ± 0.01
UGC 11820	0.15 ± 0.01	0.18 ± 0.01	0.21 ± 0.01	0.19 ± 0.02	0.20 ± 0.01	0.22 ± 0.01
UGC 12212	0.17 ± 0.02	0.24 ± 0.01	0.3 ± 0.01	0.16 ± 0.01	0.23 ± 0.01	0.29 ± 0.01

Top: Asymmetry for a $r = r_p$.
Bottom: Asymmetry for a $r = 2r_p$.

Kennicutt, 1983). Then, a difference in the asymmetry values is expected between the internal and external parts for late-type galaxies.

This is clearly seen in Figure 4, where the *A* values in the external parts ($2r_p$) are shown against the internal parts (r_p) in *R* filter. Along with the data points, the identity and 1σ lines are shown for the three angles studied here, as well as the square root fitting (dashed line).

Approximately half of the galaxies in the sample have differences in the *A* values larger than 1σ. Interestingly, galaxies with low asymmetry values, such as UGC 11820 and UGC 5242, show large differences between their inner and outer parts. Three of the four barred galaxies in our list have large differences in radius. The other galaxy, UGC 891, has a large inclination, which might cover the differences. The two galaxies with the largest inclination have the smallest differences in *A* between r_p and $2r_p$ when the average values in the filter and angle are considered for every radius.

Another reason for the increase in the *A* parameter with radius might be the interactions, present or past, suffered by the galaxies. The only peculiar galaxy in our sample that might be interacting is UGCA 74, which shows large differences and also has the largest SFR, as previously mentioned. Therefore, it can be concluded that barred galaxies or those in interaction or with an intense event of star formation are expected to show large differences in asymmetry between their inner and outer parts.

4.1.3. Asymmetry at different angles

Classical spiral, two-arm galaxies have low values of asymmetry for a 180^o rotation (Conselice et al., 2000b). In contrast, late-type spiral galaxies have, in many cases, no clear spiral pattern, sometimes with an odd number of arms. Therefore, differences in the *A* parameter might be related to the spiral structure of the galaxies. Both, Abraham et al. (1996a) and Conselice et al. (2000b) found that the asymmetry strongly depends on the angle of rotation if

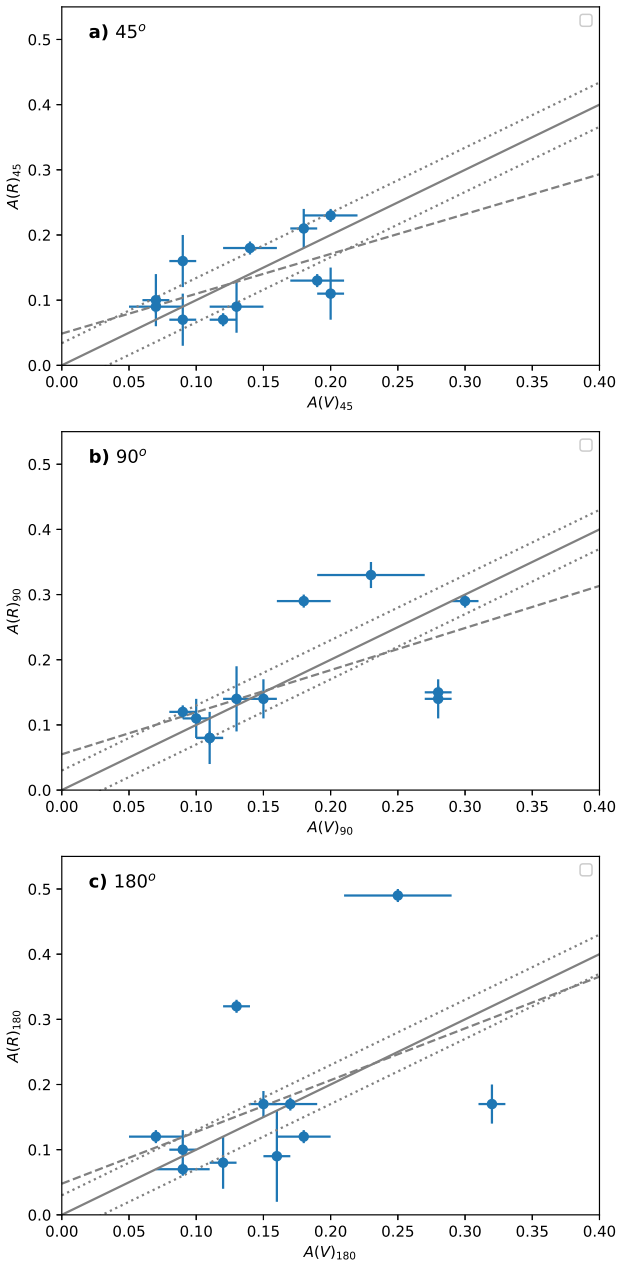

Figure 3. Comparison of asymmetry values for the galaxies in the sample in filter *R* versus filter *V* at r = r_p. The top panel (a) is for a rotation angle of 45^o, the middle panel, (b), for a 90^o angle and the bottom one, (c), for a 180^o angle.

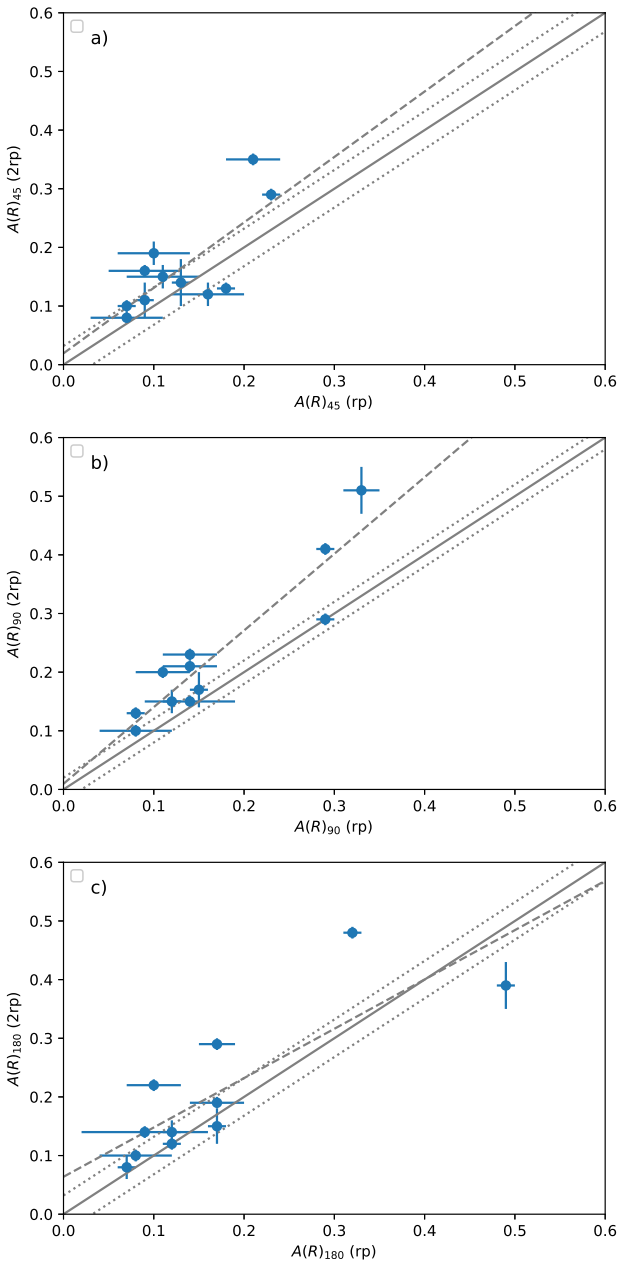

Figure 4. Comparison of the asymmetry values between the 2r_p versus 1r_p in filter *R*. The top panel, (a), is for a rotation angle of 45^o, the middel one, (b), shows values for a rotation angle of 90^o and the bottom one, (c), is for a rotation angle of 180^o.

the galaxy is very asymmetric. Finally, they concluded that the 180^o rotation was always the angle that gave the lowest asymmetry value, and such angles might indicates the existence of an axis of symmetry (Hernández-Toledo et al., 2005).

The asymmetry values for these three angles are listed in Table 3 for the different filters and radii, and they are plotted in Figure 5, with the identity and 1σ and squared fitting lines. Only the internal values of the asymmetry and the V filter were considered. Again, approximately half of the galaxies in the sample are not enclosed by the 1σ lines, but only four of them have differences larger than 2σ: UGCA 74, UGC 2301, UGC 3775, and UGC 12212. Smaller differences are present for asymmetries lower than 0.2 independently of the rotation angles considered (see Figure 5). Conselice et al. (2000b) have much larger differences in the asymmetry parameter for the majority of the galaxies in their sample.

Conselice et al. (2000b) also concluded that a 180^o rotation is particularly sensitive to interactions, whereas

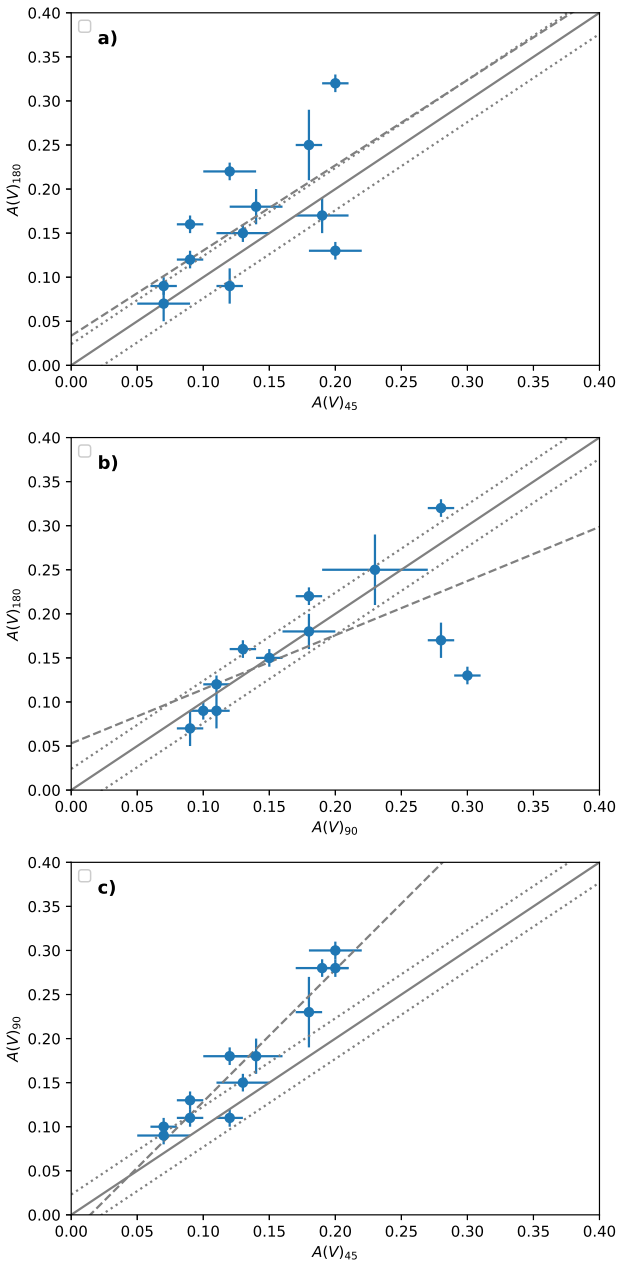

Figure 5. Comparison of asymmetry values in filter V at $r = r_p$ for different rotation angles. (a) rotation angles of 180^o vs 45^o, (b) rotation angles of 180^o vs 90^o and (c) rotation angles of 90^o vs 45^o.

higher asymmetry (A) values at 90^o or 45^o are primarily associated with star formation. Furthermore, asymmetry at 180^o correlates with morphological type, interactions, and color index ($B-V$), while the maximum asymmetry at 90^o is related to the axis ratio b/a; specifically, larger asymmetry values correspond to larger axis ratios.

Finally, the minima of the asymmetry parameter across the full rotation range (1^o to 360^o) may be linked to the number of spiral arms. In particular, a minimum at 90^o suggests the presence of a four-arm structure.

According to Table 3 (upper half, Columns 5, 6 and 7), only three galaxies have a maximum of the asymmetry at 180^o (UGCA 74, UGC 3775 and UGC 12212) however, only one of these galaxies might be in interaction and their only morphological difference is that UGCA 74 is a barred galaxy. Its color, of 0.49, is much larger than the value expected from its asymmetry, according to Figure 10 in Conselice et al. (2000b). Two of these galaxies have a similar b/a axis ratio of $0.12-0.13$ while there is no information on the third. UGCA 74 has a much larger asymmetry than expected from its low axis ratio, according to Figure 13 in Conselice et al. (2000b).

Only one galaxy has the maximum at 90^o (UGC 2301) with a axis ratio of 0.4. Finally, none of the galaxies in our sample had a maximum at 45^o. Moreover, the remaining galaxies in the sample have very similar values for all the angles studied. It is interesting to note that five of the galaxies show an increment of the asymmetry for larger rotation angles, while only one shows the contrary trend.

4.2. Concentration for dwarf spiral galaxies

The concentration parameter, as already mentioned, is related to some of the intrinsic properties of galaxies, such as dispersion velocity, size, and luminosity (Graham et al., 2001b). Moreover, it is well known that the earlier the galaxy, the larger the C values (for example Conselice, 2003, and references therein). The average value for elliptical galaxies is approximately 4.4 while for dE is 2.5 and for dI is 2.9. Hernández-Toledo et al. (2005) showed that the average concentration parameter decreases from the I to the B bands, in agreement with the finding that galaxy light distributions are more extended (less concentrated) in bluer bands than in red bands (de Jong, 1996).

Table 4 presents the concentration C values for the galaxies in our sample, determined as described in § 3, for the V filter (Column 2) and the R filter (Column 3). The first notable observation is that the C parameter remains nearly identical for both filters. This similarity may be attributed to the close central wavelengths of these filters, which result in minimal differences in galactic morphology. Furthermore, the average C value for our sample is 2.7 (see Table 5) in both filters, placing these galaxies at an intermediate level between dI and dE types but significantly lower than the average value for classical spirals (3.9 according to Conselice 2003).

Only two galaxies, UGCA 74 and UGC 2301, exhibit higher C values, while UGC 12212 has a value lower by more than 1σ. The high concentration values observed in UGCA 74 and UGC 2301 bring them closer to those of elliptical galaxies, whereas UGC 12212 displays a concentration even lower than that of Tidal Dwarf Galaxies (see Vega-Acevedo & Hidalgo-Gámez 2022). Among these three galaxies, only UGCA 74 shows high asymmetry values in its outer regions, suggesting that its elevated C values may be linked to a central star formation event triggered

Table 4. Concentration, C

Galaxy	C_V	C_R
UGCA 5	2.5±0.2	···
UGCA 74	4.1±0.3	3.9±0.2
UGC 891	3.3±0.2	3.3±0.3
UGC 2301	4.4±0.1	4.3±0.2
UGC 3775	2.4±0.2	2.2±0.2
UGC 5242	1.9±0.3	1.9±0.1
UGC 5296	2.0±0.2	1.9±0.3
UGC 6205	2.1±0.1	2.1±0.2
UGC 6304	1.9±0.2	1.9±0.3
UGC 9570	2.0±0.1	2.0±0.1
UGC 11820	3.0±0.3	3.0±0.2
UGC 12212	1.3±0.2	1.3±0.2

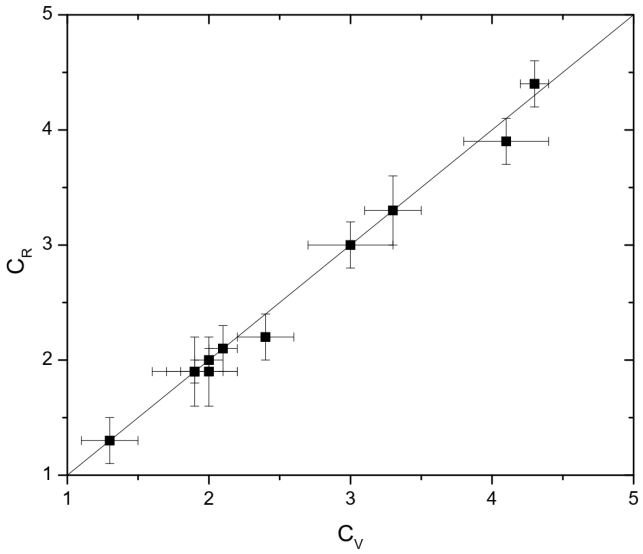

Figure 6. Plot of concentration in filter V versus concentration in filter R. The line represent a correlation one-by-one.

by an ongoing interaction. Notably, the other two galaxies also exhibit peculiar asymmetry values.

Figure 6 illustrates that the concentration values in the V and R filters follow a linear one-to-one correlation.

5. Discussion

As discussed previously, the main goal of this investigation is to determine the A and C parameters for a sample of dS galaxies and compare them with the values for other types of galaxies. In the previous sections, we obtained the asymmetry and concentration parameters, and the average values are of 0.18±0.02 and 2.55±0.02, respectively, considering the R filter, r_p and a 180^o angle.

We can compare these average values of C and A with those reported by Conselice (2003) (See Table 5). The concentration values for dS galaxies are very similar to those of dE and starburst galaxies and are slightly lower

Table 5. Averages and 1σ variations of C and A for Galaxy Types

Type	C	A
Ellipticals[a]	4.47±0.27	0.02±0.02
Early-type disks (Sa-Sb)[a]	3.75±0.59	0.07±0.04
Late-type disks (Sc-Sd)[a]	3.10±0.47	0.15±0.06
Irregulars[a]	3.25±0.69	0.33±0.26
Edge-on disks[a]	3.7±0.6	0.17±0.11
ULIRGs[a]	3.56±0.74	0.32±0.19
Starbursts[a]	2.7±0.2	0.53±0.22
Dwarf ellipticals[a]	2.46±0.28	0.02±0.02
Dwarf irregular[a]	2.87±0.30	0.18±0.10
TDG[b]	1.75±0.27	0.46±0.22
Dwarf spiral [c]	2.36±0.60	0.22±0.13

[a] From Conselice (2003).
[b] From Vega-Acevedo & Hidalgo-Gámez (2022).
[c] This work.

than those of dI galaxies. In contrast, these values differ significantly from those of late-type spirals. This suggests that, in terms of light concentration, dS galaxies resemble other dwarf galaxies more closely than larger spirals. Regarding asymmetry, the differences between dS and late-type spirals are smaller, yet the asymmetry values for dS and dI galaxies remain similar. Although it is difficult to distinguish between dS and late-type disk galaxies based solely on these data, it is notable that the C and A values of dS galaxies align more closely with those of dI galaxies than with those of late-type disks, as reported by Conselice (2003).

The reader may be concerned about the dispersion in the values presented here, particularly in the average values listed in Table 5. Although the 1σ dispersion for dwarf spiral galaxies is relatively large, it is not greater than the dispersion reported by other authors for half of the galaxy types studied (Conselice, 2003). Additionally, while the sample analyzed in this study is small (consisting of only 12 galaxies), it is comparable in size to the sample of dwarf elliptical galaxies and twice as large as the sample of starburst galaxies in Conselice′s work.

5.1. The A-C plane for late-type galaxies

The $A-C$ plane is a projection in two dimensions of the $C-A-S$ space described by Conselice (2003). It has been used to differentiate galaxies with different morphological types in a three-dimensional space (Conselice, 2003; Hernández-Toledo et al., 2005). It has been proven to be quite successful when high-redshift galaxies are studied because of the difficulties in their morphological classification. Therefore, it can be useful to shed light on the true nature of dS galaxies, as discussed in Hidalgo-Gámez (2004).

Figure 7 presents the $C-A$ plane for the galaxies in our sample. In addition to the data points for dS galaxies

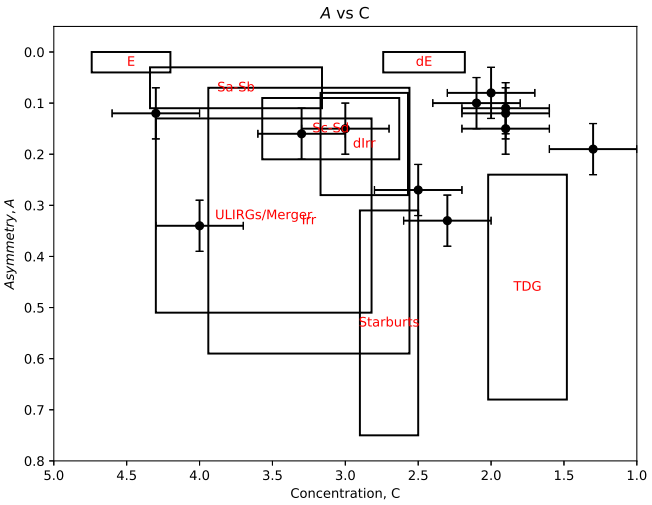

Figure 7. Plane $C-A$. The regions are centered on the average values of asymmetry, A, and concentration, C, for each galaxy type. The height and width of the regions correspond to the standard deviations of asymmetry and concentration, respectively. The values used for elliptical, E, dwarf elliptical, dE, spirals, S, early and late, dwarf irregulars, dIrr, starbursts, mergers, and URLIGS were taken from Conselice (2003). The data for TDGs from Vega-Acevedo & Hidalgo-Gámez (2022). Data for dwarf spiral, dS, were taken from Table 3 for r_p at filter V and Table 4 at filter V.

from Table 6, the regions occupied by different galaxy types, as defined by Conselice (2003) are also shown. Two main conclusions can be drawn: 1) There appear to be two distinct subsamples of dS galaxies: one clustering around $C = 2$ and another more widely distributed across the plane. 2) When considering the regions occupied by different morphological types, a continuous sequence is evident, extending from elliptical galaxies (located in the upper left of 7) toward dS and dE galaxies (upper right). Additionally, mergers, starburst galaxies, ULIRGs, TDGs, and some dS galaxies seem to form a parallel sequence at higher asymmetry values.

Overall, dS galaxies are widely scattered in the $C-A$ plane. Some exhibit values similar to those of dwarf elliptical galaxies, whereas the rest are broadly distributed. Specifically, two galaxies (UGCA 5 and UGC 3775) have high asymmetry (A) but normal concentration (C), whereas UGC 2301 and UGCA 74 display high C values, resembling elliptical galaxies, although UGCA 74 falls within the ULIRG region. In addition, two galaxies (UGC 891 and UGC 11820) lie at the boundaries of the starburst galaxy region.

However, the large dispersion in the $C-A$ plane is not exclusive of dS galaxies. All the groups are quite scattered in the $C-A$ plane, except for giant and dwarf elliptical galaxies, which occupy a small part of the plane.

5.2. Extreme galaxies

We have noticed along this investigation the anomalous A and C values of some of the galaxies, which can be seen in Figure 7. Two galaxies lie at the intersection of the late-type spiral and irregular galaxies (UGC 891 and UGC 11820). Another two have the most extreme concentration values but with the same asymmetry (UGC 2301 and UGC 12212). One more, UGCA 74, is inside the ULIRGs region, and UGCA 5 and UGC 3775 are at the edge of the starburst galaxies region. Finally, five of the galaxies (UGC 5242, UGC 5296, UGC 6205, UGC 6304, and UGC 9570) are located close to the dE.

In order to understand the location of the galaxies in the sample on the $C-A$ plane, we can study them in detail. From the values listed in Tables 3 and 4, we see that there are few galaxies with anomalous values of C and A: two of them (UGC 2301 and UGCA 74) have C values very similar to elliptical galaxies, while another two (UGCA 5 and UGC 3775) have A values similar to the starburst galaxies.

The large concentration value of UGC 2301 resides in its round, low surface brightness shape, while the small asymmetry value is due to its lack of any structure. In contrast, UGCA 74 is a barred galaxy classified as peculiar, with a clear single arm; therefore, its large A value places it in the ULIRGs locus. Moreover, it has the largest SFR of the galaxies in the sample ($0.186 M_\odot yr^{-1}$ Parkash et al. (2018)). Concerning the galaxies in the starburst locus, UGCA 5 is an isolated galaxy (Karachentsev et al., 2006, 2003) with an arm or half-ring in the eastern part of the galaxy. There are several clumps with high emission in both the UV and B bands, but not in the R or NIR bands. These clumps, as well as the half-ring, are responsible for the large asymmetry. In contrast, UGC 3775 has an SFR typical of late-type galaxies ($0.06 M_\odot\ yr^{-1}$; Magaña-Serrano et al. 2020) but with a round appearance. Therefore, despite the relationship between A and SFR, according to Conselice (2003), the location in the $C-A$ plane of UGCA 74, UGCA 5, or UGC 3775 is not because their SFR, which is actually much lower than in any starburst.

Another interesting group of galaxies comprises those with both low values of C and A which are located in the vicinity of the dE locus (UGC 5242, UGC 5296, UGC 6205, UGC 6304, and UGC 9570). In all cases, the low asymmetry and concentration values are due to their low surface brightness and lack of clear structures. Their SFR are similar to those of the galaxies in our sample belonging to the ULIRG and Starburst loci (see Magaña-Serrano et al. 2020).

5.3. Parameters affecting the C-A plane

Several parameters may influence the location of galaxies in the $C-A$ plane. One such factor is the presence of a bar. In our sample, only four galaxies are barred, and their average asymmetry parameter (A) is higher than that of non-barred galaxies (0.23 compared to 0.16). Two of these galaxies exhibited high asymmetry values, whereas the remaining

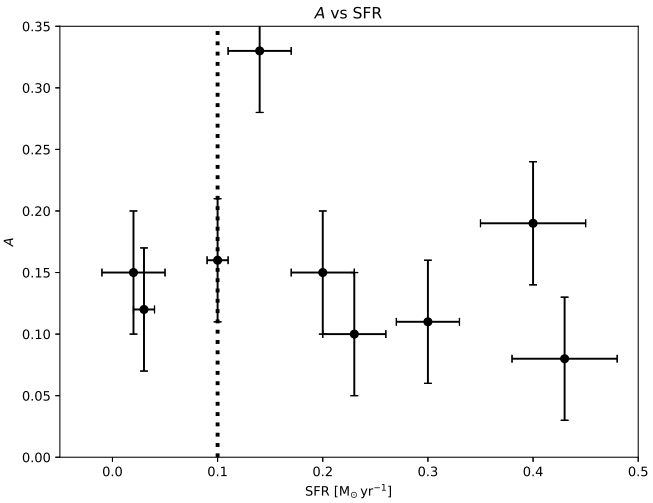

Figure 8. The relationship between the asymmetry at 180^o and the SFR for nine of the galaxies of the sample.

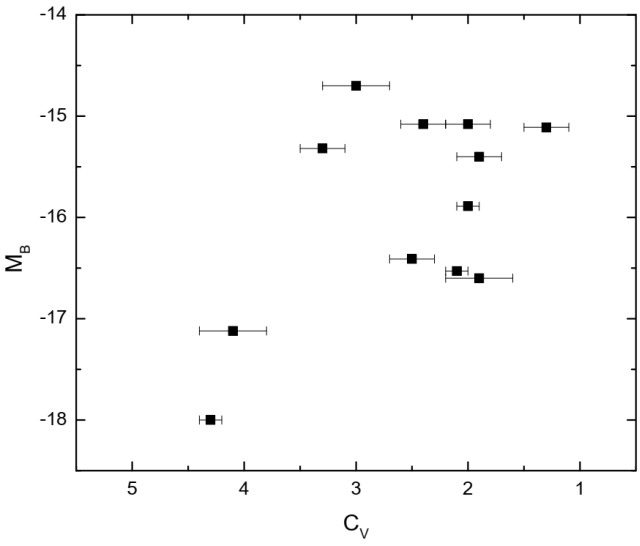

Figure 9. Plot of absolute magnitude B versus concentration in filter V.

two had intermediate values. Additionally, all galaxies with the lowest A values were non-barred.

Another factor that may affect the A value is the spiral structure of the galaxies. In a previous study of late-type galaxies by Magaña-Serrano et al. (2020), the spiral structure of eight of the 12 galaxies in our sample was analyzed. No strong correlation was found between the A parameter and the spiral structure. However, three of the four galaxies with no clear spiral structure have A values greater than 0.15.

According to Conselice et al. (2000a), A_{180} is sensitive to star-forming regions in galaxies. Therefore, a relationship between asymmetry and the star formation rate (SFR) might be expected. This relationship is shown in Figure 8 for nine galaxies in our sample. There is no clear relationship between these two parameters for these galaxies; instead, they show constant values. The galaxy with the largest SFR, UGC 9570, has a normal value of the A parameter.

In the classical work by Graham et al. (2001b), it was concluded that the concentration index is also a measure of the scale of a galaxy. Moreover, they argued that there is a correlation between the total light concentration and the stellar mass because elliptical massive galaxies have larger C values than spiral and irregular galaxies. In order to prove such a correlation for late-type galaxies, the stellar masses of some of the galaxies in the sample were estimated following the relationship between the M/L ratio (in solar units) and the AB magnitudes (from the SDSS RD7 corrected by Galactic extinction and K-correction) by Bell et al. (2003).

$$\log(M/L) = a_\lambda + (b_\lambda \times color) \quad (4)$$

A total of six different M_* values were determined from the $r-i$ and $r-z$ colors. The average of all these values was considered as the stellar mass of the galaxies. The uncertainties in the stellar masses were determined from the standard deviations of the results. The M_* values obtained are listed in Table 6.

The relationship between stellar mass and concentration in the R filter is shown in Figure 10. Although the sample size was small, a strong linear correlation was observed, with a regression coefficient of 0.86. However, the data exhibited significant dispersion. This result differs notably from the trend reported by Vega-Acevedo & Hidalgo-Gámez (2022), where the correlation was found to be exponential for galaxies with stellar masses below $2.4 \times 10^8 M_\odot$ and flat for higher masses (represented by the dashed line in the figure).

This finding is particularly intriguing given the subtle differences observed in the $C-A$ plane between the tidal dwarf galaxies and candidate galaxies analyzed by Vega-Acevedo & Hidalgo-Gámez (2022) and the dS galaxies in their study (see Figure 10). However, additional data on Sm and dS galaxies are required to establish a more conclusive relationship between these two parameters.

Finally, we briefly discuss the relationship between the SFR and stellar mass for the five galaxies with stellar mass values. This is shown in Figure 11. Although there are few data, a strong correlation between these two parameters for dS galaxies is clear. Again, more data on the stellar mass for dS galaxies are needed to check the trend emerging here.

6. Conclusions

In this study, the asymmetry and concentration parameters for a sample of Sm/dS galaxies were determined. The average asymmetry value for our sample falls between those of irregular galaxies and late-type spirals, indicating that these galaxies are less symmetrical than the latter class. Regarding concentration, the average value was lower (indicating a higher concentration) than that of both late-type spirals and irregular galaxies.

Table 6. Stellar mass and Star formation rate

Galaxy	$M_*\left[M_\odot\right]\times10^8$	$SFR\left[\mathrm{M_\odot yr^{-1}}\right]$	C_R	A
UGCA 5	···	···	2.5±0.2	0.26±0.04
UGCA 74	···	···	4.0±0.2	0.34±0.05
UGC 891	···	0.10±0.01	3.3±0.2	0.16±0.03
UGC 2301	···	···	4.3±0.1	0.20±0.05
UGC 3775	···	0.14±0.03	2.3±0.2	0.33±0.1
UGC 5242	3.67±1.09	0.20±0.03	1.9±0.2	0.15±0.02
UGC 5296	2.34±1.18	0.03±0.01	1.9±0.3	0.12±0.01
UGC 6205	5.77±2.92	0.23±0.03	2.1±0.2	0.09±0.01
UGC 6304	5.24±1.62	0.30±0.03	1.9±0.3	0.12±0.01
UGC 9570	1.20±4.66	0.43±0.05	2.0±0.1	0.09±0.01
UGC 11820	···	0.02±0.03	3.0±0.2	0.15±0.02
UGC 12212	···	0.40±0.05	1.3±0.2	0.19±0.04

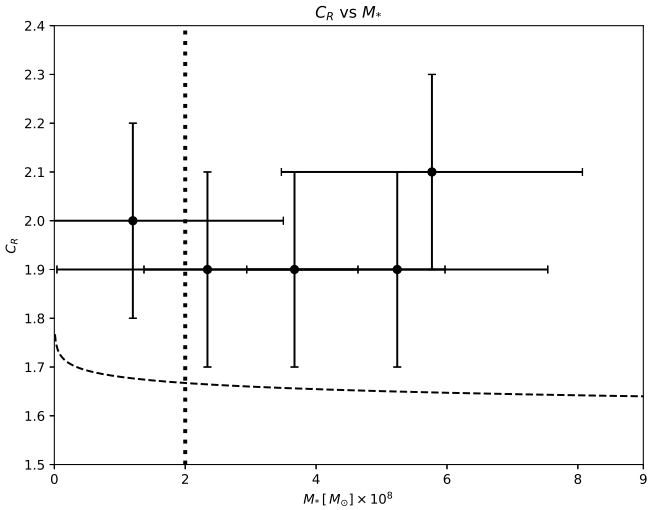

Figure 10. Concentration in R filter versus stellar mass. The dashed line is the correlation fit for TDG of Vega-Acevedo & Hidalgo-Gámez (2022).

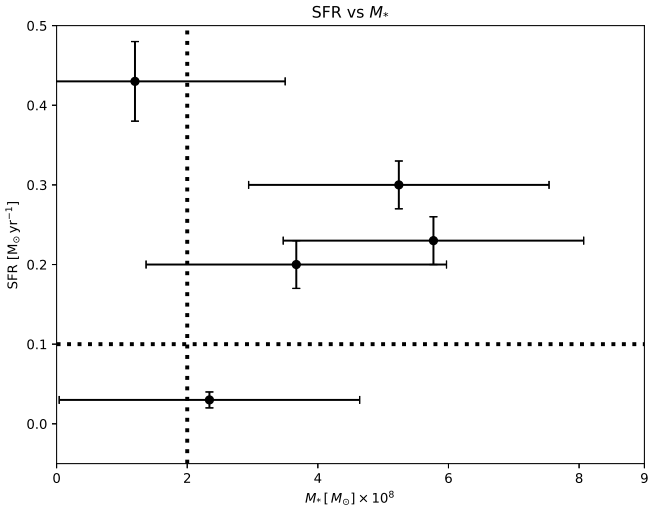

Figure 11. Plot of star formation rate versus stellar mass. The horizontal and vertical dash lines are the SFR and stellar mass mean of dwarf galaxies, respectively.

Additionally, we analyzed the variations in these parameters when different filters (V and R), rotation angles, and galaxy regions were considered. The data suggest that for Sm/dS galaxies, the asymmetry values do not exhibit significant differences between the two filters. However, variations were observed when different radii and angles were considered. The rotation angle yielding the lowest asymmetry was 45^o, while the highest asymmetry was found at 90^o at both radii. This behavior contrasts with that of large galaxies, possibly because of the looser spiral structure of smaller galaxies. Furthermore, the inner regions of galaxies are more symmetrical than the galaxy as a whole. This result aligns with the findings of Conselice (2003) on symmetry in the internal regions of galaxies.

The position of our sample in the $C-$A plane exhibits considerable dispersion, with some galaxies occupying the same locus as dE galaxies and others aligning with the starburst locus. However, the majority of the sample is located between the regions typically occupied by late-type spirals and irregular galaxies, as expected.

Finally, some interesting trends were noted regarding this sample of galaxies. There is a correlation between the concentration and stellar mass, but only for a few data points. Moreover, these galaxies are not in the same locus as irregular and TDG in this plane; instead, they align almost perpendicular to it. Considering asymmetry, there was no correlation between A and the SFR for the galaxies in our sample. The Sm/dS galaxies have, on average, similar values to those of the TDG, but the former do not show a bimodal behavior in the diagram. Finally, Sm/dS galaxies show a relationship between the SFR and stellar mass, being in between the two arms described by the TDG (Vega-Acevedo & Hidalgo-Gámez, 2022).

The discrepancies between the trends observed in our sample of Sm/dS galaxies and the results of previous studies are noteworthy and may suggest that these galaxies possess distinct structural properties, similar to those of TDG galaxies. This underscores the importance of detailed studies to better understand the specific characteristics of different galaxy types and how they vary in relation to properties, such as stellar mass and concentration.

Due to the small sample size (12 galaxies), the results are not statistically significant in this study. However, these findings are intriguing and warrant further investigation, particularly by expanding the sample size in future studies. Therefore, a larger dataset including dS, Sm, TDG, and dwarf irregular galaxies is essential for drawing more robust conclusions.

This research was supported by the Instituto Politécnico Nacional (México) under research projects SIP-20230588 and SIP-20240903. This work is part of M. en C. I. Vega Acevedo's Ph.D. thesis, sponsored by CONACyT (now SECIHTI). This investigation has made use of the NASA/IPAC Extragalactic Database (NED), which is operated by the Jet Propulsion Laboratory, California Institute of Technology, under contract with the National Aeronautics and Space Administration (NASA). This work is based in part on observations made with the GALEX Space Telescope, which is operated by the Jet Propulsion Laboratory of the National Aeronautics and Space Administration (NASA). The SDSS-III web site is http://www.sdss3.org/. SDSS-III is managed by the Astrophysical Research Consortium for the Participating Institutions of the SDSS-III Collaboration including the University of Arizona, the Brazilian Participation Group, Brookhaven National Laboratory, Carnegie Mellon University, University of Florida, the French Participation Group, the German Participation Group, Harvard University, the Instituto de Astrofísica de Canarias, the Michigan State/Notre Dame/JINA Participation Group, Johns Hopkins University, Lawrence Berkeley National Laboratory, Max Planck Institute for Astrophysics, Max Planck Institute for Extraterrestrial Physics, New Mexico State University, New York University, Ohio State University, Pennsylvania State University, University of Portsmouth, Princeton University, the Spanish Participation Group, University of Tokyo, University of Utah, Vanderbilt University, University of Virginia, University of Washington, and Yale University.

References

Abraham, R. G., Tanvir, N. R., Santiago, B. X., et al. 1996a, MNRAS, 279, L47, doi: 10.1093/mnras/279.3.L47

Abraham, R. G., van den Bergh, S., Glazebrook, K., et al. 1996b, ApJS, 107, 1, doi: 10.1086/192352

Banse, K., Crane, P., Grosbol, P., et al. 1983, Msngr, 31, 26

Bell, E. F., McIntosh, D. H., Katz, N., & Weinberg, M. D. 2003, ApJS, 149, 289, doi: 10.1086/378847

Bershady, M. A., Jangren, A., & Conselice, C. J. 2000, AJ, 119, 2645, doi: 10.1086/301386

Binney, J., & Tremaine, S. 2008, Galactic Dynamics: Second Edition (Princeton, NJ: PUP)

Carroll, B. W., & Ostlie, D. A. 2006, An Introduction to Modern Astrophysics (San Francisco: Addison-Wesley)

Conselice, C. J. 2003, ApJS, 147, 1, doi: 10.1086/375001

Conselice, C. J., Bershady, M. A., & Gallagher, III, J. S. 2000a, A&A, 354, L21, doi: 10.48550/arXiv.astro-ph/0001195

Conselice, C. J., Bershady, M. A., & Jangren, A. 2000b, ApJ, 529, 886, doi: 10.1086/308300

Curtis, H. D. 1918, PASP, 30, 159, doi: 10.1086/122707

de Jong, R. S. 1996, A&A, 313, 45, doi: 10.48550/arXiv.astro-ph/9601005

de Vaucouleurs, G. 1959, Handbuch der Physik, 53, 275, doi: 10.1007/978-3-642-45932-0_7

de Vaucouleurs, G., de Vaucouleurs, A., Corwin, Jr., H. G., et al. 1991, Third Reference Catalogue of Bright Galaxies

Graham, A. W., Driver, S. P., Petrosian, V., et al. 2005, AJ, 130, 1535, doi: 10.1086/444475

Graham, A. W., Erwin, P., Caon, N., & Trujillo, I. 2001a, ApJ, 563, L11, doi: 10.1086/338500

Graham, A. W., Trujillo, I., & Caon, N. 2001b, AJ, 122, 1707, doi: 10.1086/323090

Hernández-Toledo, H. M., Avila-Reese, V., Conselice, C. J., & Puerari, I. 2005, AJ, 129, 682, doi: 10.1086/427134

Hidalgo-Gámez, A. M. 2004, RMxAA, 40, 37

Hodge, P. W., & Kennicutt, Jr., R. C. 1983, ApJ, 267, 563, doi: 10.1086/160893

Hubble, E. P. 1926, ApJ, 64, 321, doi: 10.1086/143018

—. 1936, Realm of the Nebulae (New Haven: Yale Univ. Press)

Karachentsev, I. D., Karachentseva, V. E., & Huchtmeier, W. K. 2006, A&A, 451, 817, doi: 10.1051/0004-6361:20054497

Karachentsev, I. D., Makarov, D. I., Sharina, M. E., et al. 2003, A&A, 398, 479, doi: 10.1051/0004-6361:20021598

Magaña-Serrano, M. A., Hidalgo-Gámez, A. M., Vega-Acevedo, I., & Castañeda, H. O. 2020, RMxAA, 56, 39, doi: 10.22201/ia.01851101p.2020.56.01.06

Morgan, W. W. 1958, PASP, 70, 364, doi: 10.1086/127243

—. 1959, PASP, 71, 394, doi: 10.1086/127415

Nilson, P. 1973, Nova Acta Regiae Soc. Sci. Upsaliensis Ser. V, 0

Parkash, V., Brown, M. J. I., Jarrett, T. H., & Bonne, N. J. 2018, ApJ, 864, 40, doi: 10.3847/1538-4357/aad3b9

Pović, M., Sánchez-Portal, M., Pérez García, A. M., et al. 2009, ApJ, 702, L51, doi: 10.1088/0004-637X/702/1/L51

Roye, E. W., & Hunter, D. A. 2000, AJ, 119, 1145, doi: 10.1086/301265

Schade, D., Lilly, S. J., Crampton, D., et al. 1995, ApJ, 451, L1, doi: 10.1086/309677

Schuster, W. J., & Parrao, L. 2001, RMxAA, 37, 187

Sérsic, J. L., Pastoriza, M., & Carranza, G. 1968, BAAAR, 13, 20

van den Bergh, S., Abraham, R. G., Ellis, R. S., et al. 1996, AJ, 112, 359, doi: 10.1086/118020

Vega-Acevedo, I. 2013, Ms thesis, Estudio del parámetro de asimetría en galaxias espirales enanas, Instituto Politécnico Nacional, Ciudad de México, México

Vega-Acevedo, I., & Hidalgo-Gámez, A. M. 2022, RMxAA, 58, 61, doi: 10.22201/ia.01851101p.2022.58.01.05

Warmels, R. H. 1992, in ASPC, Vol. 25, Astronomical Data Analysis Software and Systems I, ed. D. M. Worrall, C. Biemesderfer, & J. Barnes, 115

Revista Mexicana de Astronomía y Astrofísica, 61, 25-34, (2025)

OPEN ACCESS https://doi.org/10.22201/ia.01851101p.2025.61.02.03

Deep-TAO: The Deep Learning Transient Astronomical Object data set for Astronomical Transient Event Classification

John F. Suárez-Pérez[1,2], Catalina Gómez[3], Mauricio Neira[4], Marcela Hernández Hoyos[4], Pablo Arbeláez[5] and Jaime E. Forero-Romero[2]

[1]*Tecnológico de Monterrey, Escuela de Ingeniería y Ciencias, Zapopan, México (jf.suarez@tec.mx).*
[2]*Departamento de Física, Universidad de los Andes, Bogotá, Colombia.*
[3]*Department of Computer Science, Johns Hopkins University, USA.*
[4]*Systems and Computing Engineering Department, Universidad de los Andes, Bogotá, Colombia.*
[5]*Center for Research and Formation in Artificial Intelligence, Universidad de los Andes, Bogotá, Colombia.*

Keywords: *catalogues, methods: data analysis, transients: general*

Abstract

We present the Deep-learning Transient Astronomical Object (Deep-TAO), a dataset of 1,249,079 annotated images from the Catalina Real-time Transient Survey, including 3,807 transient and 12,500 non-transient sequences. Deep-TAO has been curated to provide a clean, open-access, and user-friendly resource for benchmarking deep learning models. Deep-TAO covers transient classes such as blazars, active galactic nuclei, cataclysmic variables, supernovae, and events of an indeterminate nature. The dataset is publicly available in FITS format, with Python routines and Jupyter notebooks for easy data manipulation. Using Deep-TAO, a baseline Convolutional Neural Network outperformed traditional random forest classifiers trained on light curves, demonstrating its potential for advancing transient classification.

Resumen

Presentamos Deep-learning Transient Astronomical Object (Deep-TAO), un conjunto de 1,249,079 imágenes anotadas del Catalina Real-time Transient Survey, que incluyen 3,807 secuencias transientes y 12,500 no transientes. Deep-TAO ha sido diseñado como un recurso limpio, de acceso abierto y fácil de usar, ideal para evaluar y comparar modelos de aprendizaje profundo. Incluye eventos transientes como blazares, núcleos galácticos activos, variables cataclísmicas, supernovas y eventos de naturaleza indeterminada. El conjunto de datos está disponible públicamente en formato FITS, acompañado de rutinas en Python y cuadernos de Jupyter que facilitan su uso. Utilizando Deep-TAO, una red neuronal convolucional básica superó el desempeño de clasificadores tradicionales basados en bosques aleatorios entrenados con curvas de luz, demostrando su potencial para mejorar la clasificación de eventos transientes.

Corresponding author: John F. Suárez-Pérez *E-mail address:* jf.suarez@tec.mx
Received: January 28, 2025 **Accepted:** March 28, 2025

1. Introduction

A primary challenge in time-domain astronomy is the detection and classification of transient astronomical events. In recent years, methods for automating these processes have seen remarkable improvements in both complexity and computational efficiency, driven by the exponential growth of datasets requiring timely analysis (Kaiser, 2004; Law et al., 2009; Smartt, S. J. et al., 2015; Chambers et al., 2016; Martínez-Palomera et al., 2018; Bellm et al., 2019; Dyer et al., 2020; Nidever et al., 2021).

Machine learning (ML) (Wyrzykowski et al., 2014; D'Isanto et al., 2016; Gieseke et al., 2017; Neira et al., 2020; Sánchez-Sáez et al., 2021; Van Roestel et al., 2021) and deep learning (DL) approaches (Gieseke et al., 2017; Cabrera-Vives et al., 2017; Carrasco-Davis et al., 2019; Muthukrishna et al., 2019; Gómez et al., 2020; Sánchez-Sáez et al., 2021; Allam & McEwen, 2024; Van Roestel et al., 2021; Killestein et al., 2021) have demonstrated their capability to provide rapid and accurate solutions for transient classification tasks, offering significant advancements over traditional methods.

The further development and optimization of ML and DL algorithms critically depend on the availability of large-scale, high-quality, and representative datasets. These datasets can be constructed from real observational data (Neira et al., 2020), synthesized light curves (Carrasco-Davis et al., 2019), or image-based data derived from real (Scalzo et al., 2017) or simulated

observations (Carrasco-Davis et al., 2019). The diversity and realism of these datasets are essential for improving the generalizability and robustness of classification models in the context of astronomical transient phenomena.

The image-based datasets that can be used to test and train new DL applications usually present some limitations.

1) Restricted access. Some datasets are private, and only survey collaborators can access them. This limits the possibilities for a broader group of scientists to use the dataset to improve DL techniques.
2) Inconvenient access. Some surveys have set up public websites to access their data. However, sometimes the system is designed to retrieve information about individual objects (Drake et al., 2009; Scalzo et al., 2017; Nidever et al., 2021) and not large samples. This makes it inconvenient to compile the full dataset required for DL training.
3) Unrealistic images. Although other public, open access datasets exist, they are based on simulated images (Carrasco-Davis et al., 2019). This limits the realism required to optimally train DL architectures.
4) Incomplete labels. There are public, easy-to-gather, and realistic datasets that do not have labels on their data (Smartt, S. J. et al., 2015). These labels are required to train the supervised DL architectures.

To date, no dataset for DL transient classification has been made easily accessible to the public in the form of a fully labeled catalog based on observations.

The purpose of this study is to present a dataset to fill this gap. We denominate this dataset Deep-TAO, for Deep-Learning Transient Astronomical Objects. Deep-TAO was built using public data from the Catalina Real-Time Transient Survey (CRTS) (Drake et al., 2009), an astronomical survey searching for transient and highly variable objects. We developed a procedure for extraction and transformation from CRTS into a homogeneous data set of thousands of objects that can be used to train DL algorithms and establish benchmarks.

The remainder of this paper is organized as follows. In § 2 we describe the CRTS, together with the selection and compilation procedures. In § 3 we describe the main features of Deep-TAO, including its structure. In § 4 we describe how to connect our dataset with MANTRA (Neira et al., 2020), a light curve-based dataset built from the CRTS. Finally, in § 5 we demonstrate how Deep-TAO can be used in deep learning-based classification tasks, and then we provide a brief discussion and summary.

2. Observational Inputs to build Deep-TAO

2.1. The Catalina Real-Time Transient Survey and the Catalina Sky Survey

We retrieved the images for Deep-TAO from the public catalogs of the Catalina Real-Time Transient Survey (CTRS Drake et al., 2009; Mahabal et al., 2011), an astronomical survey for transients and highly variable objects. The area covered by the CRTS is 33,000 square degrees, and it has been observing the sky since 2007 with three telescopes: Mt. Lemmon Survey (MLS), Catalina Sky Survey (CSS), and Siding Spring Survey (SSS). We used data from the CSS telescope, an $f/1.8$ Schmidt catadioptric equipped with a 111-megapixel CCD detector. The CSS telescope and detector have a scale of 2.5 arcseconds per pixel, providing an 8 square degrees field of view. Observations were made on a grid of adjacent fields. The survey covered 4,000 square degrees per night with a limiting magnitude of 19.5 in the V-band. Each observation consist of one image obtained using an exposure time of 30 seconds.

2.2. Transient catalogs from the CRTS and the CSS

We built Deep-TAO from the public transient catalog published by CRTS. The data reports five classes: blazars (BZ), active galactic nuclei (AGN), cataclysmic variables (CV), supernovae (SN), high proper motion stars (HPM), and other events of unknown nature (Drake et al., 2009). The transient catalog lists Right Ascension (RA), Declination (Dec), V-band magnitude, discovery date, classification class, and light curve points.

The CSS catalog contains observations from 2003 to 2012. The selected fields were typically visited four times at night, and the median total number of visits over 10 years was 20. Each CSS image (of size $4,110 \times 4,096$ pixels covering an area of 29,500 square arcminutes) is divided into 1,156 smaller images called cutouts stored in the Flexible Image Transport System (FITS) format. Each cutout is about 120×120 pixels and represents an area of 5×5 arcminutes. Each cutout file stores the pixel intensities, the date on which the image was captured, a field identifier, and a number identifying the order of the image in the sequence of observations taken on a given night.

2.3. Building Regions of Interest

We used the cutouts to build a Region of Interest (RoI) centered on an object of interest. We designed RoIs to be squares of 64×64 pixels size centered on a RA/Dec coordinate of interest. This requires downloading the cutouts, assembling them into a single image, and finally cutting out the RoI around the RA/Dec of interest.

We refer to the time-ordered set of RoIs around the same coordinates as *a RoI sequence*. We built RoI sequences over a three-year interval, where the second year always included the date of maximum brightness. During this period, the time spacing between images was not uniform. The intervals ranged from days to months.

We queried the RoI sequences using web scraping techniques to automatically access and download the images using the desired RA/Dec position as an input. This process comprises five steps:

1) Download all the available cutouts that overlap with the input RA/Dec in a time span of three years for each object.

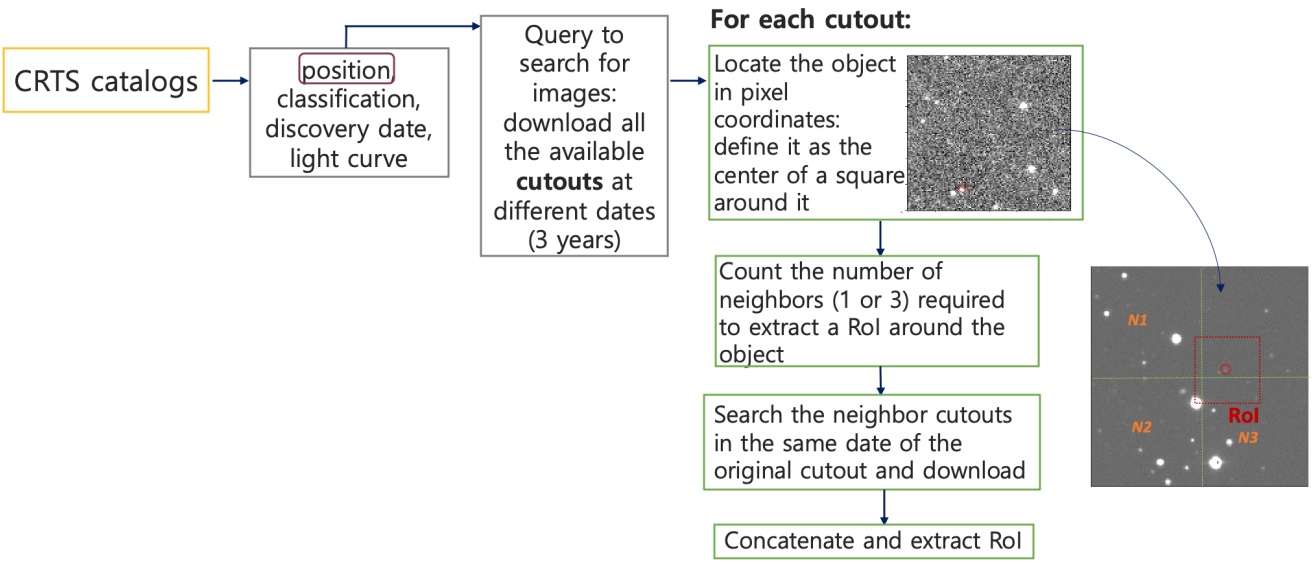

Figure 1. Overview of the search procedure to acquire the image sequences of transient objects.

2) For each cutout, locate the RA/Dec location to define a region of interest (RoI) around that coordinate.
3) Count the number of neighboring cutouts (one or three) required to build the RoI.
4) Query for the neighboring cutouts. If any of those does not exist, the RoI is not built.
5) Concatenate all cutouts to extract and store the RoI.

Figure 1 illustrates these steps. It took 11,000 CPU hours to query the CRTS/CSS database to build the full Deep-TAO dataset.

Transient objects are available in the CRTS catalogs. However, a catalog of non-transient objects is not available. To define the Non-Transient RA/Dec locations, we used transient source cutouts. All sources in the cutout of a transient at any date were detected. Then, sources at a distance greater than a threshold of 33 pixels from the transient are considered as a possible non-transient candidate.

This threshold ensures that the transient object does not appear in the RoI of the non-transient candidate. For each non-transient candidate, we computed its RA/Dec coordinates to build all the RoIs on the same dates as the parent transient sequence. Using this procedure, we compiled a total of 12,500 non-transient locations.

3. Deep-TAO Description

Figure 2 shows a grid of illustrative examples for different transients and Non-Transients in Deep-TAO. The images in that figure are a subset of the full RoI sequence for each object, the temporal spacing between images is uneven, and the time stamps are not uniform across different objects. To ease visualization, the pixel values were renormalized to have the same range across all images.

In all the cases shown in Figure 2, the variability of the central source was easy to spot by eye. This illustrative example also shows features (i.e. trails at the end of the Cataclysmic Variable sequence, overall brightness change in the first half of the Other Objects class) that might come from fluctuating observational and instrumental conditions, representing the realism of Deep-TAO.

In the following sections, we describe the overall Deep-TAO statistics, the data model used to store the information in the public repositories, and the Python-based tools to interact with Deep-TAO files.

3.1. General Statistics

Table 1 summarizes the global statistics for the Deep-TAO dataset. The first row shows the total number of targets in the original CRTS catalog. The second row indicates the number of targets for which we managed to recover a RoI sequence. Some transients in the original catalog were not included in Deep-TAO out due to the impossibility of having the transient centered in the cutout. The third row indicates the total number of RoI extracted for each class.

Figures 3, 4, 5 present some cumulative statistics computed over the RoI sequences for each class. Figure 3 shows the cumulative distribution of the number of images by sequence. The left panel shows all the transient classes, and the right panel compares transients and non-transients. This figure shows that the median value is approximately 100 RoIs per sequence. The shortest sequence had five RoIs, and the longest had approximately 300 RoIs. For non-transient sequences, there was a median of 70 RoIs, whereas for transients, the median was 100 RoIs per sequence.

Figure 4 shows the results for the average RoI signal. Here, we define the signal as the sum of all CCD counts

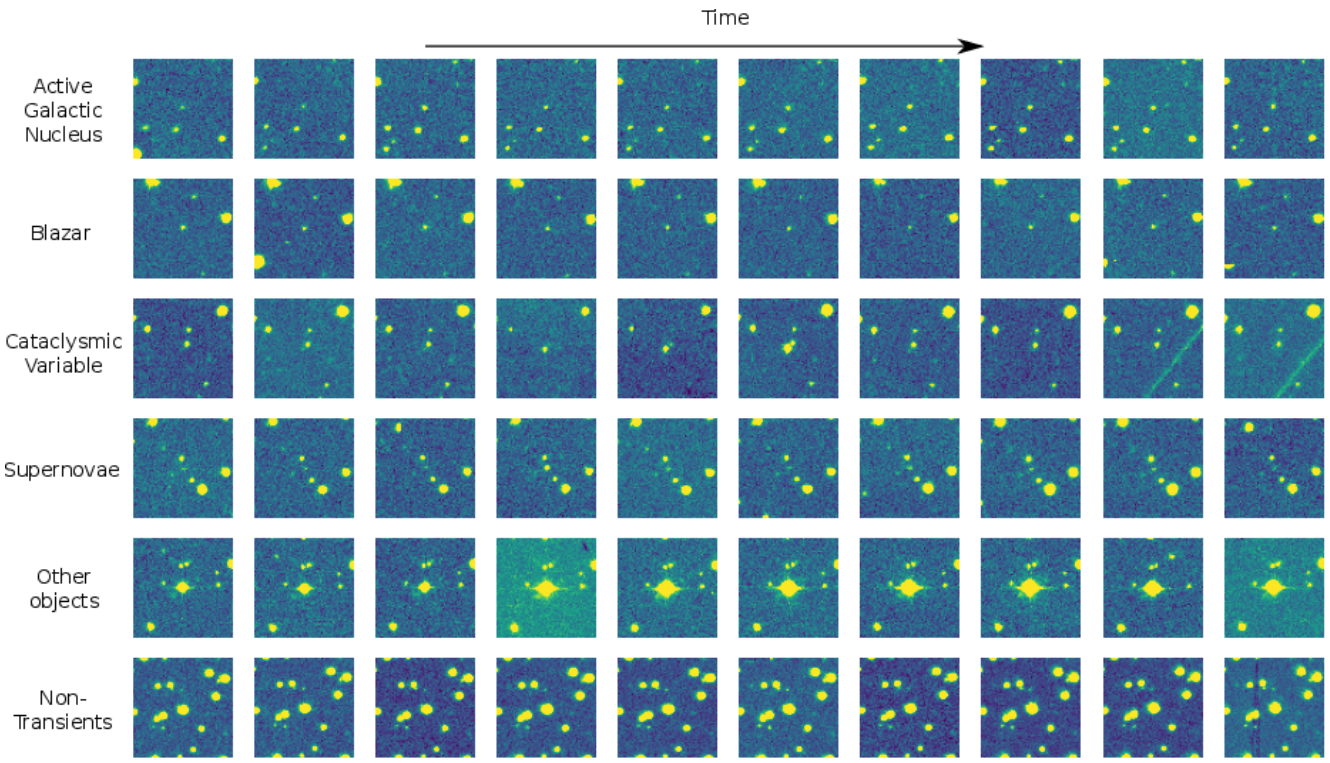

Figure 2. Sample images in Deep-TAO. Each row corresponds to a sample from a different class. The temporal spacing between consecutive images varied for each example. Images were normalized for visualization.

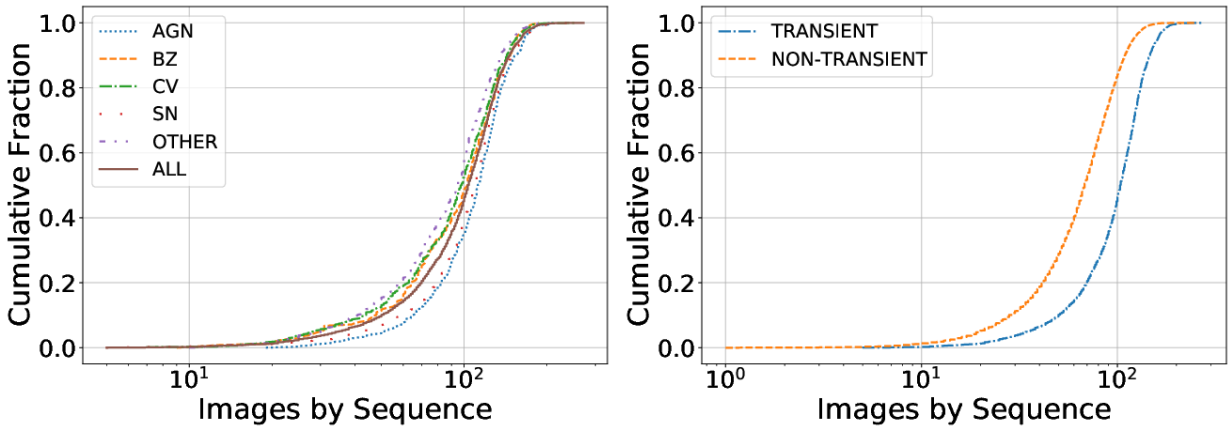

Figure 3. Cumulative distribution of RoIs per sequence. (Left) The distributions are split across the transient classes. The median was approximately 100 images per sequence. (Right) Distributions are split between transient and non-transient objects. The median for non-transients is around 70 images per sequence.

Table 1. General statistics of Deep-TAO data set*

	BZ	AGN	CV	OTHER	SN	Total Transients	Non-Transients	Total
Targets in CRTS	270	651	987	1,054	1,723	4,712	-	4,712
Targets in Deep-TAO	239	606	772	818	1,372	3,807	12,500	16,307
Total RoIs	23,429	66,998	73,739	74,536	146,847	385,549	863,530	1,249,079

*The first row corresponds to the transients included in the public CRTS transient catalog. The second row represents the number of objects for which a sequence of RoIs can be retrieved over a three-year observation period. The last row is the total number of RoIs included for each class.

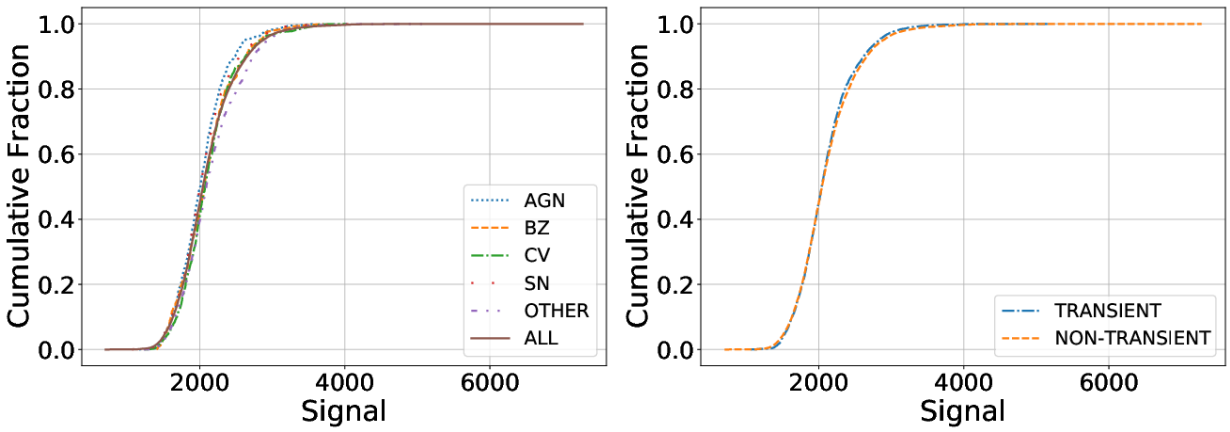

Figure 4. (Left) Cumulative fraction as a function of the median signal for the objects in each transient class and all transients objects (continuous line). (Right) Cumulative fraction between transient and non-transient objects. The shapes of these classes were similar. In both figures the media of the signal is around 2000.

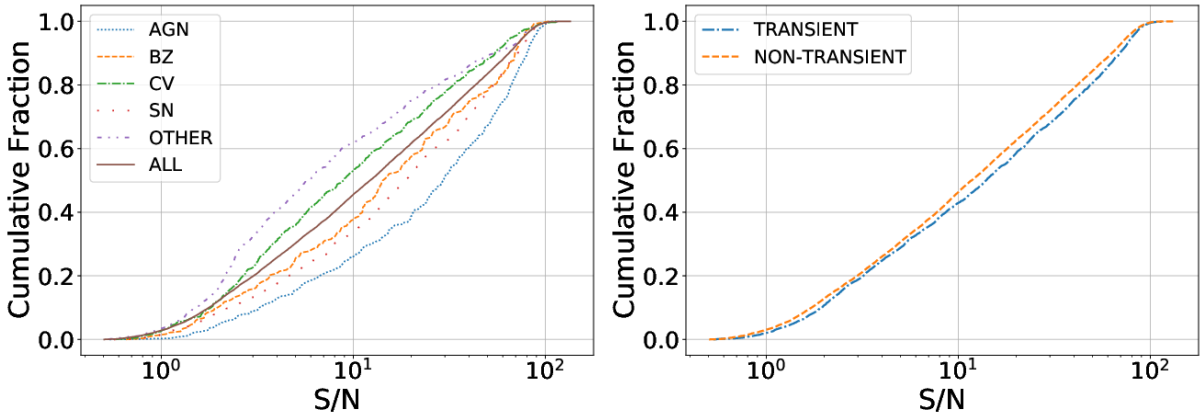

Figure 5. (Left) Cumulative distribution of the average signal-to-noise. for the object in each transient class and all transient objects (continuous line). The media of the signal/noise for all transient objects is approximately 10. (Right) Cumulative fraction between transients and non-transients objects. In both cases the media of signal/noise is around 20.

across the RoI. The left panel corresponds to all transient classes, whereas the right panel compares transients and non-transients. This figure shows that all transient classes and non-transients have similar intensity distributions.

Figure 5 shows a comparison of the average signal-to-noise (S/N) distribution for all transient classes (left) and transients versus non-transients (right). We estimated the signal-to-noise ratio for an RoI as the ratio between the sum of all CCD counts and the standard deviation of the CCD counts.

We found that the average S/N spans almost two orders of magnitude, ranging from 1 to 100. For transients, the median of the average S/N ranged between 6 and 20 across all classes, with some differences between classes. In contrast, the distributions of Transients and Non-Transients were virtually the same.

3.2. Data Model

The Deep-TAO data set is allocated on GitHub into two different repositories, one for transients objects[1] and other for non-transients[2]. The transient repository contains three main folders: `data`, `paper`, and `mantra`.

The `data` folder contains all the transient sequences separated in subfolders by class (AGN, BZ, CV, OTHERS, and SN), each subfolder contains the sequences stored in FITS files. A single FITS file stores all the RoIs associated with a transient event, and the file name is the CRTS identifier. Each file contains a header, and the FITS header in each file has minimal identifying information, such as the CRTS_ID unique identifier, the J2000 RA/Dec coordinates, the number of RoIs (`N_Images`) in the sequence, and the Universal Time UT_Date associated with the discovery date. The full list of fields included in the header is presented in Table 2.

[1] https://github.com/MachineLearningUniandes/TAO_transients
[2] https://github.com/MachineLearningUniandes/TAO_non-transients

Table 2. FITS header of the transient files

Header Dict	Description	Type
CRTS_ID	Catalina Real-time Transient Survey ID	str
RA_(J2000)	Right Ascension (degrees)	float
Dec_(J2000)	Declination (degrees)	float
N_Images	Total number of images for CRTS ID	int
UT_Date	UT Discovery Date (YYYYMMDD)	float
Mag	Unfiltered CSS magnitude	float
CSS_Images	Pre and post-discovery images ID	int
SDSS	Covered by SDSS DR-12 (yes/no)	str
Others	ID to other image data at the location (PQ, DSS, 2MASS, SDSS)	int
Followed	P60 follow up (yes/no)	str
Last	Last Observation date	str
LC	Current CSS lightcurve	int
FC	Finding chart (yes/no)	str
Class	Transient classification	str

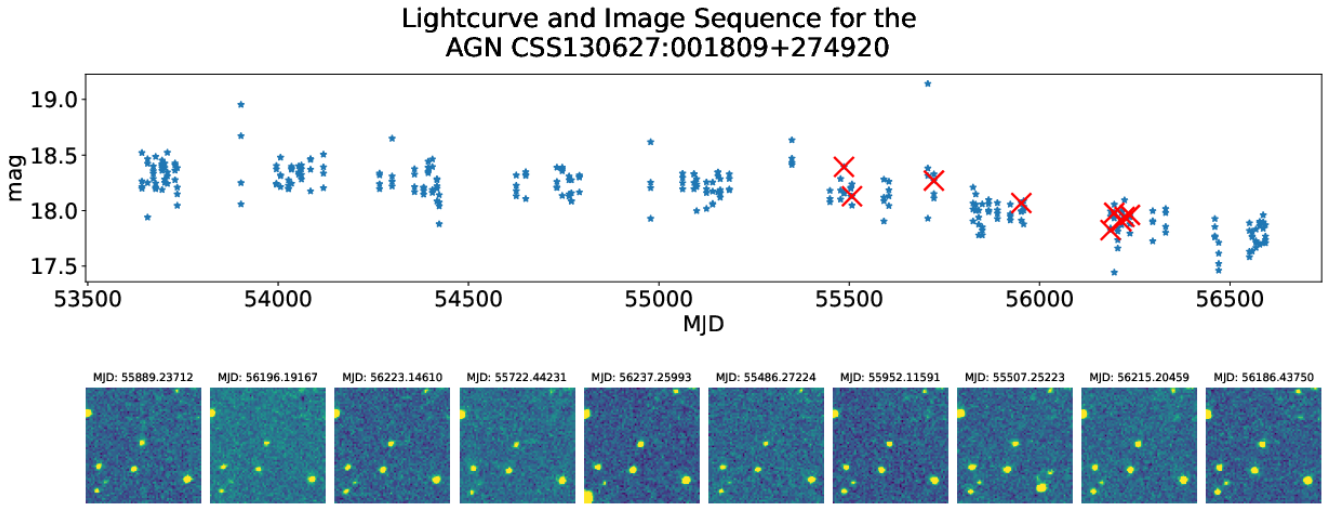

Figure 6. Lightcurve and examples of the image sequence for the AGN CSS130627:001809+274920 from MANTRA and Deep-TAO obtained using the `Connection_MANTRA` Jupyter notebook. The red cross correspond to the images plotted bottom in the figure.

The first HDU (extension 1) in the FITS files is a 2D array with the columns listed in Table 3. This array contains information for each RoI in the sequence, such as the HDU extension for each RoI and the observation date. Starting from HDU 2 onward to HDU `N_Images+1`, each HDU contains an RoI as an integer array of size 64×64.

The second main folder is `paper`, which contains Figures 3, 4, 5 which describe the general statistics of Deep-TAO. This folder also contains a Python-based tool to reproduce these results. This tool is explained in the next subsection.

The `mantra` folder contains the Figure 6, which shows an example of how to connect Deep-TAO with MANTRA (Many ANnotated TRAnsients), an annotated Machine-learning Reference lightcurve dataset in the V-band also built from the CRTS (Neira et al., 2020). More details are provided in Section 4.

Finally, the non-transient repository only contains the `data` folder with the FITS files of the non-transient objects. In contrast to the header of a Transient FITS file, the non-transient FITS header allocates the information of Table 4, which includes the CRTS_ID, the RA/Dec coordinates, the number of images in the sequence, and the image source from which it was extracted.

The first HDU in each FITS non-transient file allocates the information in Table 5: the HDU_Extension for each RoI, the date of observation, the MJD, the Field_ID, and the cutout.

Table 3. Identifiers stored first HDU: Transient files*

Key	Description	Type
HDU_Ext	HDU extension of the RoI (From 2 to `N_Images+1`)	int
Set_Number	Stands for the sequence (or set number)	str
Date	Date of observation (YYMMMDD)	str
MJD	Modified Julian Date	float
Field_ID	Field identifier	str
Obs_In_Seq	Refers to the observation's number in the sequence	str
Cutout	Cutout matrix location. Each cutout covers an area of about 5×5 arcminutes	str

*Basic information in the first HDU about the image sequence in each transient FITS file.

Table 4. FITS header of the non-transient objects

Header Dict	Description	Type
CRTS_ID	Catalina Real-time Transient Survey ID	str
RA_(J2000)	Right Ascension (degrees)	float
Dec_(J2000)	Declination (degrees)	float
N_Images	Total number of images for CRTS ID	int
Img_Ref	Image of reference where the non-transient object was identified	str

Table 5. Identifiers stored first HDU: Non-transient files*

Key	Description	Type
HDU_Ext	HDU extension of the RoI (From 2 to `N_Images+1`)	int
Date	Date of observation (YYMMMDD)	str
MJD	Modified Julian Date	float
Field_ID	Field identifier	str
Cutout	The cutout matrix location Each cutout covers an area of about 5×5 arcminutes	str

*Basic information in the first HDU of the Non-Transient objects about the image sequence in each FITS file.

3.3. Python-based tools

In the folder `data` of the transients repository, there is a Jupyter notebook to manipulate the data. The `Read_dataset` Jupyter notebook shows the mechanism for reading the FITS files for transient and non-transient objects. In the folder `paper` in the same repository, we provide the `Explore_data set` Jupyter notebook, this shows how to compute some statistics from Deep-TAO to obtain the Figures 2, 3, 4 and 5, assuming that the `data/NON` folder from the non-transient's repository is located in the `data` folder of the transient's repository. This notebook also creates a plain text file in the `paper` folder called `statistic.csv`. This file has 16,307 rows, one by object in Deep-TAO, and four columns with the class name `class` (BZ,AGN,CV,OTHER,SN, or NON), the number of images by sequence `nimages_seq`, the median of the signal/noise measure `signal_noise_median`, and the median of the signal `signal_median`.

4. Linking Deep-TAO images to MANTRA lightcurves

In Neira et al. (2020), the authors presented MANTRA, an annotated machine-learning reference light curve dataset also built from the CRTS. MANTRA contains 4,869 transients and 71,207 non-transients as a plain text file to facilitate a standardized quantitative comparison of astronomical transient event recognition algorithms. The classes included in MANTRA are supernovae, cataclysmic variables, active galactic nuclei, high proper motion stars, blazars, and flares. The data set is publicly available and easy to access [3].

In the `mantra` folder of the Deep-TAO transients repository[4], we provide the `Connection_MANTRA` Jupyter notebook to link the image sequence from Deep-TAO to the lightcurve from MANTRA. This connection is established through the unique CRTS ID. For non-transients, this connection between images and light curves cannot be

[3] https://github.com/MachineLearningUniandes/MANTRA
[4] https://github.com/MachineLearningUniandes/TAO_transients

Table 6. F-measure for the binary task*

Set	Data	Model	Transient	Non-Transient	F1 ($\mu \pm \sigma$)
Validation	Images	TAO-Net	74.46	95.06	84.76 ± 10.30

*F-measure for each class in the validation set for the binary task. The last column reports the average F-measure.

Table 7. F-measure for the transient classification*

Set	Data	Model	BZ	AGN	CV	OTHER	SN	F1 ($\mu \pm \sigma$)
Validation	Light curves	RF	19.74	42.67	53.60	56.06	55.36	45.49 ± 13.75
Validation	Images	CNN	25.17	49.77	59.48	64.04	63.39	52.37 ± 14.53

*The last column reports the average F-measure of the 5 transient categories.

established between Deep-TAO and MANTRA because both have different non-transient objects.

Figure 6 shows an example of an AGN. Using the MJD information, it is possible to connect points in the light curve to images in the sequence. In the light curve of Figure 6, the red crosses correspond to the images plotted below in this figure. Due to the constraints in the RoI construction (Section 2), not all points in the MANTRA lightcurve have a corresponding image in Deep-TAO. Another reason is that Deep-TAO includes only three-year intervals of observations.

5. Example of a Deep-TAO application

Here, we show some examples of Deep-TAO applications using a Convolutional Neural Network (CNN) to gauge its performance on three basic classification tasks:

1. binary classification between Transients and Non-Transients.
2. fine-grained classification into five transient classes (Blazar, AGN, Cataclysmic Variables, Supernovae, and Other)
3. fine-grained classification into five transient classes and Non-Transients as a sixth class.

We evaluated all tasks using metrics that were robust to class imbalances. For each class, we report the maximum F-measure (F1) from the Precision-Recall (PR) curve that we constructed by setting different thresholds on the output probabilities of each class. The global performance is the F1 average across individual classes, with an uncertainty computed as the standard deviation. In all experiments, we used 70% of Deep-TAO data for training, 25% for validation, and 5% for testing.

The CNN used here is based on the previous work by Gómez et al. (2020). They used TAO-Net, a neural network composed of two modules. First, a CNN based on the DenseNet architecture is used to extract a feature representation, and then a Recurrent Neural Network (RNN) that uses these representations to solve the classification task. Here, we only use the first part, a CNN based on a Densely Connected Convolutional Network (DenseNet) (Huang et al., 2017) with $L = 70$ layers and a growth rate $k = 32$.

We model temporal information by selecting images from the complete sequences. We considered images at three different dates in sequential order, such that they reflect differences in brightness for transient classes. We included the observation date in the three-year period when the transient object had the maximum brightness and one observation before and after that date. For the Non-Transient class, we considered the first, middle, and last dates of the sequence of ordered images. At each date, we took the first available observation and then merged the temporal information by sampling images from the complete sequences at three different dates in sequential order. This selection reflects the evolution of temporal information, evidencing the differences in brightness for transient classes.

Table 6 summarizes the results of the binary classification tasks. As expected, it was considerably easier to classify a sequence as non-transient (F1 of 95.06) than as transient (F1 of 74.46).

For the five-class transient classification task, we performed an experiment that consisted of the traditional approach for transient classification using the light curves from the CRTS. We computed the discriminatory features from the light curves to train a Random Forest (RF) classifier. All details on feature extraction and the RF classifier can be found in Neira et al. (2020). These results are equal to those of Gómez et al. (2020) because we share the same dataset and algorithm parameters.

Table 7 lists the F-scores of the transient classification tasks. The results show that classification with images using a CNN is a better option that makes a classification with light curves using a RF algorithm. With RF on the light curves, the best classification was for the OTHER class with 56.06, followed by the SN class with 55.36. The worst is the BZ class with 19.74, and the average F1-score is 45.49. The CNN on images is better with an average F1-score of 52.37, where the best classification is for OTHER with 64.04,

Table 8. F-measure for the multi-class detection*

Set	Data	Model	BZ	AGN	CV	OTHER	SN	Non-T	F1 ($\mu \pm \sigma$)
Validation	Images	CNN	21.82	37.45	54.76	40.22	46.59	95.29	49.36 ± 22.84

*The last column reports the average F-measure of the 6 classes.

followed by SN with 63.39, and the worst classification is for BZ with 25.17.

Finally, in Table 8 we present the F-scores of the multi-class classification problem, which includes the five transient classes and the non-transient class using only the CNN method with images. Compared with the previous task, the overall performance was worse for every transient class, indicating that this task is more difficult when non-transient objects are included. The F-measure shows that the best classification is for the non-transient class, with a score of 95.29. The best transient class classified correctly was the CV, with a score of 54.76, followed by the SN class, with a score of 46.59.

6. Conclusions

There is increasing interest in automated methods for detecting transient sources. Some of these methods are based on Deep Learning techniques that require the use of large, realistic datasets for training. Publicly available and easily accessible datasets can trigger the development of new deep learning applications for transient detection.

In this study, we present such a dataset. We named it Deep-TAO, for deep-learning transient astronomical objects. This is the first public and easily accessible dataset based on real images that can be used to train and improve Deep Learning algorithms for transient classification. The dataset is a compilation of images extracted and transformed from the Catalina Real-Time Transient Survey (CRTS). Deep-TAO includes 3,807 transient and 12,500 non-transient objects with a total of 1,249,079 real astronomical images. Deep-TAO is publicly available at https://github.com/MachineLearningUniandes/.

We demonstrated the utility of Deep-TAO using a set of deep learning experiments and comparisons against a machine learning algorithm. We explored the transient versus non-transient task, the fine-grained multi-classification task between five transient classes, and finally a fine-grained multi-classification task with six classes, five transient classes, and non-transient as another class.

In the three tasks we used the same architecture, a Densely Connected Convolutional Network with $L = 70$ layers and a growth rate $k = 32$ motivated by the more complex architecture proposed by Gómez et al. (2020). In the fine-grained multi-classification task between five transient classes, we compared a classification based on a CNN with images and the classification of light curves with a random forest with 200 trees based on the work by Neira et al. (2020). The results showed that CNN consistently performed better.

Deep-TAO is public with files in the FITS format to facilitate its usability in different projects. The realism of Deep-TAO provides an additional motivation to train new learning-based models to be used by next-generation experiments in time-domain astronomy, and hopefully, it will also motivate the creation of more datasets with a similar structure: realistic, fully labeled, open, and easy to access.

The authors thank the Office of the Vice Rector for Research at the Universidad de los Andes for supporting this project by the grant SPATIO TEMPORAL TRANSIENT OBJECT /P17.246622.004/01. JFSP and JEFR acknowledge the support of INV-2021-126-2256 and INV-2022-137-2394 projects of the Universidad de Los Andes, Facultad de Ciencias. We also thank contributors and collaborators of the open-source packages fundamental to our work: NumPy (Van Der Walt et al., 2011), the Jupyter notebook (Kluyver et al., 2016), matplotlib (Hunter, 2007) and pandas (McKinney et al., 2010). The CRTS and CSDR2 are supported by the U.S. National Science Foundation under NSF grants AST-1313422, AST-1413600, and AST-1518308. The CSS survey is funded by the National Aeronautics and Space Administration under Grant No. NNG05GF22G was issued through the Science Mission Directorate Near-Earth Objects Observations Program.

Data Availability

The Deep-TAO data set is publicly available at https://github.com/MachineLearningUniandes/ into two different repositories, one for transients objects (https://github.com/MachineLearningUniandes/TAO_transients) and other for non-transients (https://github.com/MachineLearningUniandes/TAO_non-transients).

References

Allam, T., & McEwen, J. D. 2024, RAS Techniques and Instruments, 3, 209, doi: 10.1093/rasti/rzad046

Bellm, E. C., Kulkarni, S. R., Graham, M. J., et al. 2019, PASP, 131, 018002, doi: 10.1088/1538-3873/aaecbe

Cabrera-Vives, G., Reyes, I., Förster, F., Estévez, P. A., & Maureira, J.-C. 2017, ApJ, 836, 97, doi: 10.3847/1538-4357/836/1/97

Carrasco-Davis, R., Cabrera-Vives, G., Förster, F., et al. 2019, PASP, 131, doi: 10.1088/1538-3873/aaef12

Chambers, K. C., Magnier, E. A., Metcalfe, N., et al. 2016, arXiv e-prints, arXiv:1612.05560, doi: 10.48550/arXiv.1612.05560
D'Isanto, A., Cavuoti, S., Brescia, M., et al. 2016, MNRAS, 457, 3119, doi: 10.1093/mnras/stw157
Drake, A. J., Djorgovski, S. G., Mahabal, A., et al. 2009, AJ, 696, 870, doi: 10.1088/0004-637X/696/1/870
Dyer, M. J., Steeghs, D., Galloway, D. K., et al. 2020, in Ground-based and Airborne Telescopes VIII, ed. H. K. Marshall, J. Spyromilio, & T. Usuda, Vol. 11445, International Society for Optics and Photonics (SPIE), 114457G, doi: 10.1117/12.2561008
Gieseke, F., Bloemen, S., van den Bogaard, C., et al. 2017, MNRAS, 472, 3101, doi: 10.1093/mnras/stx2161
Gómez, C., Neira, M., Hoyos, M. H., Arbeláez, P., & Forero-Romero, J. E. 2020, MNRAS, 499, 3130, doi: 10.1093/mnras/staa2973
Huang, G., Liu, Z., Van Der Maaten, L., & Weinberger, K. Q. 2017, in 2017 IEEE Conference on Computer Vision and Pattern Recognition (CVPR), 2261–2269, doi: 10.1109/CVPR.2017.243
Hunter, J. D. 2007, CSE, 9, 99, doi: 10.1109/MCSE.2007.55
Kaiser, N. 2004, in Society of Photo-Optical Instrumentation Engineers (SPIE) Conference Series, Vol. 5489, Ground-based Telescopes, ed. J. Oschmann, Jacobus M., 11–22, doi: 10.1117/12.552472
Killestein, T. L., Lyman, J., Steeghs, D., et al. 2021, MNRAS, 503, 4838, doi: 10.1093/mnras/stab633
Kluyver, T., Ragan-Kelley, B., Pérez, F., et al. 2016, in IOS Press, 87–90, doi: 10.3233/978-1-61499-649-1-87
Law, N. M., Kulkarni, S. R., Dekany, R. G., et al. 2009, PASP, 121, 1395, doi: 10.1086/648598
Mahabal, A. A., Djorgovski, S. G., Drake, A. J., et al. 2011, BASI, 39, 387. https://arxiv.org/abs/1111.0313
Martínez-Palomera, J., Förster, F., Protopapas, P., et al. 2018, AJ, 156, 186, doi: 10.3847/1538-3881/aadfd8
McKinney, W., et al. 2010, in Proceedings of the 9th Python in Science Conference, Vol. 445, Austin, TX, 51–56
Muthukrishna, D., Narayan, G., Mandel, K. S., Biswas, R., & Hložek, R. 2019, PASP, 131, 118002, doi: 10.1088/1538-3873/ab1609
Neira, M., Gómez, C., Suárez-Pérez, J. F., et al. 2020, ApJS, 250, 11, doi: 10.3847/1538-4365/aba267
Nidever, D. L., Dey, A., Fasbender, K., et al. 2021, AJ, 161, 192, doi: 10.3847/1538-3881/abd6e1
Sánchez-Sáez, P., Reyes, I., Valenzuela, C., et al. 2021, AJ, 161, 141, doi: 10.3847/1538-3881/abd5c1
Scalzo, R. A., Yuan, F., Childress, M. J., et al. 2017, PASA, 34, e030, doi: 10.1017/pasa.2017.24
Smartt, S. J., Valenti, S., Fraser, M., et al. 2015, A&A, 579, A40, doi: 10.1051/0004-6361/201425237
Van Der Walt, S., Colbert, S. C., & Varoquaux, G. 2011, CSE, 13, 22, doi: 10.1109/MCSE.2011.37
Van Roestel, J., Duev, D. A., Mahabal, A. A., et al. 2021, AJ, 161, 267, doi: 10.3847/1538-3881/abe853
Wyrzykowski, Ł., Kostrzewa-Rutkowska, Z., Kozłowski, S., et al. 2014, AcA, 64, 197, doi: 10.48550/arXiv.1409.1095

Revista Mexicana de Astronomía y Astrofísica, 61, 35-51, (2025)

OPEN ACCESS https://doi.org/10.22201/ia.01851101p.2025.61.02.04

Investigating Open Cluster KING 6: Detection of Three New Variables

Vaibhav Kumar Pandey[1], Arvind K. Dattatrey[2], Apara Tripathi[1], R. K. S. Yadav[2] and Shantanu Rastogi[1]

[1]*Deen Dayal Upadhyaya Gorakhpur University, Gorakhpur, Uttar Pradesh, India, 273009.*
[2]*Aryabhatta Research Institute of Observational Sciences, Manora Peak, Nainital, Uttarakhand,India, 263001.*

Keywords: *clusters, photometric, stars, variables*

Abstract

This study presents a photometric analysis of the intermediate-age open cluster King 6, utilizing photometric data in $UBV(RI)_c$ passbands and JHK_s from the $2MASS$ mission. Gaia DR3 kinematic data were used to estimate the membership probabilities, and $TESS$ data were employed to search for variable stars within the cluster. The cluster's radius is estimated to be 9′.0 based on the stellar density profile, while optical and near-infrared color-color diagrams revealed color excesses of $E(B-V) = 0.58 \pm 0.03$, $E(J-K) = 0.24 \pm 0.03$, and $E(V-K) = 1.53 \pm 0.01$ mag. The interstellar extinction law is normal in the direction of the cluster. The cluster's estimated age is ∼ 251 Myr and the distance is 724 ± 5 pc. The mass function slope was found to be $x = 0.57 \pm 0.28$ by considering stars ≥ 1 $M_\odot$. Our analysis indicates that the cluster was dynamically relaxed. Furthermore, we identified three new variable stars for the first time in the cluster region using $TESS$ data. These variables belong to the category of slow-pulsating B-type variables with periods of 46.70, 47.92, and 37.56 h.

Resumen

Se presenta el análisis fotométrico del cúmulo abierto de edad-intermedia King 6, utilizando datos en las bandas fotométricas $UBV(RI)_c$ y JHK_s del censo $2MASS$. De los datos cinemáticos de Gaia DR3 se estimaron las probabilidades de pertenencia al cúmulo y los datos de $TESS$ se utilizaron para una búsqeda de estrellas variables en el cúmulo. El radio estimado del cúmulo es 9′.0 obtenido a partir del perfil de densidad estelar. Los colores en el infrarrojo cercano revelan los excesos de color $E(B-V) = 0.58 \pm 0.03$, $E(J-K) = 0.24 \pm 0.03$, y $E(V-K) = 1.53 \pm 0.01$ mag. La ley de extinción interestelar es la normal en la dirección del cúmulo. La edad del cúmulo es ∼ 251 Myr y la distancia es de 724 ± 5 pc. La pendiente de la función de masa resulta $x = 0.57 \pm 0.28$ considerando estrellas de masa ≥ 1 $M_\odot$. Nuestro análisis indica que el cúmulo está relajado dinámicamente. Finalmente, se identificaron tres nuevas estrellas variables en la región del cúmulo utilizando datos de $TESS$. Estas estrellas son variables pulsantes lentas tipo-B con períodos de 46.70, 47.92, and 37.56 hr.

Corresponding author: Apara Tripathi *E-mail address:* apara.phy@ddugu.ac.in
Received: January 3, 2025 **Accepted:** April 7, 2025

1. General

Open star clusters serve as excellent laboratories for exploring stellar evolution and dynamics in our galaxy. They provide insights into star formation processes, thereby enhancing our understanding of the universe (Lada & Lada, 2003). Open clusters (OCs) consist of stars with similar physical properties that form simultaneously from the collapse of molecular clouds (McKee & Ostriker, 2007). Although member stars share the same age, distance, and chemical composition, their masses vary (Joshi et al., 2020a). The study of OCs using astrometric and photometric observations allows us to determine the parameters of single stars (Dias et al., 2021), partially explaining the interest in these systems. Furthermore, combining astrophysical parameters, such as distance, metallicity, and age, with the kinematic properties of stars within OCs makes them valuable tools for studying the formation and evolution of the Galactic disc (Cantat-Gaudin et al., 2020). A comprehensive photometric study based on membership determination using proper motions (PMs) and parallaxes helps to understand the stellar and dynamical evolution of clusters (Tripathi et al., 2023).

King 6 is positioned at (α_{J2000} = 03:27:55.7, δ_{J2000} = +56:26:38) corresponding to Galactic coordinates l ∼ 143°.36 and b ∼ -0°.07. Trumpler (1930) classified this cluster as II2m based on V-band images. Ruprecht (1966) reclassified it in class IV2p. Ann et al. (2002), using $UBVI_c$ CCD photometry, reported mean reddening $E(B-V)$ = 0.50 ± 0.10 mag, log(age) = 8.40 ± 0.10 and distance modulus as $(m-M)_0$ = 9.70 ± 0.40 mag. Maciejewski

& Niedzielski (2007) performed a survey in BV wide-field CCD photometry. They estimated the core radius of King 6 as $3'.60 \pm 0'.40$, a log(age) value of 8.40, a distance modulus of 11.17 ± 0.51 mag, and a reddening value of 0.53 ± 0.12 mag. These parameters indicate the absence of mass segregation within the cluster. Piskunov et al. (2008) found that this cluster is poorly populated. Bossini et al. (2019) catalogued the age and fundamental parameters of 269 open clusters using data from Gaia DR2 and reported log(age) $= 8.58 \pm 0.12$, distance modulus 9.54 ± 0.02, and $A_V = 1.06 \pm 0.03$ for King 6. Gokmen et al. (2023) reported the analysis of King 6 using CCD UBV and Gaia DR3 data. They estimated the color excess, $E(B-V)$, to be 0.55 ± 0.03 mag and determined the distance as 723 ± 34 pc, with an age of 200 ± 20 Myr. The mass function slope was found to be 1.29 ± 0.18. Their analysis indicated that the cluster was dynamically relaxed. Table 5 provides a comparative overview of the parameters we derived alongside previously reported values.

There are differences in the parameter values derived for the cluster in the literature, as shown in Table 5. Previous studies on the membership of King 6 did not provide reliable estimates of the cluster members. With the availability of astrometric data from Gaia DR3 and new optical and 2MASS near-infrared datasets, we revisited OC King 6 to study its parameters and dynamical status. Additionally, the extracted parameters of the cluster will be used to enhance the sample of clusters needed for studying Galactic structure and dynamics.

The detection of variable stars provides valuable information for constraining stellar pulsation models and refining theoretical models that predict the characteristics of stars in clusters. Pulsating stars, in particular, offer insights into the internal stellar structure and mass. Intermediate-age clusters serve as excellent laboratories for studying short-period variables (Joshi et al., 2020b). Recent work on the Pleiades cluster (Bedding et al., 2020) demonstrates the power of combining observations with Gaia (Gaia Collaboration et al., 2016) and *TESS* (Transiting Exoplanet Survey Satellite) for studying pulsating stars in OCs. The large pulsational frequency separation and frequency at maximum power can help constrain stellar evolution, structure, and oscillation models, leading to a better characterization of pulsating stars. These advancements have encouraged us to use space-based data to characterize the variables in OCs. In this study, we present the results of our search for variable stars using observational data from the *TESS* mission for King 6 and report their classifications.

The remainder of this paper is structured as follows: § 2 presents the observations and data reduction. Section 3 discusses the archival data used in this analysis. In § 4, 5, 6, and 7, we discuss the cluster parameters. In § 8, we discuss the luminosity and mass function of the cluster, followed by mass segregation, relaxation time, and tidal radius in § 9.

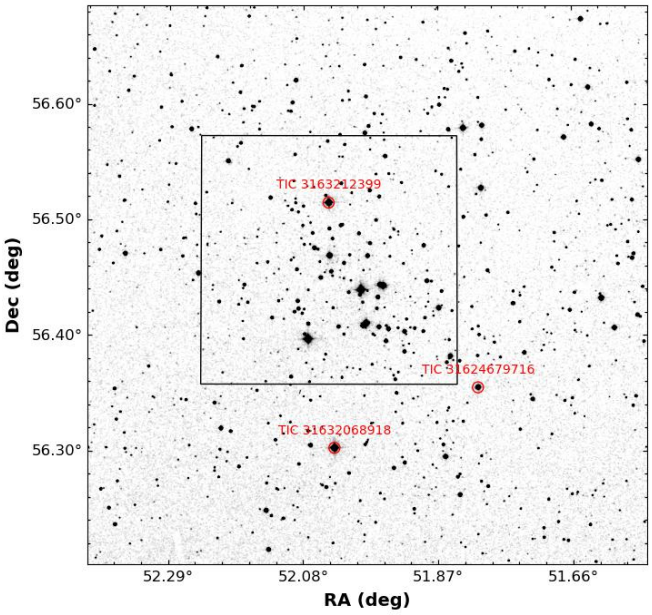

Figure 1. Identification chart for the cluster King 6, taken from SDSS. Rectangular box outlines observed region, while the red circles highlight position of variable stars.

§ 10 presents the identification of the variable stars in King 6. Finally, our work is summarized in § 11.

2. Observations and data Reduction

2.1. *UBVRI* photometric observations

This study utilized data collected with the 104-cm Sampurnanand telescope at the Aryabhatta Research Institute of Observational Sciences (ARIES) in Nainital, India. The observations were conducted from December 23^{rd} to 25^{th}, 2005. The telescope captured images in multiple bands: $UBV(IR)_C$, using a thinned back-illuminated CCD camera mounted at the f/13 Cassegrain focus. Figure 1 presents the finding chart of the cluster, which was obtained from the Sloan Digital Sky Survey (SDSS) data. The rectangular box indicates the region observed using the 104-cm Sampurnanand telescope at Manora Peak, ARIES, Nainital.

The CCD detector has pixels measuring 24 μm each, arranged in a 2048×2048 grid, providing a field of view on the sky of approximately $13' \times 13'$, with a pixel resolution of $0''.38$. A binning mode of 2×2 pixels was employed during the observations to enhance the signal-to-noise ratio. The CCD had a readout noise of 5.3 e^- and a gain factor of 10 e^-/ADU. The Observational log is shown in Table 1.

Bias and twilight flat-field frames were used for image cleaning. Multiple short and long exposures were collected for the cluster and standard fields using all filters. Calibrating the stellar magnitudes involved observing stars in the standard field PG1047+003. Several Landolt (1992) standard stars were identified within the observed field of

Table 1. Description of the optical observation for King 6 and the standard field

Cluster/ standard field	Date	Filter	Exp. time × no.of frames
King 6	$23/24^{th}$ Dec 2005	V	900×3, 120×1
		B	240×2, 1200×3
		I	60×1, 40×1
			100×2, 240×2
		R	480×3, 60×1
		U	300×2, 1800×2
PG1047+003	25^{th} Dec 2005	V	120×4, 100×1
		B	200×5
		I	60×5
		R	60×5
		U	300×5

view of PG1047+003. The IRAF data reduction package was used for the pre-processing of data frames, which includes bias subtraction, flat fielding, and cosmic ray removal. This process ensures that the data is clean for further analysis.

2.2. Photometric and astrometric calibration

Photometry on the bias-subtracted and flat-field-corrected CCD frames was performed using DAOPHOT-II software (Stetson, 1987, 2000). Quantitative values for the brightness of stars were obtained using aperture and profile-fitting photometry. The measurements of bright stars that were saturated in deep exposure frames were obtained from short-exposure frames. Least-squares linear regressions were fitted to translate the observed aperture magnitudes into standard magnitudes. The equations for calibrating the instrumental magnitudes are as follows:

$$v = V + 4.15 \pm 0.005 \text{ - } (0.002 \pm 0.004)(B - V) + (0.23 \pm 0.02)X$$

$$b = B + 4.57 \pm 0.008 \text{ - } (0.005 \pm 0.005)(B - V) + (0.38 \pm 0.02)X$$

$$i = I + 4.62 \pm 0.010 \text{ - } (0.020 \pm 0.01)(V - I) + (0.10 \pm 0.02)X$$

$$r = R + 4.08 \pm 0.006 \text{ - } (0.010 \pm 0.004)(V - R) + (0.16 \pm 0.01)X$$

$$u = U + 6.79 \pm 0.030 \text{ - } (0.006 \pm 0.01)(U - B) + (0.60 \pm 0.08)X$$

Here, V, B, I, R, and U represent standard magnitudes, and v, b, i, r, u refer to instrumental aperture magnitudes normalized for 1 s of exposure time, and X is the airmass. The zero points for the local standards were evaluated by considering the aperture growth curve, exposure time differences, and atmospheric extinction. The errors associated with the zero points and color coefficients were ~ 0.01 magnitudes.

Table 2. Description of observed errors in different filters with V magnitude bins

V range	σ_V	σ_B	σ_I	σ_R	σ_U
12-13	0.01	0.01	0.01	0.01	0.01
13-14	0.01	0.01	0.01	0.01	0.02
14-15	0.01	0.01	0.01	0.01	0.02
15-16	0.01	0.01	0.01	0.01	0.04
16-17	0.01	0.02	0.03	0.01	0.10
17-18	0.01	0.03	0.03	0.01	0.20
18-19	0.01	0.04	0.03	0.01	0.40
19-20	0.01	0.10	0.04	0.01	0.50

The internal errors calculated using DAOPHOT are plotted against V magnitudes for the $UBVRI$ filters, as shown in Figure 2. It shows an average photometric error ≤ 0.04 mag across all filters up to a V magnitude of 17. For magnitudes 17 to 20 mag, uncertainty is ~ 0.10 mag whereas for U it is ~ 0.05. Table 2 shows the error trends across the filters relative to V magnitude.

Astrometric solutions were used to obtain the celestial coordinates of all stars in $J2000.0$. We used the *CCMAP* and *CCTRAN* tasks of *IRAF* to obtain the celestial coordinates of the detected stars. The sources detected in different wavebands were merged using a matching radius of $\sim 2''$. A total of 3028 stars were detected in all five survey bands in this study.

2.3. Comparison with the previous photometry

CCD $UBVI$ photometry was previously performed by Ann et al. (2002). To verify our photometry, we cross-identified the stars with the photometry of Ann et al. (2002), which yielded 158 matched sources. We estimated the difference in magnitude and plotted it against V magnitude, as shown in Figure 3. The mean of the differences and standard deviation (i.e mean $\pm \sigma$) for V, B, I_c and U magnitude is found to be 0.02 ± 0.09, 0.01 ± 0.09, -0.05 ± 0.05, and 0.04 ± 0.64 mag, respectively.

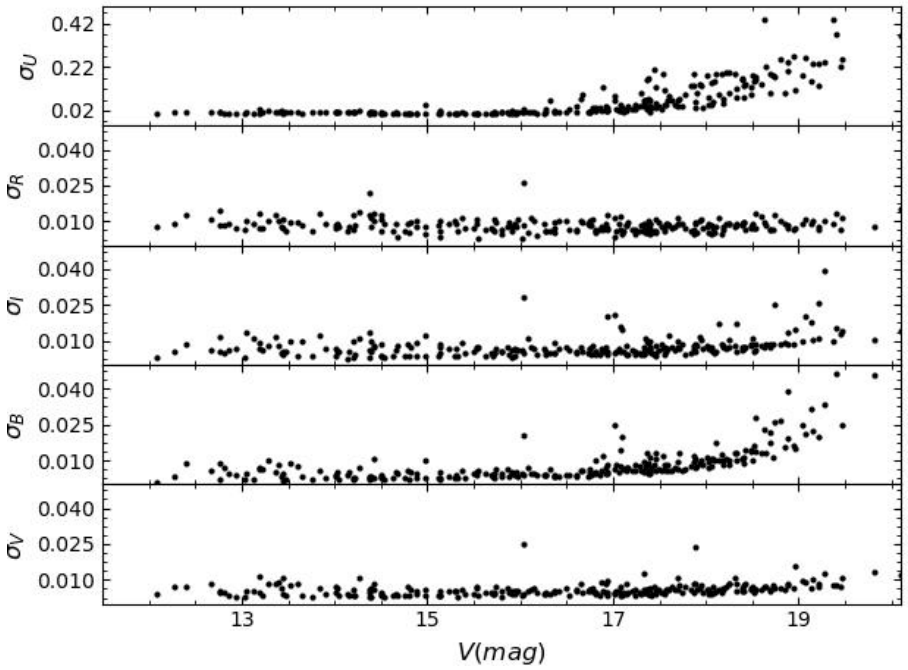

Figure 2. Photometric errors in V, B, I, R, and U against V-band magnitude. Errors on the Y-axis represent the internal error as estimated by the DAOPHOT routine.

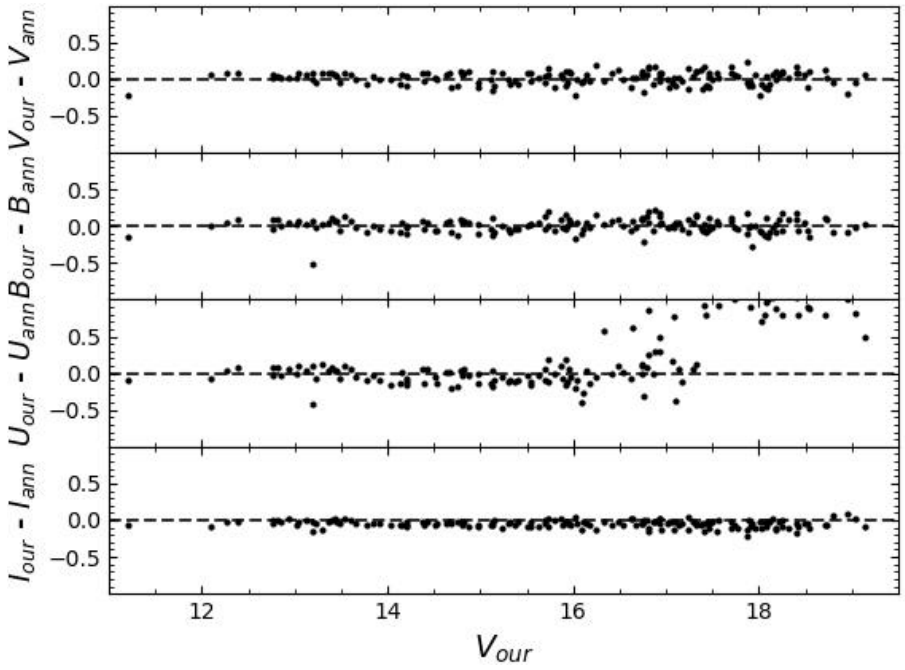

Figure 3. Comparison of the present photometry with Ann et al. (2002) in U, B, V and I_c filters against V magnitude. The dotted lines are plotted at zero value.

3. Archival Data

3.1. Gaia DR3

Gaia DR3 data were used for astrometric studies and to determine the cluster structural parameters. It provides celestial positions and G band magnitudes for a vast dataset of approximately 1.8 billion sources, with magnitude measurements extending up to 21 mag. Additionally, Gaia DR3 provides valuable parallax, proper motion, and color information ($G_{BP} - G_{RP}$) for a subset of this dataset, specifically 1.5 billion sources. The uncertainties in the parallax values are $\sim$ 0.02–0.03 milli-arcsecond (mas) for sources at $G \leq 15$ mag and $\sim$ 0.07 mas for sources with $G \sim 17$ mag. We collected data for King 6 within a radius of

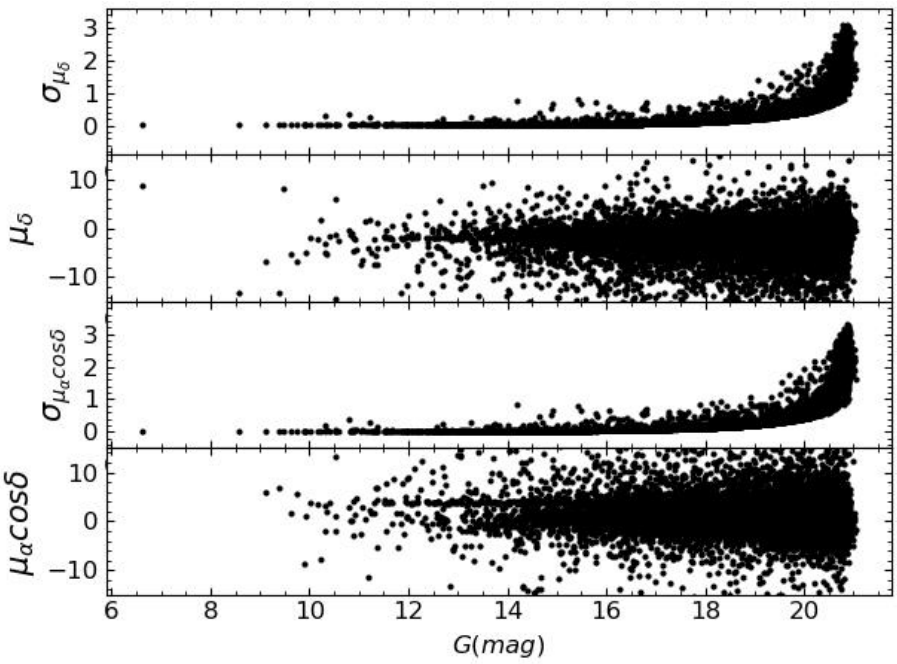

Figure 4. Proper motions in the direction of RA and DEC and its error are plotted against G mag.

Table 3. Description of uncertainties in proper motions and magnitudes against Gaia G magnitude bins

G(mag)	$\sigma_{\mu_\alpha cos\delta}$	σ_{μ_δ}	σ_G	$\sigma_{G_{RP}}$	$\sigma_{G_{BP}}$
11-12	0.020	0.020	0.002	0.003	0.004
12-13	0.020	0.020	0.002	0.003	0.004
13-14	0.030	0.030	0.002	0.004	0.004
14-15	0.040	0.040	0.003	0.005	0.005
15-16	0.050	0.050	0.003	0.006	0.005
16-17	0.070	0.070	0.003	0.010	0.005
17-18	0.114	0.110	0.003	0.030	0.007
18-19	0.198	0.196	0.004	0.070	0.013
19-20	0.384	0.385	0.005	0.120	0.024

$30'$. The proper motions of the stars in the cluster and the corresponding errors are graphically represented against G magnitude in Figure 4. The lower panel displays two prominent structures: uncertainties in the corresponding proper motion components are less than 0.04 mas up to 15^{th} magnitudes; ≤ 0.10 mas from 15^{th} to 18^{th} mag and less than 0.40 mas up to 20^{th} magnitudes. A detailed analysis of the uncertainties in the proper motion along the Right Ascension (RA), declination (DEC), and Gaia magnitudes (G, G_{BP}, G_{RP}) is shown in Table 3.

3.2. The Near-infrared Data

We used archival near-infrared photometric data from the Two Micron All-Sky Survey (2MASS Skrutskie et al., 2006), which provides photometry in the J (1.25 μm), H (1.65 μm), and K_s (2.17 μm) filters. The data have limiting magnitudes of 15.80, 15.10, and 14.30 in the J, H, and K_s bands, respectively, with a signal-to-noise ratio (S/N) greater than 10. Our optical data were cross-correlated with the 2MASS photometric catalogue, resulting in the identification of 233 common stars within a matching radius of $2''$.

3.3. TESS (Transiting Exoplanet Survey Satellite) data

We utilized *TESS* data, which features a large plate scale of $21''$ per pixel, for the analysis. This resolution often causes TESS light curves to capture the combined light from multiple stars (Higgins & Bell, 2023). In our investigation of the variable stars in our cluster, we identified three isolated stars after matching the *TESS* data with optical observations.

4. Structural Parameter of the cluster: Cluster extent

The size of a star cluster plays a crucial role in studying its dynamic evolution, which involves how the cluster changes over time owing to internal and external forces. However, determining the precise size of a cluster can be challenging because of its irregular shape, making it difficult to pinpoint the exact center and outer boundaries of the cluster. We employed a histogram-based technique to estimate the cluster center. We plotted the number of stars against their celestial coordinates (RA and DEC), as shown in Figure 5. The data for this analysis were obtained from Gaia DR3, specifically for stars with a G-band magnitude uncertainty ≤ 0.10 magnitudes and located within a $30'.0$ radius of the cluster center listed in Table 5. Our analysis reveals a cluster center at approximately (03:27:55.26, +56:26:39.07)

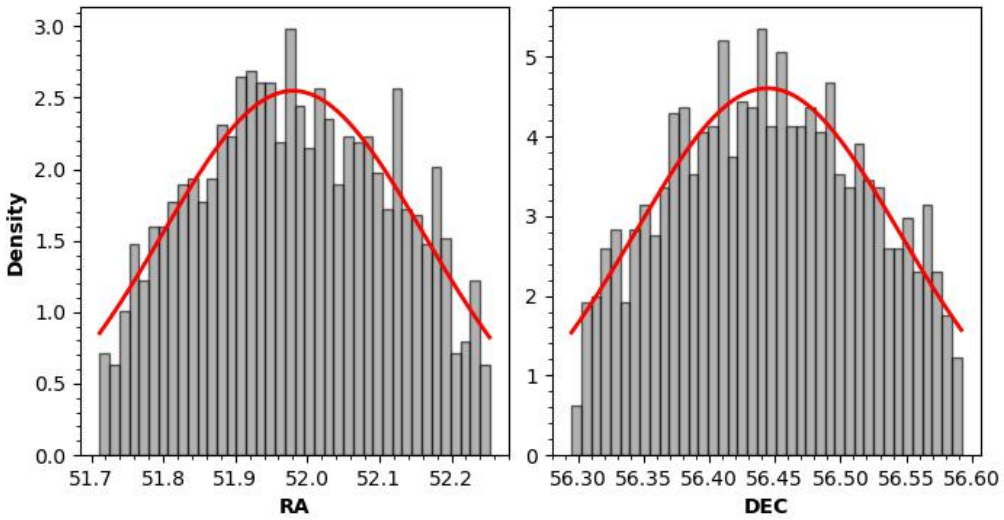

Figure 5. Histogram in RA and DEC of the stars. Solid red line represents the fitted Gaussian function.

for King 6, which is roughly 15′′.0 away from the center estimated by Ann et al. (2002).

Thus, defining the cluster radius, which indicates the point at which the internal gravitational influence becomes negligible, is crucial. We achieved this by analyzing the stellar density profile. To conduct a quantitative analysis, we created concentric annular regions (ring-shaped areas) around the estimated cluster center. We then counted the number of stars within each annular ring (width of 0′.50) and divided this count by the corresponding area of the ring to calculate the number density of stars in that region. This method allowed us to examine how the density of stars varied with distance from the cluster center, ultimately helping us determine the effective radius of the cluster. To estimate this radius, we fitted the surface density profile described by King (1962) to the stellar radial distribution. This fit was accomplished using a nonlinear least-squares routine that considered the errors as weighting factors. The radial density profile (RDP) is represented as follows:

$$\rho(r) = \frac{\rho_0}{1 + (\frac{r}{r_c})^2} + \rho_b \quad (1)$$

where ρ_0 is the central density, r_c is the core radius of the cluster, and ρ_b is the background density.

Figure 6 illustrates the best-fit solution for the density distribution of King 6, along with its associated uncertainties. As is evident from the graphs, the radial density profile for the clusters exhibits a decline, followed by a flattening behavior at approximately 9′.0. Based on this observation, we adopted 9′.0 as the cluster radius, which is slightly lower than the values previously reported by Maciejewski & Niedzielski (2007) and Gokmen et al. (2023), as shown in Table 5. For King 6, $\rho_0 = 5.88$ stars arcmin^{-2}, $r_c = 3.58$ arcmin and $\rho_b = 7.00$ stars/arcmin^2.

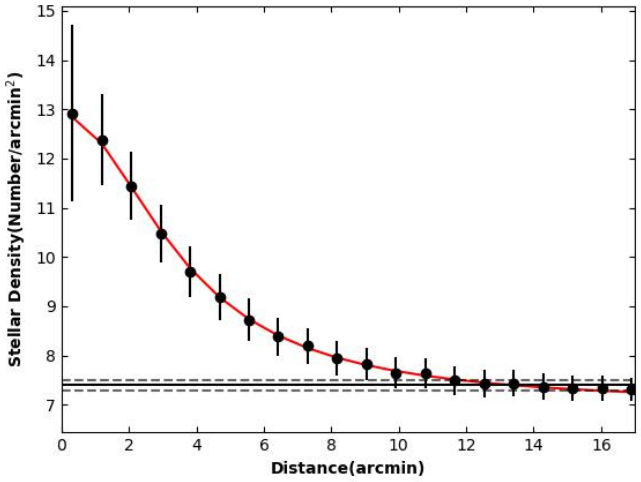

Figure 6. Radial density profile of the cluster King 6. The red solid curve represents the best fit of King (1962). Solid horizontal line represents the background density, wheras dashed lines represent the errors.

The value of the core radius r_c is comparable within error to the values reported by Gokmen et al. (2023) (see Table 5).

5. Determination of membership probability

A significant challenge in studying OCs is the presence of unrelated stars along the line of sight, known as field star contamination. Distinguishing these field stars from the actual members of the cluster is crucial for accurately estimating the cluster's physical and dynamical properties (Angelo et al., 2019, 2020). An effective method for separating members from field stars is the vector point diagram (VPD) based on proper motion (Dias et al., 2018).

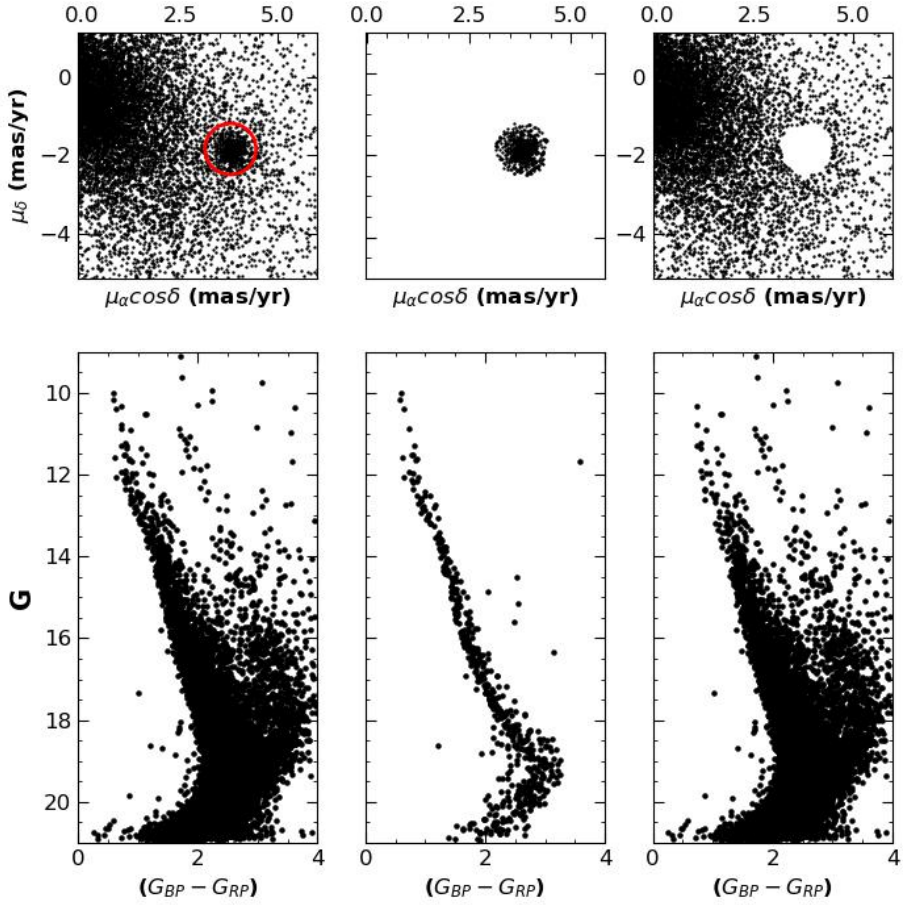

Figure 7. Initial cluster member separation using proper motion. Top panels show the VPDs and bottom panels show the respective CMDs for total, cluster and field region.

The unprecedented astrometric precision of the Gaia DR3 catalogue has significantly improved the reliability of membership determination based on kinematic data (data related to stellar motion) (Castro-Ginard et al., 2018; Castro-Ginard, A. et al., 2019); (Liu & Pang, 2019). Therefore, we used Gaia DR3 data for our kinematic analysis, member star identification, and cluster distance calculations. Figure 7 illustrates the VPDs constructed using the proper motion of cluster stars in RA and Decr. Here, the cluster stars are separated from the field stars, with the cluster members encircled in red, as shown in the upper panel of the figure, and the cluster members are separated from the field stars, as shown by the CMD in the lower panel of Figure 7. This distinction is possible because cluster stars exhibit a more concentrated proper motion distribution than field stars. The center of the red circle was determined using the maximum density method described by Joshi et al. (2020a).

The estimated value of the center of the cluster proper motion distribution is $(\mu_\alpha \cos\delta,\ \mu_\delta) = 3.82$ mas yr^{-1}, -1.90 mas yr^{-1} for King 6. We identified the stars within the red circle as probable cluster members. We identified 575 probable member stars in the cluster. To quantify the membership of the stars, we calculated the membership probabilities. We estimated the membership probabilities using a statistical approach based on the PMs of stars, as described in previous studies (Sanders, 1971; Michalska, 2019; Pandey et al., 2020).

Assuming a distance of 0.75 kpc and a radial velocity dispersion of 1 km s^{-1} for open clusters (Girard et al., 1989), a dispersion (σ_c) of ∼0.28 mas yr^{-1} in the proper motion of the cluster can be obtained. We calculated $\mu_{xf} = 0.15$ mas yr^{-1}, $\mu_{yf} = -0.74$ mas yr^{-1}, $\sigma_{xf} = 5.76$ mas yr^{-1}, and $\sigma_{yf} = 5.53$ mas yr^{-1} for the field stars. These values were used to construct the frequency distributions of the cluster stars (ϕ_c^ν) and field stars (ϕ_f^ν) using the equation given by Yadav et al. (2013). The membership probability for the i^{th} star is calculated using the following equation:

$$P_\mu(i) = \frac{n_c \times \phi_c^\nu(i)}{n_c \times \phi_c^\nu(i) + n_f \times \phi_f^\nu(i)} \quad (2)$$

where n_c and n_f are the normalized numbers of probable cluster members and field stars, respectively. We found 606 stars with $P_\mu > 0.80$ for the cluster. In Figure 8, we plot the membership probability against G magnitude. In this figure, we can see the separation between cluster members and field stars toward the brighter part, which supports the effectiveness of this technique on the Gaia data. A high

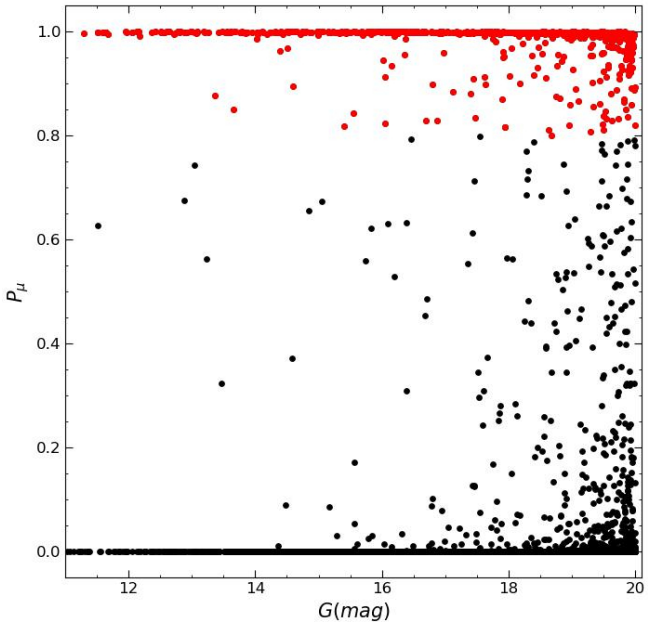

Figure 8. The Gaia membership probability is plotted against G magnitude. The red dot represents the star with a probability of $P_\mu \geq 0.80$, and the black dots represent the star with a probability of $P_\mu < 0.80$.

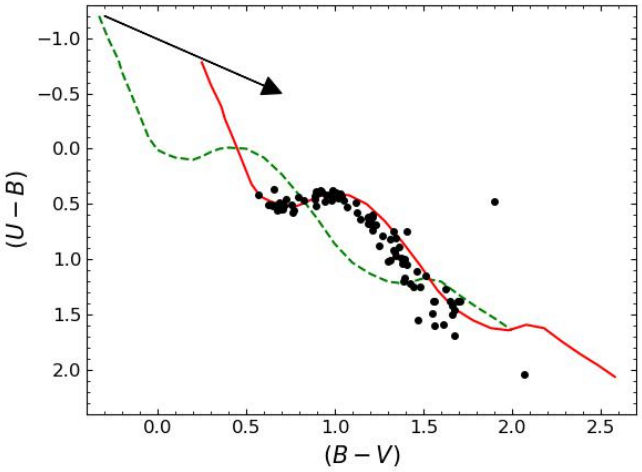

Figure 9. The color-color diagram for target region. The dashed line represents the intrinsic ZAMS, and the solid curve represents the best-fit ZAMS. Arrow illustrates the reddening vector.

membership probability extends to $G \sim 20$ mag, whereas the probability gradually decreases toward fainter limits.

We matched our *UBVRI* catalogue with the Gaia catalogue using a matching radius of $2''.0$. We found 242 optical counterparts of Gaia sources with membership probability data. We found 94 stars within the cluster radius ($9'$) with a membership probability $P_\mu \geq 0.80$.

6. Cluster parameters

6.1. *(U-B)* vs. *(B-V)* diagram

The reddening, $E(B-V)$, can be determined by fitting the intrinsic zero-age main-sequence (ZAMS) on the $(U-B)/(B-V)$ color-color diagram (Phelps & Janes, 1994). The black points denote member stars present within a $9'.0$ radius and with probability $P_\mu > 0.80$. The best fit of the intrinsic ZAMS was achieved by shifting $E(B-V)$ along the reddening vector, as shown in Figure 9. We adopted the slope of the reddening vector $E(U-B)/E(B-V) = 0.72$ and fitted the ZAMS with solar metallicity, that is, $Z = 0.02$ (Schmidt-Kaler, 1982). The best fit was achieved for a reddening value of 0.58 ± 0.03 mag. Our estimated value of $E(B-V) = 0.58 \pm 0.03$ mag is comparable to the values estimated by Maciejewski & Niedzielski (2007), Gokmen et al. (2023), and Ann et al. (2002) (see Table 5).

6.2. Total-to selective extinction value

Reddening is an important parameter for star clusters because it can significantly affect the determination of other fundamental parameters. Color-color diagrams are essential for understanding extinction laws. The photons emitted from cluster stars are scattered and absorbed in the interstellar medium by dust particles, leading to a deviation in their color from their intrinsic values. The normal Galactic reddening law may not accurately describe the reddening observed along the line of sight to many star clusters (Sneden et al., 1978). To examine the nature of the reddening law, two color diagrams, $(V-\lambda)/(B-V)$, are employed as suggested by Chini & Wargau (1990), where λ represents all filters other than V. Here, we examined the reddening law for the cluster by drawing two color diagrams, as shown in Figure 10. Because the stellar color values show a linear relationship, a linear equation was applied to calculate the slope ($m_{cluster}$). We calculated the total-to-selective extinction using the relation given by Neckel & Chini (1981),

$$R_{cluster} = \frac{m_{cluster}}{m_{normal}} \times R_{normal} \quad (3)$$

where R_{normal} is the normal value of total-to-selective extinction, taken to be 3.10, and m_{normal} and $m_{cluster}$ are the slopes of a linear fit to two color diagrams for normal extinction and extinction in the direction of clusters, respectively. The values of m_{normal} and $m_{cluster}$ are listed in Table 4. The average $R_{cluster}$ (=2.78 ± 0.30) was approximately equal to the normal value. Thus, the reddening law is normal in the direction of the cluster.

6.3. Distance and Age Determination

A CMD was used to estimate the age and distance of the cluster. V versus $(U-B)$, V versus $(B-V)$, and V versus $(V-I)$ CMDs of the member stars (represented by blue dots) within the cluster radius $9'.0$ and $P_\mu \geq 0.80$ are shown in Figure 11. The CMDs of the target cluster show a well-defined, narrow main sequence (MS) locus. The MS extends from $V \sim 11.2-18.8$ mag. The theoretical isochrone of solar metallicity $Z = 0.02$ taken from Bertelli et al. (1994) has been overplotted on the CMDs and is represented by

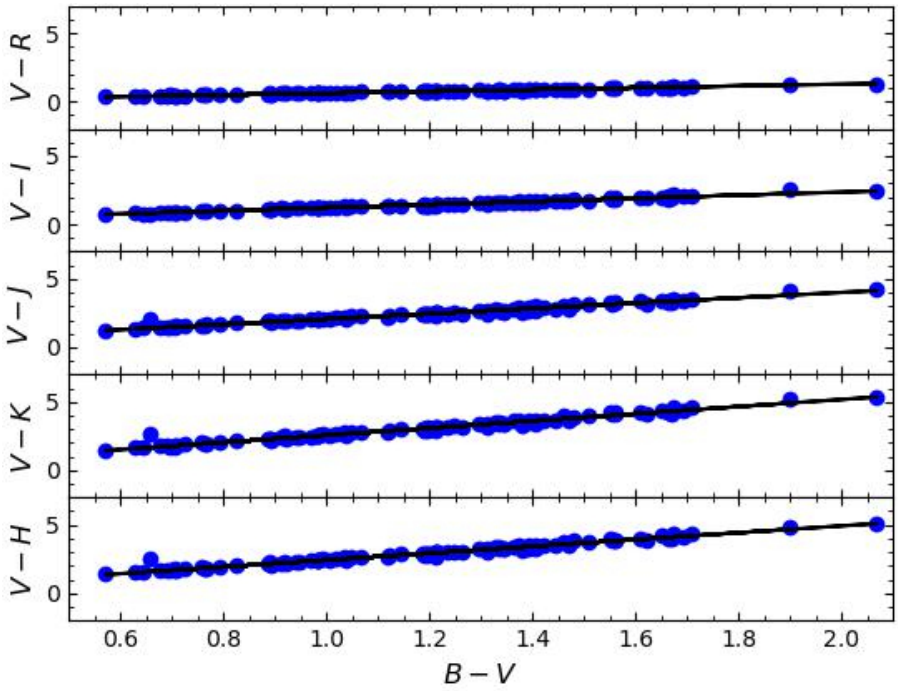

Figure 10. $(V-\lambda)/(B-V)$ color-color diagram is plotted for stars within cluster radius, with membership probability $P_\mu > 0.80$. Continuous line represents the slopes.

Table 4. The slopes of the $(V-\lambda)/(B-V)$ diagrams for the member stars and corresponding normal values

	$\frac{(V-R)}{(B-V)}$	$\frac{(V-I)}{(B-V)}$	$\frac{(V-J)}{(B-V)}$	$\frac{(V-K)}{(B-V)}$	$\frac{(V-H)}{(B-V)}$
Normal	0.80	1.70	2.23	2.72	2.42
King 6	0.66 ± 0.001	1.34 ± 0.001	$1.94 \pm 0..001$	2.61 ± 0.001	2.49 ± 0.001
$R_{cluster}$	2.56	2.44	2.70	2.97	3.19

solid lines. The reddening values derived in Section 6.1 were used for the isochrone-fitting process. The best fit of the theoretical isochrone gives the value of distance modulus as $(V-M_v) = 11.10 \pm 0.40$ mag, giving the distance as 724 ± 5 pc. Our estimated distance value is comparable to those derived by Maciejewski & Niedzielski (2007) and Gokmen et al. (2023) (see Table 5).

We also used the parallax of the stars to obtain the distance to the cluster. In Figure 12, we plot the histogram of the 0.10 mas parallax bin using the star within the cluster radius with the probability membership $P_\mu \geq 0.80$. A Gaussian function was fitted to the histogram. We found a mean parallax of 1.36 ± 0.10 mas. Using this mean parallax, we estimated the distance to be 735 ± 10 pc, which closely agrees with the value derived using the CMDs.

The age of the cluster was determined by fitting theoretical stellar evolutionary isochrones of different ages to the CMDs ($V/(U-B)$, $V/(B-V)$, and $V/(V-I)$). Isochrone fitting was performed considering the bluest envelope of the CMDs, as shown in Figure 11. After correcting for reddening, the best fit was obtained for an age of log(age) = 8.40 ($\sim$ 251 Myr), which is in good agreement with the previously estimated values by Ann et al. (2002), Gokmen et al. (2023), and Maciejewski & Niedzielski (2007), listed in Table 5.

7. Interstellar extinction in near-IR

7.1. *(V-K)* vs. *(J-K)* diagram

We combined *2MASS* JHK_s data with optical data to determine the interstellar extinction in the near-IR. The K_s magnitude was converted into K magnitude using the methods given by Persson et al. (1998). The $(J-K)$ versus $(V-K)$ color-color diagram for the cluster members is shown in the left panel of Figure 13. The solid line in the figure shows the ZAMS given by Bertelli et al. (1994). This ZAMS provides $E(J-K) = 0.24 \pm 0.03$ mag and $E(V-K) = 1.50 \pm 0.01$ mag for the cluster, respectively. The ratio $\frac{E(J-K)}{E(V-K)}$ is $\sim 0.16 \pm 0.03$, which is in good agreement with the normal interstellar extinction value of 0.19 given by Cardelli et al. (1989). This scatter is due to the large error in the *JHK* data points.

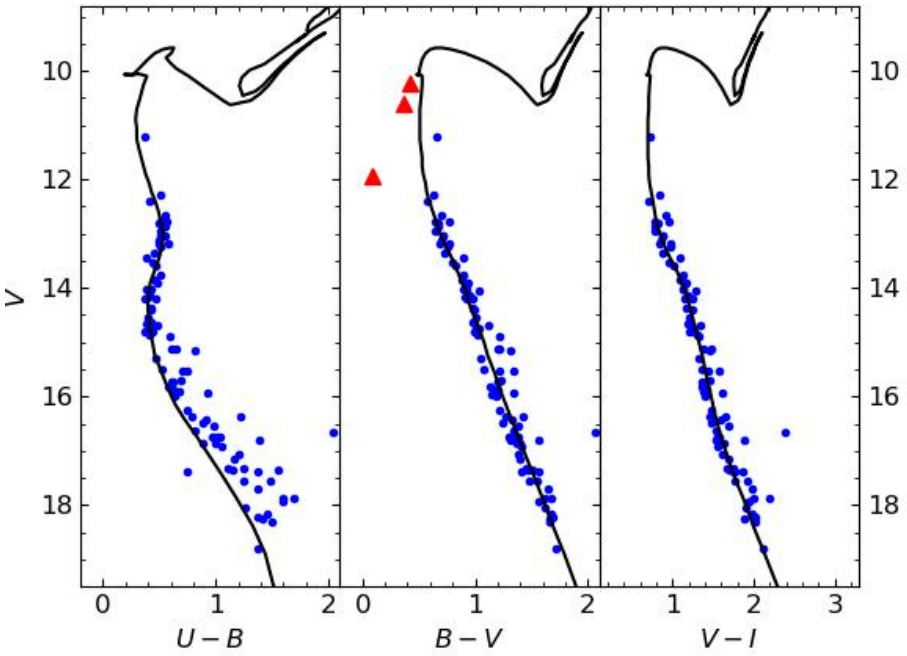

Figure 11. The color-magnitude diagrams for the member stars of the cluster with $P_\mu \geq 0.80$. The red triangles represent positions of variable stars using data from Stassun et al. (2019).

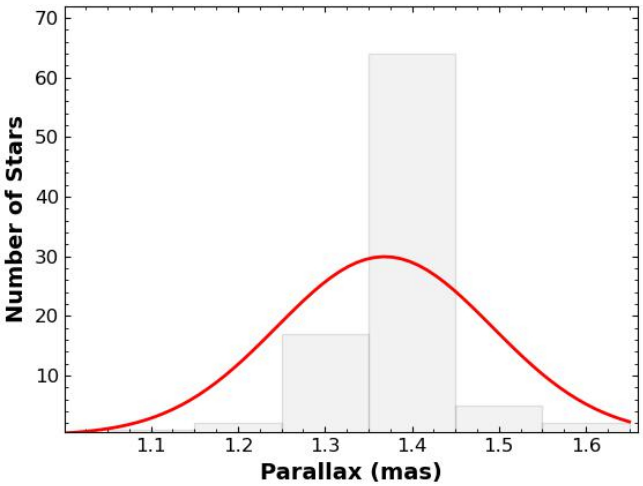

Figure 12. Histogram in parallax (0.10 mas bins) for the cluster region. Red curve represents the Gaussian function fitting.

7.2. *(B-V)* vs. *(J-K)* diagram

We have plotted $(B-V)$ versus $(J-K)$ color-color diagram for the cluster, as shown in the middle panel of Figure 13. We used the ZAMS given by Bertelli et al. (1994) to determine the relationship between the two color indices. The color excesses $E(B-V)$ and $E(J-K)$ were found to be 0.58 and 0.24 mag, respectively. This results in a ratio of $\frac{E(B-V)}{E(J-K)} \sim 0.43$ mag, which is slightly lower than the value of 0.56 reported by Cardelli et al. (1989).

7.3. *(J-H)* vs. *(J-K)* diagram

The $(J-H)$ vs $(J-K)$ color-color diagram for the cluster is shown in the right panel of Figure 13. To determine the relationship between these two colors, we utilized the ZAMS given by Bertelli et al. (1994), as indicated by the solid line in the right panel of figure. We have found that $E(J-H) = 0.15 \pm 0.02$ and $E(J-K) = 0.24 \pm 0.03$. We calculated the value of the ratio $\frac{E(J-H)}{E(J-K)} = 0.64 \pm 0.06$, which is in agreement within 2σ of the normal value of 0.55, as given by Cardelli et al. (1989).

7.4. Age and distance of the cluster using *2MASS* data

Using 2MASS data, we re-determined the cluster distance and age. We have plotted V versus $(V-K)$ in the left panel, J versus $(J-H)$ in the middle panel, and K versus $(J-K)$ in the right panel of Figure 14. We used the theoretical isochrone given by Bertelli et al. (1994) for $Z = 0.02$ of log(age) = 8.40, which has been overplotted in the CMDs. We found an apparent distance modulus of 11.10 ± 0.08, 9.82 ± 0.08, and 9.57 ± 0.08 mag using the CMDs, as shown in Figure 14. This distance modulus leads to a distance of 733 ± 7 pc. The age and distance of the cluster derived using 2MASS data agree with those derived using optical data.

8. Luminosity and mass function

8.1. Luminosity Function

We examined the brightness distribution of stars within the cluster. To achieve this, we considered stars with a probability $P_\mu \geq 0.80$ and within the cluster radius. We

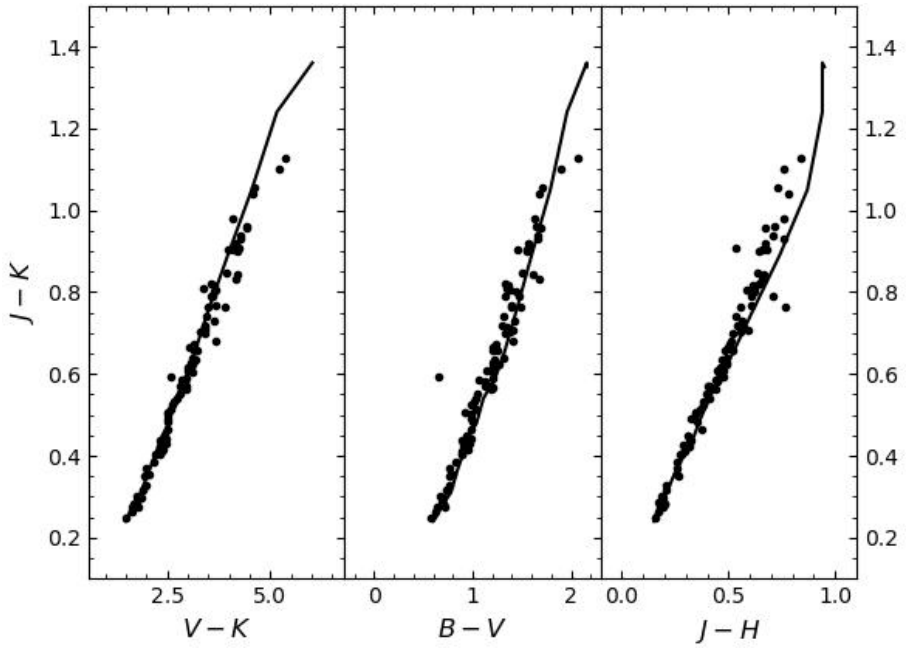

Figure 13. color-color diagram for the stars within the cluster radius and $P_\mu \geq 0.8$. Solid line is the ZAMS taken from Bertelli et al. (1994).

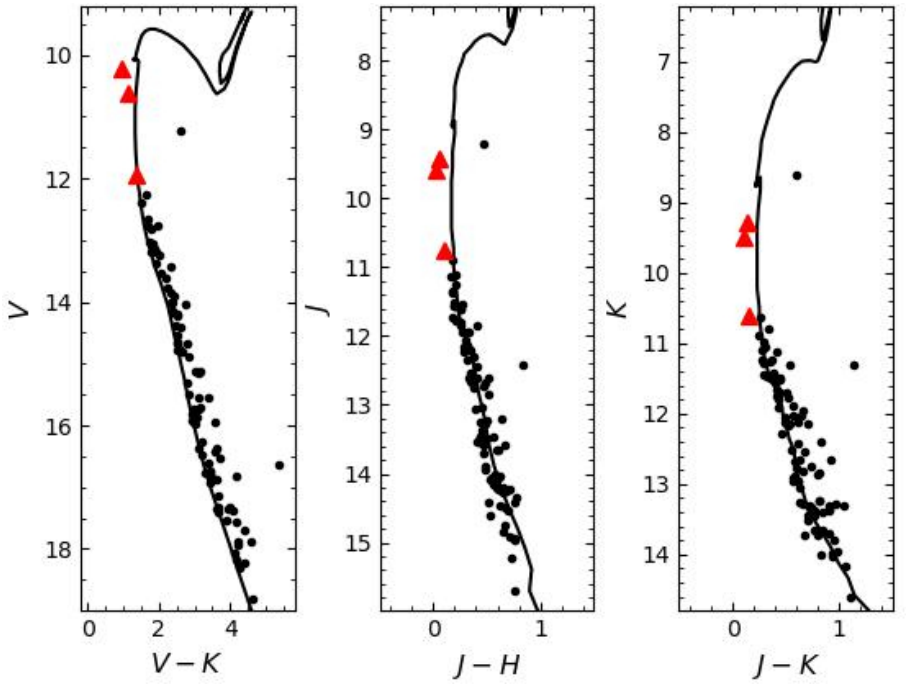

Figure 14. color-magnitude diagram for the stars within cluster radius and $P_\mu \geq 0.80$. Triangular red dots represent the position of variable stars.

considered their apparent brightness (V magnitude) and converted it to their true brightness (absolute magnitude) by accounting for the distance and correction factor (A_V). We grouped stars based on brightness (bins of 1.00 magnitude) to ensure that there were enough stars in each group for a reliable analysis. Finally, by plotting the number of stars in each brightness bin, we created a luminosity function(LF) for the cluster, as shown in Figure 15. Interestingly, this distribution shows an increasing trend up to $M_v \sim 4$ mag and a dip at ~ 5.50 mag for the cluster.

8.2. Mass Function

The mass function (MF), that is, the frequency distribution of stellar masses, is a fundamental parameter for studying

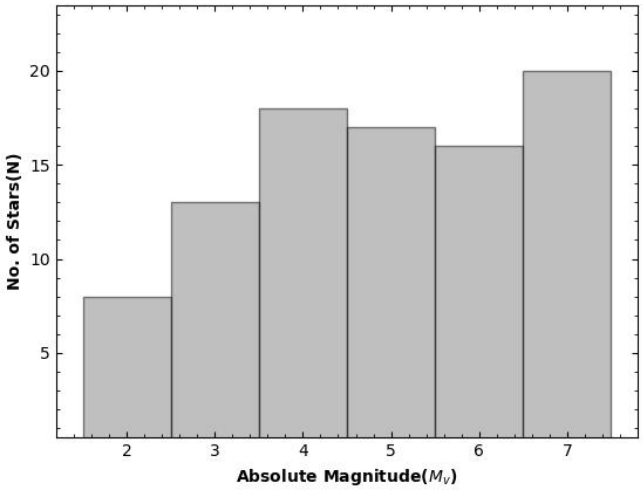

Figure 15. Luminosity function of the cluster region.

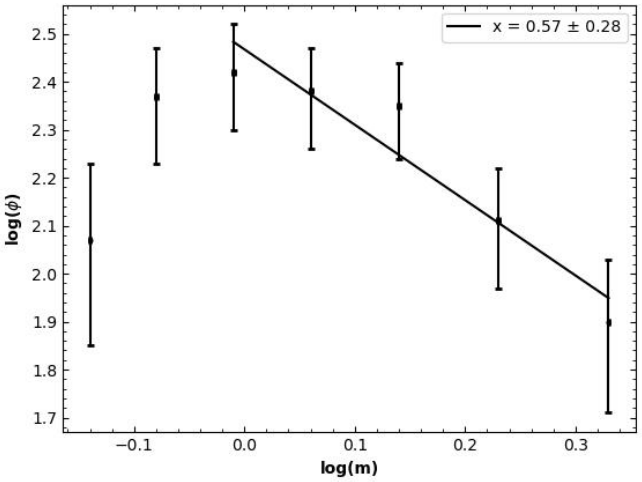

Figure 16. Mass Function for cluster under study derived using Bertelli et al. (1994) isochrone. The error bars represent $\frac{1}{\sqrt{N}}$.

star formation and evolution in clusters. It represents the distribution of stellar masses per unit volume in a star formation event, and knowledge of the MF is very effective in determining the subsequent evolution of the cluster. The MF can be derived using the linear relation

$$\log(dN/dM) = -(1+x) \times \log M + constant \quad (4)$$

where dN represents the number of stars per mass bin dM with central mass M, and x is the slope of the MF. To convert the LF to the MF, we used the theoretical evolutionary model given by Bertelli et al. (1994), and the resulting MF is shown in Figure 16. This figure shows a turn $\sim 1\,M_{\odot}$. To derive the mass function slope, we considered stars with a mass $\geq 1\,M_{\odot}$. The derived slope of the MF is $x = 0.57 \pm 0.28$, which is less than the value of 1.35 given by Salpeter (1955) for solar neighborhood stars. The calculated mass function slope is less than the mass function slope of 1.29 ± 0.18 determined by Gokmen et al. (2023) within the mass range $0.58 \geq \mathrm{M/M_{\odot}} \geq 3.59$.

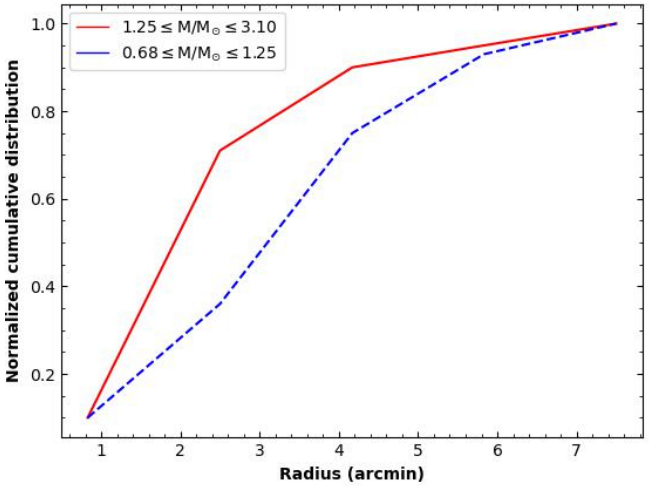

Figure 17. The cumulative radial distribution of member stars in low-mass ($< 1.25M_{\odot}$) and relatively higher-mass ($\geq 1.25M_{\odot}$) range.

9. Mass segregation, relaxation time and tidal radius of the cluster

9.1. Mass segregation

To study the mass segregation of the cluster, we plotted the cumulative radial distribution of the stars for different masses, as shown in Figure 17. To do so, we divided the main-sequence stars into two mass ranges, $3.10 \leq M/M_{\odot} \leq 1.25$ and $1.25 \leq M/M_{\odot} \leq 0.68$ for the cluster. To obtain the mass segregation effect, we selected probable members based on the membership probability and the CMD of the cluster. The figure exhibits the mass segregation effect in the sense that massive stars gradually sink towards the cluster center rather than the fainter stars. To check whether this mass distribution represents the same kind of distribution, we performed the Kolmogorov-Smirnov(K-S) test. This test indicates that the confidence level of the mass segregation effect is 98 % for the cluster.

9.2. The relaxation time

The relaxation time (T_E) is the time scale at which a cluster loses all traces of its initial condition. This is the peculiar time scale for the cluster to reach some extent of energy equipartition. The relaxation time is given by Spitzer Jr & Hart (1971),

$$T_E = \frac{8.9 \times 10^5 (N R_h^3)^{1/2}}{< m >^{1/2} log(0.4N)} \quad (5)$$

where N is the number of cluster members with probability ($P_{\mu} \geq 0.80$) and within radius $9'.00$, R_h is the half-mass radius of the cluster, and $< m >$ is the mean mass of the cluster stars (Spitzer Jr & Hart, 1971). In our case, the

Table 5. Comparison of our derived fundamental parameters of King 6 with the literature values

Parameters	Numerical Values	Reference
(RA, DEC) (deg)	$(51.98 \pm 0.18, 56.44 \pm 0.10)$	Present study
	51.98, 56.44	(Ann et al., 2002)
$(\mu_\alpha \cos\delta, \mu_\delta)$ (mas yr^{-1})	$(-3.82, -1.90)$	Present study
Cluster Radius (arcmin)	9′.00	Present study
	10′.90	(Maciejewski & Niedzielski, 2007)
	10′.00	(Gokmen et al., 2023)
Cluster Radius(pc)	1.98	Present study
Tidal Radius(pc)	3.18	Present study
ρ_0(stars/arcmin^2)	5.88 ± 0.87	Present tudy
	2.28 ± 0.24	(Gokmen et al., 2023)
r_c(arcmin)	3.58 ± 0.49	Present study
	4.68 ± 1.07	(Gokmen et al., 2023)
ρ_b(stars/arcmin^2)	7.00 ± 0.06	Present study
	5.12 ± 0.16	(Gokmen et al., 2023)
log(age)	8.40	Present study
	8.40 ± 0.10	(Ann et al., 2002)
	8.40	(Maciejewski & Niedzielski, 2007)
	8.58 ± 0.12	(Bossini et al., 2019)
	8.29	(Dias et al., 2021)
	8.30	(Gokmen et al., 2023)
Distance (pc)	724 ± 5	Present study
	426	(Ann et al., 2002)
	800 ± 270	Maciejewski & Niedzielski (2007)
	497	(Bossini et al., 2019)
	704	(Dias et al., 2021)
	723 ± 34	(Gokmen et al., 2023)
$E(B-V)$(mag)	0.58 ± 0.03	Present study
	0.50 ± 0.10	(Ann et al., 2002)
	0.53 ± 0.12	(Maciejewski & Niedzielski, 2007)
	0.34	(Bossini et al., 2019)
	0.59	(Dias et al., 2021)
	0.55 ± 0.03	(Gokmen et al., 2023)
$E(J-K)$(mag)	0.24 ± 0.03	Present study
$E(V-K)$(mag)	1.50 ± 0.01	Present study
$R_{cluster}$	2.78 ± 0.30	Present study
A_v	1.80	Present study
	1.596 ± 0.09	(Gokmen et al., 2023)
Mass function slope (x)	0.57 ± 0.28	Present study
Relaxation Time(Myr)	6.0	Present study

value of $< m >$ was found to be 1 $M_\odot$. The value of R_h is assumed to be half of the radius derived in Section 4. Using the above relation, we estimated the cluster's dynamical relaxation time T_E to be 6.0 Myr. Because the cluster relaxation time is shorter than the cluster age, we conclude that King 6 has dynamically relaxed.

9.3. Tidal radius

The tidal radius of the cluster is the extent to which the gravitational influence of the Galaxy is equal to that of the gravitational influence caused by the cluster core. This can be determined using the following procedure:

The Galactic Mass M_G inside a Galactocentric Radius R_G is given by (Genzel & Townes, 1987)

$$M_G = 2 \times 10^8 M_\odot (\frac{R_G}{30pc})^{1.2} \quad (6)$$

The value of M_G is found to be $1.83{\times}10^{11}$M$_\odot$. Using the formula by Kim et al. (2000), the tidal radius of the cluster

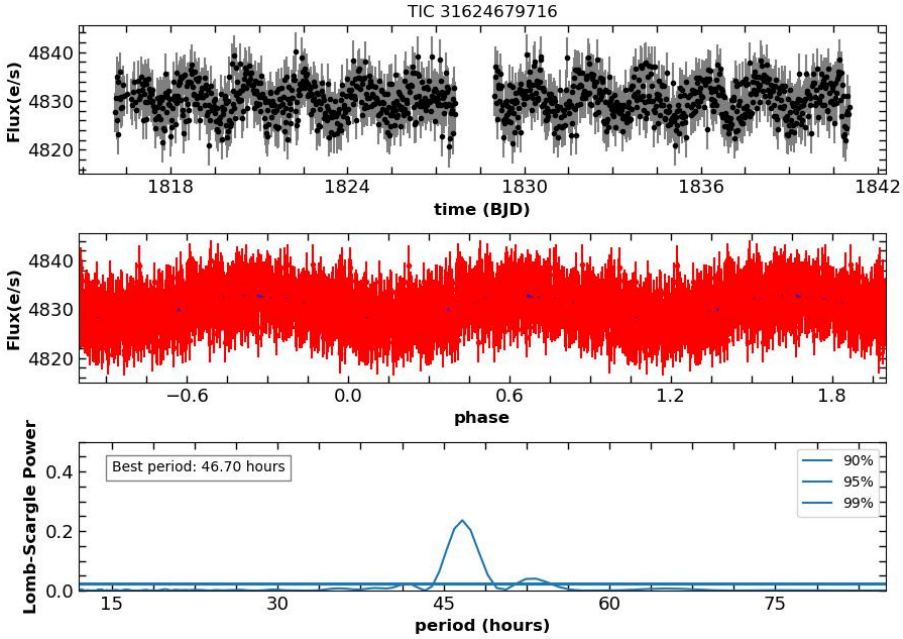

Figure 18. Light curves for the star TIC 31624679716. Upper panel shows light curve, while middle and lower panels show phase-folded light curve and the periodogram.

can be obtained as

$$R_t = (\frac{M_c}{2M_G})^{1/3} \times R_G \quad (7)$$

where R_t and M_c are the tidal radius and total mass of the cluster, respectively. The mass of the cluster was calculated by considering the overall mass function slope derived in this study within the mass range 0.68-3.10$M_\odot$. Thus, the derived tidal radius of the cluster was 3.18 pc. A comparative analysis of the fundamental parameters of King 6, as derived in this study and reported in the literature, is presented in Table 5.

10. Variable stars in the cluster King 6

Variable stars are objects that change their brightness over time. This variation provides critical insights into the physical processes that govern stars. In the present study, we used *TESS* data to search for variable stars in the cluster region. We identified three variable stars (TIC 31624679716, TIC 31632068918, and TIC 3163212399) that were isolated in the SDSS image. The variable stars are plotted in the CMDs shown in Figures 11 and 14. We used the light curve provided by *TESS* to analyze these variables. Their periodicity was determined using the Lomb-scargle algorithm provided by Scargle (1982) and Lomb (1976) for unevenly spaced light curves. The effective temperature (T_{eff}) taken from SIMBAD was 11055, 10510, and 10510 K for TIC 31624679716, TIC 31632068918, and TIC 3163212399, respectively. The temperature values suggest that they are B-type stars. The light curves of each variable are analyzed below.

10.1. TIC 31624679716

The light curve of the star TIC 31624679716 ($RA = 51.8077deg, DEC = 56.3553deg$) is shown in Figure 18. The upper and middle panels show the light and phase-folded light curves, respectively. The light curve exhibited coherent periodic variability. The light curve magnitude change was ~ 0.02 mag. The lower panel shows the Lomb-Scargle periodogram computed from the data in the upper panel. The detected period of the variable star was 46.70 h.

10.2. TIC 31632068918

Figure 19 shows the light curve of the variable star TIC 31632068918 ($RA = 52.0315deg, DEC = 56.3031deg$). The upper and middle panels display the light curve and phase-folded light curve, respectively, while the lower panel shows the Lomb-Scargle periodogram computed from the data presented in the upper panel. The variation in the magnitude was estimated to be ~ 0.01 mag. The derived period of this variable star was 47.92 h.

10.3. TIC 3163212399

The *TESS* light curve of the variable star TIC 3163212399 ($RA = 52.0408deg, DEC = 56.5152deg$) is shown in Figure 20. The upper, middle, and lower panels show the light curve, phase-folded light curve, and Lomb-Scargle periodogram, respectively. A coherent periodicity was observed in the light curve, indicating a magnitude variation of ~ 0.04 mag for the star. The determined period of the star was 37.56 h.

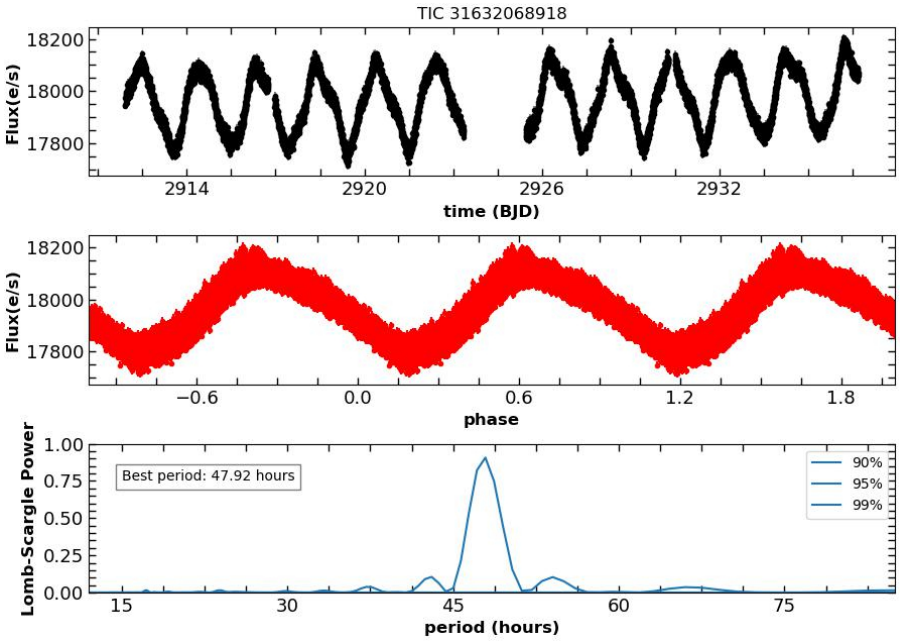

Figure 19. Same as Figure 18 for the variable star TIC 31632068918.

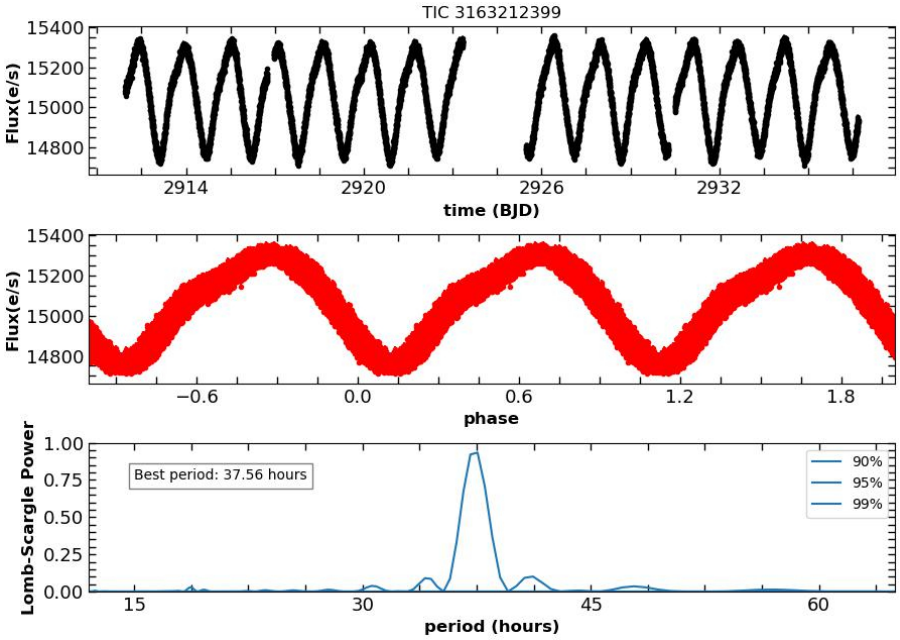

Figure 20. Same as Figure 18 for the variable star TIC 3163212399.

10.4. H-R Diagram and classification of the variables

Variable stars can be classified based on their location on the H-R diagram, shape of their light curves, variability amplitude, and periods. The variable stars searched in this study are plotted in the H-R diagram in Figure 21. The dotted line is the main-sequence curve taken from Pecaut & Mamajek (2013), and the black curve is the region for slow pulsating B-type (SBP) stars (Miglio et al., 2007). Our study identified three variables near the SBP region: the period ranged from 0.30 to 5 days for SPB-type stars, and the magnitude variation was generally less than 0.10 mag. We classified these stars as SPB variables based on their location in the H-R diagram, period, spectral type, magnitude variation, and light curve shape.

11. Conclusion

We have studied the intermediate-age open star cluster King 6 using $UBV(RI)_c$, 2*MASS JHK*, *GAIA* DR3, and *TESS* data. The main findings of this study are as follows:

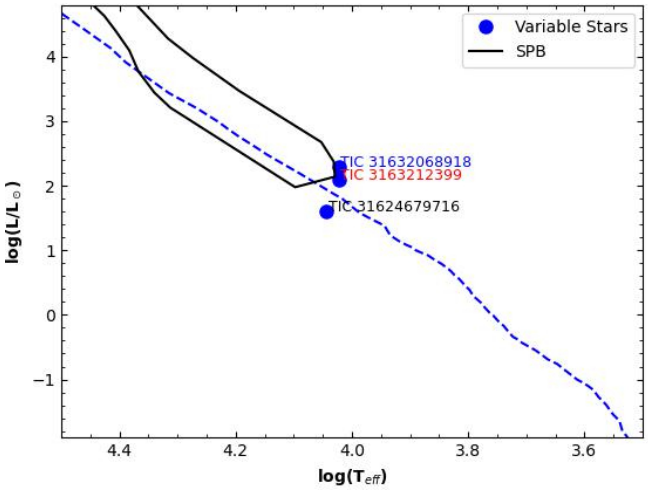

Figure 21. Hertzsprung-Russell ($\log(L/L_{\odot})$ vs. $\log(T_{eff})$) diagram for periodic variables within the cluster region.

1. The cluster radius is found to be 9′.0, which corresponds to 1.98 pc at the cluster's distance. The tidal radius of the cluster was determined to be 3.18 pc.
2. From the color-color diagram, we have estimated $E(B-V) = 0.58 \pm 0.03$ for the cluster. The *JHK* data, in combination with the optical data, provide $E(J-K) = 0.24 \pm 0.03$, and $E(V-K) = 1.50 \pm 0.01$. The value of R_v was 2.78 ± 0.30. Hence, our analysis indicates that the interstellar extinction law is normal in the direction of the cluster.
3. The age of the cluster is found to be 251 Myrs, which is determined using the theoretical isochrone of Bertelli et al. (1994) of solar metallicity $Z = 0.02$.
4. The distance of the cluster is estimated to be 724 ± 5 pc. The distance value is supported by the values determined using near-IR data and the parallax.
5. The luminosity function is determined by considering probable members. We found an increasing trend up to $M_v \sim 4.0$ mag and a dip at ~ 5.50 mag for the cluster. The overall mass function slope is 0.57 ± 0.28, which is less than the Salpeter (1955) value.
6. There is clear evidence of mass segregation within the cluster. The Kolmogorov-Smirnov test indicated a 98% confidence level for this mass segregation. Additionally, the cluster relaxation time was determined to be 6.0 Myr, suggesting that King 6 is dynamically relaxed.
7. We searched variable stars in the cluster region finding three variables with *TESS* ID *TIC* 31624679716, *TIC* 31632068918, and *TIC* 3163212399 for the first time. The variation in the magnitude of the variable stars was 0.02, 0.01, and 0.04 mag, and the period was 46.70, 47.92, and 37.56 h, respectively, classifying them as Slow Pulsating B-type stars.

We are thankful to the anonymous referee for their constructive suggestions on this paper, which significantly improved it. We also acknowledge the use of data from the European Space Agency (ESA) mission Gaia (processed by the Gaia Data Processing and Analysis Consortium, DPAC), which is publicly available from Gaia Data Release 3 (DR3), and the use of data products from the Two-Micron All Sky Survey (*2MASS*), a joint project of the University of Massachusetts and the Infrared Processing and Analysis Center/California Institute of Technology, funded by NASA and the National Science Foundation. This work used data obtained from the Transiting Exoplanet Survey Satellite (*TESS*) mission, which is funded by the NASA Science Mission Directorate. Furthermore, we are grateful to the Aryabhatta Research Institute of Observational Sciences (ARIES) for its support and contributions to this study.

References

Angelo, M. S., Piatti, A. E., Dias, W. S., & Maia, F. F. S. 2019, MNRAS, 488, 1635, doi: 10.1093/mnras/stz1709
Angelo, M. S., Santos, J F C, J., & Corradi, W. J. B. 2020, MNRAS, 493, 3473, doi: 10.1093/mnras/staa517
Ann, H. B., Lee, S. H., Sung, H., et al. 2002, ApJ, 123, 905, doi: 10.1086/338309
Bedding, T. R., Murphy, S. J., Hey, D. R., et al. 2020, Natur, 581, 147, doi: 10.1038/s41586-020-2226-8
Bertelli, G., Bressan, A., Chiosi, C., et al. 1994, A&AS, 106, 275
Bossini, D., Vallenari, A., Bragaglia, A., et al. 2019, A&A, 623, A108, doi: 10.1051/0004-6361/201834693
Cantat-Gaudin, T., Anders, F., Castro-Ginard, A., et al. 2020, A&A, 640, A1, doi: 10.1051/0004-6361/202038192
Cardelli, J. A., Clayton, G. C., & Mathis, J. S. 1989, ApJ, 345, 245, doi: 10.1086/167900
Castro-Ginard, A., Jordi, C., Luri, X., et al. 2018, A&A, 618, A59, doi: 10.1051/0004-6361/201833390
Castro-Ginard, A., Jordi, C., Luri, X., Cantat-Gaudin, T., & Balaguer-Núñez, L. 2019, A&A, 627, A35, doi: 10.1051/0004-6361/201935531
Chini, R., & Wargau, W. F. 1990, A&A, 227, 213
Dias, W. S., Monteiro, H., & Assafin, M. 2018, MNRAS, 478, 5184, doi: 10.1093/mnras/sty1456
Dias, W. S., Monteiro, H., Moitinho, A., et al. 2021, MNRAS, 504, 356, doi: 10.1093/mnras/stab770
Gaia Collaboration, Brown, A. G. A., Vallenari, A., et al. 2016, A&A, 595, A2, doi: 10.1051/0004-6361/201629512
Genzel, R., & Townes, C. H. 1987, ARA&A, 25, 377, doi: 10.1146/annurev.aa.25.090187.002113
Girard, T. M., Grundy, W. M., Lopez, C. E., & van Altena, W. F. 1989, AJ, 98, 227, doi: 10.1086/115139
Gokmen, S., Eker, Z., Yontan, T., et al. 2023, AJ, 166, 263, doi: 10.3847/1538-3881/ad08b0
Higgins, M. E., & Bell, K. J. 2023, AJ, 165, 141, doi: 10.3847/1538-3881/acb20c
Joshi, Y. C., John, A. A., Maurya, J., et al. 2020b, MNRAS, 499, 618, doi: 10.1093/mnras/staa2881

Joshi, Y. C., Maurya, J., John, A. A., et al. 2020a, MNRAS, 492, 3602, doi: 10.1093/mnras/staa029
Kim, S. S., Figer, D. F., Lee, H. M., et al. 2000, ApJ, 545, 301, doi: 10.1086/317807
King, I. 1962, AJ, 67, 471, doi: 10.1086/108756
Lada, C. J., & Lada, E. A. 2003, ARA&A, 41, 57, doi: 10.1146/annurev.astro.41.011802.094844
Landolt, A. U. 1992, AJ, 104, 340, doi: 10.1086/116242
Liu, L., & Pang, X. 2019, ApJS, 245, 32, doi: 10.3847/1538-4365/ab530a
Lomb, N. R. 1976, Ap&SS, 39, 447, doi: 10.1007/BF00648343
Maciejewski, G., & Niedzielski, A. 2007, A&A, 467, 1065, doi: 10.1051/0004-6361:20066588
McKee, C. F., & Ostriker, E. C. 2007, ARA&A, 45, 565, doi: 10.1146/annurev.astro.45.051806.110602
Michalska, G. 2019, MNRAS, 487, 3505, doi: 10.1093/mnras/stz1500
Miglio, A., Montalbán, J., & Dupret, M.-A. 2007, MNRAS, 375, L21, doi: 10.1111/j.1745-3933.2006.00267.x
Neckel, T., & Chini, R. 1981, A&AS, 45, 451
Pandey, R., Sharma, S., Panwar, N., et al. 2020, ApJ, 891, 81, doi: 10.3847/1538-4357/ab6dc7
Pecaut, M. J., & Mamajek, E. E. 2013, ApJS, 208, 9, doi: 10.1088/0067-0049/208/1/9
Persson, S. E., Murphy, D. C., Krzeminski, W., et al. 1998, ApJ, 116, 2475, doi: 10.1086/300607
Phelps, R. L., & Janes, K. A. 1994, ApJS, 90, 31, doi: 10.1086/191857
Piskunov, A., Schilbach, E., Kharchenko, N., et al. 2008, A&A, 477, 165, doi: 10.1051/0004-6361:20078525
Ruprecht, J. 1966, BAICz, 17, 98
Salpeter, E. E. 1955, ApJ, 121, 161, doi: 10.1086/145971
Sanders, W. 1971, A&A, 14, 226
Scargle, J. D. 1982, ApJ, 263, 835, doi: 10.1086/160554
Schmidt-Kaler, T. 1982, 4.1.2 Intrinsic colors and visual absolute magnitudes (calibration of the MK system): Datasheet from Landolt-Börnstein - Group VI Astronomy and Astrophysics · Volume 2B: "Stars and Star Clusters" in SpringerMaterials (https://doi.org/10.1007/10201975_2), Springer-Verlag Berlin Heidelberg, doi: 10.1007/10201975_2
Skrutskie, M., Cutri, R., Stiening, R., et al. 2006, ApJ, 131, 1163, doi: 10.1086/498708
Sneden, C., Gehrz, R. D., Hackwell, J. A., et al. 1978, ApJ, 223, 168, doi: 10.1086/156247
Spitzer Jr, L., & Hart, M. H. 1971, ApJ, 166, 483, doi: 10.1086/150977
Stassun, K. G., Oelkers, R. J., Paegert, M., et al. 2019, AJ, 158, 138, doi: 10.3847/1538-3881/ab3467
Stetson, P. B. 1987, PASP, 99, 191, doi: 10.1086/131977
—. 2000, PASP, 112, 925, doi: 10.1086/316595
Tripathi, A., Panwar, N., Sharma, S., et al. 2023, JApA, 44, 61, doi: 10.1007/s12036-023-09955-7
Trumpler, R. J. 1930, LicOB, 420, 154, doi: 10.5479/ADS/bib/1930LicOB.14.154T
Yadav, R. K. S., Sariya, D. P., & Sagar, R. 2013, MNRAS, 430, 3350, doi: 10.1093/mnras/stt136

Revista Mexicana de Astronomía y Astrofísica, 61, 52-70, (2025)

OPEN ACCESS https://doi.org/10.22201/ia.01851101p.2025.61.02.05

Confirmation and Characterization of Galactic Planetary Nebulae: Insights from a Spectroscopic Study

D. A. Beleño-Molina[1], L. Olguín[1], L. F. Miranda[2], M. E. Contreras[1] and R. Vázquez[3]

[1]*Departamento de investigación en Física, Universidad de Sonora (UNISON), México.*
[2]*Instituto de Astrofísica de Andalucía (IAA), Consejo Superior de Investigaciones Científicas (CSIC), Spain.*
[3]*Instituto de Astronomía en Ensenada, Universidad Nacional Autónoma de México (UNAM), México.*

Keywords: *catalogues, ISM: abundances, planetary nebulae: general, techniques: spectroscopic*

Abstract

We present a spectroscopic investigation of 25 objects previously reported as possible Planetary Nebulae (PNe) in recent catalogs to obtain their physical properties and establish their true nature. We found 11 objects showing intense emission lines, 11 objects where it was not possible to measure Hβ, and 3 objects where no lines were present. We used diagnostic diagrams to confirm the true PN nature of the eight objects. We obtained elemental abundances for the three objects, the values of which are in agreement with the mean PNe values for our Galaxy. Four objects show [N II] λ6583 being more intense than Hα, and for two of them, this can be explained by the presence of shocks in the gas. Finally, we report angular sizes based on Hα and [O III] λ5007 emission.

Resumen

Presentamos un estudio espectroscópico de 25 objetos reportados como posibles Nebulosas Planetarias (NPs) en catálogos recientes para obtener sus propiedades físicas y establecer su verdadera naturaleza. Encontramos 11 objetos que muestran líneas de emisión intensas, 11 objetos donde no fue posible medir Hβ y 3 que no muestran líneas. Utilizando diagramas de diagnóstico, hemos podido confirmar ocho objetos como verdaderas NPs. Para tres de estos objetos hemos determinado abundancias elementales que concuerdan con los valores del conjunto de NPs de nuestra Galaxia. Cuatro objetos muestran la línea [N II] λ6583 más intensa que Hα que puede explicarse en dos de ellos con la presencia de choques en el gas. Finalmente, reportamos tamaños angulares determinados a partir de la emisión en Hα y [O III] λ5007.

Corresponding author: D. A. Beleño-Molina *E-mail address:* a219230153@unison.mx
Received: November 22, 2024 **Accepted:** April 10, 2025

1. Introduction

Planetary Nebulae (PNe) are the product of the gas ejection of evolved stars with low and intermediate-mass progenitors (~0.8–8M$_\odot$). These stars eject the most external layers of their surface at the Asymptotic Giant Branch (AGB) evolutionary stage, with mass loss rates of approximately 10^{-8} M$_\odot$ yr^{-1}. At the tip of the AGB phase, mass loss reaches up to 10^{-4} M$_\odot$ yr^{-1}, creating an expanding shell around them (Randall et al., 2020). When the uncovered central hot core reaches an effective temperature ($T_{\rm eff}$) of approximately 30,000 K (Khushbu & Muthumariappan, 2024), it produces energetic photons capable of exciting and ionizing the previously ejected material, forming a planetary nebula (PN). Subsequent line de-excitation and recombination in the envelope produce a characteristic spectrum associated with these objects (Osterbrock & Ferland, 2006). Considering a scenario in which single and binary stars produce PNe, the predicted Galactic population of these objects is approximately 46,000 (Moe & De Marco, 2006). However, by the year 2000, the number of known PNe was still around 1500 (Kohoutek, 2001), much smaller than expected. More recently, as of April 2025, the Galactic known PNe population has increased to 3952 objects according to the HASH (Parker et al., 2016), a number larger than the previous findings but still smaller than expected. This discrepancy could be explained by high dust obscuration in the Galactic plane, the faintness of old PNe, or the compactness of sources usually identified as stars (Kwok, 2000).

During the last 20 years, many sky surveys have searched for these elusive objects, marking the golden age of PNe discovery (Kwitter & Henry, 2022; Parker, 2022). Objects included in these catalogs generally have a small angular extent, and some of them are underrepresented by their low surface brightness. Several authors have begun studying these objects (e.g. Henry et al., 2010; Acker et al., 2012; Hsia & Zhang, 2014; Ali et al., 2016; Ritter et al., 2023; Temiz

et al., 2024) but a considerable number (∼1000) still need an initial study or a deeper analysis of their properties. Since these objects are poorly studied in the literature, it is necessary to establish their true nature to understand if they could represent an evolutionary stage that has not been well-studied before and why many of them are difficult to detect. The presence of dust, highly evolved objects, or small-sized emission regions can be claimed to be responsible for the latter.

Only some of the new objects reported in recent catalogs have been confirmed as true PNe (Sabin et al., 2014). Furthermore, additional studies are needed to obtain and analyze the physical and chemical properties of the confirmed PNe. In this paper, we present a spectroscopic study of 25 objects reported as potential PNe in catalogs. We derived physical parameters and chemical abundances for some selected objects.

2. Object selection

We selected our targets from an exhaustive search of various databases, catalogs, and papers: Acker et al. (1992), Kohoutek (2001), IPHAS (Drew et al., 2005; Viironen et al., 2009; Sabin et al., 2014), MASH (Parker et al., 2006; Miszalski et al., 2008), Ferrero et al. (2015), HASH (Bojičić et al., 2017; Parker et al., 2016), and PNST[1] (Le Dû et al., 2022). Our main selection criterion was objects reported in any catalog as a possible PN, a PN candidate, and confirmed PN with limited or no previous studies.

Table 1 lists all the known, relevant, and updated information found in the literature for our selected sample of 25 objects. We also indicate whether spectra, morphologies, central stars or distances are available. Finally, we added the HASH and SIMBAD statuses for comparison.

3. Observations and data reduction

Observations were carried out at the Observatorio Astronómico Nacional on the Sierra San Pedro Mártir (hereafter OAN-SPM) and the Observatorio Astrofísico Guillermo Haro (hereafter OAGH). In both cases, we used a 2.1 m class telescope. We had three observing runs: May 7 to 10, 2016 (OAGH); May 24 to 26, 2022; and July 26 to 28, 2022 (OAN-SPM). Table 2 presents the observing log, indicating the object names, coordinates, exposure times, and the corresponding observatories. Observations at OAN-SPM were obtained with a seeing of 3.1″ in May and 2.1–2.3″ in July, while at OAGH, the seeing was 1.8–2.9″. At OAN-SPM, low-resolution long-slit spectra were obtained using the Boller & Chivens spectrograph with the SI-2 CCD and a 400 lines mm^{-1} dispersion grating, giving a spectral resolution of ≃ 6 Å (FWHM). In the case of the OAGH, low-resolution long-slit spectra were obtained with the Boller & Chivens spectrograph, the SITe CCD, and a 150 lines mm^{-1} dispersion grating, resulting in a spectral resolution of ≃ 14 Å (FWHM). A slit width of ≃ 2.6″ was used in both observatories. The slit was always oriented at a position angle (PA) of 90°, except for PN G006.5+08.7, for which a PA = 144° was used. Appendix A shows the slit positions and extraction zones over-imposed on the images of the objects available in HASH. The exposure time for most objects was 1800 s.

For flux calibration, a wider slit width of ≃ 13″ was used to observe the spectrophotometric standard stars BD+28 4211 and Feige 67. Data reduction was performed following the IRAF standard procedures for bias, flat, wavelength calibration, background, and cosmic ray corrections.

[1] Planetary Nebula Spectra Trackers (PNST) is a french amateur observational group designed to uncover and confirm new Galactic PNe.

4. Results and Discussion

From our sample of 25 objects, we found 11 objects with clear emission lines, another 11 where few emission lines were detected but it was not possible to measure Hβ, and 3 more with no emission lines. The spectra of the 11 objects with clear emission lines are shown in Figure 1. Appendix B presents the spectra of the remaining objects.

We used the ANNEB software (Olguín et al., 2011) for line identification, to derive the logarithmic extinction coefficient c(Hβ), to obtain intrinsic line intensities and to calculate physical conditions (T_e and n_e), and ionic and elemental chemical abundances. To obtain ionic abundances, ANNEB uses IRAF's NEBULAR task (Shaw & Dufour, 1995) and for deriving elemental abundances uses ionization correction factors from Kingsburgh & Barlow (1994). The uncertainties for all derived quantities were calculated by properly propagating errors in line fluxes, with the number of photons received according to the detector gain as the source of error. Tables 3 and 4 show the relative line intensities and derived physical parameters for the 11 objects with multiple emission lines. The extinction function of Cardelli et al. (1989) was adopted to deredden the observed line ratios. F(Hβ) corresponds to the observed Hβ flux, and SB(Hβ) corresponds to the surface brightness calculated in the extraction area. Three objects show high extinction with c(Hβ) > 2.0, which explains the observed weakness of their emission lines.

We present electron temperatures from low-ionization species for two PNe derived using the [N II] (λ6548 + λ6583)/λ5755 line ratio. The [O III] λ4363 line was not detected in our sample, preventing the determination of the electron temperature using medium-ionization species. In addition, we present electron densities from low-ionization species for eight PNe derived using the [S II] λ6716/λ6731 line ratio. The electron densities in the objects where they could be measured were low, which could indicate that they are possibly already evolved PNe. Another possible explanation could be that the PNe expanded at typical rates, but the ejected mass was very low, implying low-mass progenitor stars.

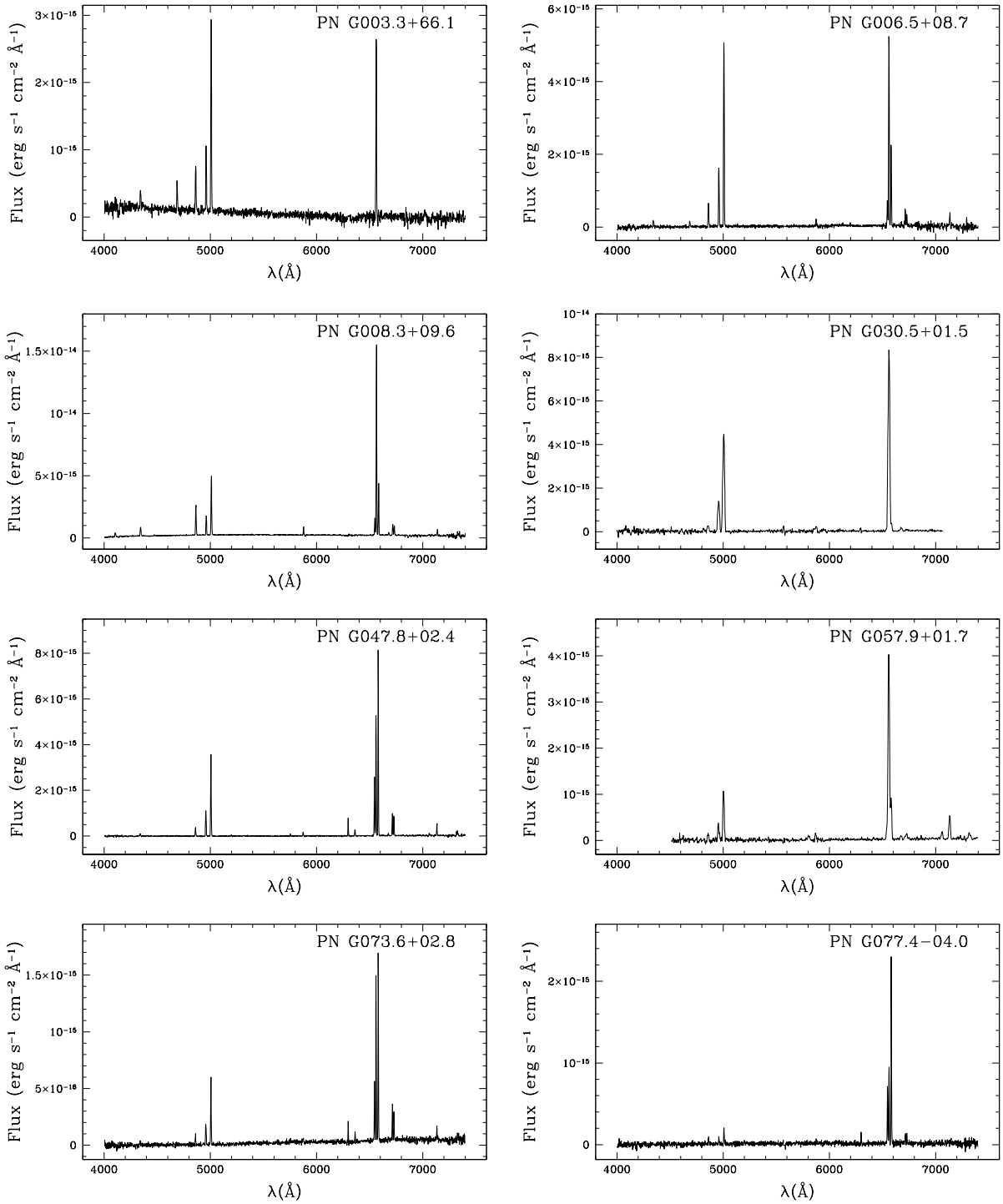

Figure 1. Spectra for 11 selected objects.

Figure 2 shows a diagnostic diagram (DD) following Frew & Parker (2010). Eight of our objects were located inside the True PNe region.

Table 5 lists the mean ionic abundances for the 11 selected objects, calculated from the collisionally excited and optical recombination lines. In cases where we could obtain T_e and n_e, these values were used in the calculations. Where it was not possible, we adopted $T_e = 10,000$ K and $n_e = 100\,\mathrm{cm}^{-3}$. Table 6 lists the elemental abundances for the three objects for which it was possible to derive them. We added some abundance references for the Sun (Asplund et al., 2021), Galactic disk PNe (southern in Kingsburgh & Barlow, northern in Stanghellini et al.) and Galactic bulge PNe (Tan et al., 2024). Values in our data are supersolar, except for O/H and S/H abundances in PN G086.2−01.2 (PN Ra 5), which are subsolar. Such a low S/H abundance

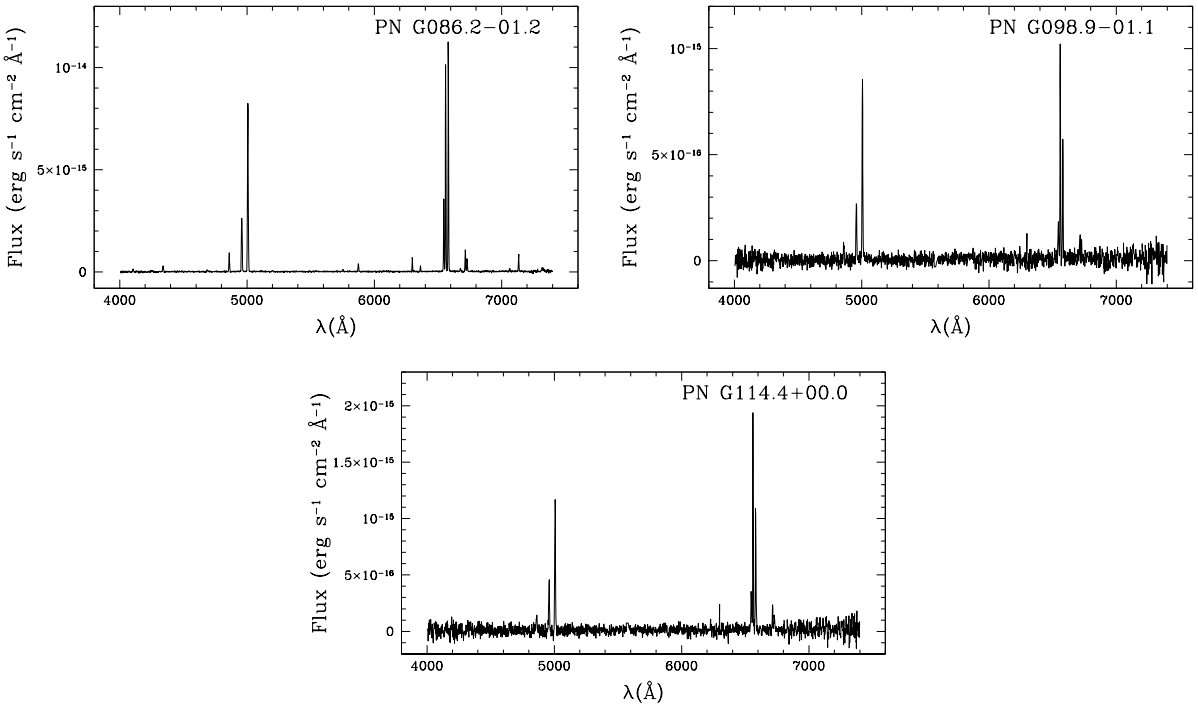

Figure 1. (Continued).

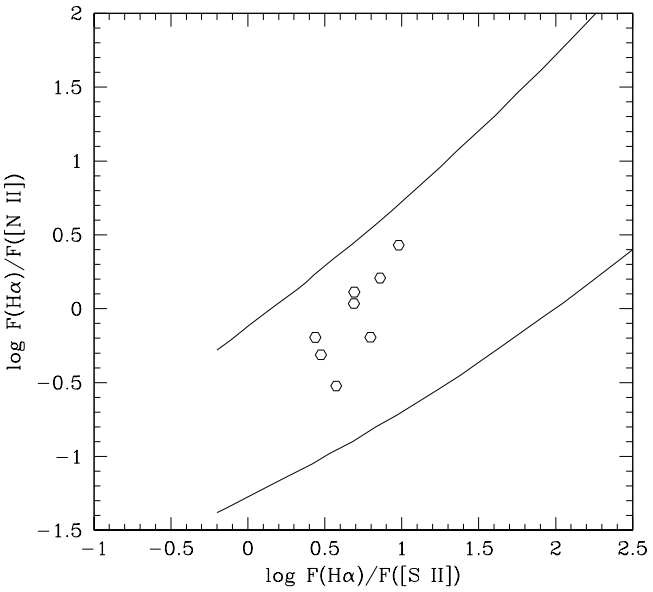

Figure 2. A $\log F(\mathrm{H}\alpha)/F([\mathrm{N\ II}])$ versus $\log F(\mathrm{H}\alpha)/F([\mathrm{S\ II}])$ diagnostic diagram. $F([\mathrm{N\ II}])$ refers to the sum of the flux of λ6548 and λ6583 nitrogen lines. $F([\mathrm{S\ II}])$ refers to the sum of λ6716 and λ6731 sulfur lines. All eight objects lie within the PNe region, as indicated by the empirical boundaries from Frew & Parker (2010). Uncertainties bars are the same size or smaller than the symbols.

could be explained by the "sulphur anomaly" (Henry et al., 2012). The elemental abundances we derived are consistent with the average values for PNe in the Milky Way. Following the classification criteria from Quireza et al. (2007), PN G047.8+02.4 can be classified as a Peimbert type IIa and PN G086.2−01.2 as a Peimbert type I. These results are in agreement with the original criteria used by Peimbert & Torres-Peimbert (1983). Type I PNe are related to massive progenitor stars (∼2.4–8.0 $M_\odot$), while type II are related to less massive progenitors (∼1.2–2.4 $M_\odot$, Quireza et al., 2007). Following equations developed by Maciel et al. (2010), we have estimated the central star mass (m_{CS}) and the stellar mass in the main-sequence (m_{MS}) obtaining $m_{\mathrm{CS}} = 0.6\,M_\odot$ and $m_{\mathrm{MS}} = 1.7\,M_\odot$ for PN G047.8+02.4 and $m_{\mathrm{CS}} = 0.7\,M_\odot$ and $m_{\mathrm{MS}} = 2.3\,M_\odot$ for PN G086.2−01.2. Following the methodology proposed by Reid & Parker (2010) and using our dereddened line intensity ratios, we could compute the excitation class (EC) based on the presence or absence of He II λ4686 in the nebular spectrum, which defines the EC of a PN. When a PN has $EC < 5$, it is considered to have low EC; if $EC \geq 5$, it is deemed to have medium to high EC. We found that PN G047.8+02.4 and PN G086.2−01.2 are classified in the medium to high EC with values of 5.7 and 6.9, respectively. In addition, adopting the criterion of $F([\mathrm{N\ II}]\lambda6583)/F(\mathrm{H}\alpha) \geq 1$ as the condition for optically thick PNe (Kaler & Jacoby, 1989), PN G047.8+02.4 and PN G086.2−01.2 are optically thick. Therefore, we can use the empirical relationship between EC and T_{eff}, defined by Reid & Parker (2010), to estimate the central star (CS) temperature. In this way, we have found $T_{\mathrm{eff}} \simeq 1.1 \times 10^5$ K for PN G047.8+02.4 and $T_{\mathrm{eff}} \simeq 1.4 \times 10^5$ K for PN G086.2−01.2.

Four low ionization objects were found (PN G047.8+02.4, PN G073.6+02.8, PN G077.4−04.0, and PN G086.2−01.2). For these objects, the [N II] λ6583 line is much more intense than Hα, especially in the case of PN G077.4−04.0

Table 1. Literature information of the observed objects

Name	HASH optical spectra[a]	Morph.[b]	Central Star[c]	d_{geo} (pc)[d]	d_{phot} (pc)[d]	HASH[e]	SIMBAD[f]
PN G003.3+66.1	...	R	1227151802340968832	729^{+176}_{-126}	464^{+32}_{-18}	P	PN
PN G339.4+29.7	...	...	...	...	...	NPN	PNC
PN G358.5+09.1	...	...	...	...	...	PG	PNC
PN G358.4+08.9	...	...	...	...	...	PG	PNC
PN G006.5+08.7	...	Ea∗	4122534632633972992	3327^{+853}_{-602}	3374^{+2278}_{-1058}	T	PN
PN G008.3+09.6	SO, 2002, 0.3m, 1×3600s	B∗	4124562102059801216	8402^{+2263}_{-1735}	7996^{+1518}_{-1495}	T	PN
PN G031.3+02.0	...	S	...	...	...	P	S
PN G030.5+01.5	SSO, 2008, 2.3m, 1×300s	E	4260148618930827008	...	...	T	ELS
PN G040.1+03.2	SAAO, 2011, 1.9m, 1×1200s	Eam†	4310230750781889920	7961^{+3458}_{-3893}	4786^{+1331}_{-1662}	T	PN
PN G038.4+02.2	KPNO, 2009, 2.1m, 1×1800s	R†	...	...	...	T	PN
PN G040.6+01.5	SAAO, 2011, 1.9m, 1×1200s	B/S‡	...	...	...	T	PN
PN G041.5+01.7	KPNO, 1993, 2.1m, 1×900s	S†	4310136536377607040	...	...	L	PN
PN G047.8+02.4	KPNO, 2009, 2.1m, 1×1800s	E†	...	...	...	T	PN
PN G050.0+01.0	...	E	4320871725541398400	...	...	T	PNC
PN G051.8+01.7	...	S	4514907211117285504	...	...	P	S
PN G052.0+01.7	...	E	...	...	...	L	MIRS
PN G051.7+01.3	OAN-SPM, 2010, 2.1m, 1×1800s	Ia‡	4322743914667694208	...	...	T	PN
PN G057.9+01.7	...	R	2019455895594998784	$5556^{+10,502}_{-2409}$	6174^{+2448}_{-2826}	T	PNC
PN G058.6+00.9	...	S	2020219403339189760	...	...	P	PN
PN G073.6+02.8	KPNO, 2009, 2.1m, 1×1800s	Eas†	...	...	...	T	PN
PN G077.4−04.0	...	Es‡	...	...	...	T	PN
PN G086.2−01.2	...	B	...	...	...	T	PNC
PN G095.8+02.6	GTC, 2011, 10.4m, 1×2400s	Eps‡	...	...	...	T	PN
PN G098.9−01.1	OAN-SPM, 2011, 2.1m, 1×1800s	Ra‡	1981477771828655488	5583^{+2964}_{-2607}	5501^{+1486}_{-808}	T	PN
PN G114.4+00.0	...	E‡	2012536875076571776	3367^{+2219}_{-1197}	4251^{+1219}_{-920}	T	PN

[a] Observatory, date, telescope diameter, and exposure time. Spectra that are not flux-calibrated were not included.
[b] Morphology. Round (R), elliptical (E), bipolar (B), star−like (S), irregular (I), sided asymmetry (a), multiple shells (m), internal structure (s), and point symmetry (p). ∗Parker et al. (2006), †Sabin et al. (2014), and ‡Sabin et al. (2021). Morphologies without references assigned by HASH.
[c] DR3 IDs (Gaia Collaboration et al., 2023) according to Chornay & Walton (2021), and González-Santamaría et al. (2021).
[d] Geometric distance (d_{geo}) and photogeometric distance (d_{phot}) calculated by Bailer-Jones et al. (2021).
[e] HASH status. For Planetary Nebula (PN): Possible (P), True (T), and Likely (L). Other objects: Not PN (NPN) and Possible galaxy (PG).
[f] SIMBAD status. PN Candidate (PNC), Star (S), Emission-line Star (ELS), and MIRS (Mid-IR Source).

(PN Ra 4), where [N II] λ6583 is more than twice as intense as Hα. This phenomenon could be related to shock processes in the nebula as an excitation mechanism (Akras & Gonçalves, 2016). To verify this possibility, we used Raga et al. (2008), Ali & Dopita (2017) and Mari et al. (2023) diagnostic diagrams, as shown in Figure 3. We found that PN G077.4−04.0 is inside a shock region, and the excess of the [N II] λ6583 line could be explained by photoionization and low-velocity shock models. In addition, PN G073.6+02.8 is very close to the contour of the high-speed-shock model. This may indicate that a weaker shock is occurring in the nebula. [N II] λ6583 excess for the remaining two objects could be explained by photoionization models. The central stars of each object in this subgroup must have low effective temperatures.

Table 7 lists 11 objects for which a reliable Hβ measurement was not possible. However, other emission lines were detected: two objects with several lines and nine with at least one evident Hα emission. F(Hα) and SB(Hα) are defined as in Tables 3 and 4 but for Hα. $c(\mathrm{H}\beta)_{\mathrm{limit}}$ is the lower limit of c(Hβ) derived using an estimation of the upper limit of the Hβ flux. This limit was estimated by adding synthetic Hβ line profiles of different intensities to our original spectrum and finally choosing a flux where the line was clearly observed in the resulting spectrum. The selected upper limit was typically thrice the noise level. We discarded the four noisiest spectra in the $c(\mathrm{H}\beta)_{\mathrm{limit}}$ calculations because the detected Hα had a very low signal to noise (S/N).

Table 8 lists the angular sizes of the PNe derived from the Hα and [O III] λ5007 emission lines in the 2D long-slit spectra. Only regions with a flux above 1% of the maximum intensity of the line were considered. Some of our values are similar to the major diameters previously reported in the literature, whereas others are new. All sizes are affected by seeing at the moment of observation. In addition, in a few cases, the PA of the slit was misaligned with the main axis of the source, which could explain the size differences from the values reported in the literature. The most significant difference was found for PN G003.3+66.1. From our sample, some objects have been previously reported, as shown in Table 1, but no in-depth studies have appeared

Table 2. Observed objects

Name	RA (2000)	DEC (2000)	t_{exp} (s)	OBSERVAT	DATE
PN G003.3+66.1	14:16:21.95	+13:52:24.25	3×1800	OAN-SPM	2022 May 24
PN G339.4+29.7	15:08:20.73	−23:14:50.47	1×1800	OAN-SPM	2022 May 24
PN G358.5+09.1	17:07:45.52	−25:03:38.87	1×1800	OAN-SPM	2022 July 27
PN G358.4+08.9	17:08:19.73	−25:13:41.60	1×1800	OAN-SPM	2022 July 26
PN G006.5+08.7[a]	17:28:14.05	−18:44:31.01	3×1800	OAN-SPM	2022 May 24
PN G008.3+09.6	17:29:13.10	−16:47:42.60	3×1800	OAN-SPM	2022 May 24
PN G031.3+02.0	18:41:25.95	−00:27:45.41	1×1200	OAGH	2016 May 07
PN G030.5+01.5	18:41:40.43	−01:25:17.72	1×1800	OAGH	2016 May 07
PN G040.1+03.2	18:53:09.40	+07:52:41.00	3×1800	OAGH	2016 May 08
PN G038.4+02.2	18:53:21.74	+05:56:42.12	1×1800	OAGH	2016 May 08
PN G040.6+01.5	18:59:57.00	+07:35:44.00	1×1800	OAGH	2016 May 10
PN G041.5+01.7	19:01:05.72	+08:25:35.93	1×1200	OAGH	2016 May 08
PN G047.8+02.4	19:10:01.10	+14:22:02.00	1×1800	OAN-SPM	2022 July 28
PN G050.0+01.0	19:19:22.92	+15:41:37.15	1×1800	OAGH	2016 May 09
PN G051.8+01.7	19:20:31.62	+17:32:48.92	1×1800	OAGH	2016 May 09
PN G052.0+01.7	19:20:54.53	+17:46:07.90	1×1800	OAGH	2016 May 09
PN G051.7+01.3	19:21:46.61	+17:20:45.80	1×1800	OAN-SPM	2022 July 26
PN G057.9+01.7	19:33:09.03	+22:58:33.63	1×1800	OAGH	2016 May 10
PN G058.6+00.9	19:37:29.33	+23:09:46.56	1×1800	OAGH	2016 May 10
PN G073.6+02.8	20:05:22.00	+36:59:42.00	1×1800	OAN-SPM	2022 July 28
PN G077.4−04.0	20:44:14.10	+36:07:37.00	1×1800	OAN-SPM	2022 July 28
PN G086.2−01.2	21:02:38.73	+44:46:46.00	1×1800	OAN-SPM	2022 July 28
PN G095.8+02.6	21:26:08.30	+54:20:15.00	1×1800	OAN-SPM	2022 July 26
PN G098.9−01.1	21:58:42.30	+53:30:03.00	1×1800	OAN-SPM	2022 July 26
PN G114.4+00.0	23:38:40.43	+61:41:40.90	1×1800	OAN-SPM	2022 July 26

[a] Only object observed with PA = 144°.

in the literature yet. We want to point out that despite the existence of some uploaded spectra in the HASH database, we decided not to use them because they are presumably being analyzed by the original authors. Therefore, we used our spectra in this study. A few objects with spectroscopic or related studies reported in the literature are discussed in the following section. Additional literature information for other objects is available in Appendix C.

5. Notes on individual objects

PN G008.3+09.6: Boumis et al. (2006) named this object as PTB 26. These authors reported an optical spectrum in which ten emission lines were detected. They derived $c(\mathrm{H}\beta) = 0.62$ and an electron density $n_e < 70$ cm^{-3}. We found 14 emission line fluxes, $c(\mathrm{H}\beta) = 0.96$ and an electron density of $n_e = 147$ cm^{-3}. In addition, we report the mean ionic abundances.

PN G030.5+01.5: HASH status is True PN, while SIMBAD reports it as an emission-line star based on Robertson & Jordan (1989). In our work, we found the expected characteristics of a PN (see emission lines, abundances, and spectrum in the text), but it does not appear in Figure 2 because the [S II] ($\lambda\lambda$6716, 6731) emission in our spectrum was found to be unreliable.

PN G040.1+03.2: We found probable C IV broad line at 5806 Å. The object was also observed by Sabin et al. (2014), and the broad emission was also clear. This could be related to a PN with a Wolf-Rayet CS, displaying a blended C IV doublet (at 5801 and 5812 Å) appearing as a broad feature due to the rapid expansion of the hot stellar wind (DePew et al., 2011).

PN G041.5+01.7: Named 1858+0821 by van de Steene et al. (1996). The strengths of [N II]λ6548 and λ6583 (relative to Hα=100) reported from a very low S/N spectrum were 24.4 and 66.4, respectively. In our spectrum we only found Hα and [N II] λ6583. The [N II]λ6548 line is blended with Hα. To correct the Hα emission by the λ6548 contribution, we estimated λ6548 using a theoretical ratio [N II]$I_{6583}/I_{6548} = 2.96$ (Ueta et al., 2019). The final strengths of the [N II] lines relative to Hα are 16 for λ6548 and 47 for λ6583. The differences found in the ratios can be explained by the very low S/N of both spectra. A deeper spectrum is required to better understand the nature of this object. However, Urquhart et al. (2009) reported a 6 cm radio flux density at 5GHz and associated the source with an object of PN nature.

6. Conclusions

We report a low-resolution spectroscopic investigation of 25 objects suspected to be PNe in this study. Using diagnostic diagrams, we confirmed eight objects as true PNe, while the remaining objects did not exhibit sufficient emission lines for reliable classification. The true PNe include PN G086.2−01.2, which was previously classified as doubtful

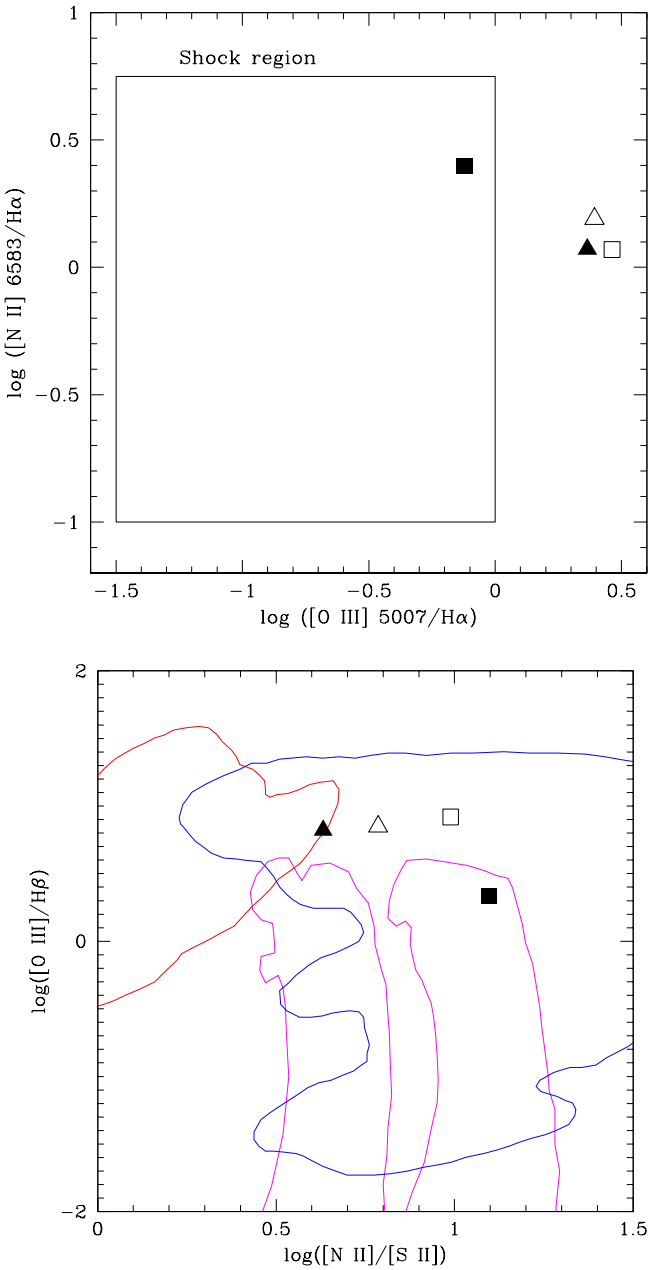

Figure 3. Diagnostic diagrams to distinguish shock-excited and photoionised regions. Top: proposed by Raga et al. (2008) with the shock region from Ali & Dopita (2017). Bottom: proposed by Mari et al. (2023). Photoionization models are represented by blue contours, low-velocity shock models by magenta, and high-velocity shock models by red. Symbols: △ PN G047.8+02.4, ▲ PN G073.6+02.8, □ PN G086.2−01.2, and ■ PN G077.4−04.0. Uncertainties are the same size or smaller than the symbols.

and reported as a candidate in SIMBAD. We calculated the electron temperatures and densities for two and eight PNe, respectively, where the S/N in the nebula spectra was appropriate. We were able to report elemental and ionic abundances for three and 11 objects, respectively. Elemental abundances are entirely consistent with Galactic PNe (Kingsburgh & Barlow, 1994, Stanghellini et al., 2006 and Tan et al., 2024). We derived masses for the central stars of PN G047.8+02.4 and PN G086.2−01.2 of 0.6 and 0.7 $M_{\odot}$, respectively. Peimbert types are also reported for these two objects. The large [N II] λ6583/Hα line intensity ratios in PN G077.4−04.0 and PN G073.6+02.8 of 2.5 and 1.2, respectively, suggest a contribution of shock excitation, as indicated by shock models. A few emission lines were detected for 11 objects for which we could not measure Hβ. Deeper spectra are needed to confirm their true nature. We measured Hα and [O III] λ5007 angular sizes for our sample, where possible. The remaining three objects were

Table 3. Intrinsic line intensities (I(Hβ) = 100) and physical parameters for the first set of objects

Ion	Line	f_λ	003.3+66.1	006.5+08.7	008.3+09.6	030.5+01.5	047.8+02.4	057.9+01.7
Hδ	4101	0.230	8 ± 1	...	27 ± 1	...	...	...
Hγ	4340	0.157	48 ± 1	52 ± 1	48 ± 1	...	51 ± 2	...
He I	4471	0.115	...	6 ± 1	6 ± 1	...	...	...
He II	4686	0.050	55 ± 1	30 ± 1	...	...	6 ± 1	...
Hβ	4861	0.000	100 ± 1	100 ± 1	100 ± 1	100 ± 1	100 ± 2	100 ± 1
[O III]	4959	−0.026	141 ± 2	236 ± 2	58 ± 1	409 ± 2	243 ± 4	165 ± 1
[O III]	5007	−0.038	366 ± 3	662 ± 6	172 ± 1	1169 ± 4	707 ± 10	471 ± 4
[N II]	5755	−0.185	...	...	...	...	6 ± 1	...
He I	5876	−0.203	...	12 ± 1	15 ± 1	20 ± 1	14 ± 1	17 ± 1
[O I]	6300	−0.263	...	...	...	...	48 ± 1	...
[O I]	6363	−0.271	...	...	...	...	17 ± 1	...
[N II]	6548	−0.296	...	48 ± 1	28 ± 1	...	143 ± 3	...
Hα	6563	−0.298	286 ± 4	287 ± 4	286 ± 2	286 ± 2	286 ± 6	286 ± 3
[N II]	6583	−0.300	...	130 ± 2	79 ± 1	5 ± 1	443 ± 9	47 ± 1
He I	6678	−0.313	...	5 ± 1	4 ± 1	6 ± 1	5 ± 1	5 ± 1
[S II]	6716	−0.318	...	25 ± 1	17 ± 1	...	51 ± 1	9 ± 1[a]
[S II]	6731	−0.320	...	15 ± 1	13 ± 1	...	46 ± 1	...
He I	7065	−0.364	...	...	...	...	5 ± 1	7 ± 1
[Ar III]	7136	−0.374	...	15 ± 1	7 ± 1	...	22 ± 1	19 ± 1
[O II]	7320	−0.398	...	...	...	...	5 ± 1	5 ± 1[b]
[O II]	7330	−0.400	...	...	...	...	12 ± 1	...
log F(Hβ)	—	—	−14.19 ± 0.01	−14.26 ± 0.01	−13.70 ± 0.01	−14.22 ± 0.01	−14.50 ± 0.01	−14.58 ± 0.01
SB(Hβ)[c]	—	—	2.75	4.62	19.40	26.37	9.05	15.73
c(Hβ)	—	—	0.09 ± 0.01	1.26 ± 0.01	0.96 ± 0.01	3.33 ± 0.01	1.83 ± 0.02	3.29 ± 0.01
T_e([N II])	—	—	....	...	...	...	10,295 ± 258	...
n_e([S II])	—	—	...	< 100	147 ± 33	...	381 ± 90	...

[a]Correspond to λ6716 and λ6731 sulfur lines blended. [b]Correspond to λ7320 and λ7330 oxygen lines blended. [c]Surface brightness ($\times 10^{-17}$erg s^{-1} cm^{-2} arcsec^{-2}).

misclassified as possible PNe: PN G339.4+29.7 is a late-type star, while PN G358.5+09.1 and PN G358.4+08.9 are galaxies.

We thank an anonymous referee for providing comments and suggestions that have improved the manuscript. This study is based on observations carried out at the Observatorio Astronómico Nacional on the Sierra San Pedro Mártir (OAN-SPM), Baja California, México. We thank the daytime and night support staff at the OAN-SPM for facilitating and helping us obtain our observations. This publication is also based on data collected at the Observatorio Astrofísico Guillermo Haro (OAGH), Cananea, México, operated by the Instituto Nacional de Astrofísica, Óptica y Electrónica (INAOE). Funding for the OAGH was provided by the Consejo Nacional de Humanidades, Ciencias y Tecnologías (CONAHCYT). DABM acknowledges support from CONAHCYT (México) grant 806246. LFM acknowledges support from grants PID2020-114461GB-I00, PID2023-146295NB-I00, and CEX2021-001131-S, funded by MCIN/AEI/10.13039/501100011033. RV acknowledges support from UNAM-DGAPA-PAPIIT grant IN103125. This study used the SIMBAD database, operated at CDS, Strasbourg, France, and the HASH PN database in hashpn.space.

Table 4. Intrinsic line intensities (I(Hβ) = 100) and physical parameters for the second set of objects

Ion	Line	f_λ	073.6+02.8	077.4−04.0	086.2−01.2	098.9−01.1	114.4+00.0
Hδ	4101	0.230	84 ± 6	...	34 ± 1	...	...
Hγ	4340	0.157	...	...	66 ± 1	...	...
He I	4471	0.115	...	...	...	...	...
He II	4686	0.050	...	...	19 ± 1	...	...
Hβ	4861	0.000	100 ± 5	100 ± 4	100 ± 1	100 ± 4	100 ± 3
[O III]	4959	−0.026	230 ± 9	66 ± 3	278 ± 3	276 ± 9	193 ± 4
[O III]	5007	−0.038	663 ± 23	216 ± 8	830 ± 8	851 ± 26	535 ± 11
[N II]	5755	−0.185	...	...	6 ± 1	...	...
He I	5876	−0.203	22 ± 1	23 ± 1	17 ± 1	...	...
[O I]	6300	−0.263	42 ± 2	34 ± 2	22 ± 1	65 ± 2	88 ± 3
[O I]	6363	−0.271	19 ± 1	7 ± 1	8 ± 1	...	...
[N II]	6548	−0.296	110 ± 5	241 ± 11	109 ± 2	60 ± 3	66 ± 2
Hα	6563	−0.298	286 ± 14	286 ± 13	285 ± 4	287 ± 13	286 ± 8
[N II]	6583	−0.300	337 ± 16	714 ± 32	336 ± 5	161 ± 7	198 ± 6
He I	6678	−0.313	...	...	5 ± 1	...	...
[S II]	6716	−0.318	57 ± 3	43 ± 2	27 ± 1	43 ± 2	33 ± 1
[S II]	6731	−0.320	47 ± 3	34 ± 2	19 ± 1	16 ± 1	26 ± 1
He I	7065	−0.364	...	...	4 ± 1	...	...
[Ar III]	7136	−0.374	16 ± 1	...	19 ± 1	...	...
[O II]	7320	−0.398	...	...	4 ± 1	...	...
[O II]	7330	−0.400	...	...	4 ± 1	...	...
log F(Hβ)	—	—	−15.29 ± 0.01	−15.24 ± 0.01	−14.18 ± 0.01	−15.20 ± 0.01	−14.83 ± 0.01
SB(Hβ)[a]	—	—	1.44	0.92	10.87	0.03	1.11
c(Hβ)	—	—	2.53 ± 0.05	1.78 ± 0.05	1.61 ± 0.01	1.75 ± 0.04	1.26 ± 0.03
T_e([N II])	—	—	...	...	11,445 ± 216	...	...
n_e([S II])	—	—	230 ± 170	175 ± 163	< 100	< 100	155 ± 111

[a] Surface brightness ($\times 10^{-17}$erg s^{-1} cm^{-2} arcsec^{-2}).

Table 5. Mean ionic abundances[a] from all the selected objects

Ion	Factor	003.3+66.1	006.5+08.7	008.3+09.6	030.5+01.5	047.8+02.4	057.9+01.7
He^{1+}	$\times 10^{-1}$	...	1.09 ± 0.02	1.08 ± 0.01	1.55 ± 0.01	1.17 ± 0.02	1.28 ± 0.01
He^{2+}	$\times 10^{-2}$	4.48 ± 0.06	2.40 ± 0.04	...	...	0.47 ± 0.03	...
N^{1+}	$\times 10^{-5}$	...	2.65 ± 0.03	1.56 ± 0.01	0.09 ± 0.01	7.94 ± 0.47	0.92 ± 0.01
O^{0+}	$\times 10^{-4}$	...	...	...	...	0.86 ± 0.07	...
O^{1+}	$\times 10^{-4}$	...	...	...	...	2.57 ± 0.50	1.95 ± 0.03
O^{2+}	$\times 10^{-4}$	1.36 ± 0.01	2.39 ± 0.01	0.60 ± 0.01	4.18 ± 0.01	2.26 ± 0.16	1.69 ± 0.01
S^{1+}	$\times 10^{-6}$	...	0.89 ± 0.01	0.69 ± 0.01	...	2.19 ± 0.17	0.34 ± 0.01
Ar^{2+}	$\times 10^{-6}$	...	1.41 ± 0.03	0.62 ± 0.01	...	1.91 ± 0.16	1.76 ± 0.02

Ion	Factor	073.6+02.8	077.4−04.0	086.2−01.2	098.9−01.1	114.4+00.0
He^{1+}	$\times 10^{-1}$	1.58 ± 0.08	1.71 ± 0.09	1.32 ± 0.02	...	...
He^{2+}	$\times 10^{-2}$	...	...	1.56 ± 0.04	...	...
N^{1+}	$\times 10^{-5}$	6.52 ± 0.23	14.01 ± 0.49	4.65 ± 0.19	3.31 ± 0.11	3.86 ± 0.09
O^{0+}	$\times 10^{-4}$	0.94 ± 0.03	0.59 ± 0.02	0.27 ± 0.02	1.26 ± 0.05	1.69 ± 0.05
O^{1+}	$\times 10^{-4}$	...	...	0.81 ± 0.08	...	...
O^{2+}	$\times 10^{-4}$	2.35 ± 0.07	0.74 ± 0.02	1.88 ± 0.09	2.97 ± 0.07	1.93 ± 0.03
S^{1+}	$\times 10^{-6}$	2.47 ± 0.19	1.79 ± 0.14	0.75 ± 0.03	1.34 ± 0.05	1.37 ± 0.08
Ar^{2+}	$\times 10^{-6}$	1.47 ± 0.09	...	1.29 ± 0.08	...	...

[a] Given as $N(X^{i+})/N(H^+)$.

Table 6. Elemental abundances[a] from some selected objects

Ion	Factor	006.5+08.7	047.8+02.4	086.2−01.2	Sun[b]	KB94[c]	SGC06[c]	TPZ24[c]
He	1	0.133 ± 0.002	0.122 ± 0.003	0.147 ± 0.002	0.082	0.115 (55)	0.123 (75)	0.115 (123)
N	$\times10^{-4}$	...	1.532 ± 0.357	1.660 ± 0.193	0.676	2.239 (47)	2.439 (63)	1.862 (122)
O	$\times10^{-4}$	...	4.964 ± 0.548	2.904 ± 0.134	4.898	4.786 (54)	3.531 (67)	5.012 (124)
S	$\times10^{-5}$	...	1.511 ± 0.124	0.626 ± 0.041	1.318	0.832 (43)	... (...)	0.794 (124)
Ar	$\times10^{-6}$	2.648 ± 0.583	3.574 ± 0.840	2.420 ± 0.550	2.399	2.455 (41)	1.262 (46)	2.754 (122)

[a]Given as $N(X)/N(H)$. [b]According to Asplund et al. (2021). [c]Average PNe abundances. KB94 is for Kingsburgh & Barlow (1994), SGC06 for Stanghellini et al. (2006), and TPZ24 for Tan et al. (2024). The number of PNe used for each average appear in parentheses.

Table 7. Objects with few emission lines detected

Ion	Line	031.3+02.0	040.1+03.2[a]	038.4+02.2	040.6+01.5	041.5+01.7	050.0+01.0
[O III]	4959	...	13 ± 1	...	...	...	...
[O III]	5007	...	30 ± 1	19 ± 1	...	...	24 ± 1
[N II]	6548	...	...	...	...	...	...
Hα	6563	100 ± 1	100 ± 1	100 ± 1	100 ± 1	100 ± 1[b]	100 ± 1
[N II]	6583	...	4 ± 1	...	...	40 ± 1	...
[S II]	6716	...	...	...	...	...	...
[S II]	6731	...	...	...	...	...	...
[Ar III]	7136	...	...	...	...	...	...
log $F(H\alpha)$	—	−14.29 ± 0.01	−13.31 ± 0.01	−13.80 ± 0.01	−14.89 ± 0.01	−14.19 ± 0.01	−14.11 ± 0.01
$SB(H\alpha)$[c]	—	6.16	16.78	11.01	1.33	10.71	10.73
$c(H\beta)_{limit}$	—	> 0.81	> 3.04	> 1.82	...	...	> 1.67

[a]We found also I(C IV) = 16 ± 1, see § 5. [b]Blended with λ6548, see § 5. [c]Surface brightness ($\times10^{-16}$erg s^{-1} cm^{-2} arcsec^{-2}).

Ion	Line	051.8+01.7	052.0+01.7	051.7+01.3	058.6+00.9	095.8+02.6
[O III]	4959	...	...	15 ± 1	...	12 ± 1
[O III]	5007	...	...	43 ± 1	...	39 ± 1
[N II]	6548	...	...	29 ± 1	...	33 ± 1
Hα	6563	100 ± 1	100 ± 1	100 ± 2	100 ± 3	100 ± 1
[N II]	6583	...	...	97 ± 2	...	110 ± 2
[S II]	6716	...	...	16 ± 1	...	12 ± 1
[S II]	6731	...	...	12 ± 1	...	8 ± 1
[Ar III]	7136	...	...	23 ± 1	...	14 ± 1
log $F(H\alpha)$	—	−14.82 ± 0.01	−13.72 ± 0.01	−14.42 ± 0.01	−15.40 ± 0.01	−14.19 ± 0.01
$SB(H\alpha)$[a]	—	2.11	13.12	0.53	0.66	1.60
$c(H\beta)_{limit}$	—	...	> 1.08	> 2.31	...	> 3.16

[a]Surface brightness ($\times10^{-16}$erg s^{-1} cm^{-2} arcsec^{-2}).

Table 8. Object sizes[a] from our sample

Name	[O III] 5007 (arcsec)	Hα 6563 (arcsec)	Literature major diameter (arcsec)
PN G003.3+66.1	106	100	50 (Frew et al., 2016)
PN G339.4+29.7	...	...	...
PN G358.5+09.1	...	...	...
PN G358.4+08.9	...	...	...
PN G006.5+08.7	47	45	51 (Parker et al., 2006)
PN G008.3+09.6	29	38	30 (Parker et al., 2006)
PN G031.3+02.0	...	3	...
PN G030.5+01.5	8	11	...
PN G040.1+03.2	5	7	12 (Sabin et al., 2014)
PN G038.4+02.2	4	4	5 (Sabin et al., 2014)
PN G040.6+01.5	...	3	5 (Sabin et al., 2021)
PN G041.5+01.7	...	3	...
PN G047.8+02.4	10	12	10 (Sabin et al., 2014)
PN G050.0+01.0	3	3	...
PN G051.8+01.7	...	3	...
PN G052.0+01.7	...	5	...
PN G051.7+01.3	23	25	34 (Sabin et al., 2021)
PN G057.9+01.7	5	6	...
PN G058.6+00.9	...	3	...
PN G073.6+02.8	10	12	11 (Sabin et al., 2014)
PN G077.4−04.0	14	23	25 (Sabin et al., 2021)
PN G086.2−01.2	15	17	12 (Ferrero et al., 2015)
PN G095.8+02.6	9	12	15 (Sabin et al., 2021)
PN G098.9−01.1	26	26	31 (Sabin et al., 2021)
PN G114.4+00.0	55	56	61 (Sabin et al., 2021)

[a] Uncertainties are determined by the seeing, with a typical value of 2 arcsec.

APPENDICES

A. SLIT POSITION AND SPECTRUM EXTRACTION ZONE

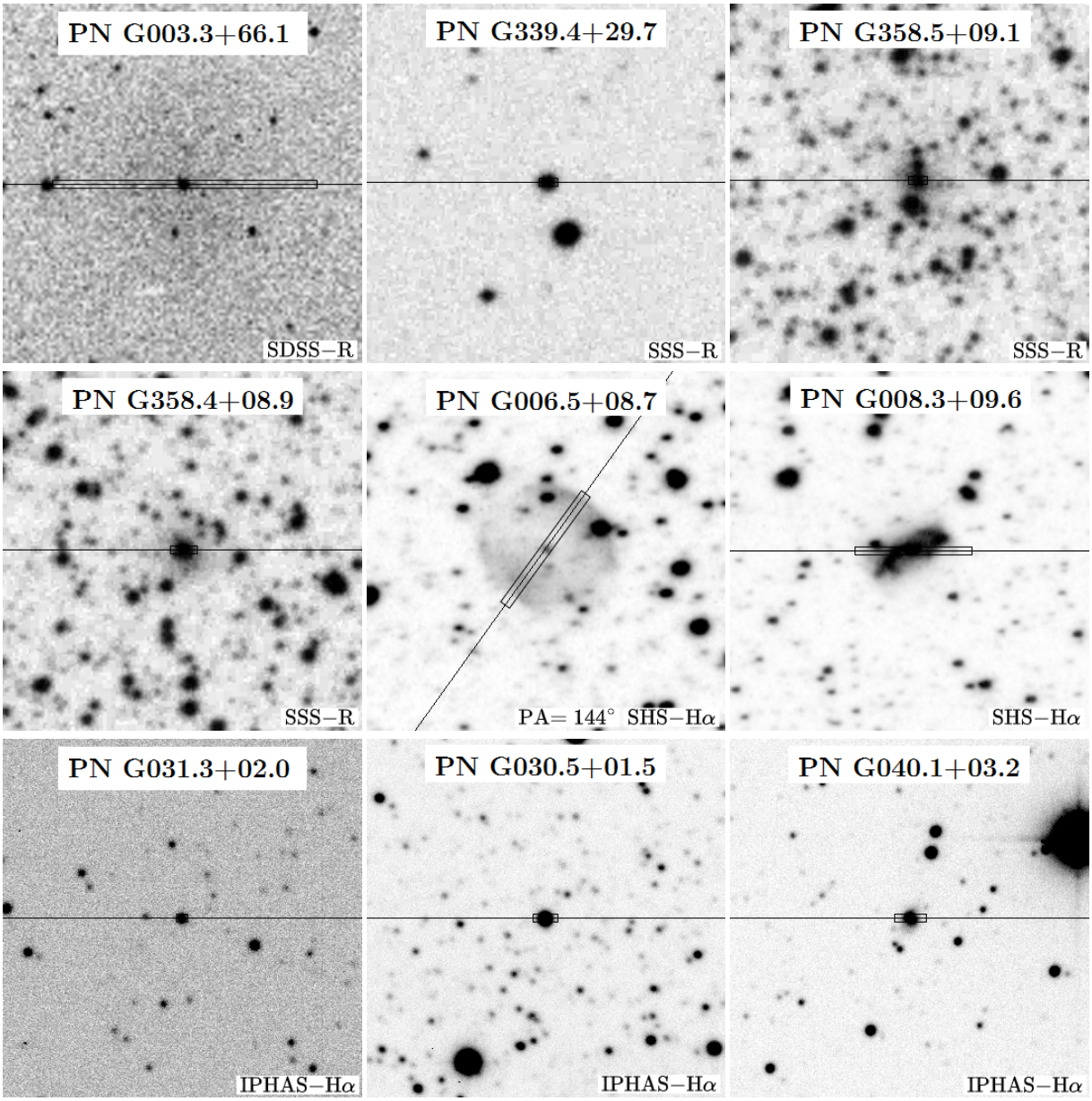

Figure 4. Visual fields available in HASH for observed objects with images taken from SDSS (York et al., 2000), SSS (Hambly et al., 2001), SHS (Parker et al., 2005), and IPHAS (Drew et al., 2005), as labeled in the bottom-right corner of each panel. North is up, East is left. Field size is 2′×2′ in all cases. The solid line represents the long-slit position, which was oriented at PA = 90° for all objects, except where indicated. The rectangle over the long-slit marks the extraction zone for the spectra shown in Figure 1 and Appendix B.

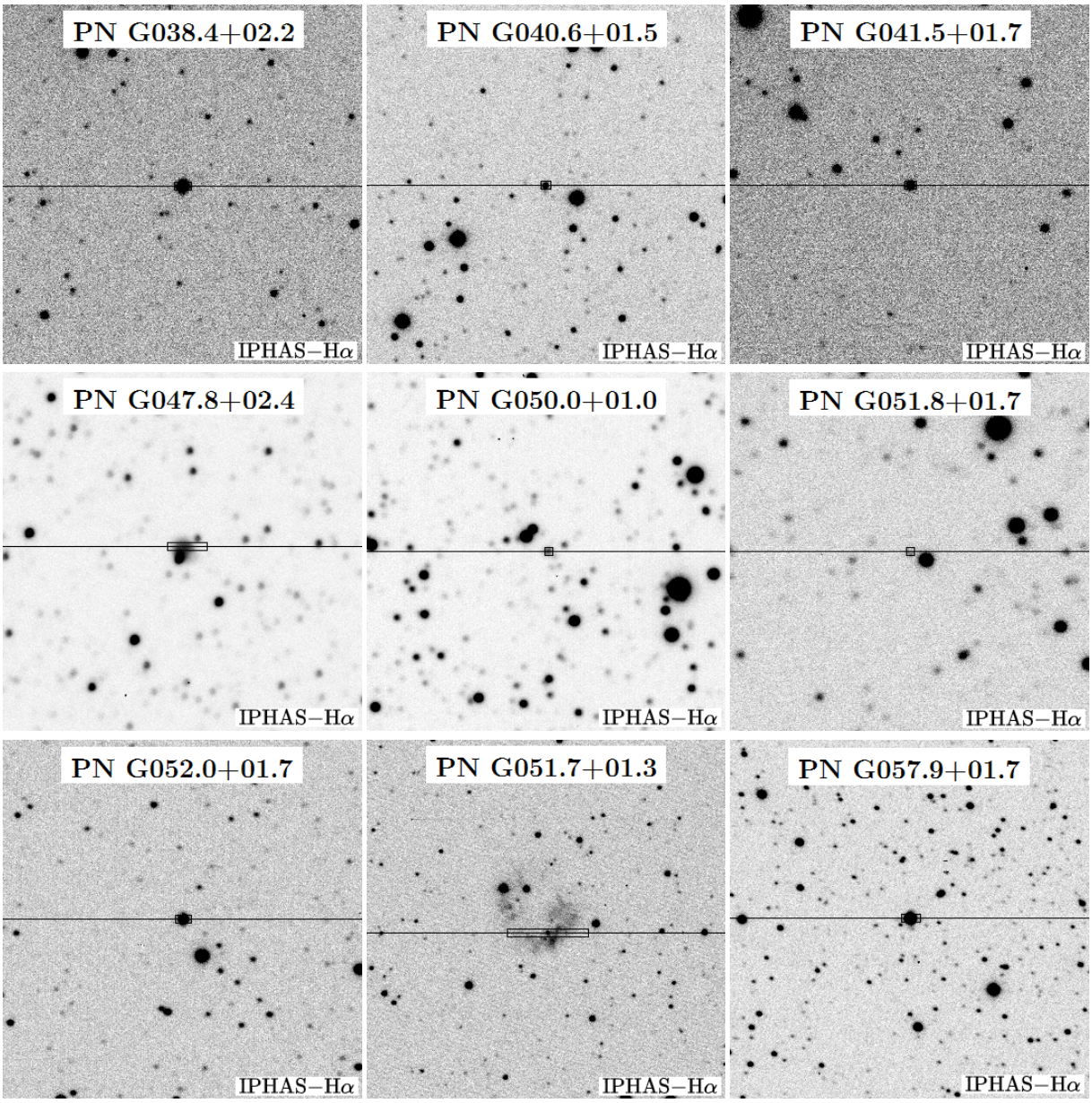

Figure 4. (Continued).

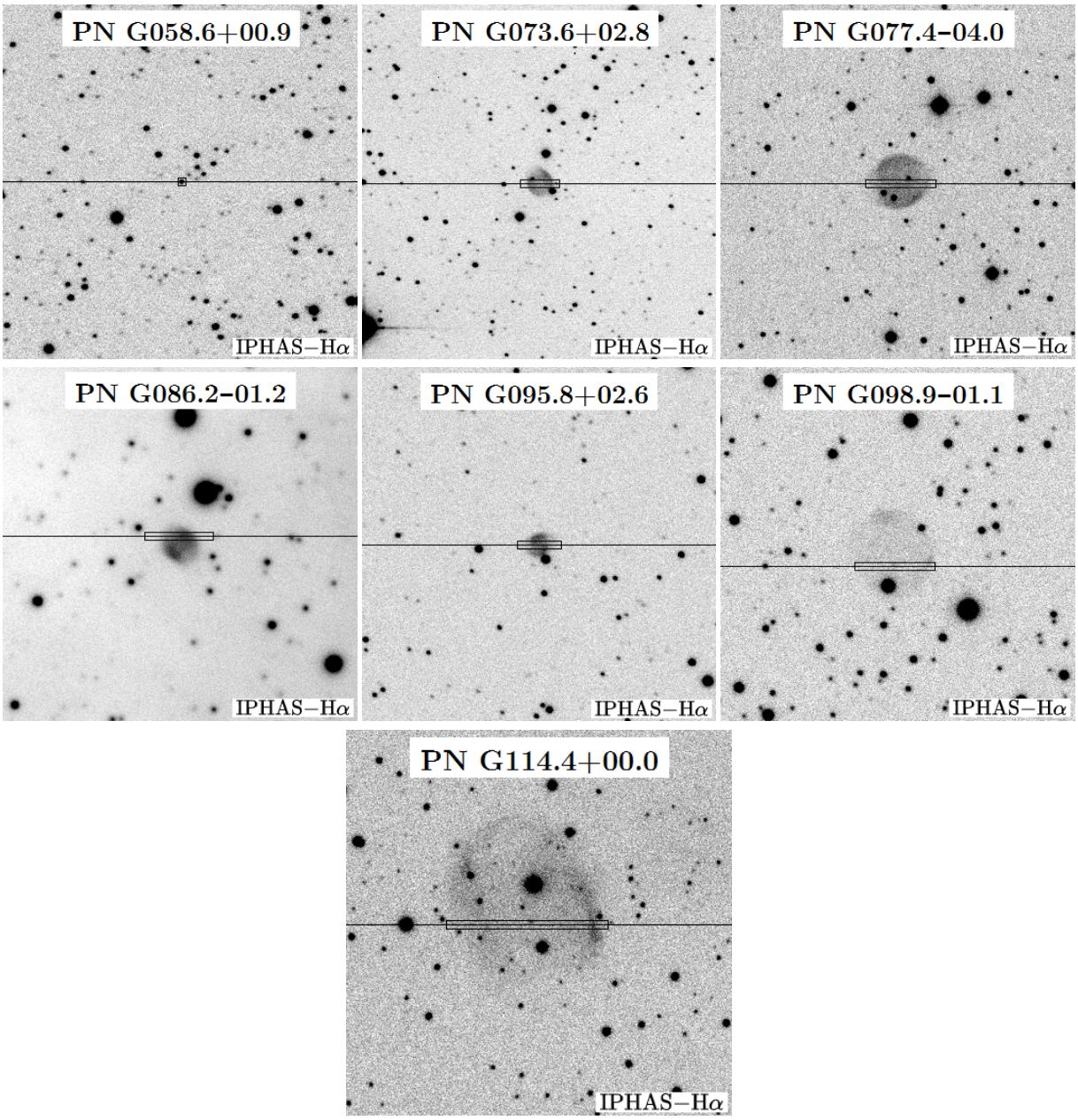

Figure 4. (Continued).

B. SPECTRA OF THE REMAINING 14 OBJECTS

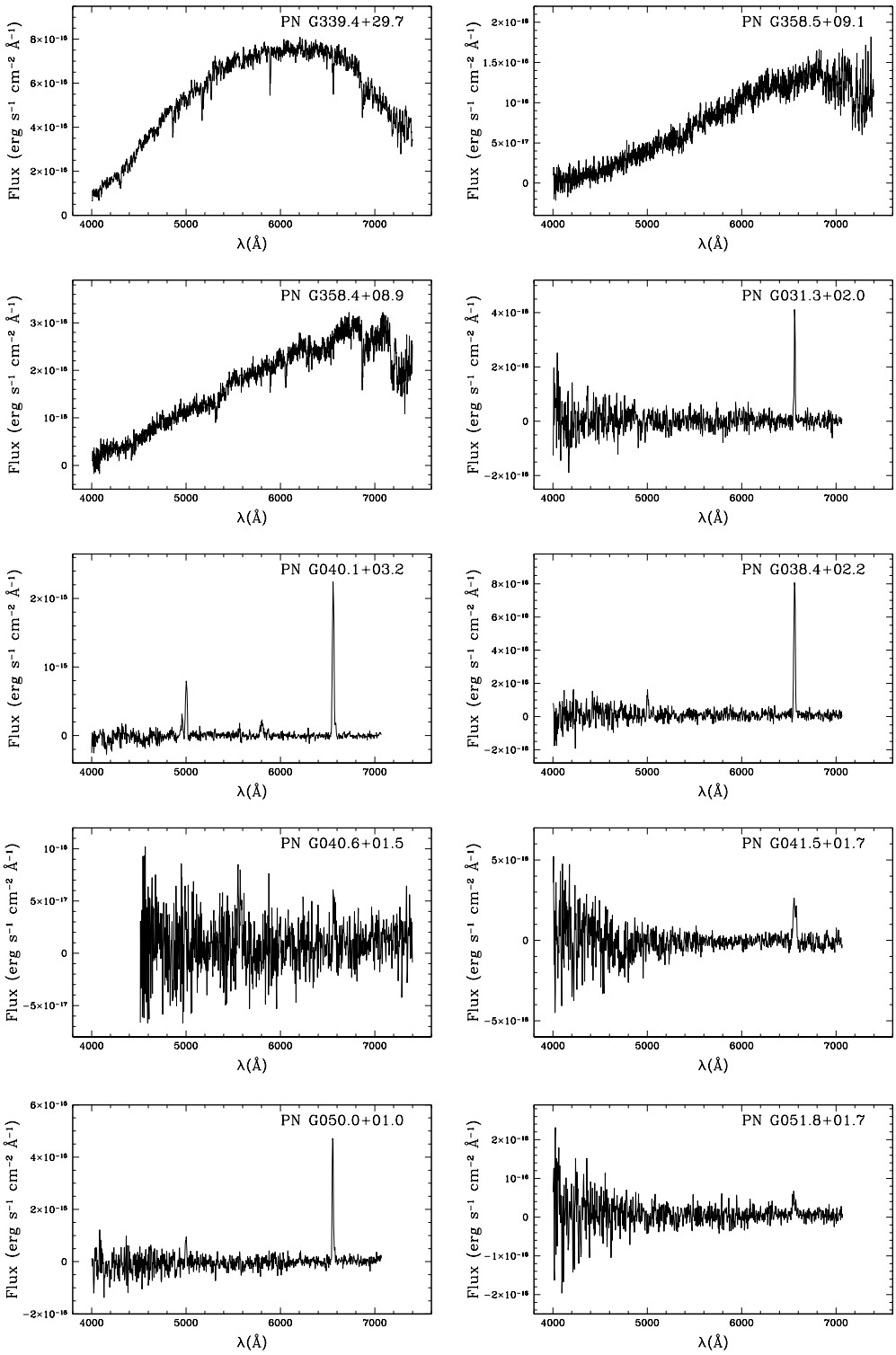

Figure 5. Spectra of 14 objects with a few or no emission lines.

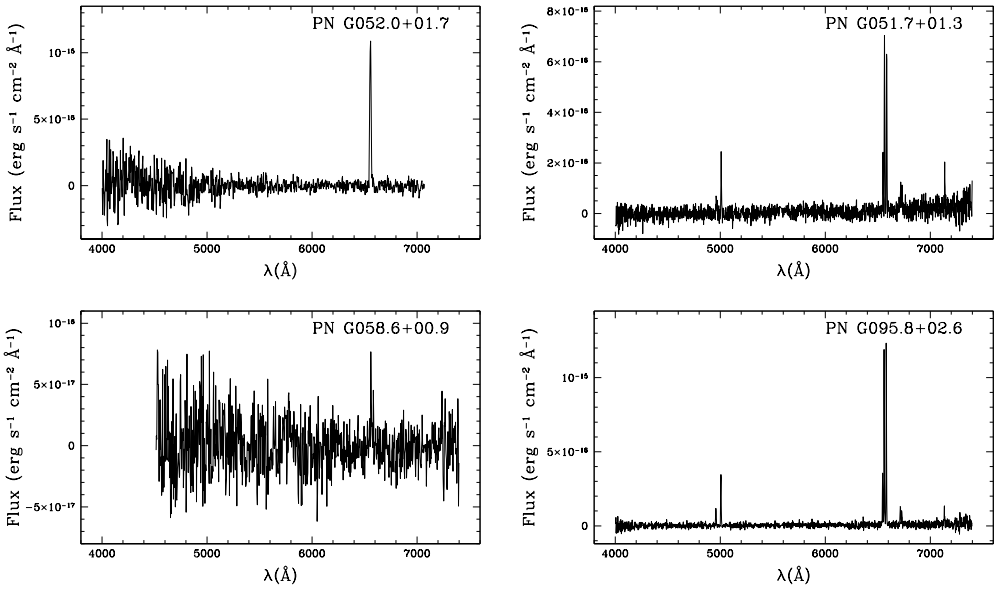

Figure 5. (Continued).

C. ADDITIONAL LITERATURE INFORMATION

There are different collective works in the literature that involve some of the objects in our sample on topics that are not related to our research. The objects and papers in which they appear are listed in Table 9.

Table 9. Collective works[a] that includes objects in our sample

Name	1	2	3	4	5	6	7	8	9	10	11
PN G003.3+66.1	...	...	...	✓	...	✓	...	...	...	✓	✓
PN G006.5+08.7	...	...	...	✓	...	...	...	...	✓	...	✓
PN G008.3+09.6	...	...	✓	...	...	...	...	...	✓	...	✓
PN G031.3+02.0	...	...	...	...	...	...	...	...	...	...	✓
PN G030.5+01.5	...	...	...	...	...	...	...	...	...	...	✓
PN G040.1+03.2	...	...	...	...	...	...	...	...	...	✓	✓
PN G038.4+02.2	...	...	...	...	...	...	...	...	...	✓	...
PN G040.6+01.5	...	...	...	...	...	...	...	...	...	✓	...
PN G041.5+01.7	✓	...	...	...	...	...	...	...	...	✓	...
PN G047.8+02.4	...	...	...	...	...	...	...	...	...	...	✓
PN G050.0+01.0	...	...	...	...	...	...	...	✓	...	...	✓
PN G052.0+01.7	✓	...	...	...	...	...	...	...	...	...	✓
PN G051.7+01.3	...	...	...	...	✓	...	...	...	...	✓	...
PN G057.9+01.7	✓	✓	...	...	...	...	...	...	...	✓	✓
PN G058.6+00.9	✓	...	...	...	...	...	...	✓	...	...	✓
PN G073.6+02.8	...	...	...	...	...	...	...	...	...	...	✓
PN G077.4−04.0	...	...	...	...	...	...	...	...	...	...	✓
PN G086.2−01.2	...	...	...	...	...	...	...	...	...	...	✓
PN G095.8+02.6	...	...	...	...	...	...	✓	...	...	...	...
PN G114.4+00.0	...	...	...	...	...	...	...	...	...	...	✓

[a] 1 (Condon et al., 1999) and 3 (Bojičić et al., 2011) reported flux density at 1.4 GHz. 2 Stanghellini et al. (2008) and 6 (Frew et al., 2016) created a catalog of statistical distances. 4 (Frew et al., 2013) made a catalog of integrated Hα fluxes. 5 (Froebrich et al., 2015) have identified extended H_2 features. 7 (Ramos-Larios et al., 2017) found that the spatial distribution of H_2 confirms its bipolar morphology. 8 (Irabor et al., 2018) reported flux at 5 GHz and brightness temperature. 9 (Jacoby et al., 2021) reported a study of the possible light curve variability on their CSs. 10 (Hajduk et al., 2021) made radio observations to find evidence of cold plasma component coexisting with hot plasma, but the objects were undetected by the experiment. 11 (Gómez-Muñoz et al., 2023) created an UV and optical catalog.

Some individual notes for other objects are:

PN G003.3+66.1 (SkAc 1): Its central star is very well studied by several authors, such as Kepler et al. (2016) showing the spectra of the white dwarf, Weidmann et al. (2020) indicating its spectral classification and Gentile Fusillo et al. (2021) listing stellar properties. Also, Douchin et al. (2015) present an image using [O III] λ5007 filter. Although it does not appear in the diagnostic diagram presented in Figure 2, Makarov et al. (2003) classified this object as a probable PN due to its low heliocentric radial velocity ($-17 \pm 2\,\mathrm{km\,s^{-1}}$).

PN G339.4+29.7 (PN Y−C 2−17): This object was discovered originally by Cesco & Gibson (1973) and it was described as a PN using only morphological features on a photographic plate; eventually, was cataloged as a Possible PN in Kohoutek (2001) and no other studies have been conducted to date. The HASH status was Not PN, whereas the SIMBAD status was PN candidate. We did not find any emission lines in our spectrum, but we identified the object as an evolved star of spectral type K3I-II.

PN G358.5+09.1 (Terz N 26, LEDA 89007): Discovered by Terzan (1985), who described it as a PN-like diffuse object from a set of R and B plates. Although Kohoutek (2001) cataloged it as Possible PN, some studies in the literature for the last 20 years consider this object a galaxy, e.g., Paturel et al. (2003) identified it as an elliptical galaxy, Tempel et al. (2016) reported a photometric redshift of 0.037633 ± 0.000167, and a distance of 165.254 Mpc. HASH status is possible galaxy, SIMBAD status is PN candidate, and NED status is galaxy. Our spectrum showed no emission lines or apparent absorption features. Therefore, it is not possible to draw a more definitive conclusion from this study.

PN G358.4+08.9 (Terz N 29, LEDA 89010): Terzan (1985) described it as a red star surrounded by nebulosity, as it appeared in R and B plates. There are few studies in the literature, but Hasegawa et al. (2000) identified this object as a type E galaxy and reported a redshift of 0.027786 ± 0.000167. Nevertheless, Kohoutek (2001) cataloged it as a Possible PN. HASH status is a possible galaxy, SIMBAD status is PN candidate, and NED status is Galaxy. We did not find emission lines in our spectrum, but several absorption features corresponding to the G-band, Mgb, NaD, and Hα typical of elliptical galaxies. We derived a redshift of $z = 0.0279$ which is in complete agreement with the previously reported value (Hasegawa et al., 2000).

PN G058.6+00.9 (PN PM 1−309, IRAS 19353+2302): Preite-Martinez (1988) proposed this object as a possible PN based on the far-IR colors of the source and reported density fluxes at 12, 25, 60, and 100 μm. He calculated the dust temperature, assuming that is the unique source observed and estimated the heliocentric distance (5.1 kpc).

References

Acker, A., Boffin, H. M. J., Outters, N., et al. 2012, RMxAA, 48, 223, doi: 10.48550/arXiv.1206.2477

Acker, A., Marcout, J., Ochsenbein, F., et al. 1992, The Strasbourg-ESO Catalogue of Galactic Planetary Nebulae. Parts I, II.

Akras, S., & Gonçalves, D. R. 2016, MNRAS, 455, 930, doi: 10.1093/mnras/stv2139

Ali, A., & Dopita, M. A. 2017, PASA, 34, e036, doi: 10.1017/pasa.2017.30

Ali, A., Dopita, M. A., Basurah, H. M., et al. 2016, MNRAS, 462, 1393, doi: 10.1093/mnras/stw1744

Asplund, M., Amarsi, A. M., & Grevesse, N. 2021, A&A, 653, A141, doi: 10.1051/0004-6361/202140445

Bailer-Jones, C. A. L., Rybizki, J., Fouesneau, M., Demleitner, M., & Andrae, R. 2021, AJ, 161, 147, doi: 10.3847/1538-3881/abd806

Bojičić, I. S., Parker, Q. A., Filipović, M. D., & Frew, D. J. 2011, MNRAS, 412, 223, doi: 10.1111/j.1365-2966.2010.17900.x

Bojičić, I. S., Parker, Q. A., & Frew, D. J. 2017, in IAUS, Vol. 323, Planetary Nebulae: Multi-Wavelength Probes of Stellar and Galactic Evolution, 327–328, doi: 10.1017/S1743921317003234

Boumis, P., Akras, S., Xilouris, E. M., et al. 2006, MNRAS, 367, 1551, doi: 10.1111/j.1365-2966.2006.10048.x

Cardelli, J. A., Clayton, G. C., & Mathis, J. S. 1989, ApJ, 345, 245, doi: 10.1086/167900

Cesco, C. U., & Gibson, J. 1973, A&AS, 11, 335

Chornay, N., & Walton, N. A. 2021, A&A, 656, A110, doi: 10.1051/0004-6361/202142008

Condon, J. J., Kaplan, D. L., & Terzian, Y. 1999, ApJS, 123, 219, doi: 10.1086/313236

DePew, K., Parker, Q. A., Miszalski, B., et al. 2011, MNRAS, 414, 2812, doi: 10.1111/j.1365-2966.2011.18337.x

Douchin, D., De Marco, O., Frew, D. J., et al. 2015, MNRAS, 448, 3132, doi: 10.1093/mnras/stu2700

Drew, J. E., Greimel, R., Irwin, M. J., et al. 2005, MNRAS, 362, 753, doi: 10.1111/j.1365-2966.2005.09330.x

Ferrero, L., Le Du, P., Mulato, L., Outters, N., & Zoll, S. 2015, LAstr, 129, 42

Frew, D. J., Bojičić, I. S., & Parker, Q. A. 2013, MNRAS, 431, 2, doi: 10.1093/mnras/sts393

Frew, D. J., & Parker, Q. A. 2010, PASA, 27, 129, doi: 10.1071/AS09040

Frew, D. J., Parker, Q. A., & Bojičić, I. S. 2016, MNRAS, 455, 1459, doi: 10.1093/mnras/stv1516

Froebrich, D., Makin, S. V., Davis, C. J., et al. 2015, MNRAS, 454, 2586, doi: 10.1093/mnras/stv1729

Gaia Collaboration, Vallenari, A., Brown, A. G. A., et al. 2023, A&A, 674, A1, doi: 10.1051/0004-6361/202243940

Gentile Fusillo, N. P., Tremblay, P. E., Cukanovaite, E., et al. 2021, MNRAS, 508, 3877, doi: 10.1093/mnras/stab2672

Gómez-Muñoz, M. A., Bianchi, L., & Manchado, A. 2023, ApJS, 266, 34, doi: 10.3847/1538-4365/acca77

González-Santamaría, I., Manteiga, M., Manchado, A., et al. 2021, A&A, 656, A51, doi: 10.1051/0004-6361/202141916

Hajduk, M., Haverkorn, M., Shimwell, T., et al. 2021, ApJ, 919, 121, doi: 10.3847/1538-4357/ac0fda

Hambly, N. C., MacGillivray, H. T., Read, M. A., et al. 2001, MNRAS, 326, 1279, doi: 10.1111/j.1365-2966.2001.04660.x

Hasegawa, T., Wakamatsu, K.-i., Malkan, M., et al. 2000, MNRAS, 316, 326, doi: 10.1046/j.1365-8711.2000.03531.x

Henry, R. B. C., Kwitter, K. B., Jaskot, A. E., et al. 2010, ApJ, 724, 748, doi: 10.1088/0004-637X/724/1/748

Henry, R. B. C., Speck, A., Karakas, A. I., Ferland, G. J., & Maguire, M. 2012, ApJ, 749, 61, doi: 10.1088/0004-637X/749/1/61

Hsia, C.-H., & Zhang, Y. 2014, A&A, 563, A63, doi: 10.1051/0004-6361/201322500

Irabor, T., Hoare, M. G., Oudmaijer, R. D., et al. 2018, MNRAS, 480, 2423, doi: 10.1093/mnras/sty1929

Jacoby, G. H., Hillwig, T. C., Jones, D., et al. 2021, MNRAS, 506, 5223, doi: 10.1093/mnras/stab2045

Kaler, J. B., & Jacoby, G. H. 1989, ApJ, 345, 871, doi: 10.1086/167957

Kepler, S. O., Pelisoli, I., Koester, D., et al. 2016, MNRAS, 455, 3413, doi: 10.1093/mnras/stv2526

Khushbu, K., & Muthumariappan, C. 2024, AdSpR, 74, 1366, doi: 10.1016/j.asr.2024.04.058

Kingsburgh, R. L., & Barlow, M. J. 1994, MNRAS, 271, 257, doi: 10.1093/mnras/271.2.257

Kohoutek, L. 2001, A&A, 378, 843, doi: 10.1051/0004-6361:20011162

Kwitter, K. B., & Henry, R. B. C. 2022, PASP, 134, 022001, doi: 10.1088/1538-3873/ac32b1

Kwok, S. 2000, The Origin and Evolution of Planetary Nebulae

Le Dû, P., Mulato, L., Parker, Q. A., et al. 2022, A&A, 666, A152, doi: 10.1051/0004-6361/202243393

Maciel, W. J., Costa, R. D. D., & Idiart, T. E. P. 2010, A&A, 512, A19, doi: 10.1051/0004-6361/200912499

Makarov, D. I., Karachentsev, I. D., & Burenkov, A. N. 2003, A&A, 405, 951, doi: 10.1051/0004-6361:20030706

Mari, M. B., Akras, S., & Gonçalves, D. R. 2023, MNRAS, 525, 1998, doi: 10.1093/mnras/stad2256

Miszalski, B., Parker, Q. A., Acker, A., et al. 2008, MNRAS, 384, 525, doi: 10.1111/j.1365-2966.2007.12727.x

Moe, M., & De Marco, O. 2006, ApJ, 650, 916, doi: 10.1086/506900

Olguín, L., Vázquez, R., Contreras, M. E., & Jiménez, M. Y. 2011, in RMxAC, Vol. 40, RMxAC, 193

Osterbrock, D. E., & Ferland, G. J. 2006, Astrophysics of gaseous nebulae and active galactic nuclei

Parker, Q. A. 2022, Frontiers in Astronomy and Space Sciences, 9, 895287, doi: 10.3389/fspas.2022.895287

Parker, Q. A., Bojičić, I. S., & Frew, D. J. 2016, in JPhCS, Vol. 728, JPhCS (IOP), 032008, doi: 10.1088/1742-6596/728/3/032008

Parker, Q. A., Phillipps, S., Pierce, M. J., et al. 2005, MNRAS,

362, 689, doi: 10.1111/j.1365-2966.2005.09350.x
Parker, Q. A., Acker, A., Frew, D. J., et al. 2006, MNRAS, 373, 79, doi: 10.1111/j.1365-2966.2006.10950.x
Paturel, G., Petit, C., Prugniel, P., et al. 2003, A&A, 412, 45, doi: 10.1051/0004-6361:20031411
Peimbert, M., & Torres-Peimbert, S. 1983, in IAUS, Vol. 103, Planetary Nebulae, ed. L. H. Aller, 233–242
Preite-Martinez, A. 1988, A&AS, 76, 317
Quireza, C., Rocha-Pinto, H. J., & Maciel, W. J. 2007, A&A, 475, 217, doi: 10.1051/0004-6361:20078087
Raga, A. C., Riera, A., Mellema, G., Esquivel, A., & Velázquez, P. F. 2008, A&A, 489, 1141, doi: 10.1051/0004-6361:20079157
Ramos-Larios, G., Guerrero, M. A., Sabin, L., & Santamaría, E. 2017, MNRAS, 470, 3707, doi: 10.1093/mnras/stx1519
Randall, S. K., Trejo, A., Humphreys, E. M. L., et al. 2020, A&A, 636, A123, doi: 10.1051/0004-6361/201935787
Reid, W. A., & Parker, Q. A. 2010, PASA, 27, 187, doi: 10.1071/AS09055
Ritter, A., Parker, Q. A., Sabin, L., et al. 2023, MNRAS, 520, 773, doi: 10.1093/mnras/stac2896
Robertson, T. H., & Jordan, T. M. 1989, AJ, 98, 1354, doi: 10.1086/115219
Sabin, L., Parker, Q. A., Corradi, R. L. M., et al. 2014, MNRAS, 443, 3388, doi: 10.1093/mnras/stu1404
Sabin, L., Guerrero, M. A., Ramos-Larios, G., et al. 2021, MNRAS, 508, 1599, doi: 10.1093/mnras/stab2477
Shaw, R. A., & Dufour, R. J. 1995, PASP, 107, 896, doi: 10.1086/133637
Stanghellini, L., Guerrero, M. A., Cunha, K., Manchado, A., & Villaver, E. 2006, ApJ, 651, 898, doi: 10.1086/507840
Stanghellini, L., Shaw, R. A., & Villaver, E. 2008, ApJ, 689, 194, doi: 10.1086/592395
Tan, S., Parker, Q. A., Zijlstra, A. A., & Rees, B. 2024, MNRAS, 527, 6363, doi: 10.1093/mnras/stad3496
Temiz, U., Aksaker, N., & Akyuz, A. 2024, MNRAS, 527, 1481, doi: 10.1093/mnras/stad2863
Tempel, E., Kipper, R., Tamm, A., et al. 2016, A&A, 588, A14, doi: 10.1051/0004-6361/201527755
Terzan, A. 1985, The Messenger, 42, 4
Ueta, T., Mito, H., Otsuka, M., et al. 2019, AJ, 158, 145, doi: 10.3847/1538-3881/ab328f
Urquhart, J. S., Hoare, M. G., Purcell, C. R., et al. 2009, A&A, 501, 539, doi: 10.1051/0004-6361/200912108
van de Steene, G. C., Jacoby, G. H., & Pottasch, S. R. 1996, A&AS, 118, 243
Viironen, K., Mampaso, A., Corradi, R. L. M., et al. 2009, A&A, 502, 113, doi: 10.1051/0004-6361/200811575
Weidmann, W. A., Mari, M. B., Schmidt, E. O., et al. 2020, A&A, 640, A10, doi: 10.1051/0004-6361/202037998
York, D. G., Adelman, J., Anderson, Jr., J. E., et al. 2000, AJ, 120, 1579, doi: 10.1086/301513

Revista Mexicana de Astronomía y Astrofísica, 61, 71-75, (2025)

OPEN ACCESS https://doi.org/10.22201/ia.01851101p.2025.61.02.06

Espartaco 2, a New Stellar Spectrograph at Universidad de los Andes

B. Oostra[1] **and M. G. Batista**[1]

[1]*Universidad de los Andes, Departamento de Física, Carrera 1 #18a - 12, 111711, Bogotá, Colombia.*

Keywords: *astronomical instrumentation, stars: radial velocity, stars: spectroscopy, astronomy education*

Abstract

We present the construction and early results of ESPARTACO 2, a new stellar spectrograph built for research and education at the Astronomical Observatory of the Universidad de los Andes in Bogotá, Colombia. This instrument offers several resolution modes, from 20,000 in the first order using a 50 μm fiber, to 100,000 in the second order in the near-infrared. Precise radial-velocity measurements were made possible by simultaneous wavelength calibration. Combined with the 40-cm Meade telescope located at our facilities, a limiting magnitude of 6 was achieved. This instrument represents a significant improvement over its predecessor in terms of throughput, reliability, and ease of use.

Resumen

Presentamos la construcción y los primeros resultados de ESPARTACO 2, el nuevo espectrógrafo estelar que fue construido con fines educativos y de investigación en el Observatorio Astronómico de la Universidad de los Andes en Bogotá, Colombia. Este instrumento tiene la capacidad de ofrecer varias resoluciones, desde 20,000 cuando se usa la fibra de 50 μm en primer orden, hasta 100,000 en el segundo orden en el infrarrojo cercano. Es posible realizar medidas precisas de velocidad radial estelar mediante la calibración simultánea en longitud de onda. Al combinarse con el telescopio Meade de 40 cm localizado en nuestras instalaciones, se logra estudiar objetos hasta magnitud de 6. Este instrumento representa una mejora respecto a su antecesor en cuanto a su eficiencia lumínica, fiabilidad y facilidad de uso.

Corresponding author: B. Oostra *E-mail address:* boostra@uniandes.edu.co
Received: April 29, 2024 **Accepted:** April 21, 2025

1. Introduction

Our campus observatory arose from the need to make observations that could complement theoretical astronomy courses. Our location near Bogotá's city center has some drawbacks, such as light pollution, severe seeing, and highly variable weather, but the advantage is that we can seize the opportunity when the conditions are good.

In this urban environment, high-resolution spectroscopy of the sun and bright stars is more promising than any other astronomical technique and has proven to be a fruitful endeavor (Oostra, 2012, 2017; Oostra & Batista, 2024) through 15 years of work with *ESPARTACO, Espectrógrafo de Alta Resolución para Trabajos Astronómicos en Colombia* (Oostra & Ramírez, 2011). This instrument is a high-resolution, low-cost spectrograph designed for undergraduate research projects. Pursuing this path, half a dozen spectrographs have been built and used at our observatory over the past three decades.

Despite achieving all the goals, ESPARTACO has several issues. It was built in 2007 with a non-optimal design using parts that were available at the time; the mismatch between these components produced a very low throughput. Moreover, wavelength calibration spectra must be taken before or after the science spectra, mechanical stability is deficient, and proper focusing is challenging.

Despite its difficulties, ESPARTACO has provided valuable experience in astronomical studies and atomic physics laboratory work. This justified some investment in more optimized optical components, prompting the construction of a new instrument, which began in 2018 and was completed in 2023. Building instruments locally is a way to reduce costs, but it also provides experience in astronomical instrumentation design. In § 2, we provide a technical description of the instrument. In § 3, we present the results of the quality tests. Finally, in § 4 we list our conclusions.

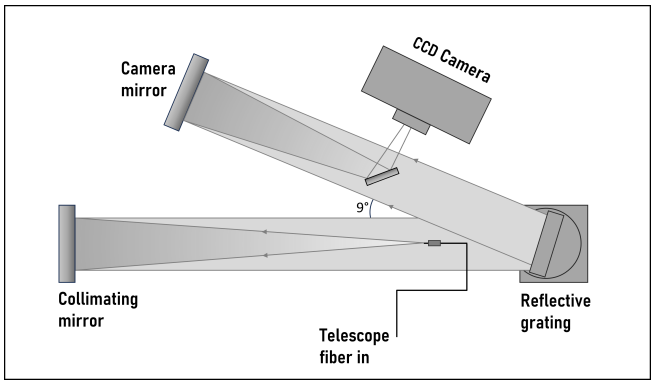

Figure 1. Optical layout of ESPARTACO 2. The angle between the collimator and camera is 9°. The only moving parts are the grating, which can rotate 360°, and the fiber support.

2. Description of the instrument

2.1. Optical layout

ESPARTACO 2 is a Czerny-Turner spectrograph with on-axis parabolic mirrors of 15 cm diameter. The grating is 14 cm wide and 12 cm high, with a density of 1200 grooves/mm and no blaze. The lengths of the collimator and camera mirror were 120 cm (F/8) and 76 cm (F/5), respectively. The instrument can be used in the first and second diffraction orders, as shown in Figure 1.

2.2. Fibers

The instrument is fed via four optical fibers of circular cross-section: three of 50 μm diameter and one of 10 μm. At the collimator end of these fibers, their tips were polished without ferrules to minimize the spacing between them. Their plastic sleeves kept the cores 0.9 mm apart, which placed the images in the camera at a vertical spacing of 63 pixels. The exit beam of these fibers was wider than that of the F/8 collimator, resulting in luminosity loss. The multiplicity of fibers makes it possible to simultaneously register the calibration spectrum on the same image as the stellar spectrum; this is necessary for precise measurements of radial velocities and was not possible with the previous spectrograph. For stellar observations, one 50 μm fiber carries the light from the star, another carries the light from a Th-Ar hollow-cathode lamp, and a third may be coupled to a neon lamp for eventual fast position or focus checks. A small horizontal offset exists between any pair of fibers, which must be measured empirically. The star fiber is coupled to the telescope via an interface from Shelyak Instruments[1].

[1]In order to reduce the size of the stellar image in the telescope's focal plane, and thus maximize the amount of light though the optical fiber, we connect to the telescope a Meade Electronic Micro-Focuser, Meade series 4000 f/6.3 focal reducer and the Shelyak FIGU (Fiber Injection and Guiding Unit) to inject the starlight into an optical fiber and a guiding camera.

2.3. Camera

The camera is a Kodak KAF1603ME CCD array of 1530×1020 pixels measuring 9 μm square. It is commonly operated at -15°C. Downloading images using a USB cable takes only a few seconds. The technical specifications are as follows:

- Full well = 100,000 electrons, converted to 65535 ADU, give a gain of 1.52 e/ADU
- Read-out noise: 10.5 ADU (RMS) = 16 electrons.
- Dark current (reported): 1 electron per pixel per second at 0°C
- Dark current (measured): 1 electron per pixel per minute at -15°C
- Quantum Efficiency: 75% at H-α, 50% at H-β.
- Sensivity range: 400 - 800 nm.

2.4. Structure

The optical components are mounted in a rigid 165×45×35 cm steel frame made of a 50-mm-wide steel angle covered with black acrylic panes. The only moving parts are the grating's support, which can rotate 360°, and the fiber support which can travel 2 cm for focusing. Both devices are driven by small stepper motors that are controlled manually. The angular position of the grating is monitored using a webcam. The stepper motors and controlling webcam are important improvements over the previous version of ESPARTACO 1 (Oostra & Ramírez, 2011).

2.5. Thermal instability

A major problem is the lack of a thermally stabilized room for the spectrographs. The instrument is located in the small dome building where the temperature may change from below 10°C at 3:00 a.m. to more than 20°C at 3:00 p.m. This necessitates an adjustment of the focus. However, extreme refocusing degrades the spectral line profile; therefore, we attempted to mitigate thermal changes using insulation (20 mm Ethafoam) and a low-power internal heating system.

3. Results

3.1. Resolution

To assess the resolution of the spectrograph, we performed a series of linewidth measurements on carefully focused spectra of our Th-Ar lamp. We used only thorium lines because they are perceptibly narrower than argon lines, possibly because of the greater atomic mass, which reduces Doppler broadening.

The measurements were made using the same 50 μm fibre that is commonly employed for stars.

For each profile, we adjusted a Gaussian fit to four or five central data points. The reported line widths are the FWHM of these fits. Each selected Th line was measured in the first and second orders.

Figures 2, 3, and 4 show the theoretical and measured line widths, theoretical dispersion, and theoretical and

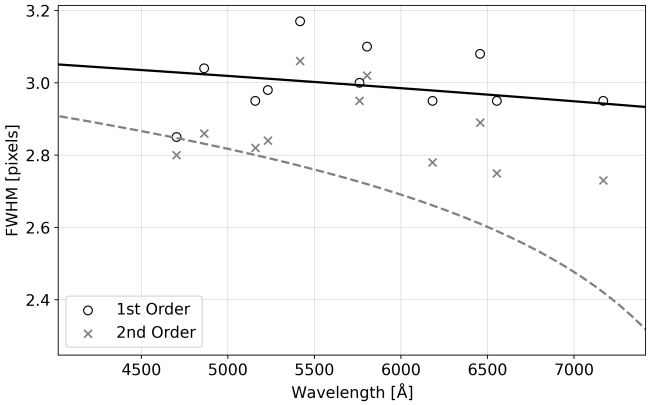

Figure 2. Measured widths of Th emission lines. The circles and crosses represent the first- and second-order measurements, respectively. Theoretical line widths are shown with solid line for the first order and dashed for second order.

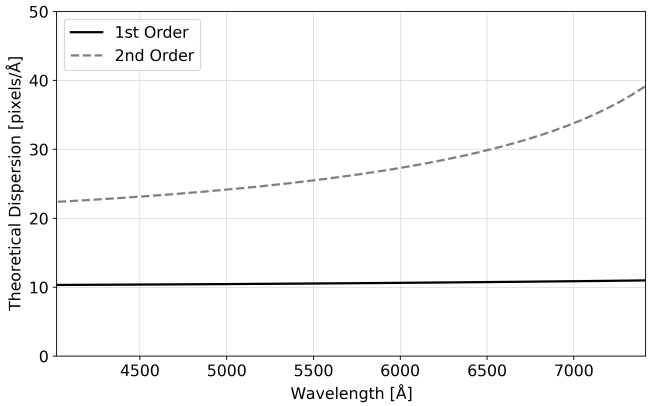

Figure 3. Theoretical dispersion of the spectrograph. The solid and dashed lines represent the first and second orders, respectively. Observed values are found to agree with the theory.

measured resolutions, respectively. For the calculations, we included only geometrical optics, no diffraction, and instead of a circular input, we assumed a rectangular entrance slit of 45 μm. As can be seen, stars must be observed at a resolution of 20.000 in the first order, which is considerably less than the 31.000 given by our previous spectrograph.

Through the narrow 10 μm fibre we took some images of the particularly strong Th 5761 line. In the first order, a width of 2.03 pixels can be readily measured, suggesting that this fiber enhances the resolution by approximately 50% for bright emission lines in the first order. In the second order, the focusing is very ambiguous and the results are unclear. In several images, it was possible to fit a Gaussian to the three central points and obtain a width of 1.8 or 1.9 pixels; however, a large amount of light was scattered outside this peak. This indicates that the diffraction effects are not negligible. A line width below the Nyquist limit of 2 pixels is not useful.

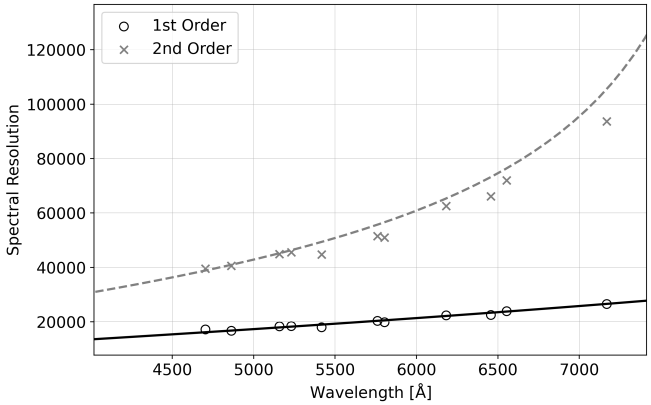

Figure 4. Spectral resolution computed from dispersion and line width. Conventions as before.

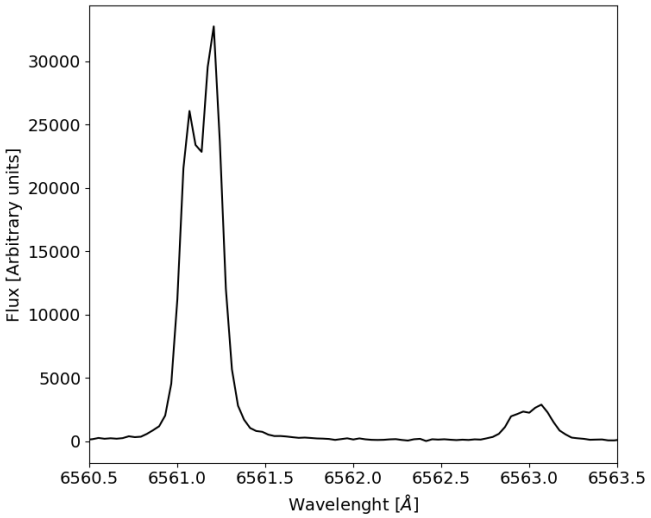

Figure 5. Spectrum of deuterium-α and its fine structure, obtained with 20 seconds of exposure using the 10 μm fiber in the second order (left). A trace of normal hydrogen, which was present in the deuterium tube, produced a small emission line on the right side. The isotopic shift constitutes regular assignments for students. For this experiment, deuterium is better than normal hydrogen because it has less thermal broadening.

The light transmitted by the 10-μm fiber is very weak, and the exposure times are prohibitively long. In contrast, continuous spectra through this fiber are modulated by intermodal interference (Hlubina, 1999; Baudrand & Walker, 2001; Lemke et al., 2011). Nevertheless, laboratory spectra are useful for studying the Zeeman effect and fine structure of deuterium (Figure 5).

3.2. Throughput and limiting magnitude around H-alpha

The main improvement of ESPARTACO 2 over our previous spectrograph is the gain in luminosity, which was also the main reason for constructing the new instrument. The new spectrograph has 14 times greater optical throughput than its forerunner, as measured by aperture photometry of neon

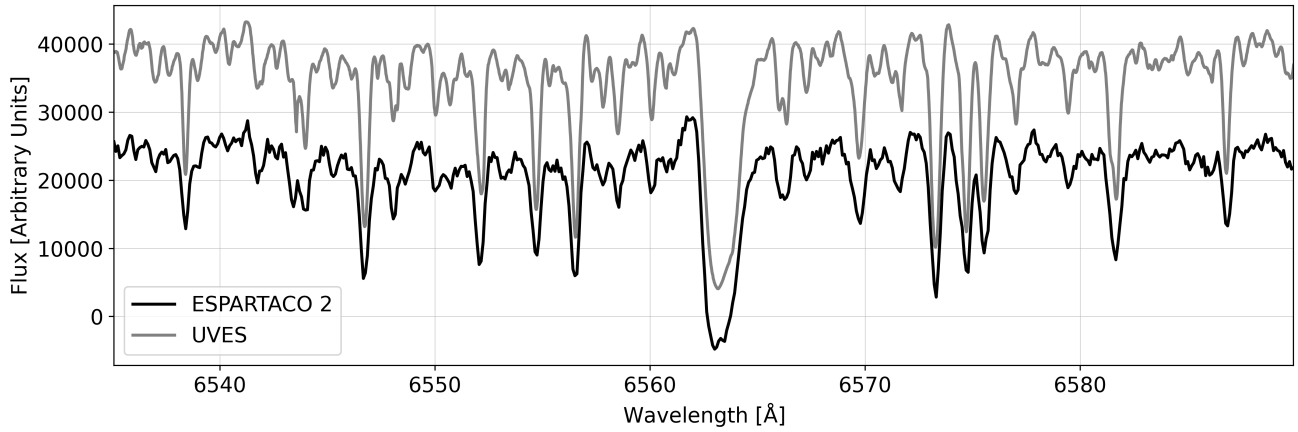

Figure 6. Spectrum of HD49331 obtained with ESPARTACO 2 (black line); for comparison, the same spectrum from UVES (grey line), at resolution 80000; (Bagnulo et al., 2003).

spectra. This represents a progress of almost three stellar magnitudes and is mainly due to the size of the new grating, 120 × 140 mm, compared with the old grating's 50 × 50 mm.

The limiting magnitude depends on the stellar spectral type and observed wavelength range. If we define the limit by an S/N ratio of 10 and an exposure time of 20 min on our 40-cm telescope, the limiting V magnitude is approximately 5 for early type stars and 6 for late-type stars observed at H-alpha in first order. As an example, Figure 6 shows the spectrum of HD49331, a red supergiant of magnitude V = 5.1, obtained with a 20-minute exposure and giving a signal-to-noise ratio of 38.

Figure 6 compares our spectrum of HD49331 with a spectrum of the same star recorded at a resolution of 80.000 by the UVES spectrograph and published under the Paranal Observatory Project (Bagnulo et al., 2003). The comparison shows that the main features are clearly legible in our data, and many smaller features are missing because of the lower resolution and signal strength.

In addition to the Sun, we can study some bright stars in the second order. Figure 7 shows the second-order spectrum of Betelgeuse obtained in a 10-minute exposure. In this configuration, the higher resolution allowed some line width measurements, and the results are shown in Table 1. The most conspicuous feature is that stellar lines are broader than telluric lines because of the turbulence and rotation of the star. This distinction is not visible in Figure 6, partly due to the lower resolution at first order and because HD 49331 is less turbulent.

Second-order spectra have the disadvantage that they span a range of only 50 Å, whereas first-order spectra cover 140 Å. Moreover, the exposure times must be long, and the limiting magnitude is approximately 1. This option is particularly useful for solar and laboratory studies.

3.3. Budget

All optical components were purchased from the market. The 15-cm mirrors and supports were obtained from Edmund Optics, as well as the diagonal mirror. Both motor stages were obtained from Optimal Engineering Systems Inc. (OES). The grating was obtained from Horiba Jobin-Yvon. The camera was obtained from SBIG (taken over by Diffraction Limited). The prices of these components add up to approximately 17000 USD.

The structural frame, mounting for the diagonal mirror, and other parts were built at our Physics Department Mechanics Laboratory. Optical fibers and other hardware were purchased at a low cost from local markets. We believe that the overall cost/benefit ratio is reasonable, considering that our environmental conditions do not justify the use of expensive equipment for monitoring.

Table 1. Prominent absorption lines in the Betelgeuse spectrum

#	λ obs [Å]	Species	Width [Å]	λ rest [Å]	RV [km/s]
1	6543.91	H_2O	0.15	6543.907	0.14
2	6547.21	Fe+Ti	0.48	6546.253	43.86
3	6548.62	H_2O	0.18	6548.622	-0.09
4	6552.63	H_2O	0.22	6552.629	0.05
5	6555.16	Ti	0.52	6554.223	42.89
6	6557.03	Ti	0.57	6556.062	44.30
7	6570.20	Fe+Fe	0.65	6569.215	45.00
8	6572.08	H_2O	0.18	6572.086	-0.27
9	6573.71	Ca	0.65	6572.779	42.49

4. Final remarks

ESPARTACO 2 will be useful for research and teaching from high school to graduate level. This instrument has the capacity to offer several resolutions, depending on the order and diameter of the optical fiber used, has a greater luminous throughput, and the advantage of moving parts

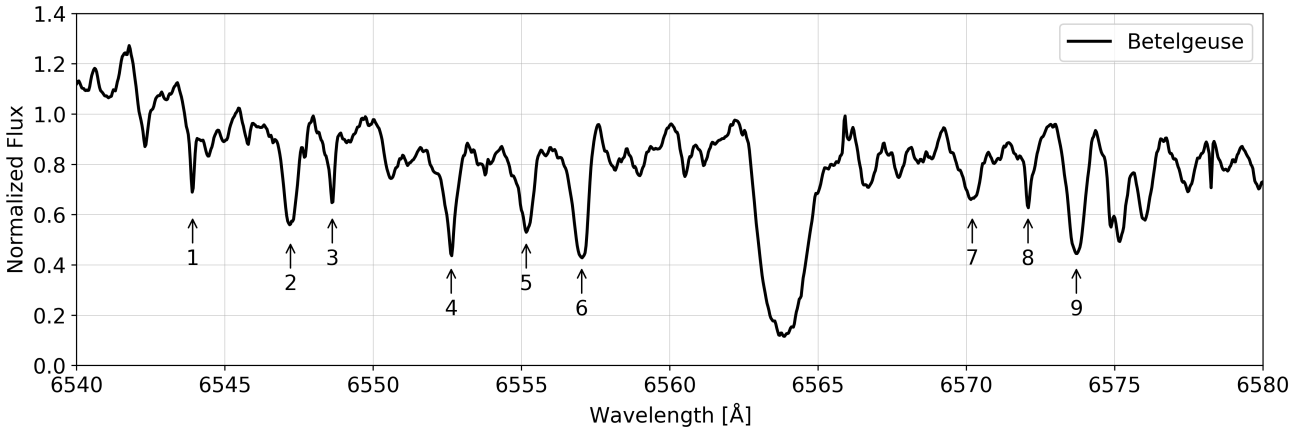

Figure 7. Spectrum of Betelgeuse obtained with ESPARTACO 2 in second order in a 10-minute exposure. Numbers 1–9 indicate the selected absorption lines discussed in the text (Table 1). In particular, lines 1, 3, 4 and 8 are telluric H_2O lines, and are evidently narrower than the stellar lines; this distinction is not visible in the first-order spectrum shown in Figure 6.

with stepper motors, delivering considerable improvements over its predecessor. However, eventual refinements and reforms may be implemented in the future to address these issues.

- Add another 50 μm fiber with a micro-lens in order to couple the fiber optimally to the collimator aperture. This would increase the limiting magnitude, albeit at lower spectral resolutions.
- Install a chiller for water-cooling the camera.
- Couple the focus motor and heating system to a thermostat.
- Implement digital encoders for the position of the grating and the focus motor.
- Replace the mirrors by off-axis paraboloids, which would eliminate the diagonal mirror and place the fibers outside the collimator beam, enhancing the image quality and luminosity.

References

Bagnulo, S., Jehin, E., Ledoux, C., et al. 2003, Msngr, 114, 10

Baudrand, J., & Walker, G. A. 2001, PASP, 113, 851, doi: 10.1086/322143

Hlubina, P. 1999, JMOp, 46, 1595, doi: 10.1080/09500349908231358

Lemke, U., Corbett, J., Allington-Smith, J., & Murray, G. 2011, MNRAS, 417, 689, doi: 10.1111/j.1365-2966.2011.19312.x

Oostra, B. 2012, AmJPh, 80, 363, doi: 10.1119/1.3684841

—. 2017, AmJPh, 85, 295, doi: 10.1119/1.4975109

Oostra, B., & Batista, M. G. 2024, RMxAA, 60, 367, doi: 10.22201/ia.01851101p.2024.60.02.14

Oostra, B., & Ramírez, D. 2011, Revista Colombiana de Física, 43(2), 312

Revista Mexicana de Astronomía y Astrofísica, 61, 76-83, (2025)

OPEN ACCESS https://doi.org/10.22201/ia.01851101p.2025.61.02.07

Spectroscopic Study of Blue Straggler Stars in the Globular Cluster NGC 3201

Gourav Kumawat[1,2], **Arvind K. Dattatrey**[3] **and R. K. S. Yadav**[3]

[1]*Indian Institute of Science Education and Research, Bhopal, MP, India.*
[2]*University of Alberta, Edmonton, AB, Canada.*
[3]*Aryabhatta Research Institute of Observational Sciences, Nainital, UK, India.*

Keywords: *Blue Straggler Stars, Globular star clusters: NGC 3201, Spectroscopy*

Abstract

We conducted a spectroscopic study of 39 blue straggler stars in the globular cluster NGC 3201. The spectra of these stars have been previously reported. We determined the radial velocity, atmospheric parameters (T_{eff}, log g), Mg abundance, and metallicity ([Fe/H]) for all sources in the sample. The mean radial velocity and [Fe/H] were determined to be 498.0±5.3 km/s and -1.42±0.27, respectively. The derived [Fe/H] is consistent, within uncertainties, with the cluster's [Fe/H] of -1.59 dex. The mean [Mg/Fe] for the sample was estimated to be 0.36±0.73. Importantly, this study is the first to estimate [Mg/Fe] for blue straggler stars in the cluster NGC 3201.

Resumen

Realizamos un estudio espectroscópico de 39 estrellas tipo blue straggler pertenecientes al cúmulo globular NGC 3201. Los espectros de estas estrellas han sido reportados previamente en la literatura. Con ellos determinamos velocidades radiales, parámetros atmosféricos (T_{eff}, log g), la abundancia de Mg, y la metalicidad ([Fe/H]) para todas las estrellas en la muestra. Los valores promedio resultantes para la velocidad radial y la metalicidad son 498.0±5.3 km/s and -1.42±0.27 dex, respectivamente. El valor de la metalicidad es consistente con el valor de [Fe/H]=-1.59 dex previamente reportado para el cúmulo, dentro de las incertidumbres. El valor promedio de [Mg/Fe] para la muestra es de 0.36±0.73 dex. Es importante mencionar que esta es la primera estimación de [Mg/Fe] para estrellas tipo blue straggler en el cúmulo NGC 3201.

Corresponding author: Arvind K. Dattatrey *E-mail address:* physics.arvind97@gmail.com
Received: March 3, 2025 **Accepted:** May 22, 2025

1. Introduction

Globular clusters (GCs) are among the oldest stellar systems, consisting of thousands of stars located at the same distance from Earth and moving together in space. Owing to their high stellar densities, frequent gravitational interactions occur within them, leading to several dynamical processes that give rise to exotic stellar pairings, including Blue Straggler stars (BSSs).

BSSs are identified as stars positioned to the left and above the main-sequence turnoff (MSTO) in the optical color-magnitude diagram (CMD). They were first discovered by Sandage (1953) in the GC M3. The position of the BSSs in the CMD suggests that they are more massive than the current cluster members. This is further supported by previous mass measurements (Shara et al., 1997; Gilliland et al., 1998; Fiorentino et al., 2014). However, GCs are completely devoid of gas, making recent star formation implausible. Consequently, the origin of BSSs is associated with a mechanism that increases the initial stellar mass through rejuvenation. The two primary mechanisms for the formation of BSSs are mass transfer (MT) from an evolved donor to a lower-mass binary companion (McCrea, 1964) and stellar collisions that lead to mergers in high-density environments (Hills & Day, 1976; Leonard, 1989). The absence of a single formation scenario that explains all observed BSSs across different clusters necessitates the identification of distinguishing characteristics for each scenario.

Chemical abundance is an indicator that distinguishes between different BSS-formation scenarios. Smooth particle hydrodynamics calculations have revealed that stellar collisions produce merged objects with surface abundances that match the envelopes of the most massive stars (Lombardi Jr. et al., 1995). In contrast, binary mass transfer exposes and accretes the deeper layers of the donor star, resulting in surface abundances indicative of partial burning of hydrogen. For example, in 47 Tuc, Ferraro et al. (2006) found many BSSs depleted in carbon (C) and oxygen (O), suggesting that they accreted CNO-processed material

Table 1. IDs, RA, DEC, Visual Magnitude, and Membership Probability of the 39 BSSs Used in This Study (Refer to Text for Details)

BSS ID	Cosmic-Lab ID	RA (degrees)	DEC (degrees)	m_V	PROB (%)
B1	1023539	154.3993515	-46.4078560	17.54	97
B2	1013700	154.3962520	-46.4182565	17.27	96.9
B3	1025211	154.3849299	-46.4076830	17.58	97.3
B4	1021152	154.4195717	-46.4093147	17.17	97.3
B5	1025619	154.3816172	-46.4041477	16.86	99.9
B6	1031149	154.4004033	-46.3970078	16.69	97.7
B7	1010831	154.4189046	-46.4216023	16.34	97.3
B8	1021331	154.4184729	-46.4027317	17.39	97.7
B9	1009786	154.4276377	-46.4137044	16.95	97.7
B10	1020369	154.4272846	-46.4087656	17.20	97.1
B11	1031222	154.3994121	-46.3927124	17.58	97.7
B12	1026151	154.3766105	-46.4000632	17.77	97.2
B13	1016643	154.3700469	-46.4114471	17.22	97.1
B14	1006762	154.3834415	-46.4321004	16.60	97.3
B15	1009269	154.4330228	-46.4137157	16.64	97.5
B16	1016923	154.3668729	-46.4150062	17.82	97.4
B17	1002749	154.4246075	-46.4282995	17.60	97.3
B18	1008650	154.4390510	-46.4182480	17.45	95.3
B19	1030901	154.4032020	-46.3843063	17.47	100
B20	2716018	154.3760880	-46.4361699	17.19	100
B21	2711709	154.4041397	-46.4461522	17.74	0.06
B22	1035238	154.3842813	-46.3772396	17.38	100
B23	2714632	154.3860264	-46.4501061	16.43	100
B24	2705506	154.4472108	-46.3887971	17.54	99.9
B25	2714006	154.3898416	-46.3689811	17.51	100
B26	2709841	154.4152943	-46.3652141	17.59	99.9
B27	2720497	154.3341108	-46.4439012	16.49	100
B28	2710692	154.4103191	-46.4691207	17.36	100
B29	2711836	154.4034550	-46.4747336	17.25	99.9
B30	2600533	154.3140993	-46.3867423	17.19	100
B31	2702518	154.4824695	-46.3775296	16.63	100
B32	2707141	154.4338850	-46.3495438	17.25	96.5
B33	2717272	154.3667567	-46.4837663	17.85	99.9
B34	2601851	154.2893054	-46.4032201	17.46	100
B35	2708408	154.4249930	-46.3192117	17.42	100
B36	2603838	154.2324762	-46.3496011	17.36	100
B37	2714749	154.3855481	-46.5545236	17.20	100
B38	2301092	154.2432987	-46.2935999	16.85	0
B39	2801544	154.6364229	-46.4157168	17.64	100

from their binary companions. These chemical anomalies may indicate mass transfer mechanisms. In particular, 47 Tuc shows a high prevalence of depleted BSSs, unlike clusters such as M4, M30, and ω Centauri, where only a few stars show a C/O signature (Lovisi et al., 2010, 2013; Mucciarelli et al., 2014). The small number of C/O-depleted BSSs suggests that either mass transfer is inefficient in GCs or that C and O depletion is transient (Ferraro et al., 2006).

Billi et al. (2023) analyzed high-resolution spectra of BSSs in NGC 3201 obtained with the Magellan Telescope to determine their rotational velocities. They determined the effective temperature and surface gravity values using isochrone fitting on the CMD locations of the BSSs. In this study, we aimed to determine the radial velocity, atmospheric parameters, and chemical abundances of BSSs using a synthetic spectral fitting method.

NGC 3201 is a low galactic-latitude halo GC located in the southern constellation Vela. The right ascension (RA) and declination (DEC) of the cluster center were $10^h17^m36.82^s$ and $-46°$ 24' 44.9", respectively. The cluster has an age

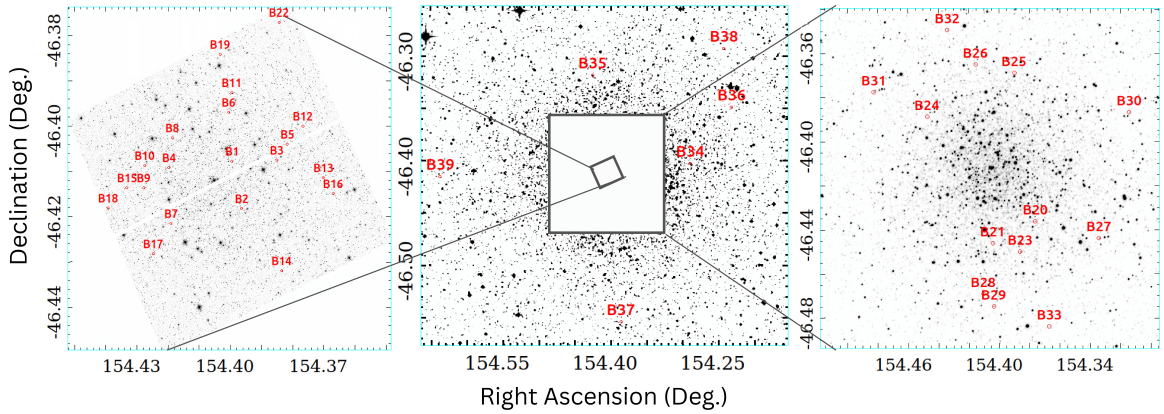

Figure 1. Spatial locations of the BSSs in different regions of NGC 3201. The BSSs are marked with red circles and labelled with their IDs in all images. **Left:** HST F606W image of the core of NGC 3201 taken by the HST ACS Wide Field Camera on March 14, 2006, with a total exposure time of 5 seconds (Nardiello et al., 2018). **Middle:** UK Schmidt telescope image of NGC 3201 taken on March 4, 1978, with a total exposure of 4200 seconds sourced from the DSS survey produced at the Space Telescope Science Institute (STScI). **Right:** ESO/MPG 2.2m telescope image of NGC 3201 in the V/89 filter taken by wide-field imager (WFI) with a total exposure of 480 seconds (credits: ESO Imaging Survey).

$\approx 12.2 \pm 0.5$ Gyr (Monty et al., 2018), a distance ≈ 4.9 kpc, metallicity [Fe/H] ≈ -1.59 dex, and reddening ≈ 0.24 mag (Harris, 1996).

The remainder of this paper is organized as follows: § 2 describes the datasets used in this study. The methodology is presented in § 3. The results of this study are described in § 4, while § 5 presents our conclusions.

2. Data

In this work, we have used BSS spectra, along with their corresponding RA & DEC and $\upsilon \sin(i)$ values, which are openly available at Cosmic-lab[1]. The spectra were acquired from the multi-object fiber system Michigan/Magellan Fiber System (M2FS), which feeds the double spectrograph MSPec mounted on the Magellan Clay Telescope at the Las Campanas Observatory in Chile. The spectra were acquired as part of the CN2019A-15 project (Principal Investigator Lorenzo Monaco). The M2FS instrument enables the simultaneous observation of up to 128 objects across a FOV of approximately 30′ in diameter. Data were collected in February-March 2019 through 16 repeated exposures in the spectral region 5127-5184 Å, with a spectral resolution of 18000. This resolution allowed us to adequately sample the first two lines of the Mg triplet at 5167.3 Åand 5172.6 Å. Two distinct fiber configurations were utilized to obtain the spectra for nearly 200 targets in the direction of the cluster. Our analysis targeted objects with spectra that reached an optimal signal-to-noise ratio (S/N) of $\sim$ 40-50. A total of six exposures, each lasting 30 min, were acquired on the first night, and 10 exposures, each lasting 20 min, were obtained on the second night (Billi et al., 2023). Billi et al. (2023) provides a detailed description of the data reduction process and their methodology for determining radial velocities, cluster membership, atmospheric parameters, and $\upsilon \sin(i)$ values for the BSSs sample.

Out of the 67 BSSs analyzed by Billi et al. (2023), we used 39 BSSs for which we were able to sample the Mg and Fe lines (see Table 2) for proper atmospheric parameter and chemical abundance estimation. The ID, RA, DEC, visual magnitude, and cluster membership probability of these 39 BSSs are listed in Table 1. The BSS IDs are named such that smaller numbers correspond to BSSs closer to the core of the cluster. The Cosmic-Lab ID, RA and DEC are directly taken from the Cosmic-Lab website. The apparent visual magnitude (m_V) was obtained by cross-matching the BSSs positions with the photometric catalogue of the Stetson database (Stetson et al., 2019). The cluster membership probabilities (PROB) are obtained from Nardiello et al. (2018) and Vasiliev & Baumgardt (2021).

The spatial locations of the BSSs in different cluster regions are shown in Figure 1. Of the 39 BSSs used in this study, 13 are within the core radius ($R_c = 1.3'$), 13 lie between the core and half-light radii, and 13 are beyond the half-light radius ($R_h = 3.1'$) of NGC 3201 (Harris, 1996). The continuum-normalized and radial-velocity-corrected spectra of the BSSs are shown in Figure 2.

3. Methodology

We used the `iSpec` software (Blanco-Cuaresma et al., 2014; Blanco-Cuaresma, 2019) for spectral analysis. `iSpec` is an integrated spectroscopic software framework[2] designed for determining astrophysical parameters and individual chemical abundances. In `iSpec`, we used a synthetic spectral fitting method to extract atmospheric parameters and chemical abundances from the BSS spectra. This method compares the observed spectrum with synthetic

[1] http://www.cosmic-lab.eu/Cosmic-Lab/BSS_rotation.html

[2] https://www.blancocuaresma.com/s/iSpec

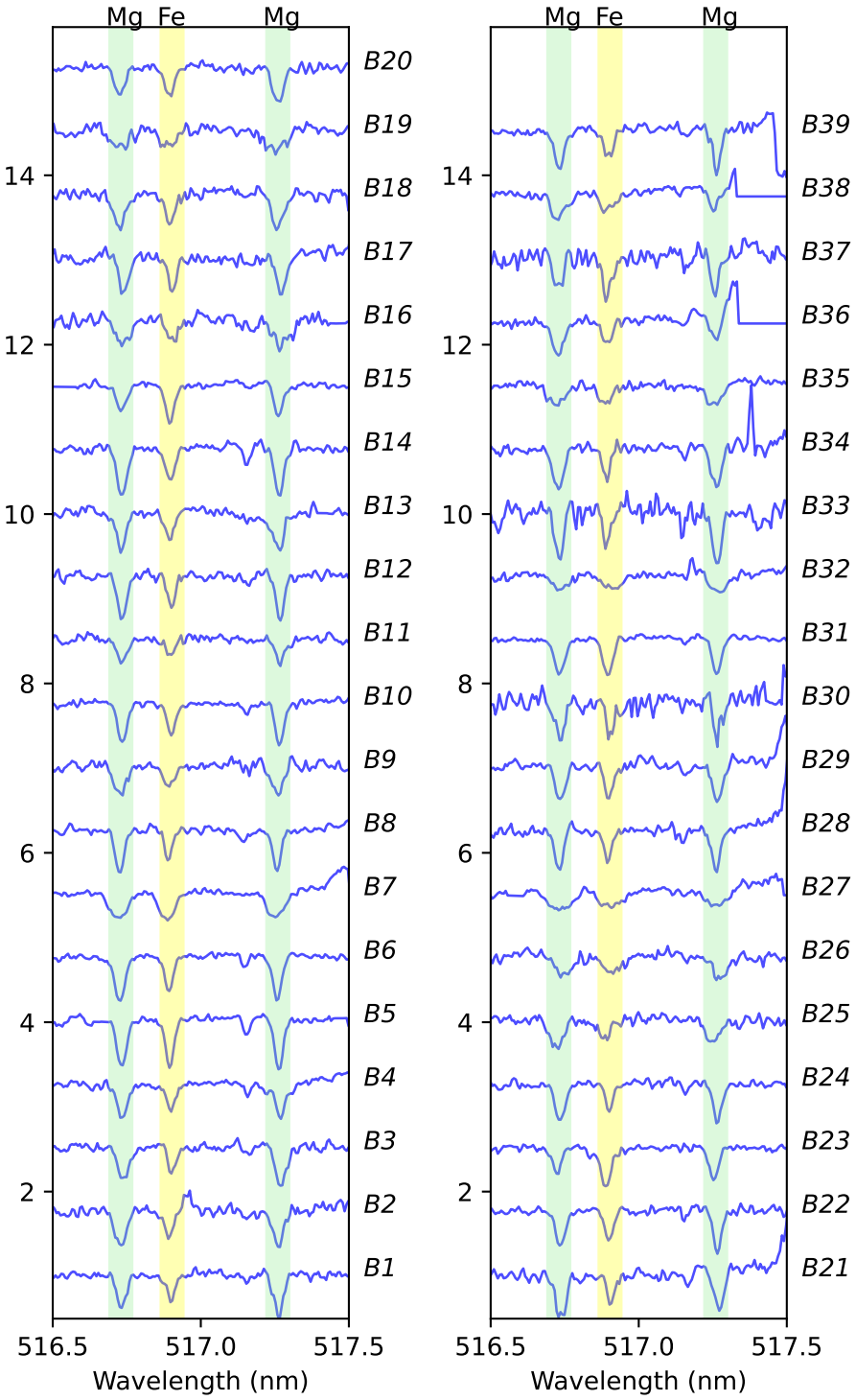

Figure 2. The normalized and radial velocity-corrected spectra of 39 BSSs (B1-B39) of the cluster NGC 3201. The Mg and Fe lines are shown with vertical bands.

spectra generated on-the-fly (Valenti & Piskunov, 1996), focusing on specific spectral features. Using a least-squares algorithm, the differences between the synthetic and observed spectra were minimized to obtain the optimal parameters.

The continuum points within the spectrum were identified by applying median and maximum filters with different window sizes. The median filter smooths out the noise, while the maximum filter disregards deeper fluxes associated with absorption

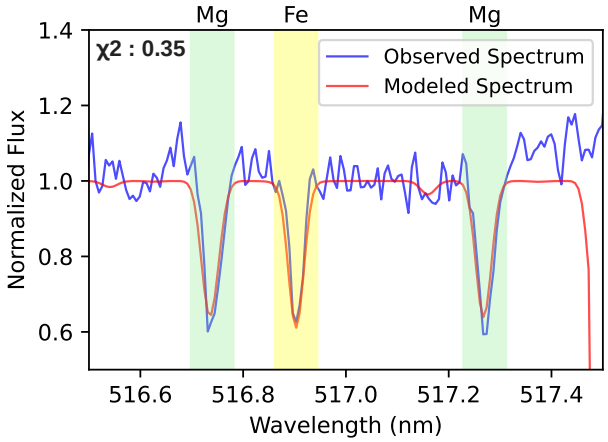

Figure 3. The observed spectrum, focusing on Mg and Fe lines, is fitted with a model. The observed spectrum is shown in blue, and the fitted model is shown in red. The light green and yellow regions represent the Mg and Fe lines.

lines (Blanco-Cuaresma et al., 2014). Subsequently, a polynomial fit was used to model the continuum. Finally, the spectrum was normalized by dividing all the flux values by the modelled continuum.

Initially, we determined the radial velocity using two lines of the Mg triplet at 5167.3 Åand 5172.6 Å. After calculating the radial velocities, the spectra were shifted to their rest wavelengths to ensure accurate alignment for further analyses.

The synthetic spectrum was fitted to the observed spectra to determine the atmospheric parameters and chemical abundances using `iSpec` (Sarmento et al., 2020; Casamiquela et al., 2022). Synthetic spectra were generated using the `ATLAS9.KuruczODFNEW` (Castelli & Kurucz, 2003) model atmosphere with the `SYNTHE` (Kurucz, 1993; Sbordone et al., 2004) radiative transfer code in `iSpec`, and the Gaia-ESO Survey line list (Heiter et al., 2015; Blanco-Cuaresma, 2019). Solar abundances were adopted from Grevesse & Sauval (1998). Figure 3 illustrates an example of model fitting, where the observed spectrum of a BSS (B17) is compared with synthetic spectra, focusing on the Mg and Fe lines. The observed spectrum (blue) is well matched to the synthetic spectrum (red), achieving a chi-squared value of $\chi^2 = 0.35$. In general, the χ^2 values for the spectral fitting of other BSSs were found to be in the range of 0-1.

To determine the atmospheric parameters, we performed synthetic spectral fitting in two steps, focusing on Mg lines in the first step and Fe lines in the second (see Table 2). The initial parameters for effective temperature (T_{eff}) and surface gravity ($\log g$) were set to 7700 K and 4 dex, respectively, based on the ranges listed by Billi et al. (6700-8700 K for T_{eff} and 3.6-4.3 dex for $\log g$). The metallicity ([M/H]) was fixed at −1.59, consistent with the cluster's [Fe/H] value (Harris, 1996). The $\upsilon \sin i$

Table 2. Mg and Fe spectral lines used in this study[a]

Element	Peak Wavelength (nm)	$\log gf$
Mg	516.732	-0.931
	517.268	-0.450
Fe	516.903	-1.000

[a]$\log gf$ Denotes the Logarithm of the Product of Statistical Weight and Oscillator Strength

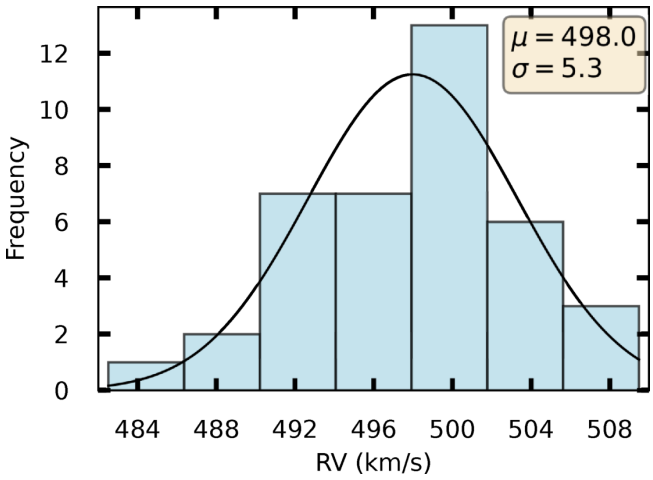

Figure 4. Histograms of Radial velocity estimated for the 39 BSSs.

values were sourced from Cosmic-Lab. Initial values for microturbulence (υ_{mic}) and macroturbulence (υ_{mac}) were estimated using the built-in functions `estimate_vmic` and `estimate_vmac` in `iSpec`, which use empirical relations based on T_{eff}, $\log g$, and [M/H]. These initial values were 2.27 km s^{-1} for υ_{mic} and 26.73 km s^{-1} for υ_{mac}.

Atmospheric parameters (T_{eff} and $\log g$) were derived independently from Mg and Fe lines. The final T_{eff} and $\log g$ values listed in Table 3 for each BSS were computed as the means of the values derived from the Mg and Fe lines, with the standard deviations representing the associated uncertainties.

Using the final atmospheric parameters, we re-ran the spectral fitting to derive the values of [Mg/Fe] and [Fe/H]. The uncertainties in [Mg/Fe] and [Fe/H] were calculated by propagating the errors in T_{eff} and $\log g$. For this, the abundances were re-computed by varying each atmospheric parameter (T_{eff}, $\log g$) within its upper and lower uncertainty limits, while keeping the others constant. The resulting variations in abundance were combined in quadrature to estimate the final uncertainty. Given the limited number of spectral lines available, these results should be considered as approximate estimates.

4. Results and discussion

Using the methodology provided in § 3, we performed a spectral analysis of the BSSs in NGC 3201. The radial

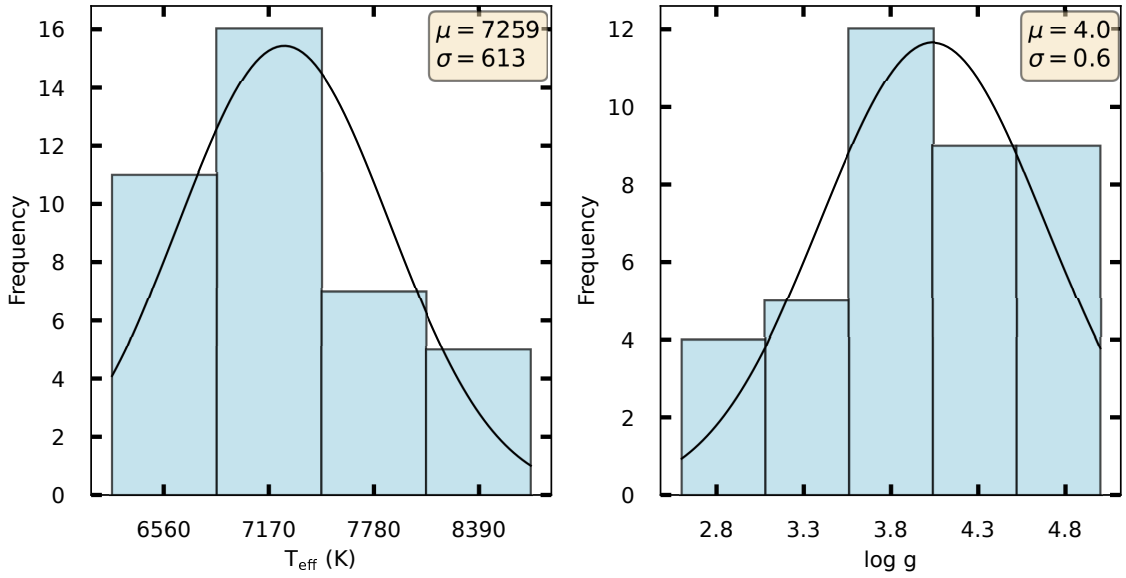

Figure 5. Histograms of T_{eff} and log g estimated for the BSSs.

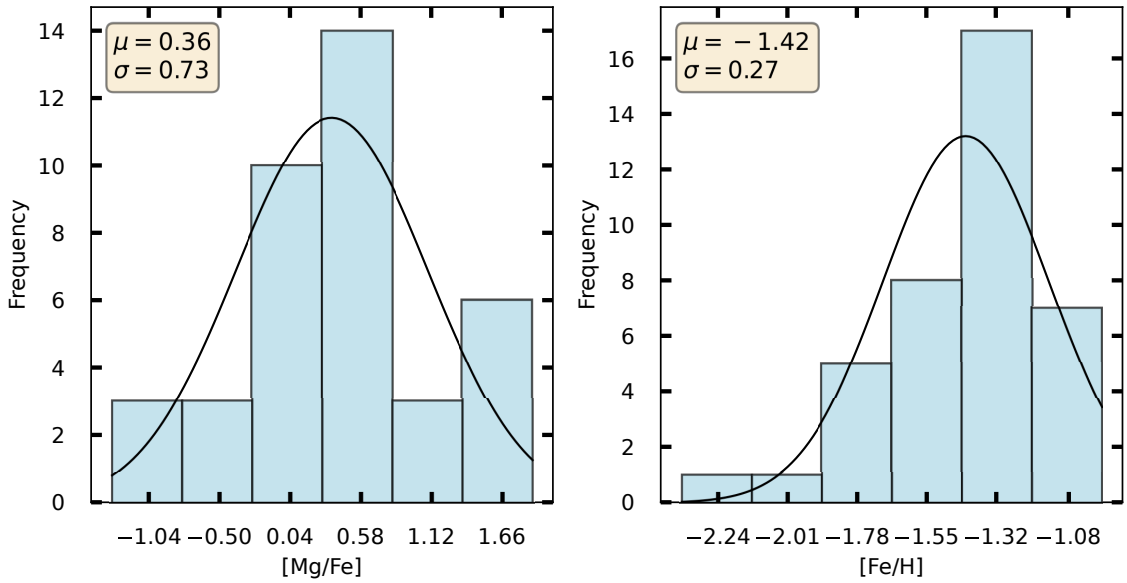

Figure 6. Histograms of [Mg/Fe] and [Fe/H] values estimated for BSSs.

velocities, atmospheric parameters (T_{eff} and log g), and chemical abundances derived from the spectra for all 39 BSSs are listed in Table 3.

Figure 4 shows a histogram of the BSS radial velocities. We performed a Gaussian fit to determine the average radial velocity for the BSSs as 498.0 ± 5.3 km s^{-1}. Comparing this with the reported radial velocity of 494.0 ± 0.2 km s^{-1}(Harris, 1996), the BSSs' average radial velocity is similar within the error margin.

Figure 5 provides insights into the obtained T_{eff} and log g values for the The ranges of T_{eff} and log g for the BSS are 6260–8690 K and 2.6–5.0, respectively. Billi et al. (2023) quoted the T_{eff} and log g in the range of 6700-8700 K and 3.6-4.3, respectively, for the BSSs in NGC 3201. The values we derived are also nearly in the same range. Gaussian fitting to the histogram provides a mean T_{eff} and log g of the BSSs of 7259 ± 613 K and 4.0 ± 0.6 dex, respectively.

Figure 6 shows histogram plots of the obtained chemical abundances of [Mg/Fe] and [Fe/H]. We performed Gaussian fitting on these distributions to determine the average values of [Mg/Fe] and [Fe/H]. The mean values obtained are [Mg/Fe] = 0.36 ± 0.73 and [Fe/H] = -1.42 ±

Table 3. Atmospheric parameters and chemical abundances of the BSSs. The values of $v \sin(i)$ is taken from Cosmic-lab

BSS ID	RV (km s^{-1})	$v \sin(i)$ (km s^{-1})	T_{eff} (K)	log g	[Fe/H]	[Mg/Fe]
B1	503.52	5 ± 2	7112 ± 529	4.5 ± 0.7	-1.47 ± 0.22	-0.14 ± 0.62
B2	502.21	12 ± 2	7830 ± 487	4.9 ± 0.1	-1.22 ± 0.11	1.39 ± 0.57
B3	482.51	13 ± 2	6951 ± 726	4.9 ± 0.1	-1.43 ± 0.33	0.49 ± 0.83
B4	492.60	9 ± 1	6910 ± 517	3.9 ± 0.9	-1.32 ± 0.61	0.32 ± 0.72
B5	493.97	5 ± 1	6260 ± 629	2.6 ± 0.9	-1.28 ± 0.34	-0.07 ± 0.56
B6	498.02	5 ± 1	6962 ± 118	3.6 ± 0.9	-1.04 ± 0.56	1.21 ± 0.46
B7	499.53	25 ± 2	6780 ± 617	3.2 ± 0.9	-1.21 ± 0.42	0.05 ± 0.44
B8	507.22	5 ± 1	7772 ± 771	4.5 ± 0.7	-1.13 ± 0.28	1.36 ± 0.81
B9	493.97	16 ± 3	7724 ± 146	4.5 ± 0.7	-1.40 ± 0.23	1.06 ± 0.23
B10	496.45	5 ± 1	6545 ± 634	3.4 ± 0.9	-1.63 ± 0.46	-0.43 ± 0.65
B11	497.79	16 ± 3	8283 ± 371	4.8 ± 0.3	-1.76 ± 0.11	0.52 ± 0.39
B12	493.97	5 ± 2	6659 ± 697	3.9 ± 0.9	-1.35 ± 0.53	0.46 ± 1.02
B13	509.48	9 ± 3	7040 ± 146	4.9 ± 0.1	-1.15 ± 0.08	0.36 ± 0.16
B14	497.79	5 ± 1	6555 ± 277	3.4 ± 0.6	-1.65 ± 0.31	0.40 ± 0.24
B15	498.02	14 ± 2	6714 ± 723	2.9 ± 0.9	-1.50 ± 0.51	-1.32 ± 0.75
B16	488.24	20 ± 2	7388 ± 772	4.9 ± 0.1	-1.38 ± 0.16	0.05 ± 1.12
B17	490.68	5 ± 2	6717 ± 856	3.3 ± 0.9	-1.96 ± 0.52	-0.80 ± 0.72
B18	498.02	15 ± 2	6899 ± 741	3.4 ± 0.8	-1.77 ± 0.59	-0.04 ± 0.52
B19	499.70	36 ± 4	7735 ± 825	5.0 ± 0.0	-1.40 ± 0.12	-0.03 ± 0.98
B20	501.61	10 ± 3	7202 ± 701	3.7 ± 0.9	-1.22 ± 0.66	-0.20 ± 0.77
B21	495.69	5 ± 2	6490 ± 409	4.0 ± 0.8	-1.67 ± 0.39	0.65 ± 0.66
B22	495.88	5 ± 2	6953 ± 712	4.0 ± 0.9	-1.47 ± 0.50	-0.08 ± 0.97
B23	503.38	9 ± 1	7010 ± 591	3.9 ± 0.9	-1.24 ± 0.52	-0.69 ± 0.59
B24	490.15	6 ± 2	6864 ± 307	4.3 ± 0.9	-1.60 ± 0.43	0.37 ± 0.58
B25	498.02	17 ± 3	8690 ± 673	4.9 ± 0.2	-1.23 ± 0.12	1.89 ± 1.06
B26	493.97	25 ± 3	8373 ± 551	3.0 ± 0.7	-2.36 ± 0.49	0.48 ± 0.52
B27	495.69	35 ± 4	7420 ± 825	4.4 ± 0.5	-1.27 ± 0.25	0.39 ± 0.91
B28	504.13	5 ± 2	7000 ± 343	3.9 ± 0.9	-1.27 ± 0.58	0.35 ± 0.50
B29	492.60	5 ± 2	6823 ± 788	3.9 ± 0.9	-1.14 ± 0.57	-0.02 ± 1.08
B30	503.52	5 ± 2	6898 ± 890	3.6 ± 0.9	-1.13 ± 0.51	-0.03 ± 1.42
B31	498.02	10 ± 1	6564 ± 900	3.0 ± 0.8	-1.38 ± 0.51	-0.70 ± 0.92
B32	498.36	26 ± 2	8419 ± 442	4.0 ± 0.7	-1.60 ± 0.60	0.69 ± 0.63
B33	501.61	5 ± 2	7365 ± 382	4.9 ± 0.2	-1.07 ± 0.09	0.80 ± 0.38
B34	501.84	5 ± 1	7660 ± 666	4.3 ± 0.8	-1.28 ± 0.28	1.37 ± 0.71
B35	499.53	27 ± 3	7877 ± 186	4.2 ± 0.8	-1.69 ± 0.56	1.03 ± 0.52
B36	495.69	13 ± 2	7964 ± 622	4.4 ± 0.9	-1.43 ± 0.32	1.61 ± 0.78
B37	507.22	5 ± 2	7217 ± 400	3.8 ± 0.9	-1.69 ± 0.67	-0.79 ± 0.46
B38	507.22	17 ± 3	8415 ± 367	4.6 ± 0.6	-1.59 ± 0.26	1.61 ± 0.53
B39	501.61	5 ± 2	7059 ± 457	4.2 ± 0.9	-0.97 ± 0.79	0.49 ± 0.71

0.27. Muñoz et al. (2013) performed a detailed chemical abundance analysis of eight red giants in NGC 3201 using high-resolution spectroscopy. They found mean values of [Fe/H] = -1.53 ± 0.01 and [Mg/Fe] = 0.38 ± 0.03. These values are comparable to the errors in the measurements of the BSSs. However, we observed significant dispersion in our abundance values, likely due to the lower SNR, resolution, and limited number of available lines. The obtained mean [Fe/H] value of -1.42 ± 0.27 is consistent with the cluster's [Fe/H] value of -1.59 within error.

As mentioned in § 1, two main scenarios have been proposed for the formation of BSS: mass transfer and stellar collisions leading to mergers. It is challenging to distinguish between the processes that give rise to BSS. However, chemical abundance analysis of BSS may be the most effective method for differentiating between these two formation scenarios. Collisional BSSs are

not expected to exhibit such abundance anomalies. In contrast, mass transfer BSSs typically show depleted surface abundances of α-elements, such as carbon (C), oxygen (O), and magnesium (Mg) (Lovisi et al., 2013). Our derived values for [Mg/Fe] have large uncertainties, which prevents us from making definitive statements about the formation mechanisms of these BSSs.

Although we attempted to identify correlations within the current dataset, no statistically significant relationships were observed. We also examined the color histogram for the BSSs, but no relationship was observed. Nevertheless, the robustness of the present analysis suggests that future studies with broader spectral coverage in NGC 3201 may yield important insights into the potential correlations between the chemical abundances and atmospheric parameters of BSSs in this cluster.

5. Conclusions

We analyzed the spectra of 39 BSSs in the globular cluster NGC 3201 and derived the radial velocity, atmospheric parameters, and chemical abundance of [Mg/Fe] and [Fe/H]. The present study draws the following conclusions:

1. The radial velocity of the 39 BSSs is determined using the Mg and Fe spectral lines, found in the 482.51 − 509.48 km/s range with a mean value of 498.0 ± 5.3 km/s.
2. The T_{eff} and log g values are found in the range of 6260 - 8690 K and 2.6 - 5.0, respectively, for the BSSs.
3. The abundance values of Mg and Fe are derived using the same lines. The mean value of [Mg/Fe] was estimated to be 0.36 ± 0.73, while that of [Fe/H] was estimated to be -1.42 ± 0.27.

We are grateful to Cosmic-Lab, especially Alex Billi and Francesco R. Ferraro for providing data on BSSs in NGC 3201 and offering insights into spectral corrections.

References

Billi, A., Ferraro, F. R., Mucciarelli, A., et al. 2023, ApJ, 956, 124, doi: 10.3847/1538-4357/acf372

Blanco-Cuaresma, S. 2019, MNRAS, 486, 2075, doi: 10.1093/mnras/stz549

Blanco-Cuaresma, S., Soubiran, C., Heiter, U., & Jofré, P. 2014, A&A, 569, A111, doi: 10.1051/0004-6361/201423945

Casamiquela, L., Gebran, M., Agüeros, M. A., Bouy, H., & Soubiran, C. 2022, AJ, 164, 255, doi: 10.3847/1538-3881/ac9c56

Castelli, F., & Kurucz, R. L. 2003, in Modelling of Stellar Atmospheres, ed. N. Piskunov, W. W. Weiss, & D. F. Gray, Vol. 210, A20, doi: 10.48550/arXiv.astro-ph/0405087

Ferraro, F. R., Sabbi, E., Gratton, R., et al. 2006, ApJ, 647, L53, doi: 10.1086/507327

Fiorentino, G., Lanzoni, B., Dalessandro, E., et al. 2014, ApJ, 783, 34, doi: 10.1088/0004-637X/783/1/34

Gilliland, R. L., Bono, G., Edmonds, P. D., et al. 1998, ApJ, 507, 818, doi: 10.1086/306363

Grevesse, N., & Sauval, A. J. 1998, SSRv, 85, 161, doi: 10.1023/A:1005161325181

Harris, W. E. 1996, AJ, 112, 1487, doi: 10.1086/118116

Heiter, U., Lind, K., Asplund, M., et al. 2015, PhyS, 90, 054010, doi: 10.1088/0031-8949/90/5/054010

Hills, J. G., & Day, C. A. 1976, ApL, 17, 87

Kurucz, R. 1993, Robert Kurucz CD-ROM, 18. https://ui.adsabs.harvard.edu/abs/1993KurCD..18.....K

Leonard, P. J. T. 1989, AJ, 98, 217, doi: 10.1086/115138

Lombardi Jr., J. C., Rasio, F. A., & Shapiro, S. L. 1995, ApJ, 445, L117, doi: 10.1086/187903

Lovisi, L., Mucciarelli, A., Lanzoni, B., Ferraro, F. R., & Dalessandro, E. 2013, MmSAI, 84, 232, doi: 10.48550/arXiv.1301.3295

Lovisi, L., Mucciarelli, A., Ferraro, F. R., et al. 2010, ApJ, 719, L121, doi: 10.1088/2041-8205/719/2/L121

McCrea, W. H. 1964, MNRAS, 128, 147, doi: 10.1093/mnras/128.2.147

Monty, S., Puzia, T. H., Miller, B. W., et al. 2018, ApJ, 865, 160, doi: 10.3847/1538-4357/aadb43

Muñoz, C., Geisler, D., & Villanova, S. 2013, MNRAS, 433, 2006, doi: 10.1093/mnras/stt868

Mucciarelli, A., Lovisi, L., Ferraro, F. R., et al. 2014, ApJ, 797, 43, doi: 10.1088/0004-637X/797/1/43

Nardiello, D., Libralato, M., Piotto, G., et al. 2018, MNRAS, 481, 3382, doi: 10.1093/mnras/sty2515

Sandage, A. R. 1953, AJ, 58, 61, doi: 10.1086/106822

Sarmento, P., Delgado Mena, E., Rojas-Ayala, B., & Blanco-Cuaresma, S. 2020, A&A, 636, A85, doi: 10.1051/0004-6361/201936296

Sbordone, L., Bonifacio, P., Castelli, F., & Kurucz, R. L. 2004, MmSAI, 5, 93, doi: 10.48550/arXiv.astro-ph/0406268

Shara, M. M., Saffer, R. A., & Livio, M. 1997, ApJ, 489, L59, doi: 10.1086/310952

Stetson, P. B., Pancino, E., Zocchi, A., Sanna, N., & Monelli, M. 2019, MNRAS, 485, 3042, doi: 10.1093/mnras/stz585

Valenti, J. A., & Piskunov, N. 1996, A&AS, 118, 595

Vasiliev, E., & Baumgardt, H. 2021, MNRAS, 505, 5978, doi: 10.1093/mnras/stab1475

Revista Mexicana de Astronomía y Astrofísica, 61, 84-97, (2025)

OPEN ACCESS https://doi.org/10.22201/ia.01851101p.2025.61.02.08

Lithium in V505 Per

Gloria Koenigsberger[1], Werner Schmutz[2], Catherine Pilachowski[3], Alan R. Mejía-Nava[4], Derek Sikorski[5] and María Cordero[3]

[1]*Instituto de Ciencias Físicas, Universidad Nacional Autónoma de México, Ave. Universidad S/N, Cuernavaca, Morelos, 62210, México.*
[2]*Physikalisch-Meteorologisches Observatorium Davos and World Radiation Center, Dorfstrasse 33, CH-7260 Davos Dorf, Switzerland.*
[3]*Department of Astronomy, Indiana University, Bloomington, Indiana, USA.*
[4]*Universidad Autónoma del Estado de Morelos, Cuernavaca, Morelos, México.*
[5]*Institute for Astronomy, University of Hawai'i, 2680 Woodlawn Drive, Honolulu, HI 96822, USA.*

Keywords: *Stars: binaries:eclipsing, Stars: binaries: spectroscopic, Stars: chemical abundances*

Abstract

We determined the surface lithium abundance of the eclipsing binary components in V 505 Per (HIP 10961) to be $A(Li)$=2.65±0.07 and 2.35±0.1, which supports the rather unexpected conclusion that their surface Li abundances differ. We find effective temperatures of 6600 K + 6550 K (∼150 K higher than previously reported), which places the stars at the hot limit of the Lithium Dip, thus alleviating the previously suggested discrepancy with cluster stars of similar ages and temperatures. These temperatures are also more consistent with the system's *Gaia* spectral energy distribution. Our iron abundances, $[Fe/H] = -0.15 \pm 0.07$ and -0.25 ± 0.1, agree with the predictions of the higher temperatures deduced from our spectra and from the evolutionary tracks. The rotation rate implied by our line profiles, 12.5±1 km s^{-1}, is smaller than the synchronous rotation rate, which is a curious result given the circular orbit and the age of the system.

Resumen

El análisis de un espectro de alta dispersión del sistema binario eclipsante V505 Per (=HIP 10961) resulta en abundancias de litio de $A(Li)$=2.65±0.07 y 2.35±0.1 por componente, consistentes con los encontrados en un estudio anterior, pero con temperaturas efectivas ∼150 grados mayores que en estudios previos, 6600 K + 6550 K. Las nuevas temperaturas colocan a las estrellas en el límite caliente del "Lithium Dip", eliminando la inconsistencia con resultados de estrellas en cúmulos de la misma edad y masa. Estas temperaturas son consistentes con la distribución espectral de energía de Gaia. Las abundancias de hierro, $[Fe/H] = -0.15 \pm 0.07$ y -0.25 ± 0.1, concuerdan con las predicciones de temperaturas más altas deducidas de nuestros espectros y de las trayectorias evolutivas. La velocidad de rotación es 12.5 ± 1 km s^{-1}, un valor menor al valor de rotación síncrona, situación curiosa dada la órbita circular y la edad del sistema binario.

Corresponding author: G. Koenigsberger *E-mail address:* gloria@icf.unam.mx
Received: November 3, 2025 **Accepted:** May 27, 2025

1. Introduction

Double-line eclipsing binaries are among the most important astrophysical objects available for understanding various physical processes. One of the many astrophysical problems they can be used to address is the one associated with the manner in which nuclear processed material is transported from inner layers to the stellar surface. This is because the two stars in the system can be assumed to have formed from the same molecular cloud at the same time, and thus have the same age. If they have the same mass, they are expected to follow identical evolutionary paths as their interior mixing processes should be the same. Any difference in chemical surface abundance would serve to quantify the differences in the mixing processes.

V505 Persei (HD 14384, HIP 10961) is a short-period, double-line eclipsing binary system in which both stars are spectroscopically very similar. The slightly brighter, larger, and more massive of the two is referred to as component A, and its companion is referred to as component B. The orbital period is well-known to be 4.22 d although, as noted by Southworth (2021), it was first thought to be 2.11 d, half the actual value, due to the nearly identical shape of the two eclipses.[1] The two components have nearly the same mass: 1.27 $M_\odot$+1.25 $M_\odot$) and radii (1.29 $R_\odot$+1.26 $R_\odot$ (Southworth, 2021, henceforth S21).The effective temperatures T_{eff}, determined by Tomasella et al. (2008) (henceforth T08), are also very similar (6515±50 K and 6460±50 K, respectively).

Although most of its properties appear to be determined with exquisite precision, there is a significant spread in the published metallicity values. T08 obtained

[1]Note that automatic period-search algorithms also commit the same mistake even in recent times (Prša et al., 2022)

[M/H]=−0.12±0.03 from a χ^2 model fit to the observed spectra. Also using model fits to spectral observations Baugh et al. (2013) obtained a similar result, $[Fe/H]$ =-0.15±0.03. According to T08, this metallicity is consistent with V505 Per's ∼1 Gyr age and the idea that element diffusion during this time reduced the surface metallicity from an initial ∼solar value. Casagrande et al. (2011a) found $[M/H]$=−0.25 based on a re-assessment of the photometric measurements listed in the Holmberg et al. (2007) Geneva-Copenhagen survey of the Solar neighborhood, where it was listed with $[M/H]$=−0.35. In contrast to these sub-solar values, S21 found a slightly super-solar metal abundance by comparing the observed properties with theoretical mass-radius and mass-effective temperature diagrams.[2] Hence, as suggested by S21, a reappraisal of metallicity is warranted.

Another curious aspect is the conclusion reached by Baugh et al. (2013) regarding the lithium abundance in these two stars. They found star A to have A(Li)∼2.67±0.1 and star B to have A(Li)∼ 2.42 ± 0.2. The T08 temperatures place both stars within the *Lithium Dip*, a region in the $A(Li)$ *vs.* T_{eff} diagram within the temperature range ∼6300 K- 6600 K, in which the surface lithium abundance is severely depleted compared to stars that are hotter and cooler than this temperature range (Boesgaard & Tripicco, 1986; Thorburn et al., 1993; do Nascimento et al., 2000). The Baugh et al. (2013) lithium abundance values are 2-5 times larger than the detections and upper limits derived in the similar metallicity and intermediate-age open clusters NGC 752 and 3680, as well as the more metal-rich and younger Hyades and Praesepe. Baugh et al. (2013) suggested that the higher A(Li) values supported the hypothesis that different rotational evolution of stars in short-period binaries affect their lithium depletion, making them different from single stars. For massive stars, Pavlovski et al. (2023) have concluded that the interior chemical element transport is not as efficient in binary star components as in their single-star counterparts in the same mass regime, and evolutionary stage. Thus, the question of internal mixing is relevant across the Hertzprung-Russell diagram.

In this paper we analyze a high resolution echelle spectrum obtained at orbital phase 0.97, when the lines of both stars are well resolved, in order to further constrain the metallicity, projected rotation velocity and lithium abundance in both components. In § 2, we describe the observations and data reduction. In § 3, we perform a light curve analysis of the *TESS* data. In § 4, we analyze the $[Fe/H]$ abundances by both a curve of growth method and a detailed comparison of the theoretical spectral lines to the observed line profiles. In § 5, we constrain the lithium abundance, and in §6, we discuss the results, and in § 7, we summarize the conclusions.

[2]These results implied a fractional metal abundance Z=0.017 and an age 1.050±0.050 Gyr. S21 noted that the $[M/H] \sim -0.12$ value could be excluded from his results because it corresponds to Z=0.0116 (for a heavy-element mixture such that the solar metallicity is $Z_\odot$=0.01524), a value outside the bounds of the range allowed by the theoretical models.

2. Observations

V505 Per (=TIC 348517784) was observed by the TESS satellite (Ricker et al., 2015) in sectors 18 (2019), 58 (2022), and 85 (2024). The 2-minute cadence data files were downloaded from the Mikulski Archive for Space Telescopes (Swade et al., 2019) using search_lightcurve (Ginsburg et al., 2019). These files contain the Simple Aperture Photometry fluxes (SAP flux) and the background counts as reduced by the TESS pipeline. The light curves are the result of aperture photometry, which gives the total counts measured from the TESS images within the photometric aperture. The light curves were extracted and normalized using the Lightkurve Collaboration software (Lightkurve Collaboration et al., 2018), excluding data that do not have a quality equal to zero and epochs with background counts higher than 50000 e^-/s, where typical count rates of the targets were 400,000 e^-/s. We also excluded the first part of the Sector 18 light curve earlier than BTJD 1794 d because the fluxes rose to 1.01 of the normalized uneclipsed level. It is not clear whether this is a real flux change or something else, and there is no other similar deviation from regular repeating orbital variations in the light curve.

Our spectroscopic observations of V505 Per were obtained on 2011 Sept 16 and 20 at the Kitt Peak National Observatory Coudé Feed telescope using the echelle grating with a slit width of 250 μm, Camera 5, and the F3KB CCD. The echelle grating provides a reciprocal dispersion of 1.9 Å/mm at λ6697 Å which, with the CCD 0.015 mm/pixel, provides a resolution R= 110000 at this wavelength.[3] Flat fields and biases were obtained throughout the night of September 20 and at the beginning and end of the night of September 16. The Julian Dates (-2400000) of our observations are 2455821.8953 and 2455825.9871, which correspond to orbital phases 0.9772 and 0.9464, respectively, based on an initial epoch T_0=JD 2458798.516720 and orbital period P=4.2220216 d given by S21 (but see below). The orbital phases are defined such that φ=0 corresponds to the deeper of the two eclipses, which occurs when star A is eclipsed by its companion B.

The Sept 16 spectrum was obtained just before ingress of primary eclipse (first contact occurs at φ ∼0.985 see Figure 2 of S21). At this phase, the lines of the two stars are barely resolved, with their centroids separated by only 19 km s^{-1}. The September 20 spectrum was obtained sufficiently far from conjunction for the lines of the two stellar components to be well separated (58 km s^{-1}), allowing a more straightforward analysis by avoiding the blending effects.

The echelle spectra were reduced according to standard methods available in IRAF. Since the wavelength calibration is not absolute, we opted to shift the spectrum so that the absorption lines belonging to the star approaching the observer are centered on the laboratory wavelengths.

[3]Willmarth, Daryl, 2.1m Coudé Spectrograph Instrument Manual, NOAO, Jan. 5, 1996.

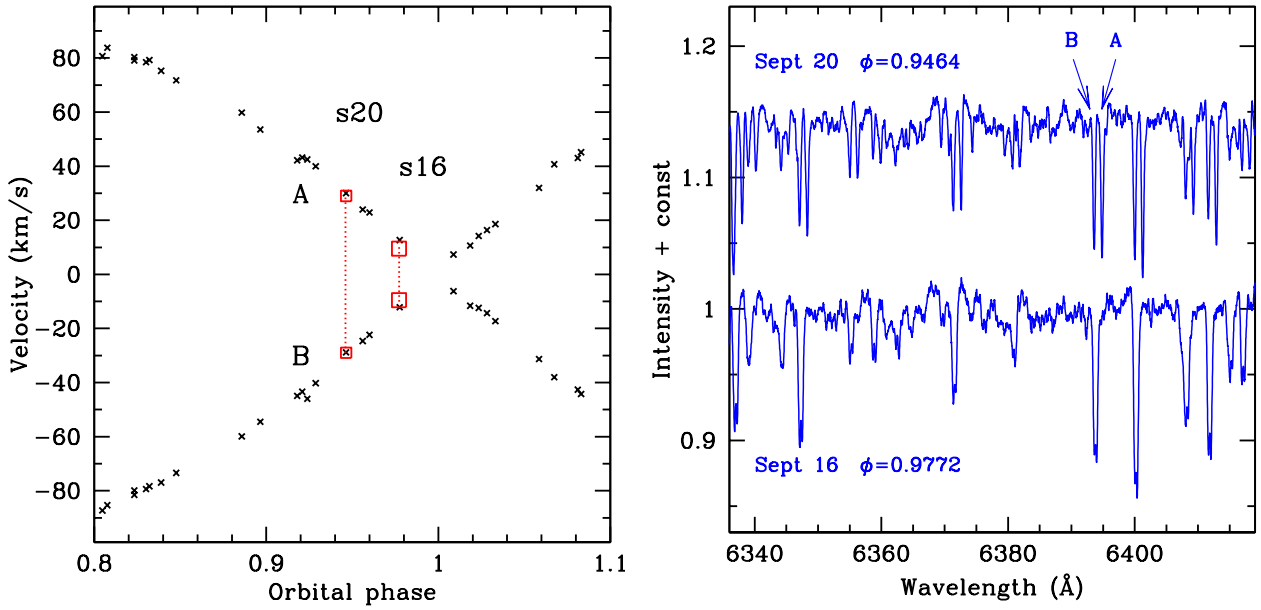

Figure 1. Left: Radial velocity curves near the ϕ=0.00 eclipse, constructed from the data in SB9 catalogue (crosses). The dotted vertical lines indicate the RV separation (ΔRV) of components A and B in our two spectra, which were obtained on September 16 and 20. At phase 0, star B is in front of star A. **Right:** Spectra of V505 Per obtained at φ=0.9464 (20 September, top) and φ=0.9778 (September 16 bottom), phases computed using Eq. 1. A constant vertical shift was introduced in the spectrum of September 20 for clarity. The star B wavelength scale is centered on the laboratory wavelength, so star A's spectrum is shifted by +58 km s^{-1} with respect to that of star B on Sept. 20 (as indicated by labels A and B). The two components were not resolved on September 16.

In our spectra, this is the lower-mass component (star B), so this is the spectrum that is centered on the laboratory wavelengths. The primary lines appear to be shifted by +58 km s^{-1}.

A compendium of V505 Per radial velocities is available in The Ninth Catalogue of Spectroscopic Binary Orbits (Pourbaix et al., 2004)[4], from which we plot in Figure 1 shows the data for the orbital phase interval 0.8 – 1.1. The location corresponding to the two observations is indicated. Since we only have relative RV measurements, we connect the data points for the primary and the secondary with a dotted line and shift them vertically on this plot to show that the relative RVs are fully consistent with published radial velocity curves.

The standard method to correct for the echelle blaze was applied in order to normalize each of the spectral orders. Corrections for a high-frequency intensity oscillation along the normalized orders were manually corrected by fitting a high-order polynomial to the visually fitted continuum level. This resulted in spectral orders where the continuum generally lies at an intensity level of unity $\pm 1\% - 2\%$. A sample spectrum is shown in Figure 1. The echelle spectra have S/N$\sim$100 per 0.02 Å pixel. For the analysis, we applied a boxcar 5-point smoothing to enhance the S/N.

[4]http://sb9.astro.ulb.ac.be

3. Light curve analysis

The TESS light curves comprise 15 primary and 14 secondary minima. The primary minima have a depth of $\sim$61.8 % of the out of eclipse light level, and the 14 secondary minima have a depth of $\sim$62.8 %. The individual light curves show a scatter in the depths of $\sim$0.1 %.

The epochs of the light curve minima were measured using the method proposed by Kwee & van Woerden (1956). The average estimated uncertainty of the method is 0.8 sec, and standard deviation of the observed minima from a fitted straight line to the epochs of minima timing is 1.1 sec.

The fits to both primary and secondary minima yield the same period within the uncertainties, from which the following ephemeris was derived:

$$\begin{aligned} \text{BJD (Min I)} = \quad & 2458798.51672(\pm 3\,10^{-5}) + \\ & 4.22201933(\pm 2\,10^{-8}) \times E \end{aligned} \qquad (1)$$

where E is an integer number corresponding to the orbital cycle. The zero epoch agrees with the time determined by S21, but the uncertainty of our determination is a factor six larger. The period of our determination is a factor of hundred more precise than that given by S21 because of the larger time base available to us.

We analyzed the folded light curve from all three TESS sectors. In a partially eclipsing systems, only the sum of the stellar radii of the two stars can be derived from the light curve, but not their ratio. Hence, we first explored

Table 1. Parameters from *TESS* light curve fit and literature

Parameter	Value	Notes
q	0.9868 (fixed)	RV curve S21
$a\sin(i)$ ($R_\odot$)	14.974 (fixed)	RV curve S21
i deg	87.859 (fitted)	light curve
a ($R_\odot$)	14.984	derived from above
$(R_A+R_B)/a$	0.1714 (fitted)	light curve
R_A+R_B ($R_\odot$)	2.5685	derived from above
T_B/T_A	0.9928 (fitted)	light curve
R_B/R_A	0.97895 (free)	Ev. Tracks

the possible range of radii ratios that could reproduce the observed light curve and found that radii ratios $rr = R_B/R_A$ in the range 0.85–1.0 yield identical light curves, all of which fit the observed one. Such a broad range of rr values introduces a large uncertainty. Thus, to further constrain the possible values, we analyzed the properties of the evolutionary tracks.

We obtained the evolutionary tracks for 1.2745 $M_\odot$ (star A) and 1.2577 $M_\odot$ (star B) by interpolating the models given by Mowlavi et al. (2012) for solar metallicity (Z=0.014) and metallicity corresponding to $[Fe/H]$ =-0.146 (Z=0.010). We extracted from these models the radii and T_{eff} as a function of age, from which we then calculated R_B/R_A, R_A+R_B and T_{eff} also as functions of age. The results are shown in Figure 2.

From the light curve solutions we get the value of the sum of the stellar radii in units of the projected orbital separation, r_A+r_B, where $r_i = R_i/a$, with a the semi-major axis of the orbit, which is obtained from the solution of the radial velocity curve (a=14.984 $R_\odot$, S21's Table V). Our light curve solution yields $(R_A+R_B)/a$=0.1714. With the above value of a, this yields R_A+R_B = 2.5685±0.001, where the uncertainty corresponds to the different results obtained from fitting the mean of all *TESS* sectors.[5] The top panel of Figure 2 shows that R_A+R_B = 2.5685 corresponds to an age 1.295 Gyr if the stars have Z=0.010 and 1.571 Gyr if they have an approximate solar metallicity. Inspection of the second and third panels in this figure shows that the predicted temperature ratio and radius ratio do not have a very strong dependence on the metallicity. For both metallicities T_{Beff}/T_{Aeff} =0.9927, similar to the 0.9328 value obtained from the light curve fit, and rr=0.97895±0.00005.

Whereas the temperature ratio is not very sensitive to metallicity, the actual temperature has a very strong dependence on metallicity. The bottom panel of Figure 2 illustrates star A's effective temperature as a function of age for the two analyzed metallicities. For an approximately

[5]Results for the individual sectors are as follows: (T_B/T_A, R_A+R_B, i, M_A+M_B)=(0.99270, 2.5691, 87.869deg, 2.53) for Sector 18; =(0.99272, 2.5684, 87.851, 2.53) for Sector 58; =(0.99280, 2.5694, 87.851, 2.53) for Sector 85. All fits performed with PHOEBE used rr=0.979

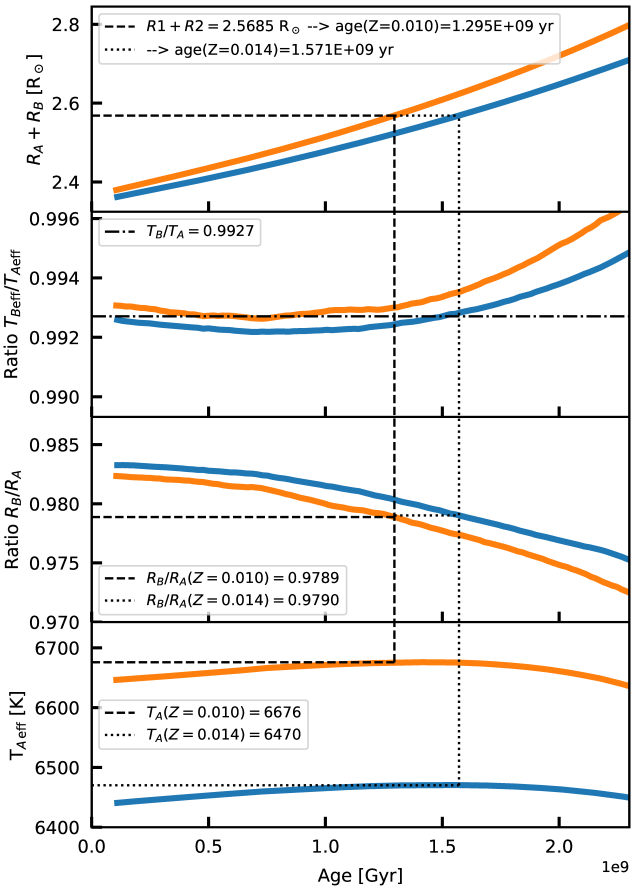

Figure 2. Evolutionary tracks for a stellar pair of M_1 = 1.2747 + M_2 = 1.2579 $M_\odot$ with solar metallicity (Z=0.014, blue) and for Z=0.010 (orange). The absicssa gives the time after the star has reached the ZAMS. The ordinate is as follows from the top to the bottom panel: the sum of the two stars' radii, R_A+R_B; the effective temperature ratio, T_{Beff}/T_{Aeff}; radii-ratio, R_B/R_A; and the value of T_{Aeff}. The R_A+R_B value is obtained directly from the solutions to the light curve and radial velocity curve, and its value for V505 Per then determines the age which, in turn, constrains the remaining parameters. The dash line gives their value for Z=0.010 and the dotted line for Z=0.014 (close to solar, $[Fe/H = -0.037)$.

solar metallicity, the temperatures are within the range determined by T08 (with the S21 uncertainties). However, the system is significantly older (1.57 Gyr instead of ~1 Gyr). However, if instead the $[Fe/H]$ values are as low as determined by Baugh et al. (2013) and Casagrande et al. (2011b), then T_{eff} must be higher than determined by T08. The bottom panel of Figure 2 indicates that T_{Aeff} ~6676 K, which from the temperature ratio means that T_{Beff} ~6627 K.

4. Iron abundance

The chemical abundance analysis of a binary system requires knowledge of the effective temperature (T_{eff}), logarithm of the surface gravity (log(g)), each star's

Table 2. Fundamental parameters of V505 Per

Parameter	Literature	This paper	
P_{orb} (d)	4.2220216(.0000023)	4.22201933(10^{-8})	⋯
M_A ($M_\odot^N$)	1.2745(.0036)[(a)]	⋯	⋯
M_B ($M_\odot^N$)	1.2577(.0030)[(a)]	⋯	⋯
rr	0.9788(.0019)[(b)]	0.9789	0.9790
light ratio	0.9367(.0037)[(c)]	⋯	⋯
i	87.9166(.0030)[(c)]	87.859	⋯
R_A ($R_\odot^N$)	1.2941(.0016)[(d)]	1.2982	⋯
R_B ($R_\odot^N$)	1.2637(.0017)[(d)]	1.2702	⋯
$\log(g)_A(\log[cgs])$	4.3194(.0010)[(e)]	⋯	⋯
$\log(g)_B(\log[cgs])$	4.3343(.0010)[(e)]	⋯	⋯
$[Fe/H]_A$	-0.25[(f1)]	Tab. 3	Tab. 3
	-0.12(.03)[(f2)]	⋯	⋯
	-0.15(.05)[(f3)]	⋯	⋯
$[Fe/H]_B$	-0.12(.03)[(f4)]	Tab. 3	Tab. 3
z	0.017[(f5)]	0.014	0.010
T_{Aeff}(K)	6512(50)[(g)]	6470	6676
T_{Bff}(K)	6460(50)[(g)]	6423	6627
$V\sin(i)_A$ (km s^{-1})	15.3(1.0)[(h)]	12.5 (1)	12.5(1)
$V\sin(i)_B$ (km s^{-1})	15.4(1.0)[(h)]	12.5 (1)	12.5(1)
ξ_{th} (km s^{-1})	1.7[(j)]	⋯	⋯
$log(L_A/L_\odot^N)$	0.434(.0013)[(k)]	0.425	0.479
$log(L_B/L_\odot^N)$	0.399(.0013)[(k)]	0.393	0.448
Age (Gyr)	1.050(0.050)[(f5)]	1.571	1.295
$D(pc)$	61.19 (.62)[(m)]	⋯	⋯
$D(pc)$	62.03 (.10)[(n)]	⋯	⋯

[(aa)] $M_\odot^N$, $R_\odot^N$, $L_\odot^N$ are the nominal solar units given by IAU 2015 Resolution B3 (Prša et al., 2016).

[(a)] Masses from the radial velocity curves solution and orbital inclination=87.916 deg.

[(b)] Radii ratio from the light curve fit.

[(c)] Light ratio from the light curve fit.

[(d)] Stellar radii from the light curve and radial velocity solutions. T08 values are the same within their uncertainties.

[(e)] The S21 et al. values derive from the masses and radii. The T08 values were obtained from the spectral fits. T08 values are the same within their uncertainties.

[(f1)] Casagrande et al. (2011a).

[(f2)] T08 from their spectrum at orbital phase 0.497, when star A nearly totally eclipses its companion.

[(f4)] T08.

[(f5)] S21 isochrone fitting; z=0.017 corresponds to $[Fe/H] = +0.05$, using $z = 0.01524 \times 10^{[Fe/H]}$, assuming a solar-proportional mix, see del Burgo & Allende Prieto (2018).

[(g)] Effective temperatures from T08 based on Kurucz model spectra fits to the data, with uncertainty values as given by S21.

[(h1)] Projected equatorial rotation velocity from T08 for star A based on their spectrum at orbital phase 0.497.

[(h2)] Projected equatorial rotation velocity from T08 for star B based on an iterative orbital solution for which the difference in the temperature between the primary and the secondary stars and fraction of the combined system light due to the two components was calculated.

[(j)] Microturbulent speed as derived by Baugh et al. (2013).

[(k)] Luminosity from the deduced T_{eff} and radius values. S21 notes that the distance implied by these luminosities "is slightly shorter than that obtained from the Gaia EDR3 parallax, a discrepancy most easily explained by uncertainty in the 2MASS K-band apparent magnitude."

[(m)] S21.

[(n)] *Gaia* (re-interpreted) EDR3 parallaxes, Bailer-Jones et al. (2021).

contribution to the continuum spectral energy distribution (w_A and w_B), and the microturbulent velocity (ξ_{th}). The two methods used to determine chemical abundances rely heavily on theoretical stellar atmosphere models. The first is the curve of growth method. It uses the equivalent widths of numerous absorption lines measured on the observed spectrum, which are compared to those of a grid of stellar atmosphere models. The second is a direct comparison of the observed absorption line spectrum with synthetic spectra predicted by a grid of theoretical stellar atmosphere models. Both methods require precise values of the relative continuum contributions from stars A and B, w_A and w_B.

Each star's contribution to the normalized continuum is obtained from the T_{eff} and rr values as follows. Defining a weight w_i=$L_i/(L_A + L_B)$, with L_i the luminosity of each star (i=A, B), and assuming that the black-body function is a valid approximation for the visual portion of the spectral energy distribution, we can write w_A/w_B=$(R_A/R_B)^2(T_A/T_B)^4$, with $w_A + w_B$=1.

The results shown in Figure 2 indicate that both rr and T_A/T_B are insensitive to metallicity. Using their values as listed in Table 1, we find w_A/w_B=1.0740, from where w_A=0.518 and w_B=0.482. These values were used for the subsequent analyses.

4.1. Equivalent widths of Fe lines

We measured the equivalent widths (W_λ) for 26 Fe I lines in the wavelength range $\lambda\lambda$6042-6718 in the September 20 spectrum. For comparison, we chose stellar atmosphere models having the T08 and S21 effective temperature, surface gravity and relative luminosities, and the microturbulent speed from Baugh et al. (2013) (see Table 2). The Fe I abundance was determined with the *abfind* driver in the LTE spectral synthesis and line analysis code *MOOG* (Sneden et al., 2012).[6] *MOOG* uses a carefully curated list of lines of well-determined gf values to synthesize a spectrum from stellar atmosphere models. The equivalent-width method for Fe-abundance determinations has the advantage that it does not depend on rotation velocity.

We tested models with [M/H] at −0.1, −0.2, −0.3, and −0.4 dex. This resulted in abundances 7.286, 7.285, 7.284, and 7.282, respectively, for star A, and 7.212, 7.212. 7.211, and 7.209 for star B. Thus, for each star we get an average ±s.d. of $\log(Fe)_A$=7.284±0.002 and $\log(Fe)_B$=7.211±0.001.

We also ran *MOOG* with the solar equivalent widths for the same list of lines, and a solar model at 5780 K and log g = 4.4 which was computed with the same program interpolating in the MARCS model grid. Many of the lines are rather strong in the Sun and give a lower abundance than the weaker lines. We eliminated lines stronger than Log W_λ = −4.8 (∼100 mA), and got an abundance of $\log(Fe)_\odot$ = 7.43 from this set, using a microturbulence of 1 km s^{-1} (which is the accepted value for the center-of-disk, consistent with the McMath atlas (Wallace et al., 1998)).

With the definition $[Fe/H] = \log(Fe/H) - \log(Fe/H)_\odot$ and assuming the same hydrogen abundances $\log(H) = \log(H)_\odot$, the above values of $\log(Fe)$ correspond to $[Fe/H]$ =-0.146 for star A and $[Fe/H]$ =-0.219 for star B. We adopt an uncertainty of ±0.07 dex due primarily to the uncertainty in continuum placement.

The iron abundance of star A is in excellent agreement with that of Baugh et al. (2013) (−0.15±0.03) and T08 (−0.12±−0.03), both of which are based on comparisons to Kurucz (1992) model atmosphere spectra. The iron abundance that we derive for star B is marginally lower, and more in line with the −0.25 value reported by Casagrande et al. (2011b). It is even closer to the Casagrande et al. (2011b) value if a solar microturbulence of 0.8 km s^{-1}ec is assumed (which gives a flatter dependence on line strength and a solar abundance of 7.47) resulting in $[Fe/H]$ = −0.186 and −0.259 for stars A and B, respectively. Column 3 of Tab. 3 summarizes the results of this experiment.

4.2. Modeling absorption-line profiles

Synthetic spectra in the $\lambda\lambda$ 6388-6418 Å region were generated using the *Pymoogi* Python wrapper for *MOOG* (Adamow, 2017).[7] We used MARCS stellar atmospheres models (Gustafsson et al., 2008), interpolating the available grid when required to produce synthetic spectra. Each model is characterized by the effective temperature T_{eff}, the logarithm of the surface gravity $\log(g)$, and the heavy element abundance $[Fe/H]$. Our grids of models were generated for T_{eff} in the range 6450 K to 6800 K, and $[Fe/H]$ in the range −0.4 to −0.1, with fixed $\log(g)$ and ξ_{th} as listed in Column 2 of Table 2.

The single-star spectra produced by MOOG were scaled and combined to synthesize V505 Per's double-line spectrum using the scaling factors w_A=0.518, w_B=0.482, as discussed above.

A detailed comparison between synthetic and observed spectra requires rotational broadening to be applied to the synthetic-spectral lines. In order to constrain the value of v sin(i) we used the *rotBroad* function included in the *pyAstronomy* package[8] to broaden a composite synthetic spectrum to projected rotation velocities in the range 10 km s^{-1}–14 km s^{-1}. A linear limb-darkening coefficient of 0.26 was adopted from S21. Figure 3 compares the observed λ6393.6 and λ6411.6 lines to the synthetic spectra broadened to v sin(i)=12 km s^{-1} and 13 km s^{-1}. These two spectral lines are relatively free from blending effects. We find that the higher speed yields a slightly better fit to the profiles of star A, while the lower speed is slightly better for star B, but both speeds are viable within the uncertainties of the data. Hence, we adopt v sin(i)=12.5 ±1 km s^{-1} as the most likely rotation speed of both stars. It

[6] http://www.as.utexas.edu/ chris/moog.html

[7] github.com/madamow/pymoogi

[8] pyastronomy.readthedocs.io/en/latest/pyasIDoc/asIDoc/rotBroad.html, github.com/sczesla/PyAstronomy/blob/master/src/pyasl/asl/rotBroad.py

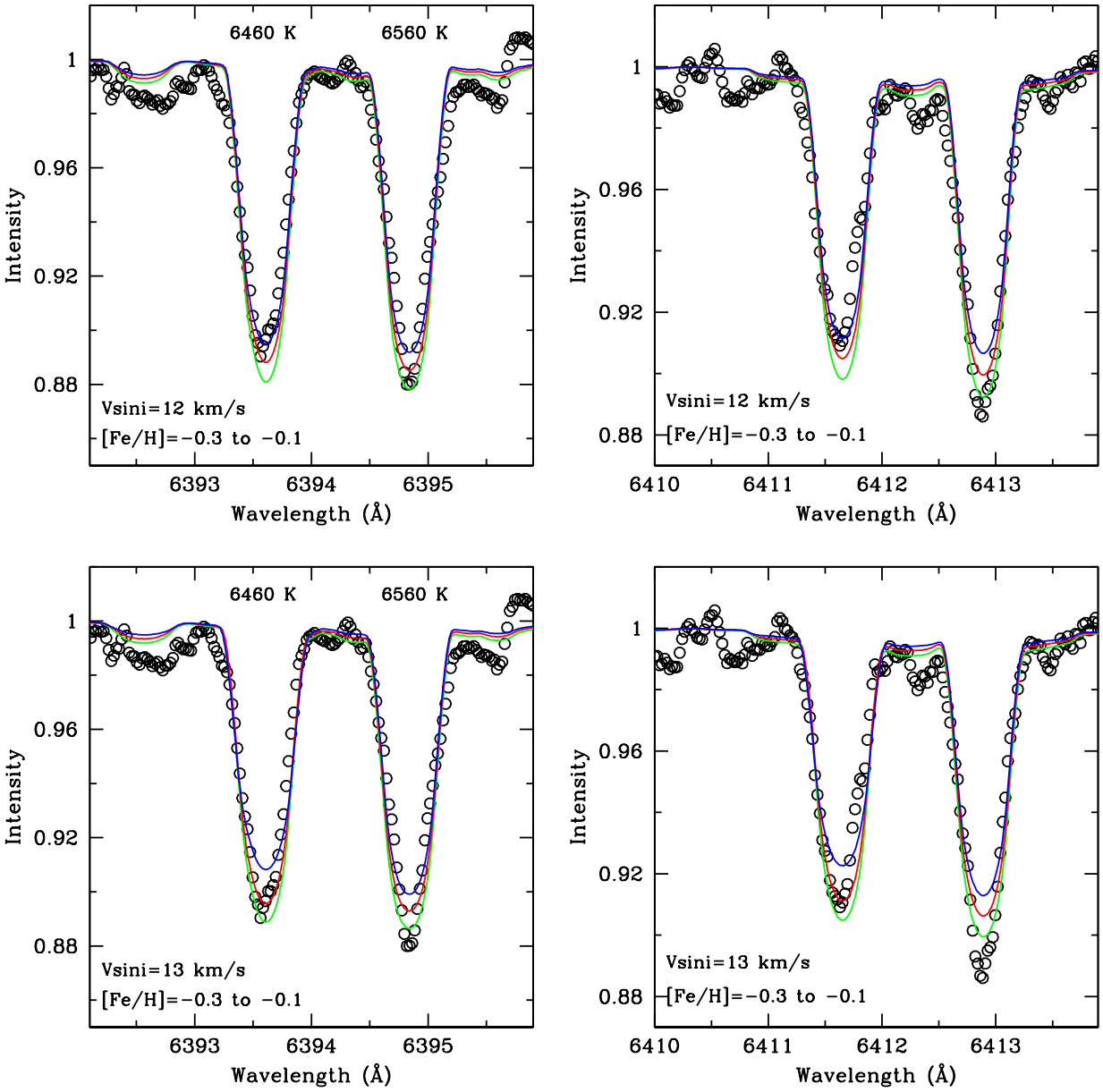

Figure 3. Determination of v sin(i): Shown are the rotationally-broadened synthetic line profiles from model atmospheres with T_{eff}, log(g), and ξ values from column 2 of Table 2, and for $[Fe/H] = -0.1$ (green), -0.2 (red) to -0.3 (blue). Rotational broadening v sin(i)=12 km s^{-1} (top) and 13 km s^{-1} (bottom) compare most favorable to the 5-point smoothed observations (dots).

is noteworthy that this value is smaller than the 15 km s^{-1} synchronous rotation velocity which was determined by T08, a discrepancy that we attribute to the lower spectral resolution of the T08 data compared to our echelle spectra.

For v sin(i) between 12 and 13 km s^{-1}, Figure 3 shows that the line profiles are consistent with $[Fe/H] = -0.10\pm0.05$ (star A) and -0.25 ± 0.1 (star B), similar to the result obtained from equivalent widths.

Figure 4 shows a selection of star A's lines compared to the synthetic line profiles from models with either T_{eff}=6460 K or 6600 K. The higher T_{eff} provides a better match to the observations and is particularly better for the Fe I λ6400 line because of the contribution from λ6400.316. This line contributes to the red wings of the blend. The lower temperature produces synthetic profiles with red wings that are clearly too extended.

The λ6400.316 line has an excitation potential 0.91 eV, compared to 3.60 eV for the λ6400.001 line, making it more sensitive to temperature. We conclude that, for star A, the best match to the line profile is with T_{eff}=6650$\pm$50 K, consistent with the $[Fe/H] = -0.15$ evolutionary track in Figure 2.

Given the constraint on the effective temperature ratio imposed by the light curve, the above results show that the

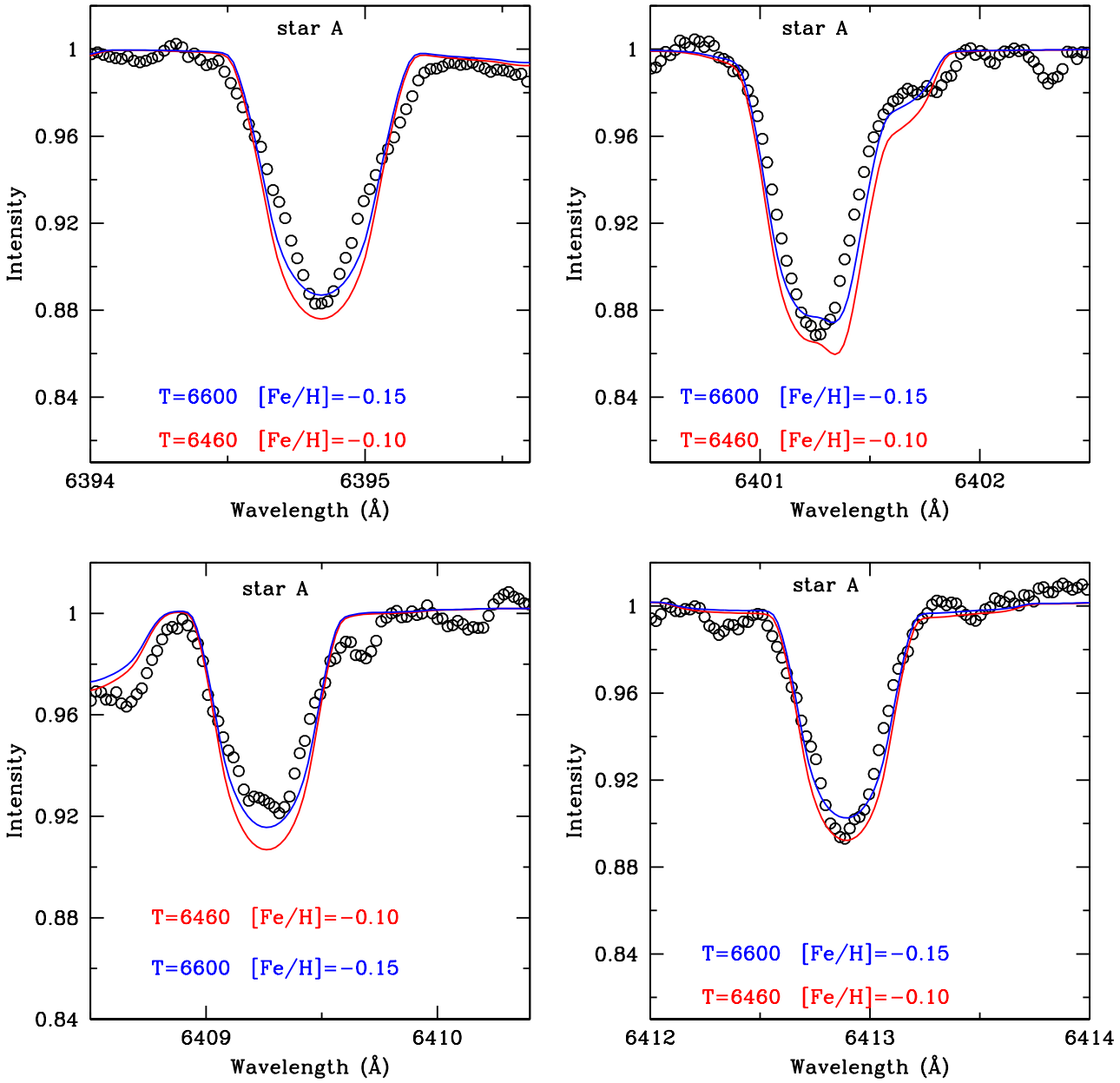

Figure 4. Line profiles of the primary star (dots) compared to model spectra with (T_{eff}, $[Fe/H]$)=(6460 K, −0.10) (red) and (T_{eff}, $[Fe/H]$)=(6600 K, −0.15) (blue). The model line profiles were broadened to v sin(i)=12 km s^{-1}. The λ6413 line is rather insensitive to T_{eff}, while λ6400.3 shows a relatively strong temperature sensitivity. This figure shows that models with $[Fe/H] > -0.1$ do not adequately represent the observations.

temperature of star A forced the effective temperature of star B to be 6550 K. Synthetic profiles computed with this temperature for star B are compared to the observations shown in Figure 5. We find that synthetic spectra with T_{eff} in the range 6460-6550 K yield viable fits to the observed profile. It is unclear whether this larger uncertainty in the secondary's temperature results from line profiles that are perturbed with respect to the predicted line shapes. What is clear is that $[Fe/H] > -0.1$ can be excluded for the entire temperature range. The constraints of the evolutionary tracks (Figure 2) lead to the conclusion that a higher temperature is favored.

5. Lithium abundance

The lithium abundance $A(Li)$ was constrained by comparing synthetic spectra constructed with MOOG with the observed spectrum in the $\lambda\lambda$6704–6710 wavelength range. We first analyzed $A(Li)$ by adopting effective temperatures of 6500 K and 6450 K, which approximately

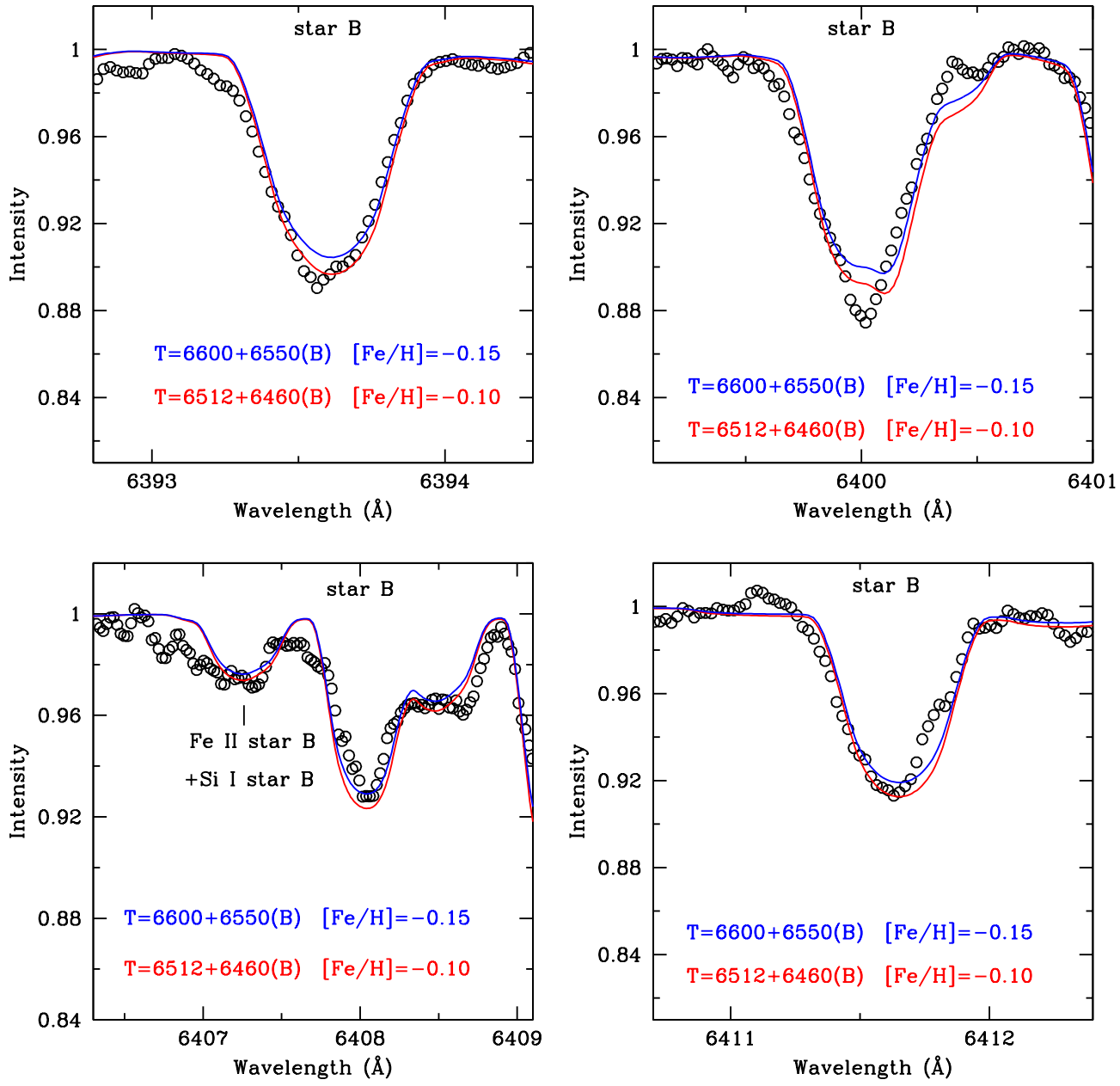

Figure 5. Line line profiles of the primary star (dots) compared to model spectra with (T_{eff}, $[Fe/H]$)=(6460 K, −0.10) (red) and (T_{eff}, $[Fe/H]$)=(6600 K, −0.15) (blue). The model line profiles are broadened to v sin(i)=12 km s^{-1}. The λ6413 line is rather insensitive to T_{eff}, while λ6400.3 shows a relatively strong temperature sensitivity. This figure shows that models with $[Fe/H] > -0.1$ would not adequately represent the observations.

correspond to those determined by T08. We found $A(Li)$ =2.45±0.07 (star A) and 2.25±0.1 (star B), values that are marginally consistent with those of Baugh et al. (2013) (2.67±0.1 and 2.42 ±0.2), and concluded that the two components seem to have slightly different Li abundances. A comparison between the synthetic spectra and observations for this case is shown in Fig. 6 (left panel).

We next analyzed the spectra under the assumption that the stars are hotter, 6650 K+ 6600 K, as implied by the λ6400 line profile. This yielded lithium abundances $A(Li)$=2.65±0.07 (star A) and 2.35±0.07 (star B), consistent with Baugh et al. (2013) determination. The strength of the Li lines does not have a significant dependence on the $[Fe/H]$ value; therefore, our results are not strongly dependent on the uncertainty in iron abundances. However, it depends more strongly on the effective temperature, as shown above. Our data are unfortunately too noisy to provide a constraint on the Li abundance to better than 0.05–0.1 dex, but both effective temperature sets do imply a somewhat lower $A(Li)$ in the secondary

Table 3. Results

Parameter	Literature	This paper		
		Equiv. Width	Line Prof.	Line Prof.
R_B/R_A	0.98	0.98f[a]	0.98f	0.98f
$[Fe/H]_A$	−0.15(.03)	−0.166(.07)[b]	−0.15(.05)	−0.15(.05)
$[Fe/H]_B$	−0.12(.03)	−0.239(.07)[b]	−0.15(.05)	−0.15(.05)
T_{Aeff}(K)	6512(50)	6512(adopted)	6500f	6600(50)
T_{Beff}(K)	6460(50)	6460(adopted)	6450f	6550(50)
v sin$(i)_A$ (km s^{-1})	⋯	⋯	12.5(.5)	12.5(.5)
v sin$(i)_B$ (km s^{-1})	⋯	⋯	12.5(.5)	12.5(.5)
$A(Li)_A$	2.67(.1)	⋯	2.45(.07)	2.65(0.07)
$A(Li)_B$	2.42(.2)	⋯	2.25(0.1)	2.35(.07)

[a]The "f" next to a value indicates that it was a fixed value.

[b]Values are the average of the results found from the two *IRAF/abfind* fits (solar microturbulent velocities 1 km s^{-1} and 0.8 km s^{-1}).

than in the primary. Future observations should aim for significantly higher S/N spectra to allow for more precise abundance determinations (as have been performed for the visual binary components of ζ Boo A and B by Strassmeier & Steffen (2022).

6. Discussion

In this study, we analyzed a high-resolution spectrum of the eclipsing binary V505 Per. The objective was to resolve three inconsistencies related to the chemical abundance of the two components: (a) The first is the subsolar Fe abundance reported by Baugh et al. (2013); Casagrande et al. (2011b), found from spectral and photometric analyses, which is inconsistent with the approximately solar abundance found by Southworth (2021) from the isochrone fitting. (b) The second is the Li abundance found by Baugh et al. (2013), which is factors of 2-5 larger than that observed in similar age and temperature single stars that lie in the Lithium Dip. (c) The third is the secondary Li abundance found by Baugh et al. (2013) is significantly lower than that of the primary, while both stars are expected to have the same age and therefore the same abundances. We first analyzed all available *TESS* photometric data to constrain the parameters that can be derived from the analysis of the eclipse light curve (Table 1), which, combined with the published solution for the radial velocity curves, yielded the first set of fundamental parameters for the system. Because the solution of the light curve only yields the sum of the stellar radii ($R_A + R_B$) and not the ratio, we used theoretical evolutionary tracks to constrain the value of R_B/R_A. We found that for a fixed value $R_A + R_B$ as derived from the light curve, neither the R_B/R_A nor the temperature ratio T_A/T_B strongly depends on metallicity, with the solar and subsolar options yielding nearly identical values. However, the actual temperature strongly depends on metallicity. If the previously published temperatures (T08) are adopted, then the system's metallicity is at least solar, as concluded by S21, but the system is significantly older (1.5 Gyr instead of ∼1 Gyr). However, if instead the values of $[Fe/H]$ are as low as determined by Baugh et al. (2013) and Casagrande et al. (2011b), then T_{eff} must be approximately T_{Aeff} ∼6670 K and T_{Beff} ∼6620 K. We compared our observed spectrum with stellar atmosphere models with T_{eff}/K in the range [6400, 6800] and $[Fe/H]$ in the range [-0.4, -0.1] and found that $[Fe/H]$ values larger than −0.1 could be excluded. Specifically, for the primary/secondary star we found $[Fe/H]$=−0.17±0.07/−0.25±0.07 from Fe I equivalent widths (§ 4.1). By comparing synthetic and observed line profiles, we found $[Fe/H] \sim -0.13\pm0.05$ (Figures 4 and 5). Most of the primary star's line profiles are best reproduced with T_{eff} ∼6600 K and $[Fe/H] = -0.15$ (Figure 4). From the temperature ratio, which is fixed by the light curve solution, this implies that the secondary's effective temperature is ∼6550 K. However, we find that synthetic spectra with T_{eff} in the range 6460-6550 K yield viable fits to the observed profile. It is not clear whether the larger uncertainty in the secondary derived parameters results from line profiles that seem somewhat perturbed with respect to the predicted line shapes. Having found that temperatures higher than the T08 values are viable, we proceeded to fit synthetic lithium line profiles to the observations. The only well-resolved Li I lines in our spectrum are those of the λ6707.83 blend. The strength of these lines is significantly more dependent on T_{eff} than on $[Fe/H]$. Thus, we modeled the Li lines with the T08 temperatures (for consistency with the results of Baugh et al., 2013) as well as at temperatures 150 K higher. We found $A(Li)$ values that are consistent with those determined by Baugh et al. (2013) within their uncertainties, and we also confirmed that the lithium abundance of the secondary was slightly lower than that of the primary.

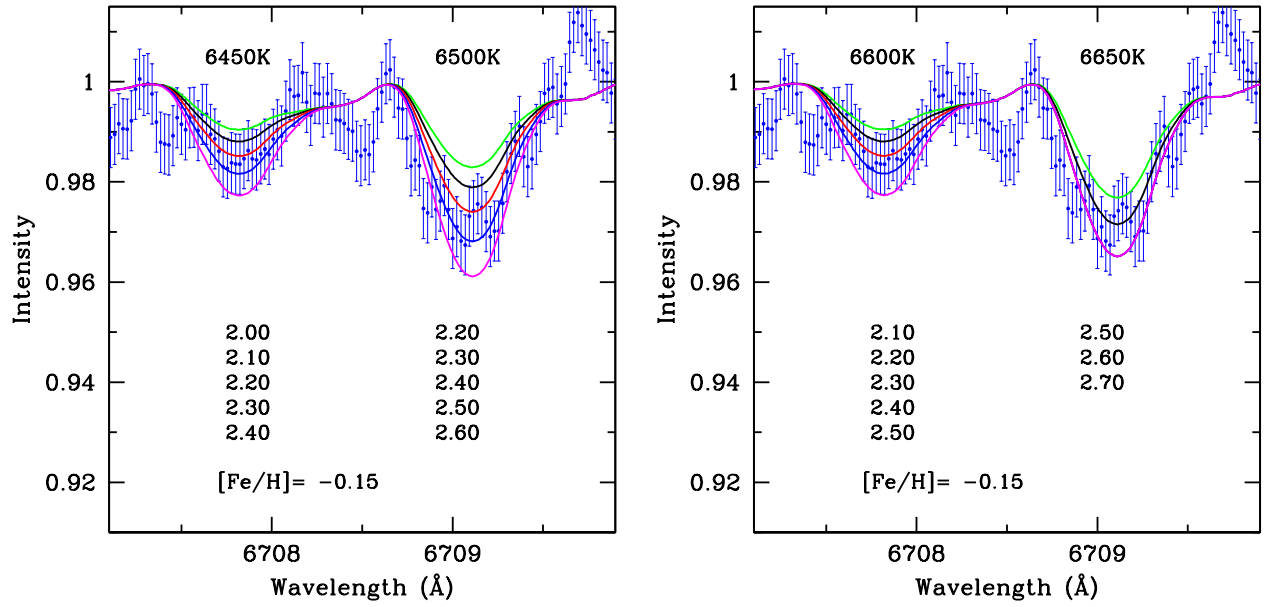

Figure 6. Synthetic spectra with different lithium abundances compared to the observed 5-point smoothed data (dots). The model A(Li) values for each star are listed below the corresponding Li line. The top value (green) corresponds to the curve with the smallest A(Li), and the bottom corresponds to the largest. The error bars indicate a 0.6% uncertainty in the 5-point smoothed data. **Left:** Composite model spectra with T08 effective temperature. **Right:** T_{eff} =(6650 K, 6600 K) for stars A and B, respectively. The synthetic spectra are all broadened to v sin(i)=12 km s^{-1}.

6.1. Higher temperatures eliminate the discrepancy with the Lithium Dip

A higher T_{eff} places the stars at the hot limit of the Lithium dip where there is a steep rise in $A(Li)$, eliminating the discrepancy between their $A(Li)$ and that of cluster stars of a similar age. This is illustrated in Figure 7, where we plot $A(Li)$ *vs.* T_{eff} from Balachandran (1995) for the Hyades cluster (age ∼ 625 Myr), Praesepe (age ∼680 Myrs), and and NGC752 (age estimates ranging from 1.34 to 1.61 Gyr).

Higher temperatures are also more in line with the Mass-T_{eff} relation for NGC 752 than with that of the younger clusters, as shown in Figure 8, where we plot the same stars as in Figure 7 with data from Balachandran (1995).

Lithium is destroyed by proton capture in stellar interiors at a temperature ∼2.5 million degrees. In main sequence solar-type stars (M∼1.0±0.10 M$_\odot$), this temperature is reached below the base of the surface convective zone, which makes it unlikely for Li-depleted material to reach the surface unless there is an additional mechanism that transports it to the convective zone. In the absence of such a mechanism, the surface Li abundance during the main sequence is not predicted to be anomalous. However, evidence for the existence of such an additional mechanism is clearly found, for example, in plots of $A(Li)$ *versus* effective temperature T$_{eff}$ in main sequence cluster stars with 6300< T_{eff} <6900 K (Boesgaard & Tripicco, 1986; Boesgaard & King, 2002) in what is called the *Li Dip*. The mechanism responsible for excess mixing during the main sequence is thought to be associated with stellar rotation. In binaries, it has long been suspected that the presence of a companion can impact the manner in which the mixing process proceeds. This is particularly true for tidally locked systems, in which differential rotation and strong currents should be suppressed, thus inhibiting strong mixing. However, asynchronous binaries may provide a mechanism by which enhanced mixing can occur as a consequence of local differential rotation gradients (Song et al., 2013; Koenigsberger et al., 2021).

Our results indicate that both components of V505 Per rotate subsynchronously. However, this result was based on a single orbital phase near conjunction. The *TESS* light curve displays a clear ellipsoidal effect, implying that the stars are distorted from a purely spherical shape. Thus, observations at other orbital phases are required to determine whether the stars are truly in subsynchronous rotation or if they undergo line profile variability, which makes the line profiles appear narrower near conjunction.

6.2. Higher temperatures are still consistent with the SED

A higher effective temperature has an impact on the spectral energy distribution (SED), so the natural question that arises is whether the SED of a T_{eff}=6650 K + 6550 K system is consistent with the observations. [9]

[9]There can be differences of up to 200 K in the effective temperatures as determined photometrically, depending on the calibrations that are used, which has an impact on the [Fe/H] values; see, for example, Balachandran

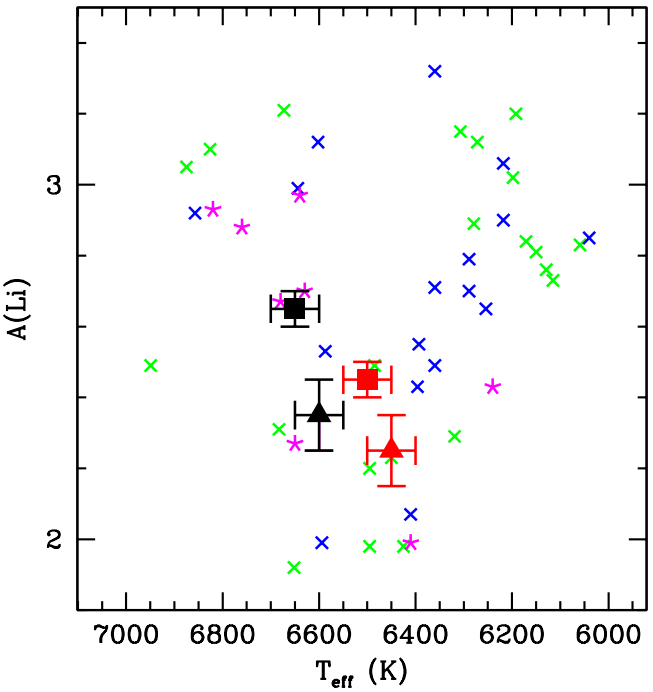

Figure 7. Lithium abundance as a function of effective temperature. Crosses indicate data from Balachandran (1995) as follows: Hyades (green, age ∼ 625 Myr), Praesepe (blue, age ∼680 Myrs), and NGC752 (magenta, age estimates ranging from 1.34 to 1.61 Gyr). Our determinations are shown with a filled-in square for star A and a filled-in triangle for star B. Red/black symbols correspond to the lower/higher effective temperatures (Table 3).

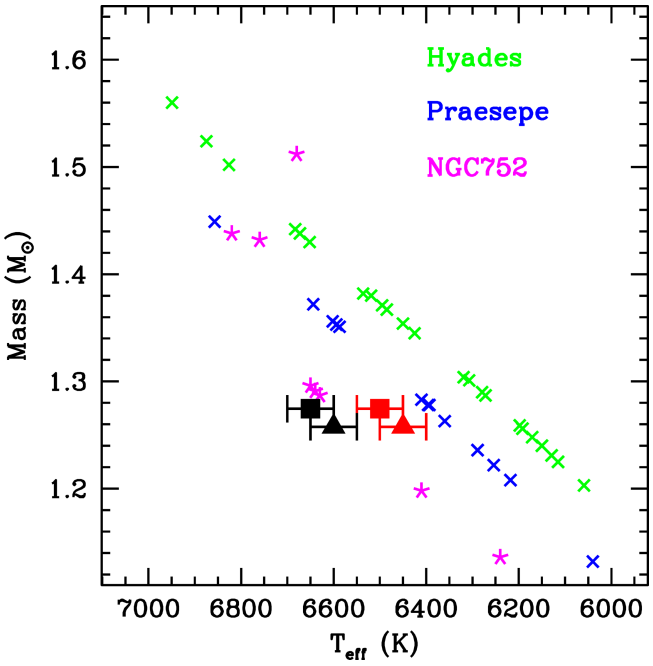

Figure 8. The Mass-Effective Temperature data from Balachandran (1995) (open squares) for the same stars plotted in Figure 7. The filled-in square and triangle are as follows: Hyades (green, age ∼ 625 Myr), Praesepe (blue, age ∼680 Myrs), and NGC752 (red, age estimates ranging from 1.34 to 1.61 Gyr). Our star A determinations are shown with a filled-in squares and starB with filled-in triangles.

We now show that higher T_{eff} values are consistent with the observed SED. In Figure 9 we plot the observed absolute flux in different wavelength bands available in the literature. Specifically, we used the Bp, G, and Rp fluxes, absolute flux calibrated as given in Vizier (Ochsenbein et al., 2000), referring to the GAIA DR3 data release (Riello et al., 2021), to the 2MASS sky survey (Skrutskie et al., 2006) for the Johnson filter J, H, K measurements (nominal effective wavelengths 1250 nm, 1630 nm, and 2190 nm respectively), and the Gaia XP spectrum (De Angeli et al., 2023). The latter is approximately 5 % brighter than the other Gaia fluxes; therefore, we scaled the XP spectrum by 0.95 to bring it into agreement with the other Gaia fluxes. The absolute fluxes are compared to composite model SEDs for three effective temperatures assuming stellar radii as determined by S21 (1.294 $R_\odot$ and 1.264 $R_\odot$) and a distance $D = 62.14 \pm 0.12$ pc, which results from a Gaia DR3 parallax of $\pi = 16.068 \pm 0.02$ mas and a zero point correction of $Z5 = -0.024$ mas according to the recipe given by (Lindegren et al., 2021).[10]

The models were interpolated for log(g)=4.3, $[M/H]$=−0.25 and T_{eff}= 6500 K, 6625 K, and 6750 K from the Atlas9 Castelli-Kurucz grids (Castelli & Kurucz, 2003)[11].

For each of the effective temperatures, the SEDs are reddened, respectively, by $E(B-V) = 0, = 0.02$, and $= 0.03$ It can be seen that there is no significant difference between these models and the observed energy distribution.

However, the obvious difference between the models and the absolute fluxes is that the models have about a 3 % too small flux in the infrared. The dominant uncertainty at these wavelengths are the Johnson filter measurements, which for the K filter is ±2 %. Thus, the difference is statistically not significant but it seems to be real because it is for both the H and K filters at approximately the same ratio. Any absolute difference at optical wavelengths can be compensated for by reddening.

7. Conclusions

Adopting the T_{eff} values from T08, Baugh et al. (2013) determined lithium abundances that are significantly higher than the lithium abundance in similar-age cluster stars at the same temperature. They also found that star A and star B have marginally different $A(Li)$. We repeated this

(1995). NOTE: This author (and others?) plot A(Li) vs. τ_{ZAM}. This means that for the older clusters, they have to assume an evolutionary model predicting the T_{ZAMS} given the current τ_{eff} and the age of the system.

[10] S21 determined a distance D=61.19±0.62 pc to the system, while the *Gaia* (re-interpreted) EDR3 parallaxes give 62.03±0.10 pc (Bailer-Jones et al. (2021)).

[11] https://wwwuser.oats.inaf.it/fiorella.castelli/grids/gridp00k2odfnew/fp00k2tab.html

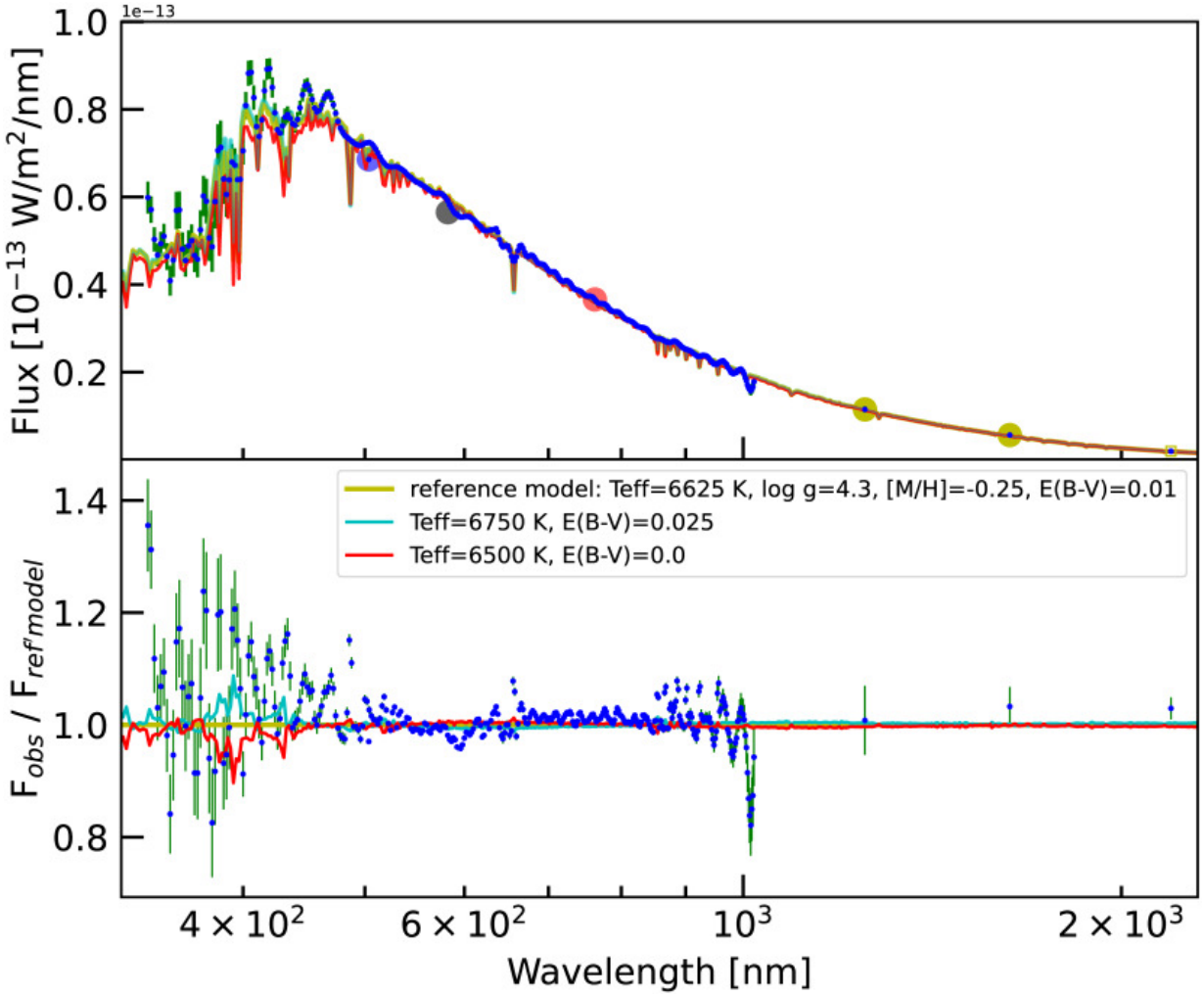

Figure 9. Top: Observed spectral energy distribution of V505 Per compared to theoretical SEDs for two stars with T_{eff}= 6500 K (red), 6625 K (dark green, Reference Model), and 6750 K (light green), and adopting a distance $D = 62.14 kpc$. The observations are as follows: large blue, grey, and red circles for the Gaia Bp, G, and Rp fluxes, respectively. large yellow circles and small blue point for Johnson J, H, and K fluxes; small blue points with green error bars for the Gaia spectral energy distribution (scaled by a factor 0.95 to make it consistent with the Gaia Rp filter flux, see text). Bottom: Ratios of the observed SED models with the reference model in the denominator. Narrow peaks in the ratio result from a mismatch of resolution, because the Kurucz model has a higher resolution than the Gaia XP low resolution data. This mismatch is particularly prominent in the hydrogen line wavelengths. Also shown are the ratios of T_{eff} =6500 K and 6750 K models to the reference model. Differences between these models and the reference model are only visible in the 400 nm region where the hotter model has a ratio larger than unity, and the cooler less than unity. In this wavelength region the combination of several strong narrow absorption lines in the Kurucz reference model and relatively large uncertainties in the observations makes it difficult to judge which model provides the best fit, although it seems likely that that the reference model with T_{eff} =6625 provides the best fit. Thus, we conclude that the observed SED is consistent with hotter T_{eff} than those determined by T08.

analysis with our R=100,000, S/N∼100 echelle spectrum to confirm these results. However, our analysis of the Fe I line profiles suggests that T_{eff} could be at least 150 K larger than the values determined by T08. Allowing for hotter T_{eff}, we find that both stars lie near the hot edge of the Lithium Dip, where such abundances are not uncommon. Higher T_{eff} values also help relieve the tension between the model line profiles of the λ6400.35 absorption line, because at lower temperatures, the red wing of the line profile is significantly stronger than that observed. In addition, the combined constraints of the eclipse light curve and the evolutionary tracks require higher T_{eff} values to satisfy the results obtained by us and other authors that $[Fe/H]$ is subsolar. The higher effective temperatures suggested by our analysis would still be consistent with the observed spectral energy distribution of the V505 Per system, although marginally larger K-band fluxes are observed than predicted by the models. If this difference is real, V505 Per may contain an as yet undetected, low mass third object.

Further high S/N and spectral resolution observations are needed to allow for more precise abundance determinations, as well as to check for orbital phase-dependent variations that could affect the line strengths and profiles, particularly because we find the stars to be in subsynchronous rotation and hence could be undergoing tidally driven perturbations which are dependent on the orbital phase.

Support from the UNAM DGAPA PAPIIT program IN105723 and the Indiana University Institute for Advanced Study are gratefully acknowledged. GK and AM thank Andrew Tkachenko for his useful comments during the early phase of this investigation.

References

Adamow, M. M. 2017, in AAS, Vol. 230, 216.07
Bailer-Jones, C. A. L., Rybizki, J., Fouesneau, M., Demleitner, M., & Andrae, R. 2021, AJ, 161, 147, doi: 10.3847/1538-3881/abd806
Balachandran, S. 1995, ApJ, 446, 203, doi: 10.1086/175779
Baugh, P., King, J. R., Deliyannis, C. P., & Boesgaard, A. M. 2013, PASP, 125, 753, doi: 10.1086/671721
Boesgaard, A. M., & King, J. R. 2002, ApJ, 565, 587, doi: 10.1086/324436
Boesgaard, A. M., & Tripicco, M. J. 1986, ApJ, 303, 724, doi: 10.1086/164120
Casagrande, L., Schöenrich, R., Asplund, M., et al. 2011a, VizieR Online Data Catalog: Geneva-Copenhagen survey re-analysis (Casagrande+, 2011), VizieR On-line Data Catalog: J/A+A/530/A138. Originally published in: 2011A&A...530A.138C, doi: 10.26093/cds/vizier.353001 38
Casagrande, L., Schönrich, R., Asplund, M., et al. 2011b, A&A, 530, A138, doi: 10.1051/0004-6361/201016276
Castelli, F., & Kurucz, R. L. 2003, in IAUS, Vol. 210, Modelling of Stellar Atmospheres, A20, doi: 10.48550/arXiv.astro-ph/0405087
De Angeli, F., Weiler, M., Montegriffo, P., et al. 2023, A&A, 674, A2, doi: 10.1051/0004-6361/202243680
del Burgo, C., & Allende Prieto, C. 2018, MNRAS, 479, 1953, doi: 10.1093/mnras/sty1371
do Nascimento, J. D., J., Charbonnel, C., Lèbre, A., de Laverny, P., & De Medeiros, J. R. 2000, A&A, 357, 931, doi: 10.48550/arXiv.astro-ph/0003010
Ginsburg, A., Sipőcz, B. M., Brasseur, C. E., et al. 2019, AJ, 157, 98, doi: 10.3847/1538-3881/aafc33
Gustafsson, B., Edvardsson, B., Eriksson, K., et al. 2008, A&A, 486, 951, doi: 10.1051/0004-6361:200809724
Holmberg, J., Nordström, B., & Andersen, J. 2007, A&A, 475, 519, doi: 10.1051/0004-6361:20077221
Koenigsberger, G., Moreno, E., & Langer, N. 2021, A&A, 653, A127, doi: 10.1051/0004-6361/202039369
Kurucz, R. L. 1992, in IAUS, Vol. 149, The Stellar Populations of Galaxies, ed. B. Barbuy & A. Renzini (Kluwer Academic Publishers, Dordrecht), 225
Kwee, K. K., & van Woerden, H. 1956, BAN, 12, 327
Lightkurve Collaboration, Cardoso, J. V. d. M., Hedges, C., et al. 2018, Lightkurve: Kepler and TESS time series analysis in Python, Astrophysics Source Code Library, record ascl:1812.013
Lindegren, L., Bastian, U., Biermann, M., et al. 2021, A&A, 649, A4, doi: 10.1051/0004-6361/202039653
Mowlavi, N., Eggenberger, P., Meynet, G., et al. 2012, A&A, 541, A41, doi: 10.1051/0004-6361/201117749
Ochsenbein, F., Bauer, P., & Marcout, J. 2000, A&AS, 143, 23, doi: 10.1051/aas:2000169
Pavlovski, K., Southworth, J., Tkachenko, A., Van Reeth, T., & Tamajo, E. 2023, A&A, 671, A139, doi: 10.1051/0004-6361/202244980
Pourbaix, D., Tokovinin, A. A., Batten, A. H., et al. 2004, A&A, 424, 727, doi: 10.1051/0004-6361:20041213
Prša, A., Harmanec, P., Torres, G., et al. 2016, AJ, 152, 41, doi: 10.3847/0004-6256/152/2/41
Prša, A., Kochoska, A., Conroy, K. E., et al. 2022, ApJS, 258, 16, doi: 10.3847/1538-4365/ac324a
Ricker, G. R., Winn, J. N., Vanderspek, R., et al. 2015, JATIS, 1, 014003, doi: 10.1117/1.JATIS.1.1.014003
Riello, M., De Angeli, F., Evans, D. W., et al. 2021, A&A, 649, A3, doi: 10.1051/0004-6361/202039587
Skrutskie, M. F., Cutri, R. M., Stiening, R., et al. 2006, AJ, 131, 1163, doi: 10.1086/498708
Sneden, C., Bean, J., Ivans, I., Lucatello, S., & Sobeck, J. 2012, MOOG: LTE line analysis and spectrum synthesis, Astrophysics Source Code Library, record ascl:1202.009
Song, H. F., Maeder, A., Meynet, G., et al. 2013, A&A, 556, A100, doi: 10.1051/0004-6361/201321870
Southworth, J. 2021, Obs, 141, 234, doi: 10.48550/arXiv.2106.04323
Strassmeier, K. G., & Steffen, M. 2022, AN, 343, e20220036, doi: 10.1002/asna.20220036
Swade, D., Fleming, S., Mullally, S., et al. 2019, in ASPC, Vol. 523, Astronomical Data Analysis Software and Systems XXVII, ed. P. J. Teuben, M. W. Pound, B. A. Thomas, & E. M. Warner, 453
Thorburn, J. A., Hobbs, L. M., Deliyannis, C. P., & Pinsonneault, M. H. 1993, ApJ, 415, 150, doi: 10.1086/173152
Tomasella, L., Munari, U., Siviero, A., et al. 2008, A&A, 480, 465, doi: 10.1051/0004-6361:20078384
Wallace, L., Hinkle, K., & Livingston, W. 1998, An atlas of the spectrum of the solar photosphere from 13,500 to 28,000 cm-1 (3570 to 7405 A)

Revista Mexicana de Astronomía y Astrofísica, 61, 98-119, (2025)

OPEN ACCESS https://doi.org/10.22201/ia.01851101p.2025.61.02.09

Physical Properties of H II Regions at Sub-kpc Scales Using Integral Field Spectroscopy on IC 342

J. K. Barrera-Ballesteros[1], S. F. Sánchez[2], K. Kreckel[3], A. Lugo-Aranda[1], H. Ibarra-Medel[1], L. Carigi[1], N. Drory[4], D. Bizyaev[5,6], J. E. Méndez Delgado[3] and Guillermo Blanc[7,8]

[1]*Universidad Nacional Autónoma de México, Instituto de Astronomía, AP 70-264, CDMX 04510, México.*
[2]*Universidad Nacional Autónoma de México, Instituto de Astronomía, AP 70-264, CDMX 04510, México.*
[3]*Astronomisches Rechen-Institut, Zentrum für Astronomie der Universität Heidelberg, Mönchhofstraße 12-14, 69120 Heidelberg, Germany.*
[4]*University of Texas at Austin, McDonald Observatory, 1 University Station, Austin, TX 78712, USA.*
[5]*Apache Point Observatory and New Mexico State University, P.O. Box 59, Sunspot, NM 88349-0059, USA.*
[6]*Sternberg Astronomical Institute, Moscow State University, Moscow, Russia.*
[7]*The Observatories of the Carnegie Institution for Science, 813 Santa Barbara St., Pasadena 91101, CA, USA.*
[8]*Departamento de Astronomía, Universidad de Chile, Camino del Observatorio 1515, Las Condes, Santiago, Chile.*

Keywords: *TBD*

Abstract

In this study, we use Integral Field Spectroscopic (IFS) observations for one of the closest galaxies to us, the grand design spiral IC 342, to derive the physical properties of H II regions at sub-kpc scales. To our knowledge, the IFS data represent the most comprehensive observational effort in the optical range for this galaxy. The final IFS datacube consists of 349 individual pointings using IFS instrumentation from the SDSS-IV MaNGA survey. Using a prototype of the data analysis pipeline that will be devoted to the SDSS-V Local Volume Mapper (LVM) survey, we measured different observables from the optical emission line. In particular, using the flux map of the Hα emission line, we derived the location and size of H II region candidates for IC 342. Using the integrated flux for different emission lines within each region, we derived the radial distribution of different physical properties from the ionized gas (e.g., optical extinction, Hα luminosity, oxygen abundance, etc.). Compared with larger samples of galaxies with IFS data, our results suggest that the physical properties of the ionized gas of IC 342 are similar to those of galaxies with similar stellar masses in the nearby universe.

Resumen

En este trabajo presentamos el análisis de las propiedades físicas de regiones H II a escalas de sub-kpc en una de las galaxias más cercanas a nosotros, IC 342, usando datos de espectroscopía de campo integral (IFS por sus siglas en inglés). Estos datos representan las observaciones más completas en el óptico de esta galaxia. El cubo de datos está compuesto por 349 observaciones individuales del cartografiado SDSS-IV MaNGA. Para el análisis de este cubo de datos usamos un prototipo del dataducto de análisis del cartografiado SDSS-V LVM, con el cual estimamos las propiedades de las líneas de emisión. En particular, usando el mapa de la línea de emisión de Hα determinamos la ubicación y el tamaño de candidatos a regiones H II. Usando las propiedades integradas para cada candidato estimamos la distribución radial para un gran número de propiedades físicas (e.g., extinción, luminosidad de Hα, abundancia de oxígeno, etc.). Comparando con galaxias de masa estelar similar y observadas con IFS, nuestros resultados muestran que las propiedades del gas ionizado para IC 342 son semejantes con dichas galaxias.

Corresponding author: J. K. Barrera-Ballesteros *E-mail address:* jkbarrerab@astro.unam.mx
Received: November 1, 2023 **Accepted:** Jul 4, 2025

1. Introduction

A theoretical H II region is a sphere of gas that surrounds young massive stars (mostly O and B type). The UV emission from these stars ionizes this gas, which cools down through emission lines, some of the brightest in the optical. Since OB stars are short-lived (< 15 Myr), the observed emission from these regions has often been used to trace recent star formation. Furthermore, thanks to the emission by the ionized gas contained in these regions, we are able to gain deep knowledge of, for instance, the luminosity function of the Hα emission line (which in turn traces the massive end of the initial mass function), the chemical content of the interstellar medium (ISM), or their dynamical stage. The size of an H II region is variable, from a few to hundreds of parsecs (e.g., the Orion Nebula and NGC 5471, from ∼8 pc to ∼1 kpc, respectively, Anderson, 2014; García-Benito et al., 2011). Aggregations of these large H II regions are considered giant H II regions, usually

observed in star-forming spirals (e.g., Hodge & Kennicutt, 1983; Dottori & Copetti, 1989; Knapen, 1998).

Observationally, these giant H II regions are usually traced as clumpy Hα emission across the optical extension of late-type galaxies (e.g., Kennicutt & Evans, 2012, and references therein). The galactocentric distribution of these regions is usually quantified by a radial gradient, suggesting that in most spirals, at their center the Hα flux of these regions is larger than that of regions located at the outskirts (e.g., Knapen et al., 2004; Bigiel et al., 2008). Using Hα narrow-band imaging it is possible to characterize the distribution of H II regions in a galaxy via the Hα luminosity function (e.g., González Delgado & Pérez, 1997; Bradley et al., 2006). Using long-slit spectroscopy, it has been possible to trace other physical properties of these regions in reduced samples of spiral galaxies, such as chemical abundances, electronic density, and the ionization parameter (e.g., Pilyugin & Grebel, 2016).

In recent years, extragalactic astronomy has witnessed a revolution in optical observations, thanks to the Integral Field Spectroscopic (IFS) technique applied to thousands of galaxies in the nearby Universe. Large IFS surveys such as CALIFA (Sánchez et al., 2012), MaNGA (Bundy et al., 2015), SAMI (Croom et al., 2012), and AMUSING++ (López-Cobá et al., 2017) have shown the spatially resolved properties of the demographics of galaxies in Of particular interest is the radial distribution of physical properties of the ionized gas derived from the emission line parameters in the optical (e.g., Sánchez-Menguiano et al., 2018; López-Cobá et al., 2017; Espinosa-Ponce et al., 2022; Barrera-Ballesteros et al., 2023). Given the success of these large IFS surveys, different research groups have employed different IFS techniques to map the properties of the ionized gas in nearby galaxies, reaching superb spatial resolutions (on the order of tens of pc). Among these different IFS surveys, the TYPHOON, SIGNALS, and PHANGS surveys are noteworthy (D'Agostino et al., 2018; Rousseau-Nepton et al., 2019; Emsellem et al., 2022).

Although there are dedicated IFS studies to explore the properties of H II regions in galaxies in the local universe ($D < 5$ Mpc), these are rather scarce. Using the MUSE instrument, it has been possible to explore the physical properties of H II regions at sub kpc scales in the LMC (McLeod et al., 2019), NGC 300 (McLeod et al., 2020, 2021), NGC 7793 (Della Bruna et al., 2020, 2021), and M83 (Della Bruna et al., 2022). These studies mainly focused on exploring how stellar feedback from recent star formation in H II regions affects the kinematics of the interstellar medium. Such studies are of great importance to bridge the gap between the observations at sub-kpc scales and those scaling relations between the star formation and the dynamical pressure at kpc scales for hundreds of galaxies (Barrera-Ballesteros et al., 2023). However, they lack a deep exploration of the physical properties of the ISM for H II regions at sub-kpc scales. With this work, we aim to shed some light on the radial distribution of the physical parameters at these physical scales derived from the emission lines in the optical.

In this study, we focused on IC 342. This galaxy is the closest grand-design spiral to the Milky Way (~3.3 Mpc Saha et al., 2002). Therefore, it was mapped at different wavelengths. From *WISE* data Jarrett et al. (2013) derived its total stellar mass ($\log(M_\star/M_\odot) \sim 10.8$, but see Zibetti et al., 2009; Zhu et al., 2010, for other estimations), and total star formation rate ($\sim 2.4 M_\odot$ yr^{-1}, see also Kennicutt et al., 2011). Its molecular and neutral gas content has also been extensively mapped either in its nucleus and arms (e.g., Rickard & Palmer, 1981; Ishizuki et al., 1990; Crosthwaite et al., 2000; Kuno et al., 2007). However, despite these studies, there have been few studies on the properties of ionized gas in IC 342. The only reported measurements of the emission line fluxes in four H II regions at different radii of this galaxy come from long-slit spectroscopy (McCall et al., 1985). Using these observations, Pilyugin et al. (2004) derived the oxygen abundance gradient for this galaxy. In this work, we present the largest integral field spectroscopic study of IC 342 in the optical. We took advantage of ancillary observations from the MaNGA survey (Bundy et al., 2015) devoted to mosaicing this galaxy. In particular, we focus on the radial distribution of the physical parameters that could be derived from the observed properties of the different emission lines in the optical within a given H II region. Owing to its high angular resolution, the current dataset also provides us with a unique opportunity to test the data-analysis pipeline that is being used to determine the physical properties in the Local Volume Mapper (Drory et al., 2024), an ongoing SDSS-V survey (Kollmeier et al., 2017) aimed at mapping the physical properties of the ionized gas within the Milky Way and galaxies included in the Local Volume (Konidaris et al., 2020).

The remainder of this paper is organized as follows: In § 2 we present the IFS observations of IC 342 as well as the data analysis pipeline used to derive the maps of the quantities from the observations. In § 3 we describe the method used to estimate the position and size of the H II regions, the derived physical quantities for each region, and their classification in an emission-line diagnostic diagram. In § 4 we present the galactocentric distribution of the physical properties derived from the H II regions. In § 5 we present the Hα luminosity function for IC 342 derived from the H II regions. In § 6 we explore the correlations between the radial residuals of the derived physical properties. In § 7 we summarize and discuss our results in the framework of recent IFS surveys.

2. Data

2.1. IFS observations as MaNGA ancillary program

The observations to map the disk of IC 342 were part of an ancillary program included in the MaNGA survey (PI. K. Kreckel). The MaNGA (Mapping Nearby Galaxies at Apache Point Observatory; Bundy et al., 2015) survey

was part of the fourth generation of surveys included in the Sloan Digital Sky Survey (SDSS-IV; Blanton et al., 2017). This survey observed more than 10000 galaxies in the nearby universe using the IFS technique. Here, we briefly review the main features of this survey. Observations were conducted at the Apache Point Observatory using a 2.5-m telescope (Gunn et al., 2006). It used two spectrographs from the BOSS survey (Baryon Oscillation Spectroscopic Survey Smee et al., 2013). BOSS spectrographs achieve a nominal spectral resolution of $R \equiv \lambda/\Delta\lambda \sim 1900$ covering a large portion of the optical spectra (from 3000 to 10000 Å). These spectrographs were fed by joined fibers in bundles distributed in a hexagon-like array (also known as integral field units, IFUs). The number of fibers in a given bundle, or IFU, varied from 19 to 127. Because the diameter of each fiber is $\sim 2''$, the field of view (FoV) for each IFU varies between $12''$and $32''$. Observations of MaNGA targets were performed using a plugplate system, where the locations for each IFU (and corresponding sky fibers), 12 spectrophotometric standard stars, and 16 guide stars were pre-drilled. This provides the necessary observations for the acquisition, guiding, and dithering of targets, along with all the calibration data needed in the data reduction pipeline. A detailed description of the instrumentation used in the survey can be found in Drory et al. (2015). The reader is referred to Law et al. (2016) for a detailed explanation of the data strategy (acquisition, reduction, etc.). The MaNGA reduction pipeline includes wavelength calibration, corrections from fiber-to-fiber transmission, subtraction of the sky spectrum, and flux calibration (Yan et al., 2016). The final product is a datacube with x and y coordinates corresponding to the sky coordinates and the z-axis corresponding to the wavelength.

The IC 342 observations were taken as part of an ancillary program that was needed to provide additional MaNGA science targets when the Milky Way was above. IC 342 has been neglected in optical studies as it suffers from high foreground Milky Way extinction ($A_V = 1.530$; Schlafly & Finkbeiner 2011), but at a galactic latitude of ∼10 deg it was well situated for this ancillary program.

The goal was to produce a uniform, contiguous mosaic covering the central $11' \times 11'$ (10 kpc × 10 kpc) region. This reaches 0.25 $R_{25} \approx 1.25$ R_e ($R_{25} = 22'$), which is well matched to the primary MaNGA sample. Each of these pointings results in a datacube with a spaxel size of $0.5''$(the spatial resolution is given by the average size of the PSF per fiber, which is typically $2.54''$, Law et al., 2016). Given the distance of IC 342 this corresponds to a spatial resolution of ∼ 32 pc. Thus, these IFS data represent observations with significantly higher physical resolution than typical MaNGA targets (∼3 kpc), surpassing even what is achieved with other nearby galaxy surveys, such as PHANGS-MUSE (∼70 pc; Emsellem et al. 2022).

The final mosaic of IC 342 uses 49 plates and was observed between early 2017 and late 2021. Three pilot plates (plate numbers: 9673-9675) were initially observed to test the feasibility of this survey, with IFUs placed on HII regions that provided good radial and azimuthal coverage. A total of 46 plates (with plate numbers: 10141-10150, 10480-10491, 12027-12050) were used to uniformly mosaic the central 10 arcmin diameter disk of IC 342. In some cases, these overlapped with the positions of the IFUs in the pilot plates. Plate 10490 had one dropped IFU bundle, leading to a gap in coverage. An additional 15 plates were planned but not completed before the end of the MaNGA survey operations. Each plate was observed at three dither positions, following the standard MaNGA procedure to fill the interstitial regions(Law et al., 2016), and only the two largest IFUs were used (i.e., the bundles with 127 and 91 fibers). Individual IFU positions are tiled such that no gaps exist when all IFU fibers are combined into a single data cube. As a result, seven large contiguous regions were observed (Figure 1) with a total of over 10^5 spectra (including the dither positions).

Each of these plates was observed using the same strategy as a standard MaNGA plate; thus, it was possible to use the same data reduction pipeline as that used for the rest of the survey. The diameter of the IC 342 is sufficiently small that sky fibers can be placed successfully for each IFU within the $14'$patrol field. Exposure times in the pilot observations were limited to a total of 1 h (two visits of 30 min, with 10 min per dither), but in the full survey, the total integration time was 1.5 h (two visits of 45 min, with 15 min per dither).

2.2. Deriving emission line properties using the LVM-DAP

As mentioned in the previous section, given the close distance of IC 342, the IFS dataset provided by the MaNGA observations has a superb angular resolution, making it very suitable for using an analysis pipeline dedicated to IFS datasets from Local Volume galaxies. Therefore, we used the IFS dataset from IC 342 as a test-bed for the data analysis pipeline (DAP). The DAP is used to analyze the data observed by the Local Volume Mapper (LVM) survey, which is part of the fifth generation of the SDSS collaboration. The details of the LVM-DAP are described in (Sánchez et al., 2025), and its preliminary results are presented in (Drory et al., 2024). Here, we provide a brief description of the main features of this DAP, focusing on the extraction of physical properties from ionized gas. Although with significant variations, the LVM-DAP follows a methodology similar to that of the `pyPipe3D` pipeline (Lacerda et al., 2022). This DAP is an update of the pipeline `Pipe3D` (Sánchez et al., 2015a, 2016), which has been widely used to extract two-dimensional distributions of physical properties from both the stellar and ionized gas components for heterogeneous datasets (e.g., CALIFA, MaNGA, AMUSING++).

In contrast to nearby galaxies, for those galaxies included in the Local Volume (including the Milky Way), it is no longer valid to assume that the stellar continuum of a portion of a galaxy is composed of the linear combination

of single stellar population spectra (SSPs). Thus, the LVM-DAP derives the stellar population using a technique called resolved stellar population (RSP) to estimate the best stellar continuum of the data observed at the LVM. A detailed description of this extraction and the physical properties derived for the stellar component of the spectra will be described elsewhere (Mejia et al., in prep.) In this case, the estimation of the best stellar continuum is no longer based on a linear combination of different SSPs but on a library of individual stellar spectra covering a wide range of stellar properties (e.g., effective temperature, gravity, and chemical abundances). For each spectrum in each reduced datacube. The DAP starts by deriving the systemic velocity, velocity dispersion, and optical extinction from the stellar continuum by fitting only four stellar spectra. Once the best estimations for these parameters were derived, a stellar model was derived and subtracted from the observed spectra, and a set of Gaussian profiles was fitted to a pre-defined set of emission lines. These Gaussian profiles are then subtracted from the observed spectra, and a new fit of the stellar component is performed using a large set of stellar spectra, yielding the final continuum model. The remaining "gas-only" spectrum was then analyzed using a weighted-moment non-parametric procedure to estimate the integrated flux, velocity, velocity dispersion, and EW of a pre-defined set of 192 emission lines. Contrary to DAP, where the data are stored in the form of RSS tables, the data for IC 342 are stored in the usual format of the MaNGA survey for each pointing, as maps for each of the properties for each of the analyzed emission lines. Furthermore, for each property derived by the DAP in IC 342 we perform a mosaic using the maps from individual pointings. These maps have a scale of 1 arcsec per pixel. For the details of the algorithms and their implementation we refer the reader to Sanchez (in prep) and Lacerda et al. (2022) [1]. In Figure 1 we show the map of the Hα line, whereas in Appendix A we present the maps of other strong emission lines. The maps of the physical properties from all the pointings can be found in https://ifs.astroscu.unam.mx/MaNGA/IC342/output_dap/.

2.3. The AMUSING++ sample

To compare the trends derived for the H II regions within IC 342 with respect to the sample of H II regions located in a larger sample of galaxies, we used the AMUSING++ sample (López-Cobá et al., 2020). This sample is an extension of the All-Weather MUse Supernova Integral Field Nearby Galaxies survey (AMUSING Galbany et al., 2016, 2020). This compilation of galaxies observed with the MUSE instrument includes observations from a wide variety of scientific goals (see details in López-Cobá et al., 2020). Although the initial compilation included 635 galaxies (López-Cobá et al., 2020), an updated sample comprised 678 galaxies (Lugo-Aranda et al., 2024). The galaxies in the AMUSING++ sample were selected so that the MUSE field of view had a good spatial coverage ($\sim$ 2 effective radius), and that they are nearby galaxies ($0.004 < z < 0.06$). This sample has significant coverage in both stellar masses and morphology (see details in Lugo-Aranda et al., 2024). The inclusion of nearby galaxies in the sample ensures a good spatial resolution ($\sim$ 100 to 1000 pc). Using the latest compilation of the AMUSING++ sample, Lugo-Aranda et al. (2024) characterized the physical properties of more than 52 000 H II regions. We used the data for these H II regions to compare them with the trends observed in the H II regions located in IC 342 (see § 3.3).

3. Analysis

3.1. Detecting HII regions using PyHIIEXTRACTOR

With maps of the physical properties derived from the different emission lines, we used the Hα emission mosaic to determine the locations and sizes of the H II regions. To do this, we used the code PyHIIEXTRACTOR (Lugo-Aranda et al., 2022). This code detects and extracts the properties of clumpy regions considered as H II regions using an Hα emission-line image. If IFU data are available for that image, this code can also extract the physical properties within each of the detected H II regions (e.g., physical properties for each observed emission line and properties from the stellar continuum). Although PyHIIEXTRACTOR also models the Hα diffuse emission (also known as diffuse ionized gas, DIG), in this study, we focus only on the physical properties of the H II regions. In a future study, we will explore the properties of DIG for IC 342. To proceed with the estimation of the location and size of the H II regions, the code requires a set of initial values. We refer the reader to Lugo-Aranda et al. (2022) for a detailed description of those parameters; here, we describe the parameters we use to extract the physical information of the H II regions. For this study, we systematically varied (i) the Hα flux threshold above which the code detects clumpy regions and (ii) the maximum size of the detected H II regions. We also set the code to search for H II regions with 300 different sizes, varying from one spaxel to the maximum size. By visually inspecting the resulting sizes and locations of the H II regions derived by PyHIIEXTRACTOR, we find that appropriate initial values for the code are a value for (i) of $\sim 5 \times 10^{-18}$ erg s^{-1} Å^{-1} and for (ii) the spatial resolution of the observations (set by the size of the fiber, $\sim 2.5''$). Because the range of sizes of the H II begins with one spaxel (which does not have a physical meaning), we discard regions with one spaxel of radius. We explore a wide range of maximum sizes for our H II regions; however, we find that having larger maximum sizes yields spurious large H II regions. In total, we detected 4701 clumpy regions; however, as described below, to guarantee that we have reliable measurements of the physical properties of the H II regions, we apply further selection criteria. In Figure 1 we display the locations and sizes of the H II regions for IC 342

[1] http://ifs.astroscu.unam.mx/pyPipe3D/

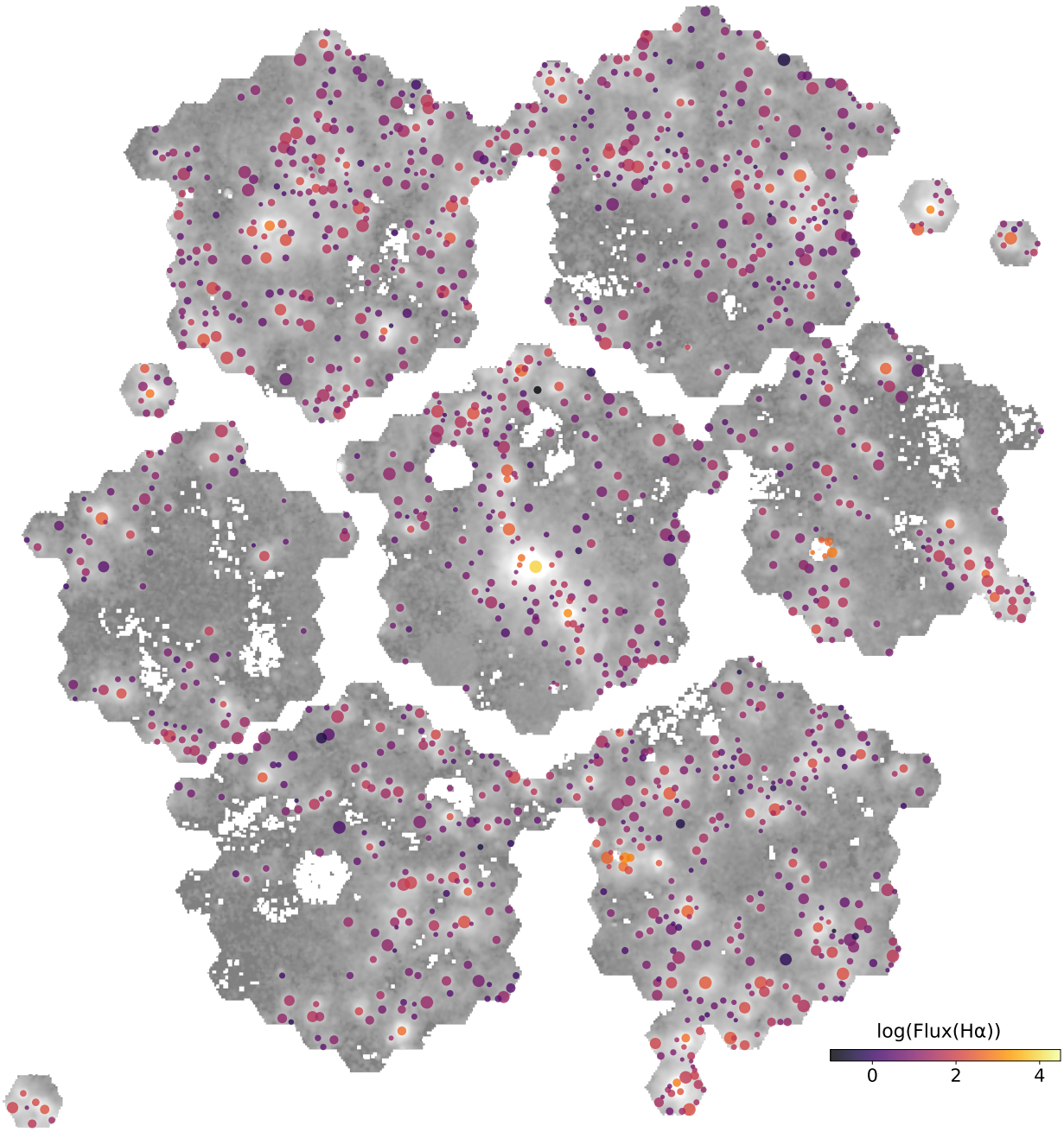

Figure 1. Flux of the Hα emission line from H II candidates detected by PYHIIEXTRACTOR overplotted over the Hα emission line map derived using the DRP-LVM.

as red circles. As expected, most of the H II regions are located within the arms of the galaxy.

To provide reliable estimations of the physical properties for each of the detected H II regions, we used the following criteria: each region should have (i) all the emission line fluxes with positive values, and (ii) the signal-to-noise ratio of the Hα emission line has to be larger than three. In the next section, we classify regions according to their location in their BPT diagram and their Hα equivalent width. From these criteria, we obtained a final sample of 1155 H II regions.

3.2. Derived Properties

For each of the selected H II regions, we used the integrated/averaged properties derived from the LVM-DAP within its radius. Thus, for each emission line, we spatially integrated the flux and averaged the other properties, such as the equivalent width and FWHM. Using this dataset, we derived the physical properties that we will cover in

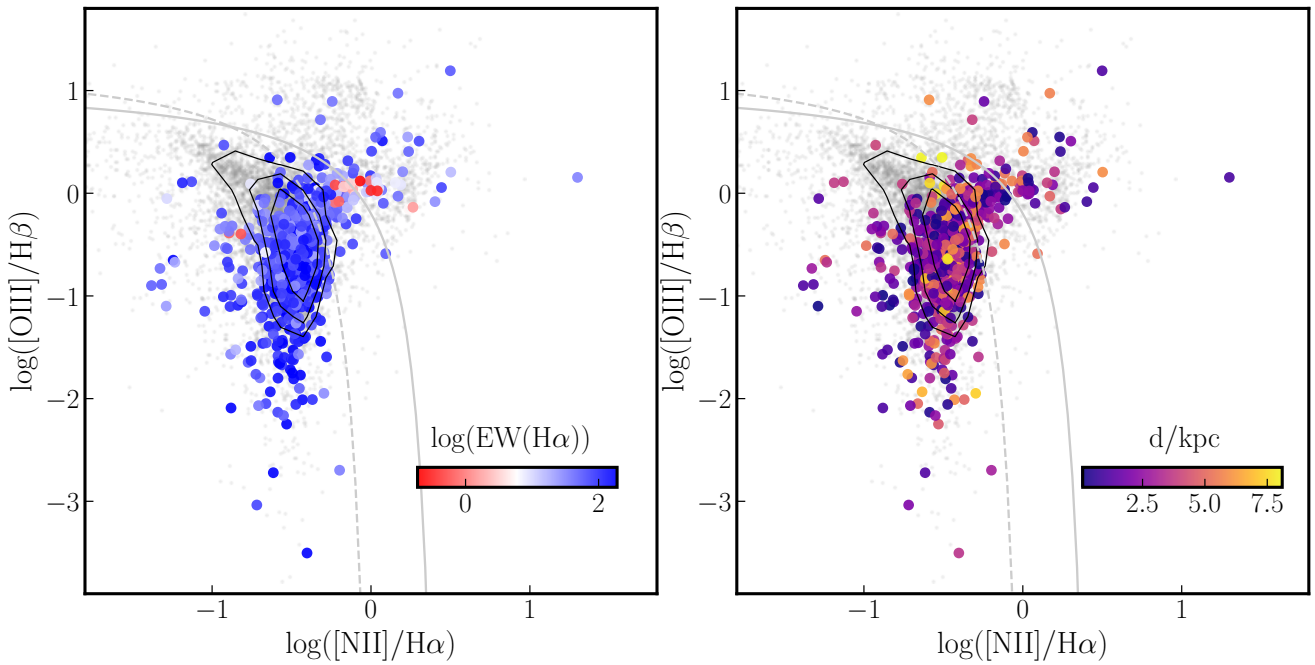

Figure 2. H II candidates in the BPT diagram. *Left:* Candidates color-coded by their Hα equivalent width. *Right:* Candidates color-coded by their galactocentric distance. The dots represent the properties of the AMUSING++ sample. In both panels, the solid and dashed lines represent the Kauffman and Kewley demarcation lines, respectively. We use this demarcations lines and the Hα equivalent width to select *bona fide* star-forming regions in IC 342.

this study. From the Hα/Hβ ratio, known as the Balmer decrement, we derived the optical extinction, A_V, following the prescription outlined by Catalán-Torrecilla et al. (2015). Using this estimation of A_V, we derived the dust-corrected Hα luminosity for each region. However, to derive other physical properties such as oxygen and nitrogen abundances, electronic density, and ionization parameter, we also use the integrated flux from other emission lines, including the optical range of the observations. We refer the reader to the study by Espinosa-Ponce et al. (2022) for a complete list of emission lines used in this study to derive the physical parameters mentioned above. We note that although there is a large list of oxygen abundance calibrators in this study, we use the one provided by Ho (2019). Finally, regarding the kinematic properties of each region, we averaged the systemic velocity and velocity dispersion.

3.3. The BPT diagnostic diagram and the classification of HII regions

Diagnostic diagrams have been widely used to classify galaxies and regions according to their ionizing sources. This is the case for the BPT diagram (Baldwin et al., 1981). In this section, we present the locations of the IC 342 candidates in the BPT diagram. Along with their EW(Hα), we used these line ratios to select the *bona fide* H II regions.

In Figure 2, we plot the H II candidates in the classical BPT diagram (i.e., [O III]/Hβ vs [N II]/Hα). For comparison, we also plotted the line ratios from the AMUSING++ sample. Although most of the regions from both samples are located in the so-called 'star-forming branch', we note that the AMUSING++ sample covers a wider dynamical range in the [N II]/Hα axis than the H II candidates from IC 342. This is related to the differences we find previously in the radial distribution of the O3N2 ratio in these two samples. Furthermore, there are also AMUSING++ candidates with larger values of the [O III]/Hβ ratio compared to those derived from the IC 342 sample. We suspect that this is due to regions with sources of ionization that are different from star formation. However, further exploration of the AMUSING++ sample of H II candidates is beyond the scope of this study and will be addressed elsewhere (Aranda-Lugo et al. in prep.)

A quantitative classification of the different ionization mechanisms is given by the demarcation lines proposed by Kauffmann et al. (2003); Kewley et al. (2001, see the dashed and solid lines in Figure 2, respectively). Galaxies/regions below these demarcation lines are usually classified as star-forming, while those above these demarcations could have different classifications (i.e., composite-like galaxy/regions if the line ratios are between these demarcations or AGN-like galaxy/region if the ratios are above the Kewley demarcation line). We find that the majority of regions lie below these demarcation lines in the BPT diagram (~80% and ~92% for the Kauffmann and Kewley demarcation lines, respectively).

The Hα equivalent width, along with the [N II]/Hα ratio, has also been used to characterize the ionization source of

galaxies/regions (e.g., Cid Fernandes et al., 2010; Lacerda et al., 2018). In the left panel of this figure, we color-code our candidates in the BPT diagram by their EW(Hα). We note that almost all the regions below these demarcation lines have large values of EW(Hα) with an average of ~100 Å. Conversely, most of the regions with low EW(Hα) are above the demarcation line (~40 Å). In comparison to the AMUSING++ sample, the IC candidates have large values of EW(Hα), both above and below the demarcation lines. The right panel of Figure 2, we color-code the candidates according to their galactocentric distance. We do not find a clear trend between the distance and location of the candidates in the BPT diagram. Regions above and below the demarcation line are distributed across the optical extension of the IC. Given that flux ratios above the Kewley demarcation line are typically associated with nuclear activity, this result suggests that a physical process other than nuclear activity could be responsible for the ionization in those regions.

Depending on the study, there are different thresholds for selecting star-forming galaxies/regions. Cid Fernandes et al. (2011) used as threshold EW(Hα) > 6 Å. In this study, we used a more conservative value to select star-forming regions (EW(Hα) > 14 Å Lacerda et al., 2020). Thus, to obtain *bona fide* H II regions from our sample of candidates, we selected those regions with flux ratios below the theoretical demarcation line proposed by Kewley et al. (2001), as well as regions with the aforementioned EW(Hα) values. Using these criteria from the sample of 1155 candidates in IC 342 we selected 960 star-forming regions. Although it is beyond the scope of this study, we note that for those nebulae that were selected as non-star-forming, a significant fraction are regions with low EW(Hα) below the Kewley demarcation line (121/195). This could indicate that the ionizing source is different from that expected from supernova remnants (e.g., Vicens-Mouret et al., 2023). Further studies are required to assess the true nature of the ionization of these sources.

4. Radial Distribution of Physical Parameters

4.1. Properties derived from Balmer lines

To obtain the Hα dust-corrected luminosity for our sample of H II regions, it is necessary to estimate the extinction using the Hα/Hβ ratio. In this section, we explore the radial distribution of extinction. We also explored the radial distribution of both the Hα line equivalent width and the Hα luminosity.

Optical Extinction, A_V: In Figure 3 we plot the radial distribution of A_V for the sample of H II candidates with a Hα/Hβ ratio larger than 2.86. First, we note that the average extinction derived from the Balmer decrement for these candidates is close to one, $A_V \sim 1.3$ mag, with a large scatter measured from the standard deviation, $A_V \sim 1.4$ mag. Although the distribution of extinctions presents a large scatter, once the extinctions are represented against the galactocentric distance of the regions, they

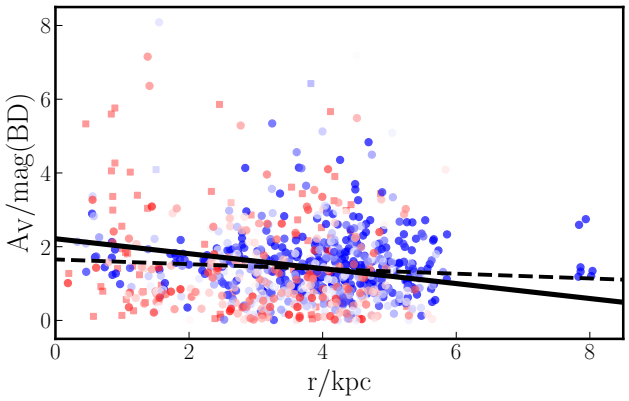

Figure 3. Radial distribution of the optical extinction, A_V, derived for the H II regions in IC 342. The symbols are color-coded according to their EW(Hα). The solid line represents the best-fit radial gradient for the data. In average, we do not find a significant variation of A_V for IC 342.

follow a decreasing trend. To further quantify this trend, we derived the radial gradient of the optical extinction by fitting a single-slope line to the dataset (black solid line in Figure 3). We found that the best slope and zero-point were -0.18 mag / kpc and 2.21 mag, respectively. We note that there are regions with an extinction significantly larger than the median value, or, in other words, significantly above the best-fit gradient. These high-extinction regions are across the extension of the galaxy, with no clustering at a specific galactocentric distance. We also note that these regions cover a wide range of values of EW(Hα), as seen by the color codes of the data points in Figure 3. In this figure, we also segregate the candidates according to the selection criteria described in § 3.3, that is, between star- and non-star-forming regions (circles and squares, respectively). We note that in the central region (r < 2 kpc), most of the regions with high extinction are non-star-forming candidates, whereas at larger radii, these regions are mostly star-forming. To further understand the origin of these regions with high extinction, we mapped the residuals of extinction with respect to its gradient, as shown in Figure 20. We note that some of these regions appear to be clustered towards the arms of IC 342 (e.g., the north-west at ~ 4 kpc or the south-east at ~ 8 kpc). In the following sections, we explore whether these atypical regions correlate with other properties of the regions.

EW(Hα): Contrary to the the optical extinction, we find that in general the radial distribution of the EW(Hα) from the H II candidates follows an increasing trend (see Figure 4). We plot this radial distribution, color-coded by the star formation status. We found that the star-forming regions followed a positive radial trend, in contrast to non-star-forming regions, which had a large scatter and no evident trend (green circles and pink squares, respectively). In contrast, when we derived the best single gradient for this radial distribution, we found that selecting only

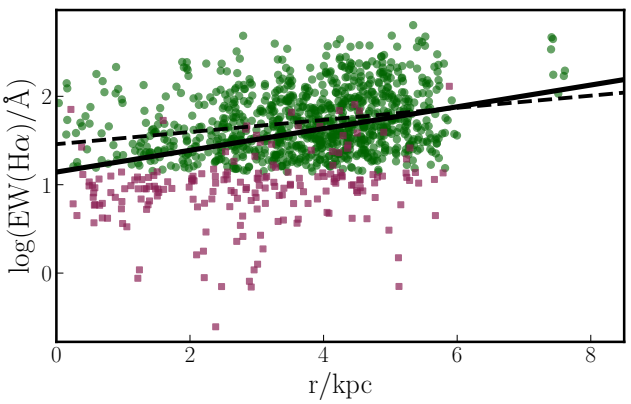

Figure 4. Radial distribution of the EW(Hα) for the H II candidates in IC 342. The green and pink symbols represent the star-forming and non-star-forming regions, respectively. The solid and dashed lines represent the best-fit radial gradient for the entire data and using only H II regions, respectively.

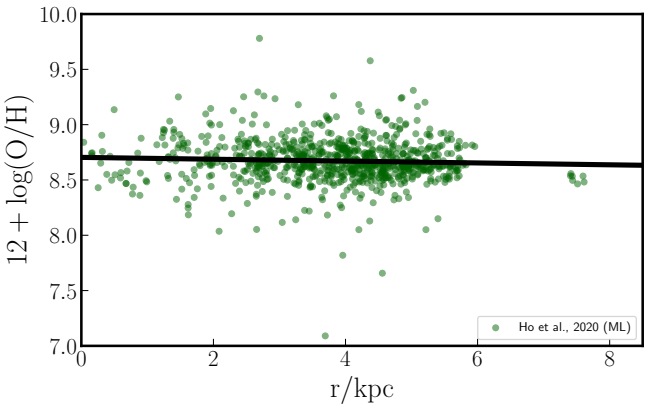

Figure 6. Radial distribution of the oxygen abundance using the calibrator from Ho (2019) for star-forming regions. The black solid line shows a best gradient fit representing the almost flat radial distribution of the oxygen abundance for the star-forming regions in IC 342.

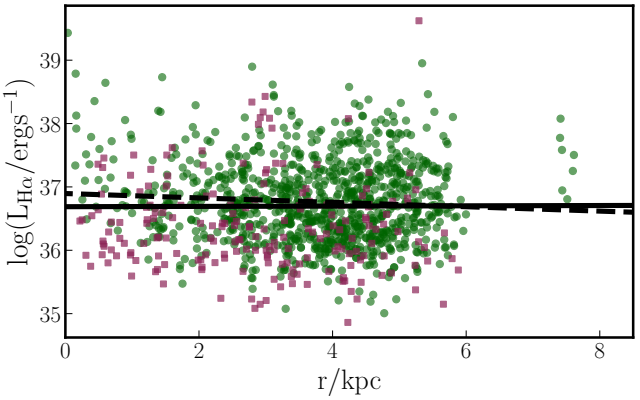

Figure 5. Radial distribution of the Hα luminosity. Colors of the symbols and lines are similar as those derived in Figure 4.

star-forming regions led to a shallower gradient than that derived using all H II candidates (dashed and solid lines, respectively). In Figure 21 we color-code the residual of the EW(Hα) with respect to the radial gradient derived above for each position and radius of the H II candidates. We find that the central star-forming regions are those with a larger enhancement of EW(Hα), whereas some of the external star-forming regions (e.g., at the outskirt north-west direction). On the other hand, we find that most non-star-forming regions have a deficit in their EW(Hα) in comparison to the derived gradient and are distributed in the central region of IC 342. In the next section, we explore how the residuals from this radial gradient correlate with other physical properties derived from the emission lines.

Hα luminosity: In Figure 5, we plot the radial distribution of these luminosities. They follow a rather flat distribution with respect to their galactocentric distances. When we segregated our sample into star- and non-star-forming regions, we did not find a significant difference between the radial distributions of their Hα luminosities. For a given galactocentric distance, both samples show a large scatter in their Hα luminosities. For the previous parameters, we derived the best radial gradient for these luminosities. We find a mild negative gradient, which becomes even flatter when we derive it using only star-forming regions (solid and dashed lines, respectively).

4.2. Oxygen Abundances

In Figure 6, we plot the radial distribution of oxygen abundance for the sample of star-forming regions in IC 342. As mentioned in § 3, from the large set of abundance calibrators, we use as a fiducial calibrator the one derived from Ho (2019). We note that the gradient provided by the best-fit is rather flat with a slightly negative slope. As with the other properties, we have mapped in Figure 22 shows the residuals of the oxygen abundance for each star-forming region, where it is possible to derive the oxygen abundance. We did not find a cluster or specific location of regions with an excess or deficit in their abundance. In § 6, we further explore how the radial residuals of different physical properties correlate with each other.

To quantify the impact of the abundance calibrators on the estimation of the best gradient, we used each of the calibrators presented in § 3 to derive the oxygen abundance gradient. In Figure 7 we plot the slope and zero-point from the best fit for the set of 23 calibrators. We note that, although there are significant variations in both parameters, the average value of the slope is consistent with a flat radial distribution of oxygen abundance. The central abundance given by the average zero-point is close to solar abundance. Finally, we note that the number of star-forming regions employed to estimate the best gradient varies depending on the calibrator. This difference in sampling is due to (i) the emission lines required to derive a specific calibrator and (ii) the dynamic range imposed for each of them.

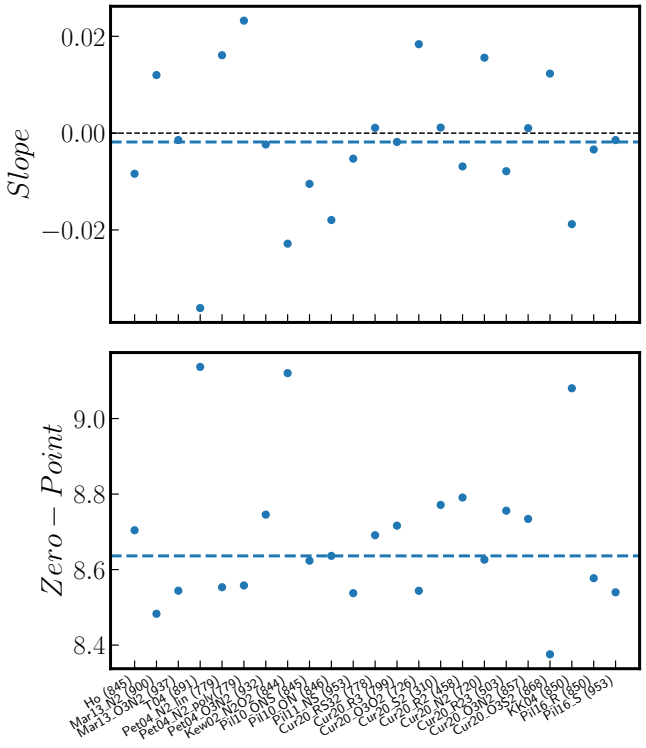

Figure 7. Best-fit parameters for the radial gradient of oxygen abundance using the set of calibrators described in § 3: slope and zero-point (top and bottom panels, respectively). In the top panel, the black dashed line represents a flat gradient, while the blue dashed line represents the average of the slopes from the different sets of calibrators. In the bottom panel, the blue dashed line represents the average of zero-points from the different calibrators. On average, the distribution of oxygen abundance in the star-forming galaxies of IC 342 is rather flat, with a central oxygen abundance close to solar. We describe the number of star-forming regions used for each calibrators in parenthesis.

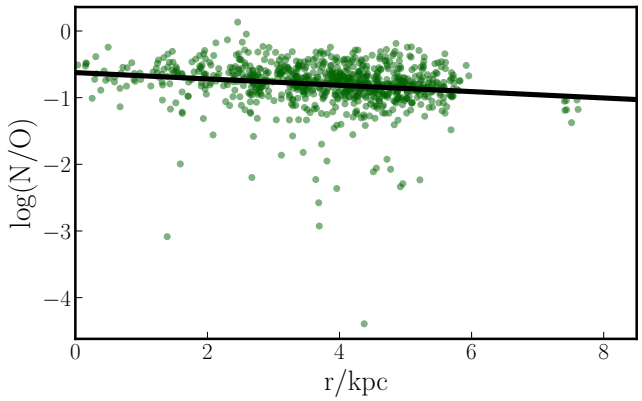

Figure 8. Radial distribution of the N/O ratio for star-forming regions.As for the oxygen abundance, the black line represent the best fit for this radial distribution.

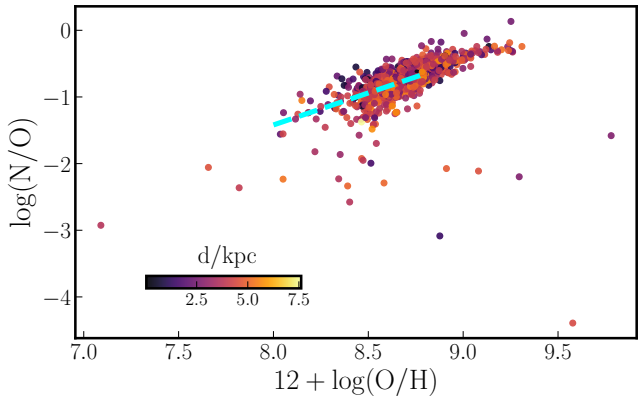

Figure 9. Nitrogen-to-oxygen ratio against the oxygen abundance ratio. The cyan-dashed line represents the best fit for these two parameters derived from H II regions observed in the CALIFA survey (Espinosa-Ponce et al., 2022). We note that in comparison to a large sample of regions, those from IC 342 have large N/O ratios.

4.3. N/O ratio

The measurement of chemical abundances from elements with different nucleosynthesis processes allows us to trace the scales of star formation in the evolution of IC 342. Short-lived massive stars are traced by oxygen abundance, whereas nitrogen abundance traces longer lifetimes and lower mass stars. As mentioned in § 3, the nitrogen abundance was measured using the calibrator presented in Pilyugin & Grebel (2016), whereas for the oxygen abundance, we used our fiducial calibrator (Ho, 2019).

In Figure 8, we plot the radial distribution of the N/O ratio for the sample of H II regions detected in IC 342. We find that a large fraction of the H II regions show a decreasing value of this ratio as the galactocentric distance increases with increasing galactocentric distance. For a few regions (<5%), their N/O ratio is significantly smaller than that of regions at a similar galactocentric distance. The best fit of the radial distribution of the O/H ratio confirmed a negative gradient (black line in Figure 8). As for oxygen abundance, in Figure 23 we color-coded the H II regions with the residuals of the N/O ratio with respect to the derived radial gradient. We did not find a specific location where there was a larger deficit or enhancement of this ratio. We also did not find a possible correlation between the deficit and morphological features (e.g., an arm, inter-arm, etc.).

To further understand this ratio in the context of galaxy evolution, in Figure 9 we plot the N/O ratio against the oxygen abundance color-coded by their distance. We find that most of the regions, independent of the distance, are clustered in the well-studied linear relation between N/O and O/H (e.g., Belfiore et al., 2017; Espinosa-Ponce et al., 2022). We note that with respect to large samples of H II regions included in a large number of galaxies (e.g., the CALIFA survey Espinosa-Ponce et al., 2022, , see

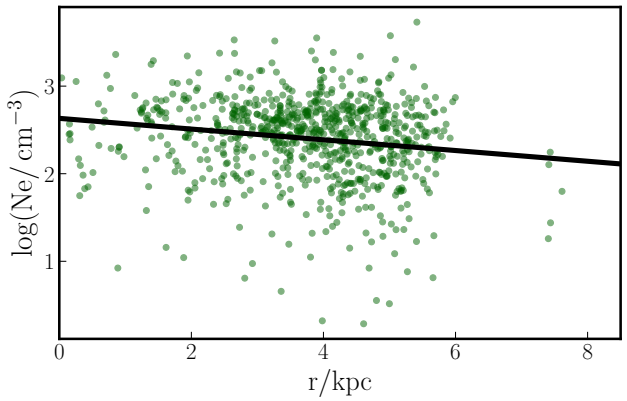

Figure 10. Similar to Figure 8, radial distribution of the electronic density for star-forming regions.

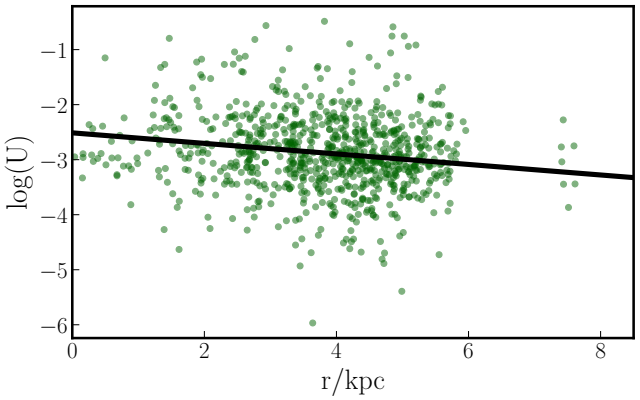

Figure 11. Similar to Figure 8, radial distribution of the ionization parameter for star-forming regions.

cyan-dashed line in Figure 9), those from IC 342 exhibit large metallicities and thus large N/O ratios. In relation to the regions with a large deficit of the N/O ratio, we find that these H II regions cover a wide range of metallicities. In conclusion, the bulk of the H II regions for IC 342 exhibit a similar trend in the N/O-O/H plane as the H II regions in other extragalactic sources. Furthermore, some H II regions in this galaxy show larger values of the oxygen abundance and N/O ratio than the others. These regions appear to follow the linear trend described by large samples of H II surveys. Finally, the underlying reason for the significant deficit of the N/O ratio in H II regions remains unclear.

4.4. Electronic density and Ionization parameter

In Figure 10 we show the radial distribution of the electron density, n_e, for the sample of H II regions where we can measure this physical property. Despite the large scatter, we find that regions at larger galactocentric distances tend to have lower densities than those at closer distances. This is expected, as regions in the center (where the stellar and gas densities are larger) are prone to be under larger pressure than regions at the outskirts (e.g., Barrera-Ballesteros et al., 2021; Barnes et al., 2021). This trend is further quantified by the best radial gradient, which has a negative slope. As for the other properties, we also explored how the residuals of n_e with respect to this gradient were spatially distributed (see Figure 23). We did not find any significant patterns in the spatial distribution of these residuals.

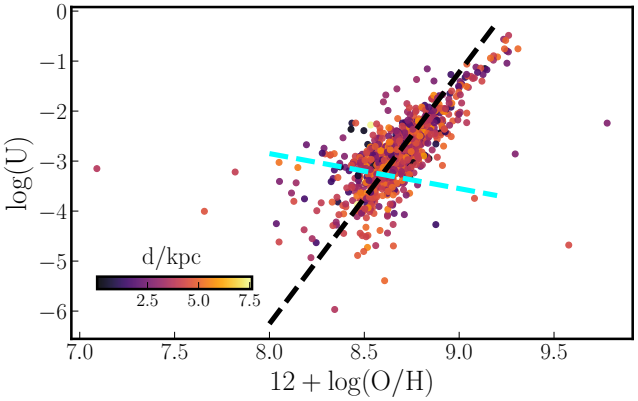

Figure 12. Comparison between the ionization parameter and the oxygen abundance for our sample of star-forming regions. Data points are color-coded with respect to the galactocentric distance. The black dashed line represent the best linear fit to the data, while the cyan dashed line represents the best fit presented in (Espinosa-Ponce et al., 2022).

In Figure 11, we plot the radial distribution of the ionization parameter for our sample of H II regions. Similar to other properties of the H II regions, we find that this parameter decreases as the galactocentric distance of the regions increases. This was confirmed by the negative slope obtained from the best-fit gradient. Similar radial trends have been observed in other nearby galaxies (e.g., Kreckel et al., 2019; Grasha et al., 2022). A significant relationship has been suggested between the oxygen abundance (and N/O ratio) and the ionization parameter for star-forming regions. Initial studies of the properties of H II regions suggested that these two parameters exhibit an anti-correlation, that is, log(U) decreases as the oxygen abundance increases (e.g., Dopita & Evans, 1986). A similar trend has been found using empirical calibrators of log(U) as those used in this study, for a large sample of star-forming regions included in galaxies observed in CALIFA (see, for example, Figure 3 in Sánchez et al., 2015b). The negative radial gradients from these two parameters derived for our sample of H II regions indicate otherwise. To explore the correlation between these two parameters, we plotted the data shown in Figure 12 where these two parameters are color-coded by the galactocentric distance of the regions. As expected, we found a clear positive trend between these two parameters: metal-rich regions have a large ionization parameter. This is further quantified by the slope of the best linear fit between the two properties (black dashed line). This result contrasts with recent characterizations of large samples of H II regions in

the nearby universe. Using the same calibrators for both properties, Espinosa-Ponce et al. (2022) found a negative correlation between these two parameters (see cyan dashed line). However, they noted that for their sample of regions with low abundances ($12+\log(O/H) \lesssim 8.4$), there is indeed a negative trend of $\log(U)$ with $12 + \log(O/H)$ whereas for regions with high abundances, the trend changes to a positive one. They also mentioned that this relationship, contrary to others, is highly dependent on the calibrator of the ionization parameter. As described above, the average oxygen abundance of the regions from IC 342 is larger than that of regions in a larger sample of galaxies, such as that presented by Espinosa-Ponce et al. (2022). Thus, our results are in agreement with those presented in these studies, that is, $\log(U)$ increases with the oxygen abundance for regions with high metallicity. Although there are different possible explanations for the relationship between these two parameters (see a detailed discussion in Ji & Yan, 2022), it is important to keep in mind that we are using empirical calibrators as tracers of these two parameters. In particular, for $\log(U)$ we consider that these empirical calibrators trace the hardness of the ionizing source. However, as discussed by Espinosa-Ponce et al. (2022), these calibrators gauge the excitation level of the ionized gas, which depends on both the hardness and shape of the ionizing source. Finally, we note that similar positive trends have been observed in the 20 nearby galaxies included in the PHANGS-MUSE survey (Groves et al., 2023), suggesting that the differences in the correlations could be caused by resolution effects.

4.5. Kinematic Properties

In Figure 13 we plot the radial distribution of the kinematic properties of the H II regions detected in IC 342. For the systemic velocity (top panel), we used the value reported by (Tully, 1988, that is, 32 km s^{-1}). Regarding the line-of-sight velocity of the H II regions, we find that the north-west regions present a receding velocity, whereas the south-east regions present an approaching velocity. Our results are in agreement with those derived previously for this galaxy using Fabry-Perot observations (Hernandez et al., 2005). Although it is beyond the scope of this study, it is also necessary to explore how the variations in the line-of-sight velocity with respect to the expected circular velocity for a given radius correlate with other physical properties of the galaxy. This would be significantly useful to understand the impact of, for instance, shocks or other non-circular motions in the physical properties of the ISM. Given that a dynamical model is necessary to obtain the curve that best describes the radial distribution of the velocity of the H II regions, we do not attempt to derive a fit. As mentioned above, this is beyond the scope of this study.

The bottom panel of Figure 13 we show the radial distribution of the velocity dispersion for our sample of H II regions. As expected for a disk galaxy, the dispersion is small ($\sigma_{H\alpha} \sim 30$ km s^{-1}). Furthermore, there is no evident significant variation in the Hα velocity dispersion with

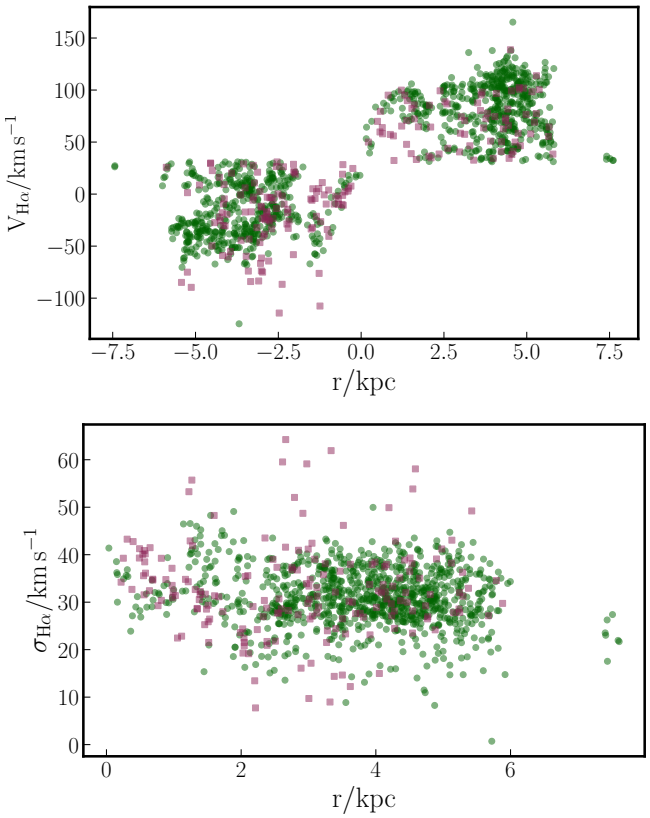

Figure 13. Radial distribution of the systemic velocity and the velocity dispersion of the H II regions (top, and bottom panels, respectively). Similar to previous plots, we segregate the regions between star and non-star forming (green circles and pink squares, respectively) .

respect to the galactocentric distance. We also note that for the outer parts of the galaxy (i.e., r > 2 kpc), the regions with larger Hα velocity dispersion are those that we consider non-star forming. In § 6 we explore whether the velocity dispersion is related to the radial residuals derived for the other physical parameters derived in this study.

5. Hα Luminosity Function

Since the Hα luminosity in an H II region is considered a tracer of the formation of young massive stars, exploring the Hα luminosity function in these regions (HαLF) will trace the massive end of the mass function in galaxies. Thanks to the spatial resolution of the dataset explored in this study, we were able to derive the HαLF for the H II candidates of IC 342, which is one of the closest galaxies where the HαLF has been explored so far. Because this function is basically a histogram of the Hα luminosity function of H II regions, the estimation of the best slope is heavily dependent on how the binning of that histogram is selected. This slope is derived using the brightest H II regions; thus, it is required to select a minimum luminosity (L_{min}), which could vary depending on the adopted binning scheme (e.g., same number of regions per bin or fixed luminosity per bin). Instead of

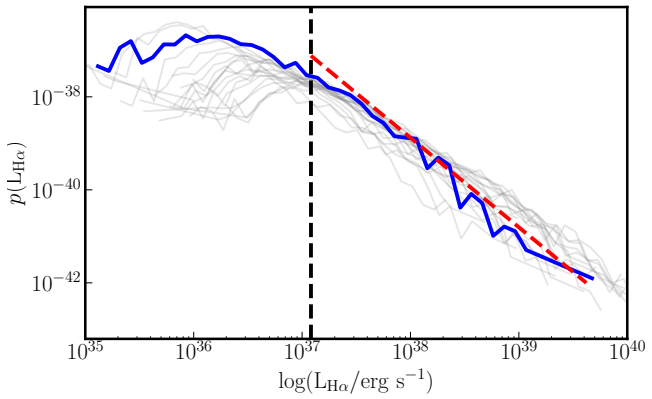

Figure 14. Probability distribution function of the Hα luminosity for the H II regions detected in IC 342 (blue solid line). This distribution function was compared with those derived for galaxies included in the PHANGS-MUSE survey (Santoro et al., 2022, gray solid lines). The red dashed line represents the best fit of the power-law to the dataset. The vertical dashed line represents the minimum luminosity used to derived the fit.

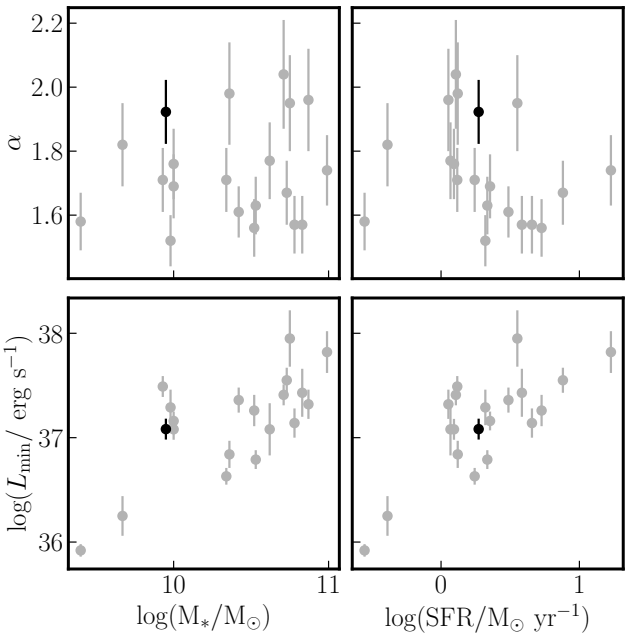

Figure 15. Comparison between the best fit parameters derived for IC 342 (α, and L_{min}; black circles) and those derived for the PHANGS-MUSE galaxies (gray circles). Right panels show these two parameters against the total stellar mass of galaxies while left panels show these parameters against the integrated SFR.

using a histogram, we followed a procedure similar to that presented by Santoro et al. (2022) to derive the HαLF for a sample of 19 galaxies included in the PHANGS-MUSE survey. Following a similar methodology also allows us to provide a direct comparison between nearby galaxies observed with IFS. In a few words, the method does not depend on any binning scheme, as it models the probability distribution function (PDF), $p(L)$, using a power-law of the form:

$$p(L) = (\alpha - 1)\, L_{\rm min}^{\alpha-1}\, L^{-\alpha} \ \text{ with } \ L \geq L_{\rm min}. \qquad (1)$$

The best fit of the HαLF was obtained using the Python package POWERLAW (Alstott et al., 2014). This algorithm uses a maximum likelihood estimation method in combination with Kolmogorov-Smirnov statistics to derive the best values of L_{min} and α, providing a robust statistical way to derive these parameters (Clauset et al., 2009; Santoro et al., 2022). To derive the uncertainties for these parameters, we ran 1000 realizations of the HαLF varying the values of the fluxes of the Hα emission within their uncertainties.

In Figure 14, we plot the PDF of the H II regions detected in IC 342 (blue solid line), the best fit of the HαLF (red dashed line), and the PDFs derived for the PHANGS-MUSE galaxies from (Santoro et al., 2022, gray lines). The PDF of IC 342 covers a similar range of luminosities as those derived for the PHANGS-MUSE sample. Its shape is also similar to that of some galaxies. The find that the best-fit values for IC 342 are $\alpha = 1.9 \pm 0.1$ and $\log(L_{min}/\mathrm{erg\ s^{-1}}) = 37.1 \pm 0.1$. We also compared these parameters with those derived for the PHANGS-MUSE galaxies. In Figure 15 we plot α and L_{min} against the integrated stellar mass and SFR (left and right panels, respectively) for the PDFs presented by (Santoro et al., 2022, grey circles) and those derived in this study for IC 342. In general, we observe that the slope of the HαLF for IC 342 and the value of L_{min} are within the dynamical range of those derived for nearby galaxies. However, we note that IC 342 exhibits one of the steepest slopes compared to those derived for the PHANGS-MUSE galaxies. This is evident for galaxies with similar stellar masses (i.e., $\log(M_*/M_\odot) \sim 10$) and SFR. In contrast, L_{min} is in the average of the values of other galaxies and follows a similar trend as the luminosities derived from the PHANGS-MUSE galaxies, as they increase with both the stellar mass and the SFR.

6. Correlation with residuals from radial trends

In § 4 we describe the radial trend of the derived properties of the H II regions in IC 342. As mentioned in that section, it is important to explore whether the correlations between the parameters still exist after removing the radial trend of these parameters. In Figure 16, we plot the correlation matrix for the radial residuals of the parameters described in § 4. This plot provides a deeper exploration of the possible relationships that these residuals could have.

From left to right, in the first column of Figure 16 we plot the radial residuals of the explored properties against the Hα luminosity residual, $\Delta L_{H\alpha}$. For $\Delta L_{H\alpha}$, we found that it strongly correlated with the residuals of EW(Hα), $\Delta EW(H\alpha)$. This is expected because the flux

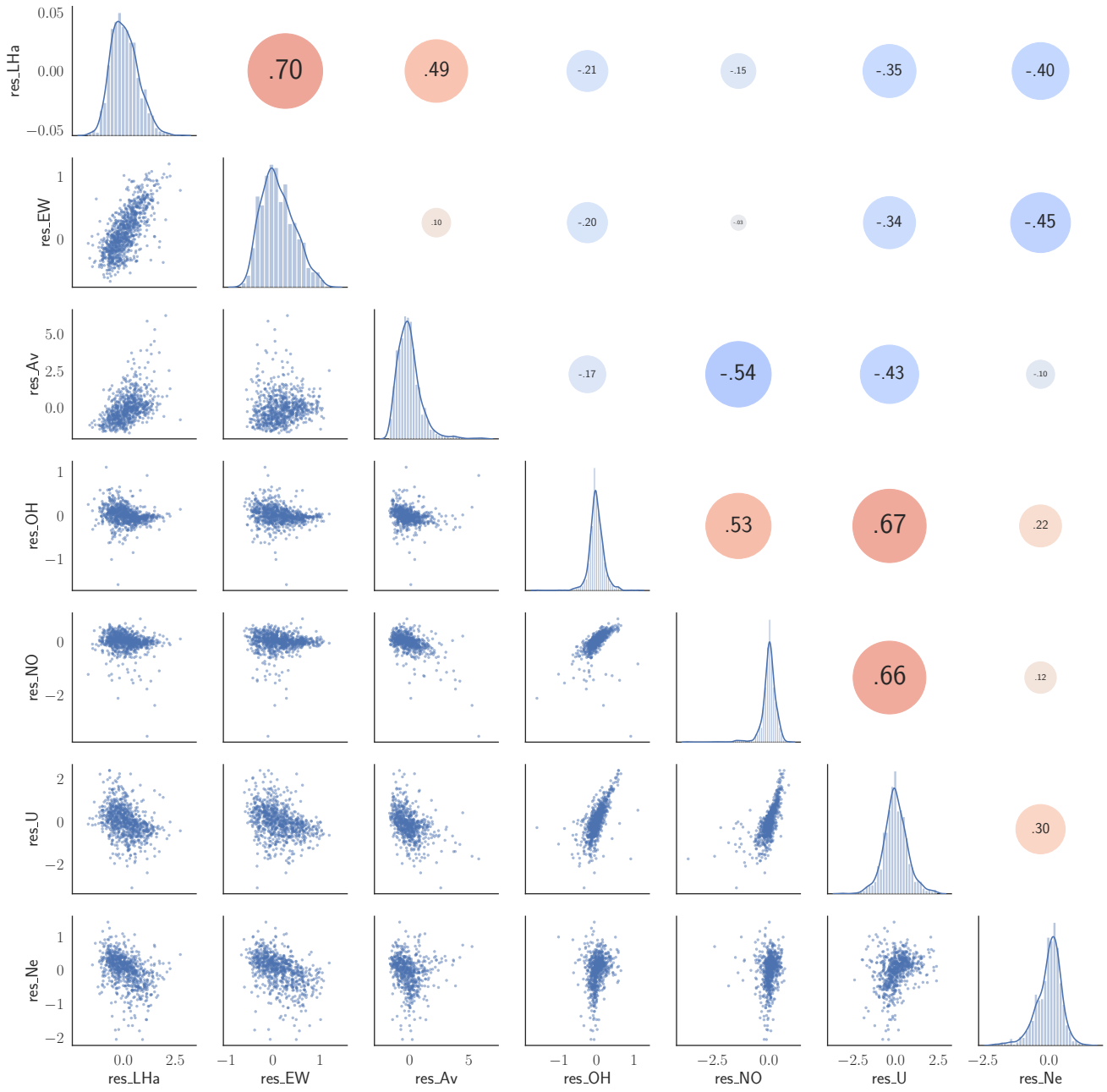

Figure 16. Correlation matrix comparing the radial residuals of the different physical properties of the regions considered as star-forming. The diagonal panels show the histogram of the residuals whereas the lower off-diagonal panels show the distributions and the upper off-diagonal panels show the Pearson's correlation coefficient for parameters corresponding to the transposed panel.

of the Hα emission line is significantly larger than the adjacent continuum for regions with a large Hα luminosity. Furthermore, the fact that we find this strong correlation using the radial residuals suggests that this correlation is independent of the galactocentric distance. In addition, the other positive correlation we find for Δ $L_{H\alpha}$is with the residuals of the optical extinction, $\Delta(A_V)$. As mentioned in Barrera-Ballesteros et al. (2020), the optical extinction in nearby galaxies traces the amount of cold gas at kpc scales. Thus, because these two parameters are usually associated with the current star-formation and the amount of available cold gas to form new stars, we could think that this is a manifestation of the well-known star-formation law (e.g., Kennicutt & Evans, 2012). For the residuals related to the chemical enrichment of the H II regions, we do not find significant correlations (i.e., $\Delta O/H$, and $\Delta N/O$, respectively). This is relevant, as it indicates that the luminosity of a given H II region does not strongly correlate

with the chemical abundance of the ISM, suggesting that the chemical content of star-forming regions is associated with the chemical enrichment from previous generations of stars (for example, Sánchez et al., 2015b). However, previous studies have suggested significant correlations between $L(\mathrm{H}\alpha)$ and the residuals of the oxygen abundance, suggesting the influence of star formation with chemical enrichment within H II regions (e.g., Kreckel et al., 2019). Finally, we found mild negative correlations between $\Delta\,\mathrm{L}_{\mathrm{H}\alpha}$ and the radial residuals of the ionization parameter and electronic density. Although we find that these three parameters present a negative radial gradient, in other words, they follow the same trend with galactocentric distance, once we remove the contribution from the radial gradient, these two properties decrease as $\Delta\,\mathrm{L}_{\mathrm{H}\alpha}$ increases. At first glance, it is not clear why for a given galactocentric distance brighter regions in Hα tend to have lower densities.

Contrary to $\Delta\,\mathrm{L}_{\mathrm{H}\alpha}$, for the residuals of EW(Hα), we do not find significant correlations with other radial residuals, except for the one derived for the electronic density. Our analysis indicates that for a given galactocentric distance, regions with large EW(Hα) tend to have lower electron densities. As for $\Delta\,\mathrm{L}_{\mathrm{H}\alpha}$, it is not clear why regions associated with large star-formation activity are less dense than those where star-formation is reduced.

For the radial residuals of the optical extinction, $\Delta(A_V)$, we found that they mainly anti-correlate with the residuals of the N/O ratio and the ionization parameter (panels in the third column from left to right in Figure 16). If N/O traces the ratio between the yield produced by old over young stars in the ISM, this result suggests that regions with chemical enrichment mostly from young stars have a larger extinction for a given galactocentric radius. This is quantitatively in agreement with the large correlation that we found between $\Delta\,\mathrm{L}_{\mathrm{H}\alpha}$ and $\Delta(A_V)$. Regarding the anti-correlation between $\Delta(A_V)$ and the residual of the ionization parameter, it could be that regions with larger amounts of dust hamper the strength of ionization. As mentioned above, the empirical calibrator that we used traces both the hardness and strength and spectral shape of the ionization source.

For the radial residuals of the oxygen abundance, $\Delta\,\mathrm{O/H}$, we find strong and similar relations to those derived previously between the oxygen abundance, N/O ratio, and ionization parameter (see Figures 9, and 12, respectively). These results suggest that these relations are independent of galactocentric distance. Regarding the residuals of the N/O ratio, as for the case of $\Delta\,\mathrm{O/H}$, we also found a significant correlation between this residual and that derived for the ionization parameter. Finally, we note that the radial residuals of the ionization parameter have a mild but present correlation with the electronic density.

As mentioned in § 4.5, we explore how the residuals of the physical relations correlate with or not with the velocity dispersion derived from Hα emission line width, $\sigma_{\mathrm{H}\alpha}$. In Figure 17, we compared the radial residuals against $\sigma_{\mathrm{H}\alpha}$. We find weak but existing anti-correlations with the other parameters derived from the Hα emission line (i.e., $\Delta\,\mathrm{L}_{\mathrm{H}\alpha}$, and ΔEW(Hα), respectively). This suggests that for a given region located in a given galactocentric distance, the smaller $\sigma_{\mathrm{H}\alpha}$, the brighter the luminosity of that region; similarly for ΔEW(Hα). This suggests that dynamically cold regions are more prone to forming new stars. We also found a mild negative correlation with the radial residual of the extinction, $\Delta\mathrm{A_V}$. This again suggests that regions with a large amount of dust, thus cold gas, are those with the lowest velocity dispersion for a given galactocentric distance. In contrast to these parameters, we found that the parameters related to the chemical abundance and ionization of the ISM mildly correlated with $\sigma_{\mathrm{H}\alpha}$. In particular, we find that $\sigma_{\mathrm{H}\alpha}$ appears to increase with the radial residual of the oxygen abundance, $\Delta\mathrm{O/H}$ suggesting that regions with large velocity dispersion are enriched in comparison to dynamically cold regions.

7. Discussion and conclusions

In this article, we explore the physical properties at sub-kpc scales of H II regions of the nearby galaxy IC 342. This study was made possible by the Integral Field Unit observations provided by the MaNGA survey. These observations, along with the data analysis pipeline devoted to the SDSS-V Local Volume Mapper (LVM), allowed us to measure the properties of the ionized gas in H II-region candidates. In comparison to other regions from large IFS surveys (such as AMUSING++), these candidates are similar in a BPT diagram, as well as in the radial distribution of their properties (see Figure 2). Depending on the explored property, IC 342 exhibits positive, flat, or negative gradients (e.g., the EW(Hα), Hα luminosity, or N/O ratio, respectively). Using a large heterogeneous set of oxygen abundance calibrators, we find that, despite the large scatter, on average, the radial gradient of the oxygen abundance for the star-forming regions in IC 342 is close to zero (see Figures 6 and 7). Other properties, such as the electron density and ionization parameter, exhibit trends similar to those derived for large samples of H II regions. Regarding the kinematic properties of these H II regions, we find that the velocity dispersion for each H II region is relatively flat across the extension of the galaxy ($\sigma_{H\alpha} \sim 30\,\mathrm{km\,s^{-1}}$). We also find that the probability distribution function of the HαLF of IC 342 is similar to that derived for other nearby galaxies (see Figure 14). Finally, in § 6 we study the possible relationships among the residuals from the radial distribution of the physical properties. Our analysis shows that, in general, the relations among different physical parameters are independent of the radial distribution of the H II regions.

Currently, there are IFU observations of thousands of galaxies, thanks to the MaNGA survey (Bundy et al., 2015). Thus, it is worth asking how the radial properties we derive for IC 342 compare to those derived for this sample of galaxies. In particular, one can ask how the oxygen

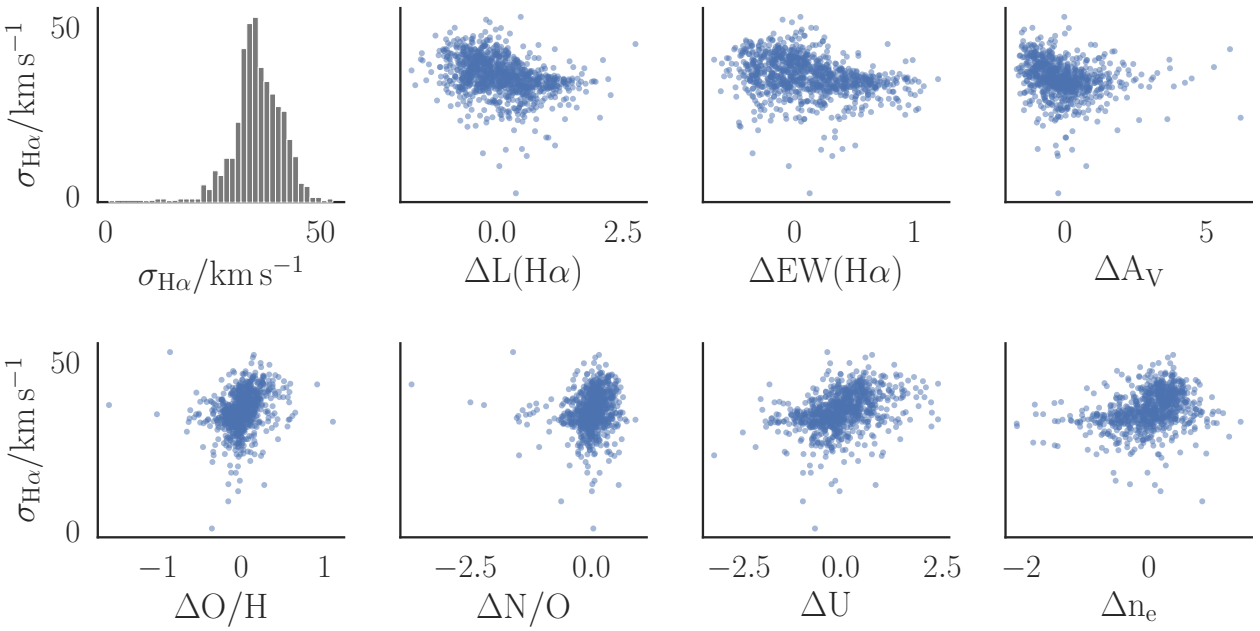

Figure 17. Comparison of the Hα velocity dispersion of the H II regions with the residuals from the different physical properties derived from the ionized gas presented in this study.

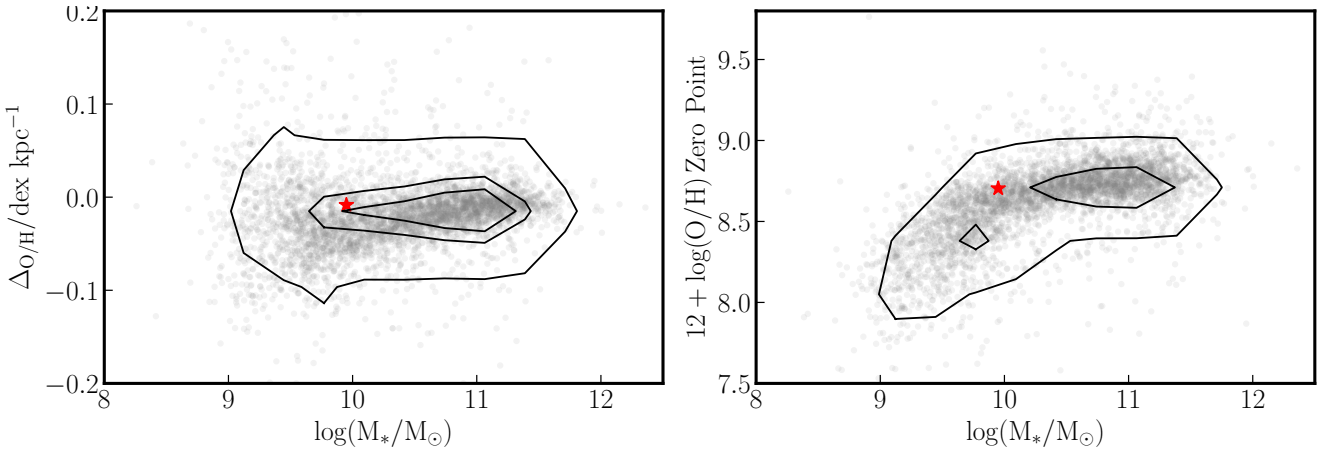

Figure 18. Comparison of the gradient (left-panel) and zero-point (right-panel) of the best of the radial distribution of the oxygen abundance derived in § 4.2 (red star) with those derived for 7533 galaxies included in the MaNGA survey (gray data points).

abundance gradient of the stellar mass of IC 342 compares with those derived from the MaNGA survey, as shown in Figure 18. In the left and right panels of this figure, we compare the slope and zero-point derived for IC 342 in § 4.2 using the Ho calibrator (red star) with those derived for 7533 galaxies drawn from the MaNGA survey (Barrera-Ballesteros et al., 2023)[2], respectively. We find that for the stellar mass of IC 342 the slope and zero-point of the oxygen abundance gradient are similar to those of galaxies with similar stellar masses in the MaNGA survey. In other words, IC 342 shares similar radial properties, at least in its oxygen abundance distribution, with galaxies of similar mass in the nearby universe. This evidence, along with the results from § 5 indicates that IC 342 has similar properties to those reported for other nearby galaxies. Thus, this encourages studies in other galaxies, particularly in the local universe (with higher spatial resolution), to quantify the role of angular resolution in setting the spatially resolved properties of galaxies.

[2]We note that for the comparison between IC 342 and the MaNGA survey, we derived a single gradient for the oxygen abundance. Furthermore, we quantified this gradient in units of dex/kpc. This is slightly different from our previous study, where we used a piece-wise analysis and the slope was measured in units of dex/R_{eff}.

Acknowledgments

J.B-B acknowledges funding from grant IA-101522 (DGAPA-PAPIIT, UNAM) and support from the DGAPA-PASPA 2025 fellowship (UNAM). L.C. thanks the support from the grant IN103820 (DGAPA-PAPIIT, UNAM). J.B-B thanks Laurent Drissen and Carmelle Robert for their useful comments that helped improve the quality of this article. KK gratefully acknowledges funding from the Deutsche Forschungsgemeinschaft (DFG, German Research Foundation) in the form of an Emmy Noether Research Group (grant number KR4598/2-1, PI Kreckel) and the European Research Council's starting grant ERC StG-101077573 ("ISM-METALS"). This research made use of Astropy,[3] a community-developed core Python package for Astronomy (Astropy Collaboration et al., 2013, 2018).

Funding for the Sloan Digital Sky Survey IV has been provided by the Alfred P. Sloan Foundation, U.S. Department of Energy Office of Science and the Participating Institutions.

SDSS-IV acknowledges the support and resources from the Center for High Performance Computing at the University of Utah. The SDSS website is www.sdss.org.

SDSS-IV is managed by the Astrophysical Research Consortium for the Participating Institutions of the SDSS Collaboration including the Brazilian Participation Group, the Carnegie Institution for Science, Carnegie Mellon University, Center for Astrophysics | Harvard & Smithsonian, the Chilean Participation Group, the French Participation Group, Instituto de Astrofísica de Canarias, The Johns Hopkins University, Kavli Institute for the Physics and Mathematics of the Universe (IPMU) / University of Tokyo, the Korean Participation Group, Lawrence Berkeley National Laboratory, Leibniz Institut für Astrophysik Potsdam (AIP), Max-Planck-Institut für Astronomie (MPIA Heidelberg), Max-Planck-Institut für Astrophysik (MPA Garching), Max-Planck-Institut für Extraterrestrische Physik (MPE), National Astronomical Observatories of China, New Mexico State University, New York University, University of Notre Dame, Observatário Nacional / MCTI, The Ohio State University, Pennsylvania State University, Shanghai Astronomical Observatory, United Kingdom Participation Group, Universidad Nacional Autónoma de México, University of Arizona, University of Colorado Boulder, University of Oxford, University of Portsmouth, University of Utah, University of Virginia, University of Washington, University of Wisconsin, Vanderbilt University, and Yale University.

APPENDICES

A. Spatial distribution of brightest emission lines

In § 2 we describe how the LVM-DAP can extract maps of the physical properties of the ionized gas emission. In Figure 19 we present the maps of the brightest four emission lines in the optical: Hα, Hβ, [N II], [O III] (from left to right, top to bottom). These maps are color-coded to the same scale, so it is easy to see that the two brightest lines are Hα, and [N II]. The weakest emission among them is [O III]; however, it is evident that the nuclear emission is brighter than the rest of the galaxy. Despite the difference in brightness, these emission lines followed a spatial distribution similar to that of the Hα emission. We used the information from these emission lines to derive the physical properties of the H II regions.

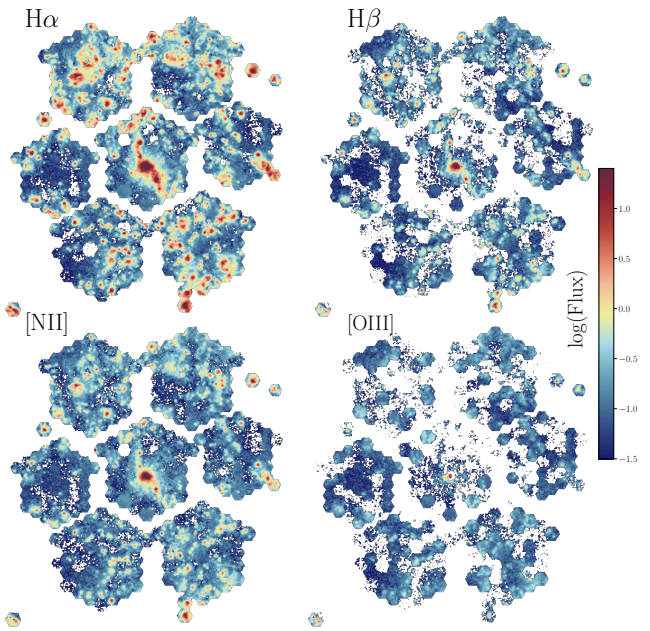

Figure 19. Maps of the flux from the four brightest emission lines in the optical measured from the MaNGA observations. From top to bottom, left to right, the Hα, Hβ, H II, and [O III] emission lines are shown. The flux units are the same for all the lines: 10^{-17}erg cm^{-2} s^{-1}.

[3] http://www.astropy.org

B. Spatial distribution of physical properties from candidates

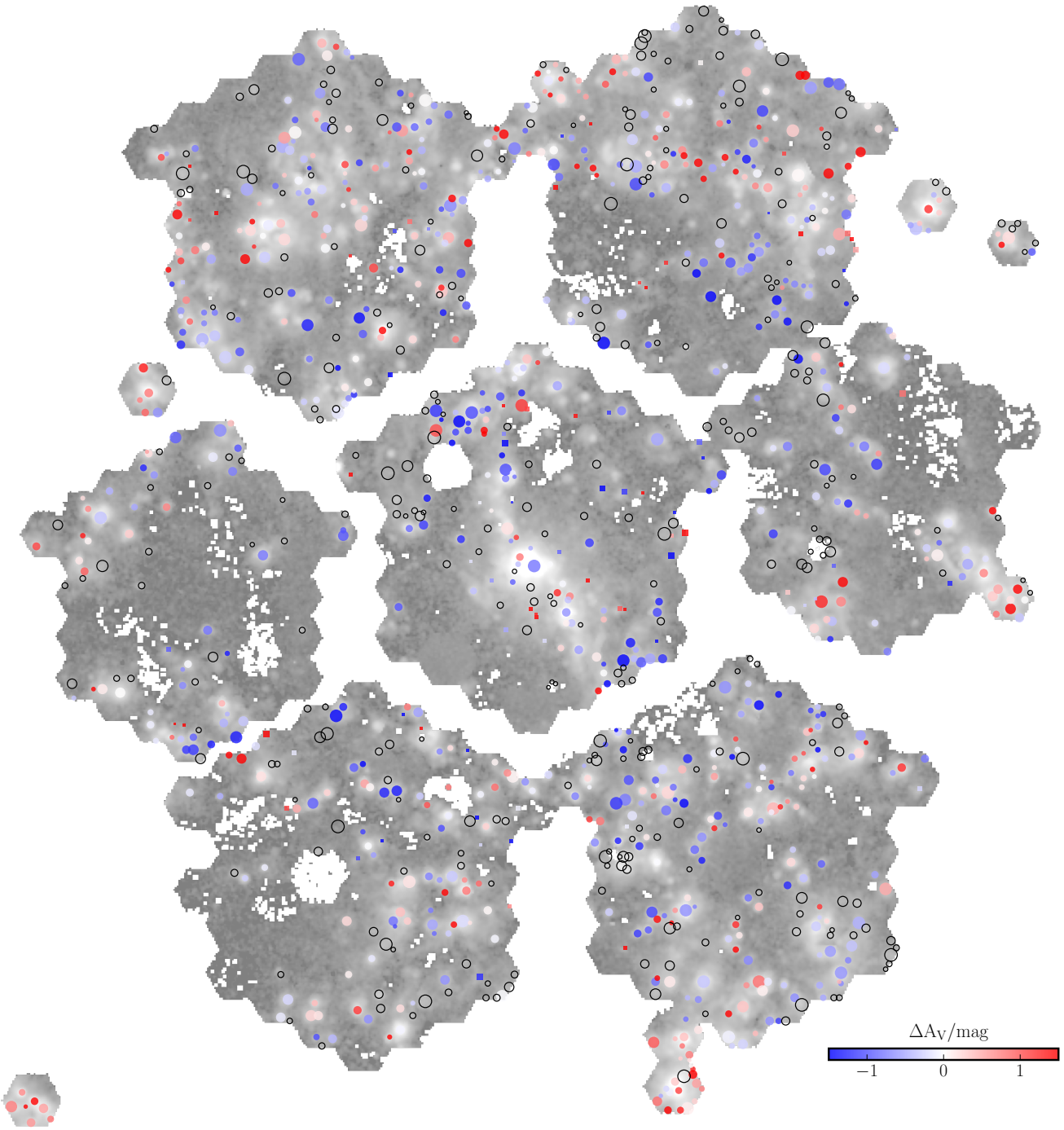

Figure 20. Similar to Figure 1, with the H II candidates color-coded by the residual with respect to the gradient of A_V derived in § 4.1. The empty regions represent those where $H\alpha/H\beta < 2.86$. Circles and squares represent star- and non-star-forming regions, respectively, according to the selection criteria described in § 3.3.

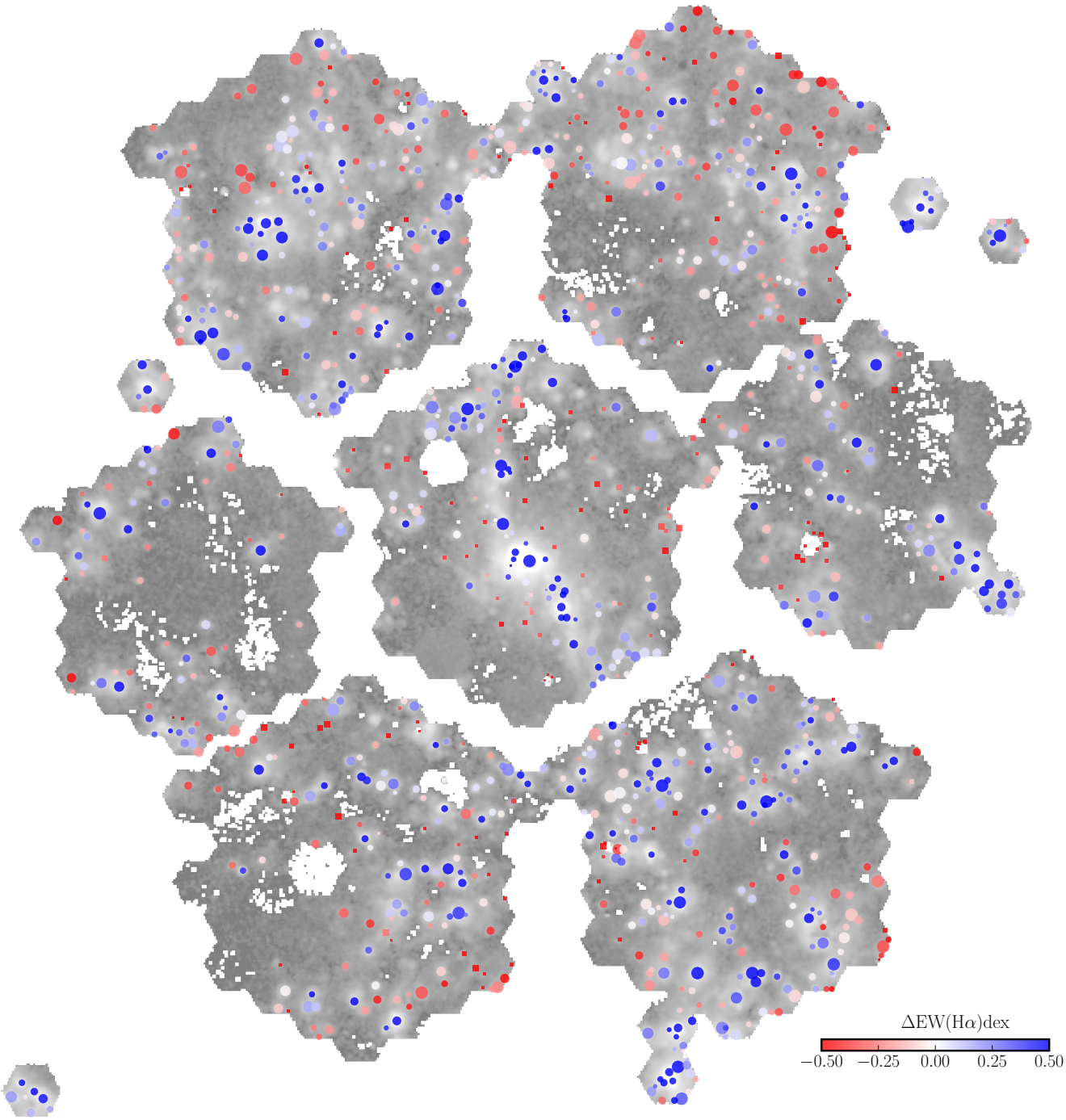

Figure 21. Similar to Figure 1, with the H II candidates color-coded by the residual with respect to the radial gradient of EW(Hα) derived in § 4.1. Circles and squares represent the star and non-star forming regions, respectively, according to the selection criteria described in § 3.3.

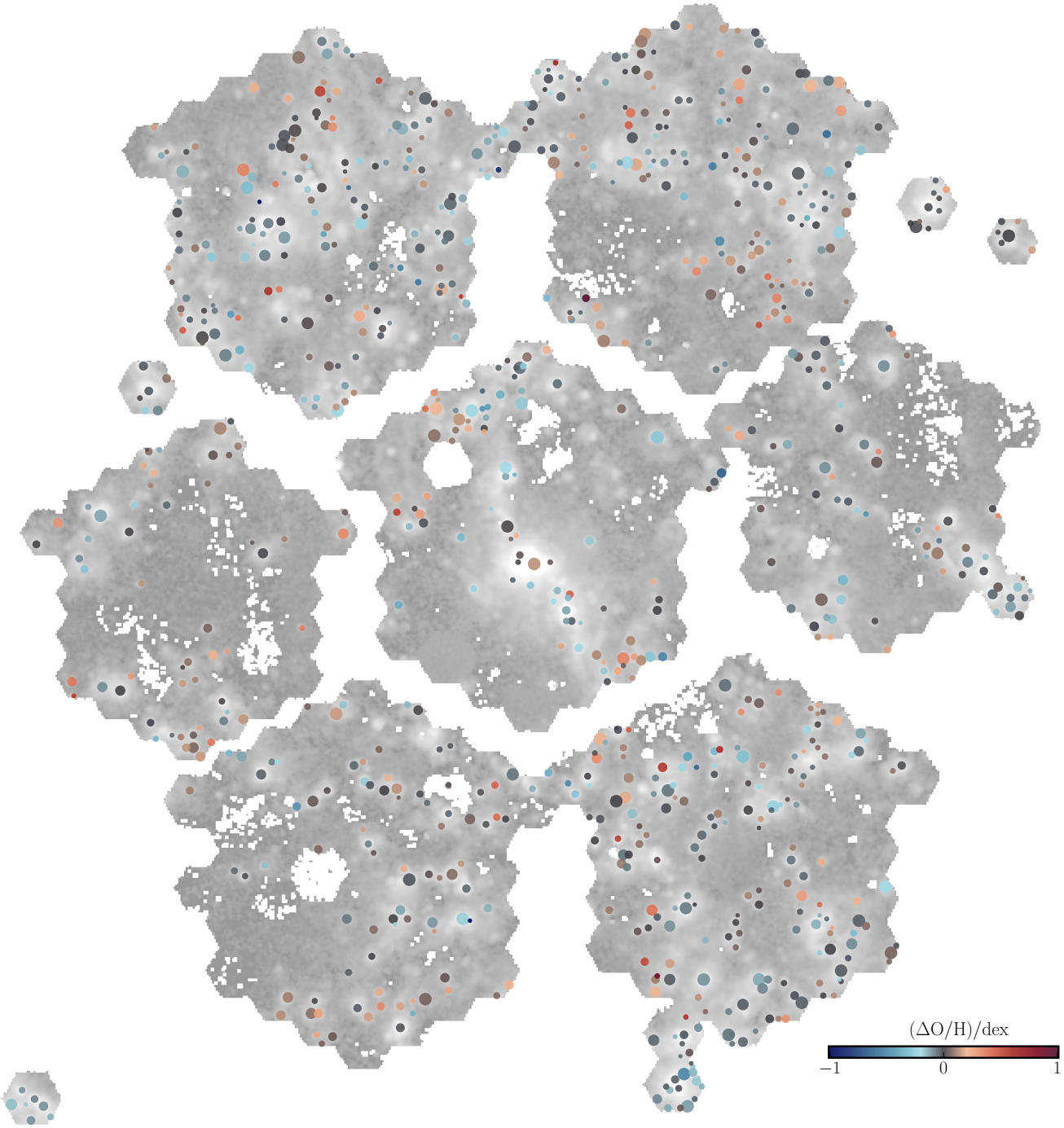

Figure 22. Similar to Figure 1, with the H II candidates color-coded by the residual with respect to the radial gradient of the oxygen abundance derived in § 4.2.

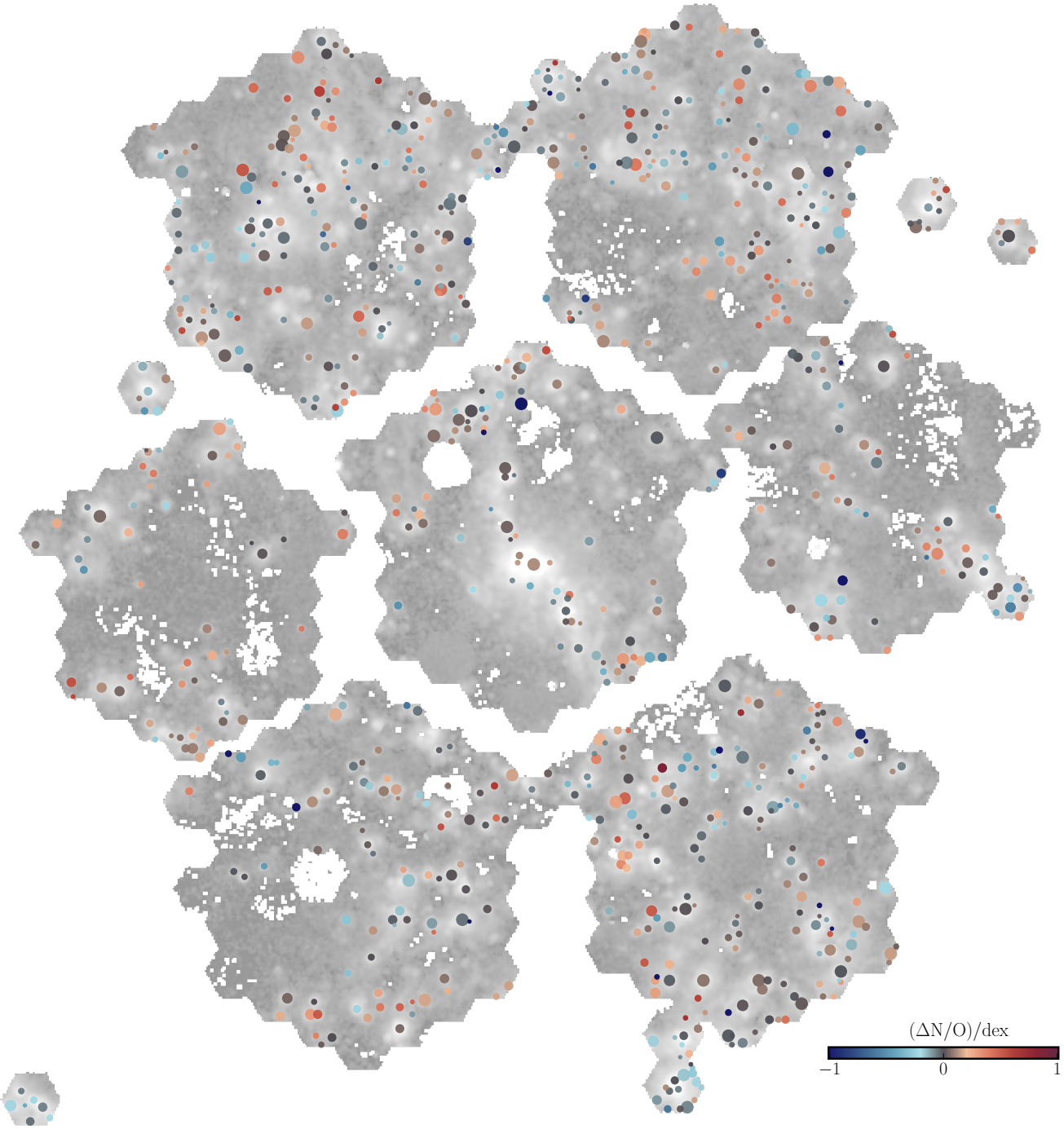

Figure 23. Similar to Figure 1, with the H II candidates color-coded by the residual with respect to the radial gradient of the N/O ratio derived in § 4.3.

References

Alstott, J., Bullmore, E., & Plenz, D. 2014, PLoS ONE, 9, e85777, doi: 10.1371/journal.pone.0085777

Anderson, L. D. 2014, in AAS, Vol. 223, American Astronomical Society Meeting Abstracts #223, 312.01

Astropy Collaboration, Robitaille, T. P., Tollerud, E. J., et al. 2013, A&A, 558, A33, doi: 10.1051/0004-6361/201322068

Astropy Collaboration, Price-Whelan, A. M., SipHocz, B. M., et al. 2018, AJ, 156, 123, doi: 10.3847/1538-3881/aabc4f

Baldwin, J. A., Phillips, M. M., & Terlevich, R. 1981, PASP, 93, 5, doi: 10.1086/130766

Barnes, A. T., Glover, S. C. O., Kreckel, K., et al. 2021, MNRAS, 508, 5362, doi: 10.1093/mnras/stab2958

Barrera-Ballesteros, J. K., Utomo, D., Bolatto, A. D., et al. 2020, MNRAS, 492, 2651, doi: 10.1093/mnras/stz3553

Barrera-Ballesteros, J. K., Sánchez, S. F., Heckman, T., et al. 2021, MNRAS, 503, 3643, doi: 10.1093/mnras/stab755

Barrera-Ballesteros, J. K., Sánchez, S. F., Espinosa-Ponce, C., et al. 2023, RMxAA, 59, 213, doi: 10.22201/ia.01851101p.2023.59.02.06

Belfiore, F., Maiolino, R., Tremonti, C., et al. 2017, MNRAS, 469, 151, doi: 10.1093/mnras/stx789

Bigiel, F., Leroy, A., Walter, F., et al. 2008, AJ, 136, 2846, doi: 10.1088/0004-6256/136/6/2846

Blanton, M. R., Bershady, M. A., Abolfathi, B., et al. 2017, AJ, 154, 28, doi: 10.3847/1538-3881/aa7567

Bradley, T. R., Knapen, J. H., Beckman, J. E., & Folkes, S. L. 2006, A&A, 459, L13, doi: 10.1051/0004-6361:20066151

Bundy, K., Bershady, M. A., Law, D. R., et al. 2015, ApJ, 798, 7, doi: 10.1088/0004-637X/798/1/7

Catalán-Torrecilla, C., Gil de Paz, A., Castillo-Morales, A., et al. 2015, A&A, 584, A87, doi: 10.1051/0004-6361/201526023

Cid Fernandes, R., Stasińska, G., Mateus, A., & Vale Asari, N. 2011, MNRAS, 413, 1687, doi: 10.1111/j.1365-2966.2011.18244.x

Cid Fernandes, R., Stasińska, G., Schlickmann, M. S., et al. 2010, MNRAS, 403, 1036, doi: 10.1111/j.1365-2966.2009.16185.x

Clauset, A., Shalizi, C. R., & Newman, M. E. J. 2009, SIAMR, 51, 661, doi: 10.1137/070710111

Croom, S. M., Lawrence, J. S., Bland-Hawthorn, J., et al. 2012, MNRAS, 421, 872, doi: 10.1111/j.1365-2966.2011.20365.x

Crosthwaite, L. P., Turner, J. L., & Ho, P. T. P. 2000, AJ, 119, 1720, doi: 10.1086/301302

D'Agostino, J. J., Poetrodjojo, H., Ho, I. T., et al. 2018, MNRAS, 479, 4907, doi: 10.1093/mnras/sty1676

Della Bruna, L., Adamo, A., Bik, A., et al. 2020, A&A, 635, A134, doi: 10.1051/0004-6361/201937173

Della Bruna, L., Adamo, A., Lee, J. C., et al. 2021, A&A, 650, A103, doi: 10.1051/0004-6361/202039402

Della Bruna, L., Adamo, A., Amram, P., et al. 2022, A&A, 660, A77, doi: 10.1051/0004-6361/202142315

Dopita, M. A., & Evans, I. N. 1986, ApJ, 307, 431, doi: 10.1086/164432

Dottori, H. A., & Copetti, M. V. F. 1989, RMxAA, 18, 115

Drory, N., MacDonald, N., Bershady, M. A., et al. 2015, AJ, 149, 77, doi: 10.1088/0004-6256/149/2/77

Drory, N., Blanc, G. A., Kreckel, K., et al. 2024, arXiv e-prints, arXiv:2405.01637, doi: 10.48550/arXiv.2405.01637

Emsellem, E., Schinnerer, E., Santoro, F., et al. 2022, A&A, 659, A191, doi: 10.1051/0004-6361/202141727

Espinosa-Ponce, C., Sánchez, S. F., Morisset, C., et al. 2022, MNRAS, doi: 10.1093/mnras/stac456

Galbany, L., Anderson, J. P., Rosales-Ortega, F. F., et al. 2016, MNRAS, 455, 4087, doi: 10.1093/mnras/stv2620

Galbany, L., Anderson, J. P., Sánchez, S. F., et al. 2020, in XIV.0 Scientific Meeting (virtual) of the Spanish Astronomical Society, 38

García-Benito, R., Pérez, E., Díaz, Á. I., Maíz Apellániz, J., & Cerviño, M. 2011, AJ, 141, 126, doi: 10.1088/0004-6256/141/4/126

González Delgado, R. M., & Pérez, E. 1997, ApJS, 108, 199, doi: 10.1086/312950

Grasha, K., Chen, Q. H., Battisti, A. J., et al. 2022, ApJ, 929, 118, doi: 10.3847/1538-4357/ac5ab2

Groves, B., Kreckel, K., Santoro, F., et al. 2023, MNRAS, 520, 4902, doi: 10.1093/mnras/stad114

Gunn, J. E., Siegmund, W. A., Mannery, E. J., et al. 2006, AJ, 131, 2332, doi: 10.1086/500975

Hernandez, O., Carignan, C., Amram, P., Chemin, L., & Daigle, O. 2005, MNRAS, 360, 1201, doi: 10.1111/j.1365-2966.2005.09125.x

Ho, I. T. 2019, MNRAS, 485, 3569, doi: 10.1093/mnras/stz649

Hodge, P. W., & Kennicutt, R. C., J. 1983, ApJ, 267, 563, doi: 10.1086/160893

Ishizuki, S., Kawabe, R., Ishiguro, M., Okumura, S. K., & Morita, K.-I. 1990, Natur, 344, 224, doi: 10.1038/344224a0

Jarrett, T. H., Masci, F., Tsai, C. W., et al. 2013, AJ, 145, 6, doi: 10.1088/0004-6256/145/1/6

Ji, X., & Yan, R. 2022, A&A, 659, A112, doi: 10.1051/0004-6361/202142312

Kauffmann, G., Heckman, T. M., White, S. D. M., et al. 2003, MNRAS, 341, 54, doi: 10.1046/j.1365-8711.2003.06292.x

Kennicutt, R. C., & Evans, N. J. 2012, ARA&A, 50, 531, doi: 10.1146/annurev-astro-081811-125610

Kennicutt, R. C., Calzetti, D., Aniano, G., et al. 2011, PASP, 123, 1347, doi: 10.1086/663818

Kewley, L. J., Dopita, M. A., Sutherland, R. S., Heisler, C. A., & Trevena, J. 2001, ApJ, 556, 121, doi: 10.1086/321545

Knapen, J. H. 1998, MNRAS, 297, 255, doi: 10.1046/j.1365-8711.1998.01493.x

Knapen, J. H., Stedman, S., Bramich, D. M., Folkes, S. L., & Bradley, T. R. 2004, A&A, 426, 1135, doi: 10.1051/0004-6361:20041584

Kollmeier, J. A., Zasowski, G., Rix, H.-W., et al. 2017, arXiv e-prints, arXiv:1711.03234, doi: 10.48550/arXiv.1711.03234

Konidaris, N. P., Drory, N., Froning, C. S., et al. 2020, in SPIE, Vol. 11447, Ground-based and Airborne Instrumentation for Astronomy VIII, ed. C. J. Evans, J. J. Bryant, & K. Motohara, 1144718, doi: 10.1117/12.2557565
Kreckel, K., Ho, I. T., Blanc, G. A., et al. 2019, ApJ, 887, 80, doi: 10.3847/1538-4357/ab5115
Kuno, N., Sato, N., Nakanishi, H., et al. 2007, PASJ, 59, 117, doi: 10.1093/pasj/59.1.117
Lacerda, E. A. D., Sánchez, S. F., Cid Fernandes, R., et al. 2020, MNRAS, 492, 3073, doi: 10.1093/mnras/staa008
Lacerda, E. A. D., Sánchez, S. F., Mejía-Narváez, A., et al. 2022, NewA, 97, 101895, doi: 10.1016/j.newast.2022.101895
Lacerda, E. A. D., Cid Fernandes, R., Couto, G. S., et al. 2018, MNRAS, 474, 3727, doi: 10.1093/mnras/stx3022
Law, D. R., Cherinka, B., Yan, R., et al. 2016, AJ, 152, 83, doi: 10.3847/0004-6256/152/4/83
López-Cobá, C., Sánchez, S. F., Moiseev, A. V., et al. 2017, MNRAS, 467, 4951, doi: 10.1093/mnras/stw3355
López-Cobá, C., Sánchez, S. F., Anderson, J. P., et al. 2020, AJ, 159, 167, doi: 10.3847/1538-3881/ab7848
Lugo-Aranda, A. Z., Sánchez, S. F., Barrera-Ballesteros, J. K., et al. 2024, MNRAS, 528, 6099, doi: 10.1093/mnras/stae345
Lugo-Aranda, A. Z., Sánchez, S. F., Espinosa-Ponce, C., et al. 2022, RAS Techniques and Instruments, 1, 3, doi: 10.1093/rasti/rzac001
McCall, M. L., Rybski, P. M., & Shields, G. A. 1985, ApJS, 57, 1, doi: 10.1086/190994
McLeod, A. F., Dale, J. E., Evans, C. J., et al. 2019, MNRAS, 486, 5263, doi: 10.1093/mnras/sty2696
McLeod, A. F., Kruijssen, J. M. D., Weisz, D. R., et al. 2020, ApJ, 891, 25, doi: 10.3847/1538-4357/ab6d63
McLeod, A. F., Ali, A. A., Chevance, M., et al. 2021, MNRAS, 508, 5425, doi: 10.1093/mnras/stab2726
Pilyugin, L. S., & Grebel, E. K. 2016, MNRAS, 457, 3678, doi: 10.1093/mnras/stw238
Pilyugin, L. S., Vílchez, J. M., & Contini, T. 2004, A&A, 425, 849, doi: 10.1051/0004-6361:20034522
Rickard, L. J., & Palmer, P. 1981, A&A, 102, L13
Rousseau-Nepton, L., Martin, R. P., Robert, C., et al. 2019, MNRAS, 489, 5530, doi: 10.1093/mnras/stz2455
Saha, A., Claver, J., & Hoessel, J. G. 2002, AJ, 124, 839, doi: 10.1086/341649
Sanchez, S. in prep, LVM Data Analysis Pipeline
Sánchez, S. F., Kennicutt, R. C., Gil de Paz, A., et al. 2012, A&A, 538, A8, doi: 10.1051/0004-6361/201117353
Sánchez, S. F., Pérez, E., Sánchez-Blázquez, P., et al. 2015a, ArXiv e-prints. https://arxiv.org/abs/1509.08552
Sánchez, S. F., Pérez, E., Rosales-Ortega, F. F., et al. 2015b, A&A, 574, A47, doi: 10.1051/0004-6361/201424873
Sánchez, S. F., Pérez, E., Sánchez-Blázquez, P., et al. 2016, RMxAA, 52, 171. https://arxiv.org/abs/1602.01830
Sánchez, S. F., Mejía-Narváez, A., Egorov, O. V., et al. 2025, AJ, 169, 52, doi: 10.3847/1538-3881/ad93bb
Sánchez-Menguiano, L., Sánchez, S. F., Pérez, I., et al. 2018, A&A, 609, A119, doi: 10.1051/0004-6361/201731486
Santoro, F., Kreckel, K., Belfiore, F., et al. 2022, A&A, 658, A188, doi: 10.1051/0004-6361/202141907
Schlafly, E. F., & Finkbeiner, D. P. 2011, ApJ, 737, 103, doi: 10.1088/0004-637X/737/2/103
Smee, S. A., Gunn, J. E., Uomoto, A., et al. 2013, AJ, 146, 32, doi: 10.1088/0004-6256/146/2/32
Tully, R. B. 1988, JBAA, 98, 316
Vicens-Mouret, S., Drissen, L., Robert, C., et al. 2023, MNRAS, 524, 3623, doi: 10.1093/mnras/stad2154
Yan, R., Tremonti, C., Bershady, M. A., et al. 2016, AJ, 151, 8, doi: 10.3847/0004-6256/151/1/8
Zhu, Y.-N., Wu, H., Li, H.-N., & Cao, C. 2010, RAA, 10, 329, doi: 10.1088/1674-4527/10/4/004
Zibetti, S., Charlot, S., & Rix, H.-W. 2009, MNRAS, 400, 1181, doi: 10.1111/j.1365-2966.2009.15528.x